Thermo-mechanical loading of intact rock and discontinuities

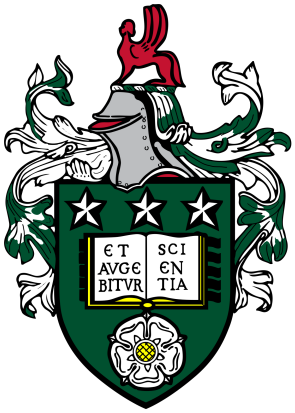

James Woodman

University of Leeds

School of Earth & Environment

Submitted in accordance with the requirements for the degree of

Doctor of Philosophy

March, 2020

Intellectual Property Statement

The candidate confirms that the work submitted is his own and that appropriate credit has been given where reference has been made to the work of others.

Acknowledgements

The research presented in this thesis was generously supported by the Engineering and Physical Sciences Research Council (EPSRC), through an Industrial Cooperative Award in Science and Technology (iCASE) partnership with Arup.

I would like to acknowledge Dr. Bill Murphy for guidance whilst also providing a working environment in which I was able to overcome challenges independently, and Dr. Mark Thomas for general supervision and support.

Laboratory testing underpins this study, and I would like to thank Dr. Helen Reeves for making the use of the Rock Mechanics & Physics Laboratory (RMPL) at the British Geological Survey (BGS) possible. The team you have developed in Keyworth is enviable, and I appreciate your advice as I have evolved as an early career scientist. I would not have completed this PhD without the guidance of Dr. Audrey Ougier-Simonin. Thank you for always finding the time for me regardless of other challenges and commitments. Your passion for science and outlook on life in general is admirable. I hope to continue to work with you if you'll have me back in your lab. Thanks also go to Marcus Dobbs and Matt Kirkham for their input into experimental design (however cynical), and for baby sitting me in the early days whilst I caused destruction.

From Tom Berry's initial project proposal the connection with Arup throughout this work has been indispensable. The insight Dr. Tasos Stavrou and Dr. Ioannis Vazaios provided to modelling was invaluable. I'm glad the battle with UDEC has been won (for now). Amy Nettleship, Sue Thomson, Mike Osborne, and all other colleagues, I have enjoyed working with you. The culture at Arup is unique.

Discussions with those in office 7.131 (past and present) over the last few years have taught me more than I wanted to know about life, and probably more than I have learnt about rock mechanics. Nonetheless you have kept me sane throughout, thank you all.

Finally I would like to thank my parents, family, friends, and Jennifer for your love and support, always.

I'm proud of the work produced herein, and I hope you all can be too.

Abstract

Coupled thermo-mechanical processes present challenges in a number of areas of geological understanding. Thermal loading can occur due to the natural geothermal gradient or the introduction of an anthropogenic heat source in a rock mass. In this study the thermo-mechanical behaviour of intact rock and discontinuities is investigated through both laboratory experiments and their numerical simulations. A new method was devised for creating synthetic discontinuous specimens with representative discontinuity topography suitable for thermo-mechanical triaxial testing. Different synthetic compositions were trialled to achieve a composition representative of a sedimentary lithology. Whilst synthetic discontinuities could repeatedly be created with representative topography, a synthetic composition with mechanical characteristics of a sedimentary lithology could not be created. Following testing of synthetic specimens, thermo-mechanical triaxial experiments were then performed on intact specimens of sandstone at temperatures up to 100 °C. Additionally these experiments were repeated under the same thermo-mechanical conditions on specimens with a single pre-existing discontinuity running through the specimens at 30° from the vertical, allowing shearing to occur on the discontinuity under triaxial conditions. Laboratory results of testing on sandstone showed a reduction of up to 15% peak strength with increasing thermal loading between ambient temperature and 100 °C for intact specimens, whereas specimens with discontinuities present an initial increase in discontinuity peak shear strength with increasing thermal loading to 50 °C, before a reduction in peak shear strength thereafter. The laboratory experiments were replicated using thermo-mechanically coupled discrete element method grain based models. The grain based models highlight the build up of thermally induced localised stresses within the intact specimens due to grain scale heterogeneity of thermal properties, resulting in the initiation and accumulation of tensile thermal micro-cracks, causing reduced strength. When a discontinuity is introduced to the models, the discontinuity allows room for thermal expansion resulting in thermal closure, until maximum thermal closure is reached. Thermal micro-cracking then occurs as observed in the intact specimens, causing a reduction in strength. These findings offer new contributions to the understanding of the thermo-mechanical behaviour of intact rock and discontinuities.

Contents

List of Figures

List of Tables

LIST OF TABLES

Abbreviations

2D	Two dimensional	EDXA	Energy-dispersive X-ray analysis
3D	Three dimensional	FDM	Finite difference method
ABS	Acrylonitrile butadiene styrene	FEM	Finite element method
ANOVA	Analysis of variance	*FISH*	FLAC-ish
APSE	Äspö Pillar Stability Experiment	FJM	Flat-joint model
ASTM	American Society for Testing & Materials	GBM	Grain based model
BEM	Boundary element method	GDF	Geological disposal facility
BGS	British Geological Survey	HLW	High-level radioactive waste
BPM	Bonded particle model	HRL	Hard Rock Laboratory
BSEM	Backscattered electron imaging	ICP	Iterative closest point
c.	Circa	ISRM	International Society for Rock Mechanics
CAC	Calcium aluminate cement	LVDT	Linearly variable displacement transducer
CAD	Computer aided design	M3C2	Multiscale model to model cloud comparison
D	Fractal dimension	Ma	Million years ago
DDA	Discontinuous deformation analysis	MK	Metakaolin
DEM	Discrete element method	NDA	Nuclear Decommissioning Authority

ONWI	Office of Nuclear Waste Isolation
PFC	Particle Flow Code
PID	Proportional-integral-derivative
PLA	Polylactic acid
PTFE	Polytetrafluoroethylene
R^2	Coefficient of determination
RMEGG	Rock Mechanics Engineering Geology & Geotechnics
RMPL	Rock Mechanics & Physics Laboratory
RMS	Root mean square
SEM	Scanning electron microscope
SJM	Smooth
THM	Thermo-hydro-mechanical
UCS	Uniaxial compressive strength
UDEC	Universal Distinct Element Code
UK	United Kingdom
URL	Underground research laboratory
XRD	X-ray Diffraction

Nomenclature

α_A	Area thermal expansion coefficient	$\sigma_1^{'}$	Major effective principal stress
α_L	Linear thermal expansion coefficient	σ_2	Intermediate principal stress
β	Angle	σ_3	Minor principal stress
δ_{ij}	Kronecker delta	$\sigma_3^{'}$	Minor effective principal stress
Δu_d	Displacement of discontinuity	σ_a	Axial stress
Δu_i	Displacement of intact material	σ_n	Normal stress
Δu_t	Total displacement	σ_t	Tensile strength
$\Delta\tau_b$	Stress drop between peak and residual shear strength	σ_{tm}	Micro-tensile strength
μ	Coefficient of friction	σ_{tmr}	Micro-residual tensile strength
ν	Poisson's ratio	σ_{xx}	x-component of stress
ν_m	Micro-Poisson's ratio	τ	Shear stress
κ	Thermal diffusivity	τ_p	Peak shear stress
ϕ	Friction angle	τ_r	Residual shear stress
ϕ_b	Basic friction angle	ε	Strain
ϕ_m	Micro-friction angle	ε_a	Axial strain
ϕ_{mr}	Micro-residual friction angle	ε_c	Circumferential strain
ϕ_r	Residual friction angle	ε_d	Diametral strain
φ	Porosity	ε_r	Radial strain
ρ	Density	ε_v	Volumetric strain
ρ_d	Dry density	Ø	Diameter
ρ_w	Density of water	c	Cohesion
σ_1	Major principal stress	CD	Crack damage

CI	Crack initiation	h	Convective heat transfer coefficient
c_m	Micro-cohesion	i	Inclination angle
c_{mr}	Micro-residual cohesion	JCS	Joint compressive strength
c_j	Apparent joint cohesion	JRC	Joint roughness coefficient
c_p	Specific heat capacity	K	Bulk modulus
D	Fractal dimension	K_m	Micro-bulk modulus
D	Shear displacement	k	Thermal conductivity
$\mathrm{D_0}$	Shear displacement at an extrapolation with residual shear stress	k_{ij}	Thermal conductivity tensor
$\mathrm{D_a}$	Shear displacement at peak shear stress	k_n	Normal stiffness
$\mathrm{D_a}$	Shear displacement at peak shear stress	k_{ni}	Initial normal stiffness
$\mathrm{D_{app}}$	Apparent shear displacement	k_s	Shear stiffness
$\mathrm{D_c}$	Shear displacement at residual shear stress	k_n/k_s	Stiffness ratio
$\mathrm{D_{el}}$	Elastic component of apparent shear displacement	L	Length
$\mathrm{D_{wc}}$	Shear displacement between peak and residual shear stress	M	Mass
E	Young's modulus	M_{sat}	Saturated-surface-dry mass
E_m	Micro-Young's modulus	M_{sub}	Saturated-submerged mass
F_n	Normal force	m_i	Hoek-Brown material constant
F_s	Shear force	M_s	Dry mass
G	Shear modulus	P	Peak load
$\mathrm{G_c}$	Fracture energy	Q_i	Thermal flux
$\mathrm{G_{c1}}$	Fracture energy to reach peak shear stress	Q_{net}	Net heat flow
$\mathrm{G_{c2}}$	Fracture energy between peak and residual shear stress	r	Radius
G_m	Micro-shear modulus	R_p	Roughness profile index

T	Temperature
t	Time
t	Thickness
u_{max}	Maximum normal displacement (closure)
u_n	Normal displacement (closure)
u_{nc}	Current normal displacement (closure)
V	Bulk volume
V_w	Water volume
Z_2	Root mean square first derivative

Chapter 1

Introduction

1.1 Research motives

The mechanical behaviour of intact rock, rock discontinuities and the way in which they interact to behave as a rock mass, are relatively well understood at low stresses and ambient temperatures. This understanding allows the successful engineering design of structures on rock and in rock at shallow depths, such as rock slopes, dams, shafts, tunnels and caverns. However, as a result of the increasing needs of modern society in infrastructure, resources and underground facilities, engineering capabilities and technologies are being continually developed and advanced. This results in structures being designed within rock masses at greater depths, where they are expected to withstand not just greater stresses, but also elevated temperatures, and for longer design lives. The thermal loading of a rock mass can occur due to the geothermal gradient in the cases of deep tunnelling, mining and geothermal heat production, or due to the heat generation from high-level radioactive waste (HLW) in a geological disposal facility (GDF). Characterising the behaviour of intact rock and discontinuities at these thermal and mechanical conditions is therefore paramount to understanding the way their behaviours combine as rock mass behaviour.

Whilst the thermo-mechanical behaviour of rock at temperatures and stresses applicable to Earth crustal processes have been well studied, the engineering properties of rocks under thermo-mechanical conditions applicable to engineering design are less well researched. It is however known from large scale thermo-hydro-mechanical (THM) experiments, primarily at underground research laboratories (URLs) related to the development of GDFs (Barton, 1982; George et al., 1999; Hardin et al., 1982; Zimmerman et al., 1985), that thermal loading can induce localised compressive and tensile stresses, potentially complicating stress distributions around excavations and thermally closing discontinuities. Thermal loading also has potential to produce differing deformation modulus, and lower thermal expansions than expected (Barton, 2007).

Modern engineering design is normally validated with analytical calculations and numerical simulations, however neither currently commonly include thermo-mechanical effects. If thermo-mechanical effects are included in large scale numerical design simulations, for example in the simulation of GDFs, finite element method (FEM) modelling

is commonly used where discontinuities are not simulated, and hence the thermal behaviour of discontinuities is not explicitly accounted for. Before such phenomena can be intelligently included in engineering design they first require further investigation at a smaller scale, where the fundamental thermo-mechanical behaviour of intact rock and discontinuities can be isolated and identified. If these effects are identified as being of importance for engineering design of structures in rock masses exposed to thermo-mechanical loading, these mechanisms can then be upscaled and included in new constitutive models to allow more intelligent design.

1.2 Research aim and objectives

The aim of this study is to provide a better understanding of the thermo-mechanical behaviour of intact rock and discontinuities that is currently not accounted for in the design of engineering structures in geological environments. Specifically, this study will investigate the properties of lower strength sedimentary lithologies (Metcalfe et al., 2015), which are one group of generic lithologies proposed for siting a GDF in the UK. This study will utilise laboratory testing and numerical modelling to address the following objectives:

- design a method to consistently create replica rock discontinuities with identical topographies in synthetic specimens suitable for laboratory triaxial shear testing under thermo-mechanical conditions encountered in engineering environments;
- create a synthetic composition with strength and stiffness properties representative of a lower strength sedimentary lithology, into which replica rock discontinuities can be created and tested under different thermo-mechanical loads;
- identify a suitable lithology (or lithologies) and characterise the mechanical properties at ambient temperature conditions, to provide inputs for numerical modelling and for use as baseline properties;
- carry out thermo-mechanical laboratory testing on both intact specimens and discontinuities in the above lithology (or lithologies), to explore the differences in behaviour at ambient conditions and under thermal loading;
- create numerical simulations calibrated to the mechanical characterisation labor-

atory testing of intact rock specimens;

- thermally couple the numerical simulations to allow further investigation of the mechanisms of damage due to thermal effects; and
- introduce a discontinuity to the numerical simulations with properties and topography representative of the discontinuities in laboratory specimens and further explore the processes occurring in thermo-mechanical triaxial testing on discontinuous specimens.

1.3 Thesis outline

As per the flow diagram presented overleaf, this thesis contains seven chapters. Chapter 2 provides a review of published literature on the thermo-mechanical behaviour of rock. This includes a review of cases of thermo-mechanical loading in geological environments, in addition to sections on the techniques used to investigate different aspects of thermo-mechanical behaviour, particularly through laboratory experiments, as well as through different numerical modelling techniques. Chapter 3 outlines the specimen preparation techniques, laboratory apparatus and test methods used to undertake laboratory testing throughout Chapters 4 and 5. In Chapter 4, a new technique for the preparation of identical synthetic specimens containing discontinuities with the same topographical and mechanical characteristics is presented, as well as testing different synthetic compositions for suitability as rock analogues. In Chapter 5, thermo-mechanical testing on intact and discontinuous specimens of two lower strength sedimentary lithologies is carried out and discussed. In Chapter 6, thermo-mechanically coupled grain based numerical simulations are presented of the laboratory testing undertaken in Chapter 5, to allow further investigation of the thermo-mechanical processes. Finally, in Chapter 7, the key findings from each results chapter are discussed with broader implications, and conclusions drawn in accordance with the research objectives. In addition, suggestions are proposed for related areas of future research highlighted by the work within this study.

Aim

To provide a better understanding of the thermo-mechanical behaviour of intact rock and discontinuities that is not currently accounted for in engineering design.

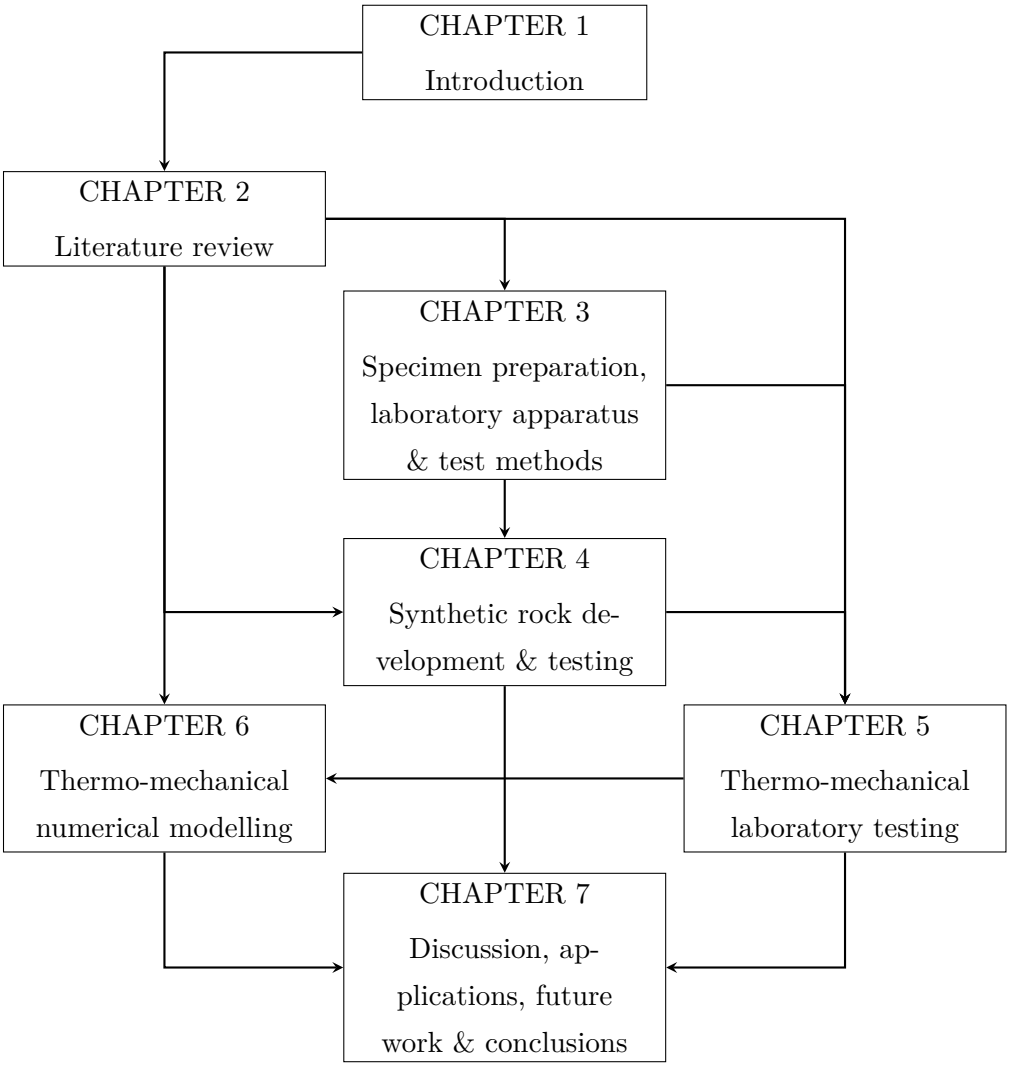

Chapter 2

Thermo-mechanical behaviour of rock: a review

2.1 Introduction

This chapter provides a review of the different parts of this study. Firstly a brief review is provided of general cases of thermo-mechanical loading in rock. This is followed by more detailed sections on the typical techniques used to investigate different aspects of thermo-mechanical behaviour of intact rock and discontinuities at an engineering scale, including the development of the science, and the limitations and assumptions of previous studies. The chapter culminates with a summary of how this study builds on the current body of research to help understand the thermo-mechanical behaviour of intact rock and rock discontinuities with applications for engineering design.

2.2 Thermo-mechanical loading in geological environments

Thermo-mechanical loading of rock occurs naturally in the geological environment due to the geothermal gradient. In typical continental crust the geothermal gradient in the first 5 km is approximately 25 °C km^{-1}, with localised fluctuations occurring due to ground surface temperature, localised geothermal heat flow, geological structure, thermal conductivity and water circulation (Rybach and Pfister, 1994). Understanding the mechanical behaviour of rocks at elevated temperatures is important for investigating a number of geological processes in the Earth's crust including folding, geothermal activity, magmatic intrusions and plate tectonics (Heuze, 1983). Thermal loading due to the geothermal gradient is also of importance in engineering scenarios. The world's deepest mine, the TauTona gold mine in South Africa, at a depth of 3.9 km, is currently operating at rock temperatures of 60 °C (Neingo and Tholana, 2016). Deep tunnelling projects also experience elevated temperatures, with rock temperatures of 46 °C experienced at the Gotthard Base Tunnel at a depth of 2.5 km (AlpTransit, 2016; Rybach and Pfister, 1994).

Climate and weather can also induce thermo-mechanical loading in surface rock, with diurnal temperature fluctuations of greater than 50 °C causing strength and stability issues, termed thermal stress erosion (Eppes and Keanini, 2017). Cases have been documented in natural environments, such as rock falls in Yosemite, California, induced due to thermal exfoliation of the granite rock cliffs (Collins and Stock, 2016) and

thermal spalling of dolerite boulders in Antarctica (Lamp et al., 2017). Thermal stress erosion can also occur to building stone and façade materials, both from diurnal solar temperature fluctuations, as well as fire damage, potentially causing micro-cracking, increased porosity, strength loss and spalling (Siegesmund et al., 2018).

Thermo-mechanical loading of rock also occurs due to anthropogenic sources, such as in underground coal gasification processes, and in the emplacement of radioactive waste in GDFs. HLW is defined in the United Kingdom (UK) as waste in which the temperature may rise significantly as a result of its radioactivity, such that it should be taken into account in designing disposal facilities. The disposal of HLW in a GDF in a suitable underground geological formation, is considered the best option to isolate HLW from the biosphere until it has decayed to levels that pose no significant risk (Fairhurst, 2004). The construction of a GDF is the UK Government's policy for the long term management of HLW. Different countries globally are at different stages in researching and developing their GDF with different storage methods and host lithologies being investigated (Table 2.1). The UK is still in the early stages of GDF development, currently undertaking a national geological screening, and discussing potential siting locations with local communities (Department for Business Energy & Industrial Strategy, 2018).

Country	Location	Geology	Status
Belgium	-	clay	under discussion
Finland	Olkiluoto	gneiss	under construction
France	-	mudstone	siting
Germany	Saxony	evaporite	on hold
United Kingdom	-	-	siting
United States	Yucca Mtn, Nevada	ignimbrite	cancelled (2010)

Table 2.1: Location, geology and status of some different geological disposal facilities globally.

Although in the early stages of GDF development, the Nuclear Decommisioning Authority (NDA) has commissioned numerous generic research studies, including looking at the potential degree of thermal loading on host rock lithologies (Quintessa, 2012). Following the UK model for geological disposal, a single package of HLW will be out-

putting 17 kW of power when first deposited, degrading over the first 5,000 years after emplacement. The thermal loading on the rock mass due to the emplaced packages occurs predominantly through conduction and is dependent on the thermal conductivity of the geological unit, the GDF layout, canister spacing, barrier system, degree of saturation, and the size and depth of the GDF. The worst case thermal load on the rock mass in the near vicinity of emplaced canisters is likely to be approximately 60 °C in addition to the geothermal gradient, peaking approximately 50 years after emplacement and decreasing thereafter (Quintessa, 2012).

Whilst the UK is still in a siting process for a GDF, Radioactive Waste Management (RWM) has proposed six potential generic host lithologies. One proposed lithology, which is the target of this study, is a lower strength sedimentary lithology. In Chapter 4, it will be attempted to create a synthetic lithology analagous to a lower strength sedimentary lithology, to allow repeated testing under various conditions. In Chapter 5, two sedimentary lithologies with mechanical properties within the ranges proposed by Metcalfe et al. (2015) for a lower strength sedimentary lithology (§ 4.6) will be tested under thermo-mechanical triaxial conditions in the laboratory.

2.3 Brittle deformation and failure of intact rock

The brittle behaviour of intact rock in compression is key to many rock engineering problems. During engineering construction the stress field may be altered, causing the peak strength of the rock to be exceeded and failure to occur. Failure such as spalling can also occur in high stress environments when the rock mass is excavated and unloaded, as long as the stress is above the crack initiation threshold and micro-cracking has been induced (Diederichs, 2007, 2003). It is therefore key to understand the full deformation behaviour of intact rock and its behaviour under different loading conditions, as the stress environment does not necessarily need to be near the peak strength of the rock for failure to occur.

The initiation of cracks was first studied by Griffith (1921), who examined the propagation of cracks from small flaws, so-called 'Griffith Cracks', in glass rods under tensile loading. Cracks propagate when an excess in energy develops due to loading, which

causes an increase in crack length. Griffith (1924) expanded his failure criterion to include compressive loading, proposing that cracks propagate along flaws due to locally induced tensile stresses at crack tips exceeding the tensile strength of the contact. In crystalline and granular rocks, the Griffith flaws are the grain boundaries and during loading, stress can be concentrated at these flaws resulting in micro-crack initiation.

Brace et al. (1966) studied the brittle failure in rocks under uniaxial compressive loading. It was found that when increasing loading, cracks began to initiate causing a deviation from linearity in the volumetric compaction of the specimen (Fig. 2.1C). The axial stress at which this occurs was termed fracture or 'crack initiation' (CI) by Bieniawski (1967). Various methodologies have since been proposed to determine this point of crack initiation in the laboratory, including using acoustic emissions (Eberhardt et al., 1998), axial strain (Stacey, 1981) and lateral strain (Martin and Chandler, 1994). From the point of crack initiation, further tensile fractures develop in a stable manner parallel to the applied load (Lajtai and Lajtai, 1974) (Fig. 2.1D), before becoming randomly distributed throughout the specimen. At the crack damage (CD) threshold micro-cracks begin to interact, coalesce and localise (Fig. 2.1E). The crack damage threshold has been shown to be detected in the laboratory as the point of volumetric strain inflection from compaction to dilation. Unstable crack growth then occurs up to the peak strength and the formation of a macroscopic discrete fracture occurs, which then undergoes shearing to a residual strength (Fig. 2.1G).

Of particular importance to the brittle behaviour of clastic sedimentary lithologies is the role of porosity. There is an negative exponential relationship between porosity and brittle strength (Dunn et al., 1973), because with increasing porosity fewer tensile micro-cracks between grains are required before coalescence into a macroscopic shear fracture occurs. Additional deformation processes can also occurs in porous rocks, with pore collapse occurring until the grains become rigidly interlocked, at which point tensile micro-cracking is then initiated (Dunn et al., 1973).

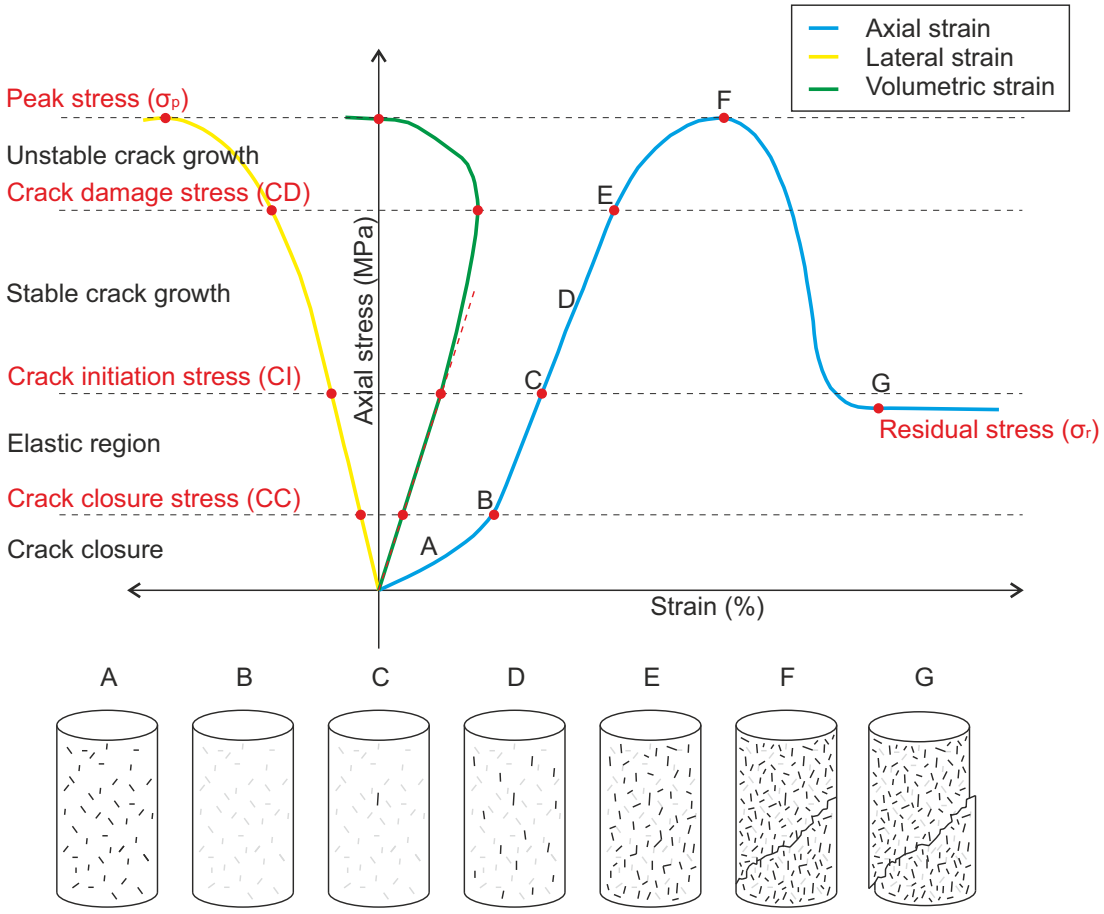

Figure 2.1: Different stages of micro-cracking and damage accumulation within specimens of intact rock loaded in compression.

2.4 Mechanics of discontinuities

2.4.1 Definition of a 'discontinuity'

Definitions of what comprises a discontinuity vary widely between geologists, engineers and the different international standards. Geologists commonly loosely and somewhat subjectively refer to discontinuities as being planes of weakness within rock masses, without having to infer geological origins. However, because joints are the most common type of discontinuity encountered in rock mechanics and engineering, the word 'joint' is often used synonymously with 'discontinuity'. There are many types of discontinuity, commonly categorised by their method of formation e.g. joints; fractures; faults; shear zones; and bedding, and the geological origins of a discontinuity can affect the mechanical properties of the discontinuity. The International Society for Rock Mechanics (ISRM, 1978) define a discontinuity as "any mechanical planar feature in a rock mass having zero or low tensile strength". Whilst the American Society for Testing Materials' (ASTM, 2008) definition includes features with considerably greater strength such as cleavage and bedding. Throughout this study the terms tabulated in Table 2.2 will be used to refer to different planes of weakness.

Type	Definition
Discontinuity	a pre-existing plane of weakness in rock regardless of geological origin
Fracture	the formation of a new discrete macroscopic plane of failure due to mechanical or thermal loading
Micro-crack	the formation of a discrete microscopic plane of failure due to mechanical or thermal loading

Table 2.2: Definitions of different planes of weakness used throughout this study.

2.4.2 Shear strength of discontinuities

The main components contributing to the shear strength of clean rock discontinuities are:

- true cohesion - this only exists in incipient discontinuities, where localised intact rock along a discontinuity contributes to the strength;
- friction due to large scale roughness - large-scale first order undulations and waviness (metre scale, measurable in the field) and second order roughness (centimetre scale, measurable in the laboratory) (Patton and Deere, 1970); and
- basic friction (ϕ_b) due to small scale roughness - textural friction due to interaction of the discontinuity surfaces at an asperity level.

This study is focussed on fully persistent discontinuities, therefore the components of shear strength of importance are purely frictional, and as the study is focussed at the laboratory scale, second order roughness at a centimetre scale is of importance, as well as basic friction at an asperity level.

The first attempts to examine the frictional behaviour of discontinuities are linked to classical studies of friction between surfaces. Leonardo da Vinci first worked on the fundamentals of friction between 1452 and 1519, but it was Amontons' Second Law of friction developed by Amontons (1699), which deduced that the basic friction of two planar surfaces being sheared is independent of the size of the surface being tested, and that the shear stress (τ) required to cause motion between two surfaces is directly proportional to the normal stress (σ_n) pressing the surfaces together, giving the coefficient of friction (μ) as:

$$\tau = \mu\sigma_n \tag{2.1}$$

Amontons (1699) also found that μ was independent of the contacting materials and the surface finish of the contact region with a value of approximately 1/3. However, further work by Bowden and Tabor (1956) on various materials found values of μ to vary from 0 for polytetrafluoroethylene (PTFE) to PTFE contacts, to values as high

as 1.5 for nickel to nickel contacts. Bowden and Tabor (1956) also showed experimentally, albeit primarily on metals, that one component of basic friction is adhesion, with adhesion and the actual area of contact increasing with increasing normal load on the discontinuity surfaces. The other component of basic friction is due to micro-scale roughness interlocking, with rougher surfaces having greater interlocking, and an increase in interlocking occurring proportionally to normal load (Coulson, 1971; Hencher, 1976).

The original and simplest model relating roughness to shear strength is the Mohr-Coulomb Criterion (Coulomb, 1776), in which shear strength (τ) is a function of cohesion (c), σ_n and ϕ (Fig. 2.2a):

$$\tau = \sigma_n \tan(\phi) + c \tag{2.2}$$

Patton (1966) was one of the first studies focussed purely on rock discontinuities, with interest in modelling discontinuous rock masses for geotechnical calculations. The Patton Criterion (Patton, 1966) provided a quantitative measure of the roughness of a discontinuity. The two relations for peak shear strength (τ_p, Fig. 2.2b) and residual shear strength (τ_r) are similar to the Mohr-Coulomb Criterion, but take in to account the inclination angles of asperities (i), apparent joint cohesion (c_j), and the residual friction angle (ϕ_r):

$$\tau_p = \sigma_n \tan(\phi_b + i) \tag{2.3}$$

$$\tau_r = \sigma_n \tan(\phi_r) + c_j \tag{2.4}$$

The Patton Criterion was based on studies of discontinuities with saw-toothed asperities, however the model did not properly represent the complex behaviour of natural discontinuity roughness. Barton (1973, 1976) established an empirical law for the description of the shear strength of rock discontinuities, which introduced the concept of a joint roughness coefficient (JRC) to evaluate the roughness contribution to shear strength as:

$$\tau = \sigma_n \tan\left[\phi_b + JRC\log_{10}\left(\frac{JCS}{\sigma_n}\right)\right] \tag{2.5}$$

where JCS is the compressive strength of the discontinuity walls. To aid calculations, Barton and Choubey (1977) also presented roughness profiles and corresponding JRC values for ten planar roughness profiles allowing visual comparison of discontinuity roughness (Fig. 2.2c). The JRC system is widely used throughout academia and industry, having been adopted by the ISRM (ISRM, 1978) as well as being built in to multiple rock mass classification systems. There have however been wide criticisms of the JRC system due to the subjectivity of characterising the roughness by visual comparison (Beer et al., 2002), despite the original authors advising tilt tests to also be carried out alongside visual assessments (Barton et al., 1985). Ferrero (1999) showed that 20 different profiles chosen randomly on one discontinuity could be given a range of JRC values from 8 to 20. With the development of digital profiling systems, there have since been various statistical and fractal interpretations quantifying the original empirical work of Barton and Choubey (1977), as well as attempting to expand roughness quantification to three dimensions (discussed further in § 4.4).

However, the above constitutive models on the shear behaviour of discontinuities are concentrated on mechanical behaviour, and do not explore thermal behaviour. Ohnaka et al. (1997) used fracture mechanics and fracture energy theory to deduce a constitutive model for the shear failure of intact rock in the brittle field at elevated temperatures, but under lithospheric rather than engineering conditions.

2.4.3 Discontinuity deformation

Discontinuity deformability (also termed stiffness or closure) was first studied by Goodman in Goodman et al. (1968) and Goodman (1974), and introduced the terms 'normal stiffness' (k_n) and 'shear stiffness' (k_s) to describe the rate of change of σ_n with respect to normal displacement (u_n) and of τ with respect to shear displacement (D) respectively. Both k_n and k_s have since become fundamental input data for both explicit physical models and numerical modelling techniques. Goodman's experiments showed that u_n varies in a non-linear hyperbolic trend under increasing σ_n, causing k_n to be

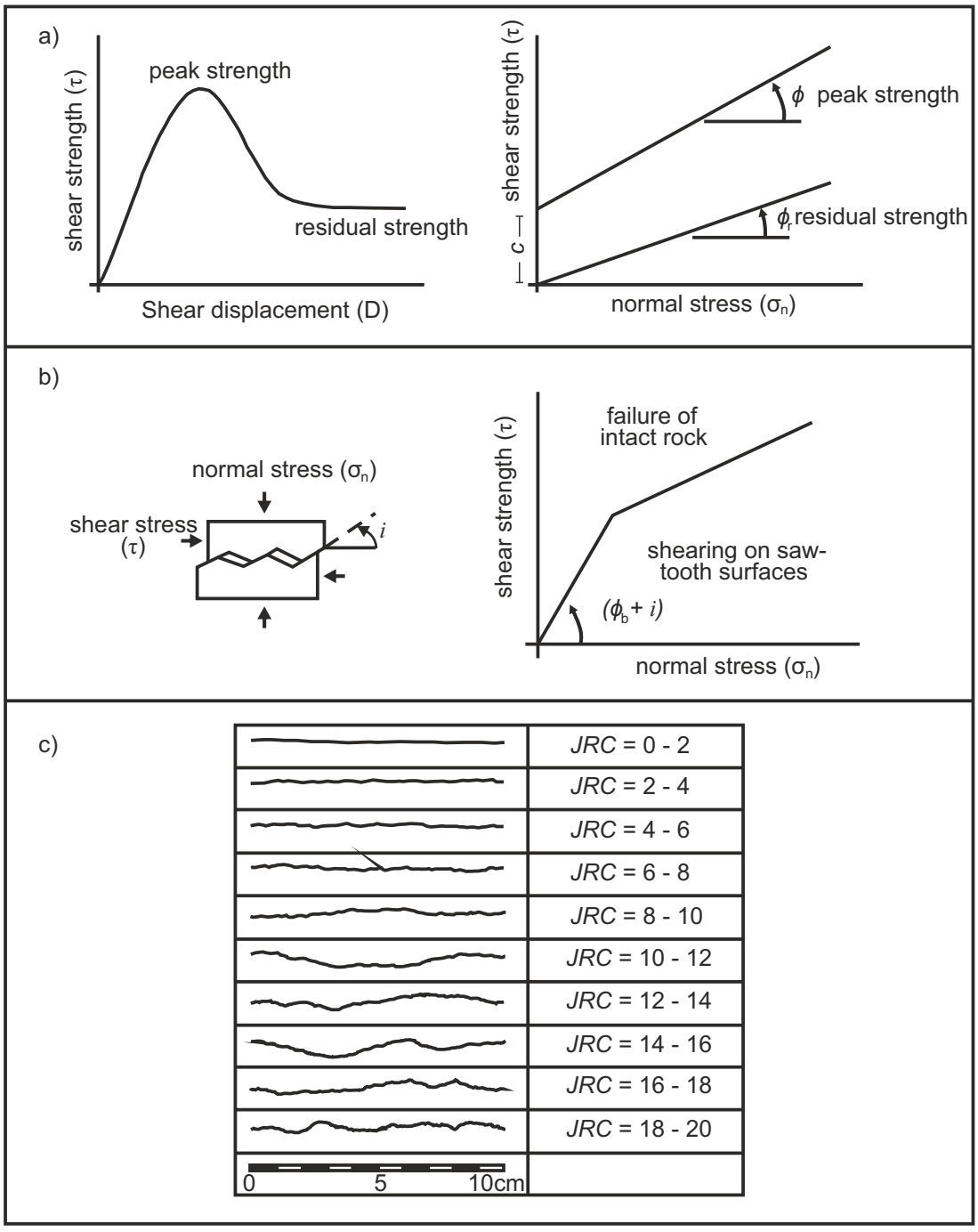

Figure 2.2: a) Mohr-Coulomb shear strength. b) Patton's experiment on the shear strength of saw tooth specimens (Patton, 1966) and the derived bilinear behaviour. c) Roughness profiles and corresponding *JRC* values (after Barton and Choubey (1977)).

stress dependent to a point of maximum closure (u_{max}), and the factors effecting the k_n of rock discontinuities are:

- the actual contact area and the initial aperture between discontinuity walls;
- the discontinuity roughness. The small scale roughness is of most importance;
- the strength and stiffness of individual asperities on the discontinuity walls; and
- the thickness and physical properties of any infilling material if present.

k_s is also non-linear with increasing σ_n before reaching τ_p (Bandis et al., 1983), and the $k_n : k_s$ ratio varies with σ_n and can range from 1 to 100.

2.4.4 Discontinuity over-closure

Mechanical discontinuity over-closure was first reported by Barton (1972) and Bandis (1980). It is the principle that a discontinuity, which has previously been compressed under normal stresses considerably higher than that at which shear failure occurs, will display a higher peak shear strength than a discontinuity that has not undergone previous compression, essentially a hysteresis effect. It is known that more weathered discontinuities and rougher discontinuities undergo greater over-closure effects than fresher or smoother discontinuities due to better interlocking of the two discontinuity surfaces (Bandis, 1980). Babanouri et al. (2011) studied the effects of discontinuity roughness on over-closure and shear strength on analogous specimens moulded with plaster. JCS, τ_p and the degree of over-closure was found to increase with increasing discontinuity roughness and normal load and the results were used to develop a model extending Barton's JRC failure criterion to incorporate the effects of over-closure.

Barton (2007) provides a summary of large scale THM experiments, primarily at URLs related to the development of GDFs, including heated plate jacking tests (George et al., 1999), in-situ heated block tests (Barton, 1982; Hardin et al., 1982; Zimmerman et al., 1985), and other large scale heating of rock masses (Yow and Wilder, 1994). All experiments reported different deformation moduli than expected and lower thermal expansion coefficients. Barton (2007) attributes this to discontinuity closure and over-closure, occurring not just due to mechanical loading, but also thermal loading, with thermal loading alone being capable of causing over-closure effects. One example is the heated

block test undertaken by TerraTek at Colorado School of Mines on behalf of the Office of Nuclear Waste Isolation (ONWI) in 1980 and 1981 (Hardin et al., 1982). A single rough ($JRC = 13$) diagonal discontinuity in quartz monzonite was subjected to a series of different loading, unloading, heating and cooling sequences (Fig. 2.3) and whilst the aperture was reduced by 20.9 µm under thermal loading from 12 °C to 75 °C it was found that when cooling again and partial unloading only 3.1 µm of aperture was recovered, that is, the discontinuity remained thermally over-closed.

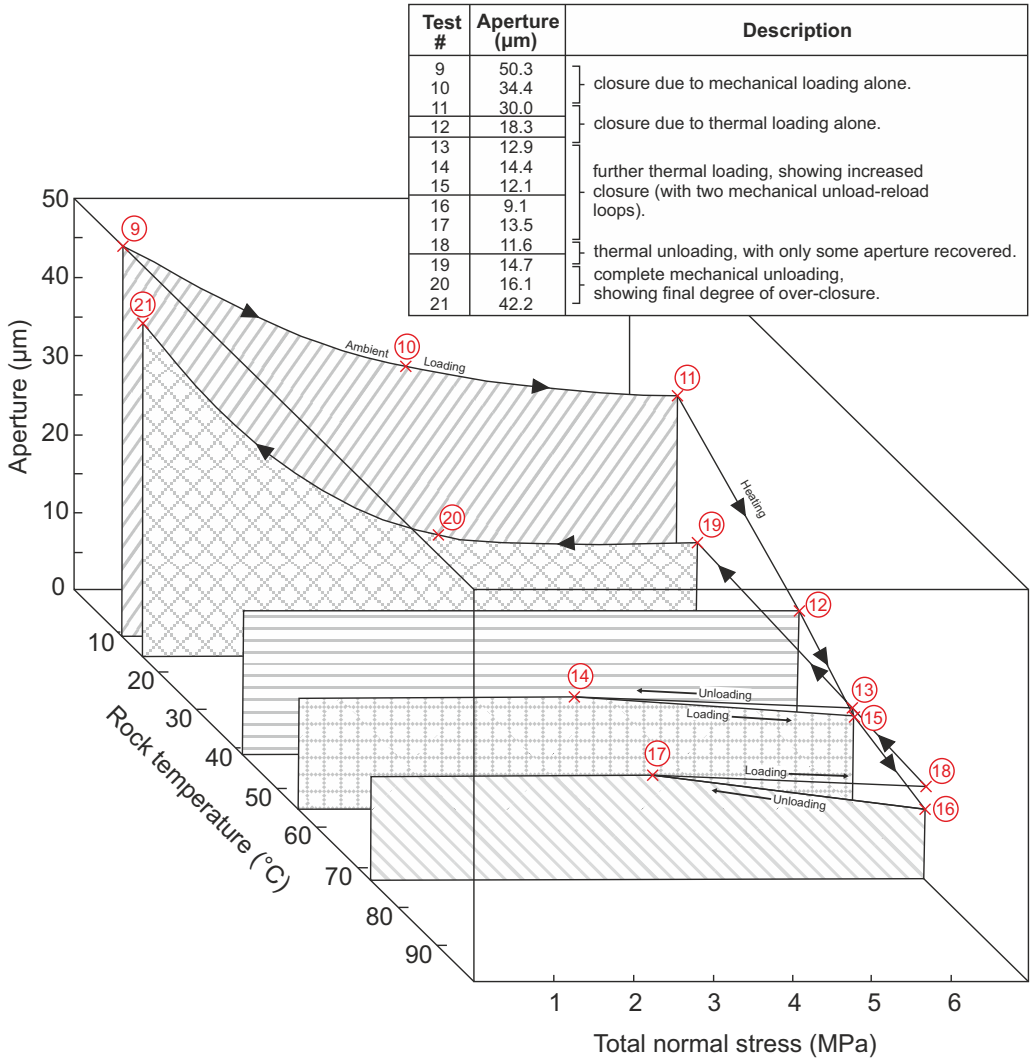

Figure 2.3: Thermo-mechanical behaviour back-calculated from in-situ heated block test at TerraTek/-Colorado School of Mines (Hardin et al., 1982), showing unexpected thermal discontinuity over-closure. After Barton (1982).

2.4.5 Experimental measurement of the shear strength of discontinuities

Measurements of the shear strength of discontinuities have previously been made using configurations Fig. 2.4a to d. In configuration Fig. 2.4a the two surfaces are pressed together by a normal force (F_n) and sheared by a tangential shear force (F_s) (Bowden, 1954; Horn and Deere, 1962; Penman, 1953). To ensure even normal loading of the discontinuity, a direct shear box is commonly used in the laboratory environment, such as the Golder Associates direct shear box (details outlined in Hencher and Richards (1982, 1989)), however normal stresses are limited to approximately 2 MPa on 100 mm specimens. Hoskins et al. (1968) used configuration Fig. 2.4b, with F_n applied by flat pressure cells and F_s applied using a hydraulic rock testing rig. In this configuration, the amount of contact area remains constant, but the contact does not occur over precisely the same surfaces throughout the process. The rotary shear system (Fig. 2.4c) has the advantage that the same surfaces and surface areas are in contact regardless of the amount of displacement throughout the test (Niemeijer et al., 2008; Tullis and Weeks, 1986).

The most commonly used configuration, and the configuration used throughout this study is shown in Fig. 2.4d. In this configuration a cylindrical core specimen has a discontinuity running through it at an angle β to the diametral plane, the specimen is then placed in a triaxial testing rig in a jacketing system and a confining pressure ($\sigma_2 = \sigma_3$) is applied to the lateral curved surface of the specimen prior to an axial stress (σ_1) being applied to the specimen. This method allows for high normal and

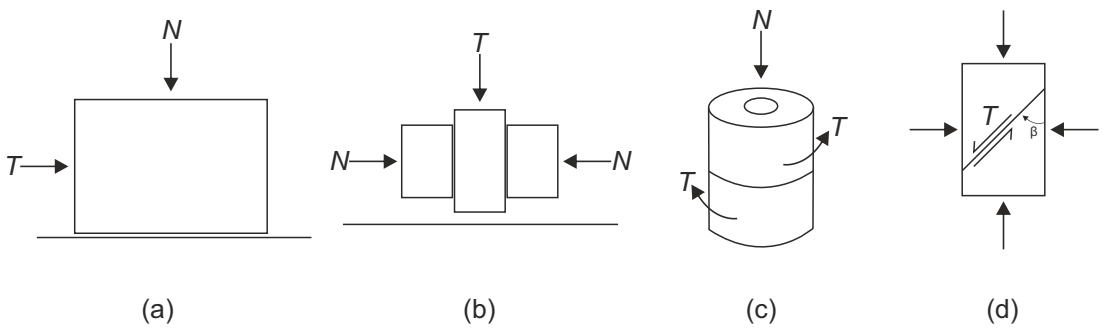

Figure 2.4: Different configurations for testing the shear strength of discontinuities.

shear stresses to be applied to the discontinuity, but a change in discontinuity contact, stress or both occurs as soon as slippage occurs on the discontinuity. Three variations of this configuration may be used (Fig. 2.5). In configuration (a) the cylindrical specimen is situated between rigid platens whose faces are perpendicular to σ_1 (Blanpied et al., 1995; Goodman, 1974; Lockner et al., 1982; Ohnaka et al., 1997; Stesky et al., 1974; Wong, 1982b). It can be difficult to obtain the correct alignment of the discontinuity during specimen preparation therefore in this configuration, even axial loading of the specimen can be hard to achieve, and if a servo-control system is not being used then after initial slip has occurred, a lateral stress is produced whose magnitude is unknown. In configuration (b) a single spherical seat is used, in which case the specimen rotates into configuration (c) as slip occurs, after which contact no longer exists over the original elliptical cross section. If two spherical seats are used as in configuration (d), the specimen halves rotate with displacement to maintain the angle of contact, however the contact area decreases as slip proceeds. For small amounts of shear, consistent results can be obtained using all three methods (Jaeger et al., 2007). In this study a version of configuration (b) was used, with a single spherical seat and as was used by Jaeger (1959) and Byerlee (1967). Of particular importance in this study is that this configuration also allows for easy thermal loading as well as mechanical loading, as the confining fluid within the triaxial pressure vessel can easily be heated, compared to heating a shear box or other form of rigid configuration, likely to impart uneven stress concentrations due to thermal expansion.

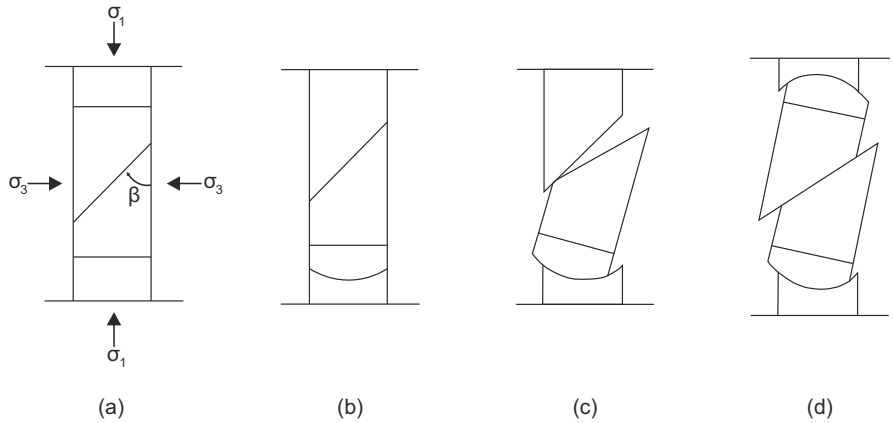

Figure 2.5: Different configurations for shearing discontinuities under triaxial conditions. a) No spherical seats. b) One spherical seat. c) One spherical seat after shear displacement. d) Two spherical seats. After Jaeger et al. (2007).

2.5 Use of analagous materials in rock mechanics testing

Synthetic materials have been used extensively in rock discontinuity mechanics. For testing frictional behaviour, the preparation of identical synthetic specimens with the same topographical and mechanical characteristics overcomes the problem of natural heterogeneity (Papaliangas, 1996). This allows fundamental mechanical (Bobet and Einstein, 1998; Bombolakis, 1968; Grasselli, 2001; Hoek and Bieniawski, 1965; Papaliangas, 1996; Shen, 1995; Stimpson, 1970; Wong and Einstein, 2009) and thermal (Belayachi et al., 2019) behaviour to be defined through the testing of identical discontinuities under varying conditions. Nearly all cases of the use of synthetic lithologies in rock mechanics testing are applied to low stress, surficial environments, for example discontinuity shear strength for slope stability problems. This study will attempt to use a synthetic lithology analagous to a lower strength sedimentary lithology under higher stresses analagous to those that may be encountered in a GDF.

Studies have used many different synthetic materials as analogues to natural lithologies. Stimpson (1970) carried out a review of the use of different materials from non-granular materials such as metals and plastics, to granular materials with binding agents such as plaster, cement, wax and resins and suggested approximate properties and suitability. The most commonly used synthetic materials have a granular aggregate and a cementing material like plaster or cement, such as those used by Papaliangas (1996) and Grasselli (2001). Other materials include glass (Hoek and Bieniawski, 1965), Columbia resin 39 (Bombolakis, 1968) and moulded gypsum (Bobet and Einstein, 1998; Shen, 1995; Wong and Einstein, 2009), however justification and validation of the mechanical behaviour of the synthetic material under the desired loads in comparison to the desired lithology is rare. In nearly all cases, the specimen creation consists of creating a mould of the desired discontinuity surface, before casting a specimen in to this mould using the synthetic material of choice. This is straight forward when casting specimens for shearbox testing at low stresses, as the discontinuity is perpendicular through a cubic specimen, it is more difficult when testing under triaxial conditions and the discontinuity is required to be cast at an angle. Kim and Jeon (2019) recently published a casting methodology for triaxial specimens, utilising aluminium casts (Fig. 2.6b).

There has also been a recent rise in the use of additive manufacturing or 3D printing

to directly create discontinuity specimens in synthetic materials, typically in plastics such as polylactic acid (PLA) or acrylonitrile butadiene styrene (ABS) (Jiang et al., 2016a,b; Kong et al., 2017). 3D printing in plastics typically produces specimens with very low stiffness, and an inherent anisotropy due to the layering process of the printing (Kong et al., 2017). Promising results have been shown for 3D printing representative discontinuity topographies to micron resolution (Jiang et al., 2016a). Specimens of 'sandstone' have also been 3D printed directly using a silica sand, bonded with an acid activated binding agent (Osinga et al., 2015). However, further research is still required to understand the mechanical behaviour of these materials, how the manufacturing process alters this mechanical behaviour, and whether they are representative for use as rock analogues.

2.6 Thermo-mechanical loading of rocks in the laboratory

To better understand the thermo-mechanical loading of rocks and isolate the behaviour of intact material vs. discontinuities, laboratory scale thermal triaxial experiments will be utilised in this study. This section provides a summary of previous laboratory studies that have undertaken thermal and mechanical loading of intact rock and discontinuities in the laboratory.

2.6.1 Thermo-mechanical loading of intact rock

Research in to the thermo-mechanical loading of rock specimens under laboratory conditions began in the 1970s, with studies focussed on the Earth's crustal behaviour. These early studies primarily in crustal lithologies such as granite, gabbro, dolerite and rhyolite as well as sandstone found that thermally loading specimens from room temperature up to temperatures as high as 800 °C induced micro-cracking and caused irrecoverable thermal expansion. This thermal micro-cracking was attributed to result from localised stress concentrations induced by the thermal expansion heterogeneity of adjacent minerals with different thermal expansion coefficients, and occurred in the absence of a thermal gradient across a specimen (Richter and Simmons, 1977), as well as under confining pressures (Bauer and Handin, 1983; Heard and Page, 1982; Wong and Brace, 1979). The thermally induced micro-cracking was found to be significant enough

Mineral	Linear thermal expansion coefficient (α_L) 10^{-5} K^{-1}	Thermal conductivity (k) Wm^{-1} K^{-1}	Specific heat capacity (c_p) J g^{-1} K^{-1}
Quartz	1.60 [1]	7.69 [2]	698 [2]
Muscovite	1.16 [3]	2.32 [2]	760 [4]
Albite	0.54 [3]	2.31 [2]	709 [2]
Chlorite	0.90 [5]	5.14 [2]	600 [4]
Kaolinite	1.86 [5]	0.30 [6]	945 [6]
Microcline	0.53 [3]	2.49 [2]	680 [2]

Table 2.3: Thermal properties for some common rock forming minerals.

to affect Young's modulus (Bruner, 1979; Heard and Page, 1982; Simmons and Cooper, 1978), ultrasonic velocities (Johnson et al., 1978), seismic attenuation (Clark et al., 1981; Johnson et al., 1978), fracture toughness (Meredith and Atkinson, 1985), permeability (Bauer and Johnson, 1979) and produce acoustic emissions (Chen and Wang, 1980; Johnson et al., 1978). The thermal properties of some common rock forming minerals are tabulated in Table 2.3, quite a wide range of thermal expansion coefficients, thermal conductivities and specific heat capacities exist, causing the localised stress concentrations and inducing micro-cracking.

Scanning electron microscopy (SEM) shows that thermal micro-cracking is initially dominantly inter-granular (along grain boundaries), before intra-granular cracking then occurs at higher temperatures (i.e. cracking through the grains themselves) (Fredrich and Wong, 1986). The threshold for the transition between inter-granular and intra-granular cracking is lithology dependent, but was observed by Fredrich and Wong (1986) in granite at approximately 250 °C. Fredrich and Wong (1986) observed inter-granular micro-cracks commonly initiated at triple junctions between grains, and then

[1] (Park et al., 2015)
[2] (Čermák and Rybach, 1982)
[3] (Siegesmund et al., 2018)
[4] (Waples and Waples, 2004)
[5] (McKinstry, 1965)
[6] (Michot et al., 2008)

tended to grow unimpeded until encountering a grain boundary with a sharp change in geometry. Fredrich and Wong (1986) also found that quartz/feldspar grain boundaries cracked more readily than microcline/plagioclase, and least likely to crack were boundaries between grains of the same mineralogy. This is likely due to the localised stresses at grain boundaries due to heterogeneous thermal expansion, but could also reflect different strengths in grain contacts. Grain size is also likely a critical parameter for the formation of thermally induced micro-cracks. Fredrich and Wong (1986) heated an untextured limestone with an average grain size of 0.075 mm to 500°C before observing evidence of thermal micro-cracking, however Widhalm et al. (1997) observed acoustic emissions from thermal micro-cracking in marbles with larger grain sizes from temperatures of 50 °C.

More recently studies have been undertaken on lithologies more alike the ones used in this study (granular or crystalline quartz rich lithologies), and at temperatures applicable to engineering environments (up to 100 °C), in comparison to the early studies focussed on crustal processes. Siegesmund et al. (2018) studied the thermal expansion of 65 different granitic lithologies up to 100 °C, with implications for the use of granitoids as building stones and façade materials. It was found that due to quartz having a relatively high thermal expansion coefficient, quartz rich granitoids underwent greater thermal expansion and thermal micro-cracking than feldspar and plagioclase rich lithologies. Thermal expansion of different lithologies was also related to pre-existing micro-cracking and pore space, with greater initial porosity allowing for potential pore closure under initial thermal expansion, prior to the initiation of thermal micro-cracking. Plevová et al. (2011) also undertook thermal studies on four different sandstone lithologies and found greater thermal expansion and micro-cracking in lithologies with higher quartz content.

Zhou et al. (2016) studied the thermal expansion of bedded fine-grained sandstone in the laboratory, with specimens taken perpendicular and parallel to bedding and heated up to 200 °C. By 200 °C macroscopic fractures occurred along bedding planes, in addition to further micro-cracking within the matrix seen in SEM imaging. Zhang et al. (2013) also heated specimens of fine grained sandstone to different temperatures before imaging using a micro-photometer. It was observed that from room temperature to 120 °C existing flaws between grains were seen to close, whilst new inter-granular

micro-cracks began to form. At 180 °C these micro-cracks began to accumulate and interact to form macroscopic fractures.

Sirdesai et al. (2017) and Lü et al. (2017) carried out Brazilian disc indirect tensile tests on thermally treated specimens of fine-grained sandstone. Sirdesai et al. (2017) thermally treated specimens in a furnace prior to testing. Some specimens were tested immediately after removal from the furnace, whilst others were allowed to cool prior to testing. The tensile strength of all specimens reduced after heating to 50 °C and 100 °C regardless of the thermal treatment process, showing the thermal micro-cracking damage as being irreversible. Lü et al. (2017) also observed a reduction in tensile strength and a reduction in P-wave velocity after thermally treating specimens to 100 °C.

All of the above studies show that thermo-mechanical loading of granular and crystalline lithologies results in the development of irreversible thermally induced micro-cracking, causing reduced tensile and compressive strength as well as increased permeability. The temperature for the initiation of thermal micro-cracking and the degree of micro-cracking development is however dependent on inherent properties of the lithology in question, as well as the conditions of the loading.

2.6.2 Thermo-mechanical loading of discontinuities

Whilst research efforts focussed on the thermo-mechanical loading of discontinuities for the engineering design of GDFs have only occurred relatively recently, a body of work from the wider geosciences dates back half a century, with laboratory triaxial shear experiments trying to replicate tectonic faulting and shearing conditions under hydrothermal and geothermal conditions. Various lithologies have previously been tested over a wide range of temperatures and pressures with different moisture contents, pore pressures, and discontinuity infill, but using very similar experimental configurations.

Olsson (1974) carried out triaxial shear tests on limestone at 25 °C, 100 °C and 300 °C and confining pressures of 5 to 200 MPa. Little effect on frictional properties was seen by increasing temperatures from 25 °C to 100 °C, but at 300 °C a clear reduction in peak shear strength was seen at all confining pressures. Drennon and Handy (1972)

also carried out shear tests on limestones at elevated temperatures up to 200 °C, albeit at much lower normal stresses (0.75 to 2 MPa) in a heated shearbox apparatus, and found that at these lower stresses an increase in temperature led to an increase in the coefficient of friction. These tests were however undertaken on saturated specimens, and the increase in the coefficient of friction is therefore likely due to the driving off of moisture from the discontinuity surface and hence the decrease in lubrication and increase in friction.

Lockner et al. (1982) tested both intact specimens and sawcut discontinuous specimens of sandstone in triaxial conditions, with confining pressures ranging from 20 to 100 MPa and at temperatures of 150 °C and 240 °C, corresponding to lithostatic pressures and temperatures of the Geysers geothermal field in California. Triaxial tests were undertaken on 47.6 mm long cylinders (diameter (Ø) 19.1 mm) at axial strain rates of 10^{-4} to $10^{-6}\,s^{-1}$. Sawcut specimens were cut at 30° from the vertical and lapped with 400 mesh silicon carbide powder to produce smooth surfaces. All specimens were tested after being saturated with distilled water. As expected, peak strength of intact specimens was dependent on confining pressure, but independent of temperature or strain rate, and no change was observed in the shear strength of the sawcut discontinuities with confining pressure, strain rate or temperature.

Odedra et al. (2001) summarised similar earlier experimental work conducted on granites (Tullis and Yund, 1977; Wong, 1982a), as well as undertaking additional tests on both wet and dry granite, with confining pressures ranging from 70 to 480 MPa, temperatures ranging from room temperature to 480 °C and an axial strain rate of $10^{-5}\,s^{-1}$. In all studies, no temperature dependence of mechanical behaviour was seen until approximately 300 °C, where a transition from a brittle to ductile deformation regime was reported, with large losses in strength by 480 °C, close to approaching the α/β phase transition in the mineralogical structure of quartz (587 °C) (Glover et al., 1995).

Triaxial shear experiments on discontinuities in granite with a layer of granite powder, simulating a fault gouge were conducted by Blanpied et al. (1995). Tests were undertaken from room temperature up to 600 °C, from dry up to saturated with pore pressures up to 100 MPa, and discontinuity normal stresses up to 400 MPa. No changes in strength or friction were seen in dry specimens below 845 °C, or below 350 °C in

wet specimens, similar results to earlier thermo-mechanical granite gouge experiments undertaken by Stesky (1978) and Lockner et al. (1986).

Stesky et al. (1974) carried out triaxial shear experiments to simulate fault shearing behaviour in gabbro, granite, peridotite and sandstone, at pressures ranging from 250 to 600 MPa and temperatures up to 700 °C. Although some variation was found between lithologies, little variation in peak shear strength was found below 265 °C, with a transition from stick-slip to stable-sliding above this temperature, attributed to the possible brittle-ductile transition of amphiboles.

All of these studies were carried out to investigate Earth crustal behaviours, hence the testing conditions such as temperature, confining pressures and pore pressures being extremely high. Whilst the mechanical behaviour of discontinuities in these studies at elevated temperatures are clearly lithology dependent, as well as highly dependent on the discontinuity infilling, moisture content and pore pressures, in general little temperature effect is seen at these high confining pressures. Temperatures and stresses in the realms of rock engineering problems are however expected to be considerably lower, with temperatures up to 150 °C and confining pressures up to 20 MPa. It is therefore necessary to investigate the shear behaviour of discontinuities under these engineering thermo-mechanical boundary conditions. In addition, the majority of these studies work on sawcut specimens due to the difficulties of testing identical discontinuity topographic surfaces in different tests and the complexities of the experiments. This negates potential effects of discontinuity roughness.

A recent study by Kim and Jeon (2019) undertook triaxial THM shear experiments on sawcut specimens of granite, diorite and sandstone (Fig. 2.6a) at boundary conditions analogous to those for a GDF, with tests undertaken at room temperature and 80°C, and confining pressures up to 20 MPa. In addition, Kim and Jeon (2019) undertook tests on cementitious synthetic specimens with roughnesses of both $JRC = 2$ and $JRC = 12$ cast from aluminium replica discontinuity surfaces (Fig. 2.6b). At the elevated temperature of 80 °C, the peak friction angle showed no change in the granite, and showed a slight increase in the diorite, sandstone and cementitious specimens. Normal stiffnesses or shear stiffnesses were not seen to change with elevated temperatures either, however all specimens showed decreasing frictional strength with the presence of water,

which could be due to increased pore pressure with the thermal expansion of pore water (Alonso and Pinyol, 2010).

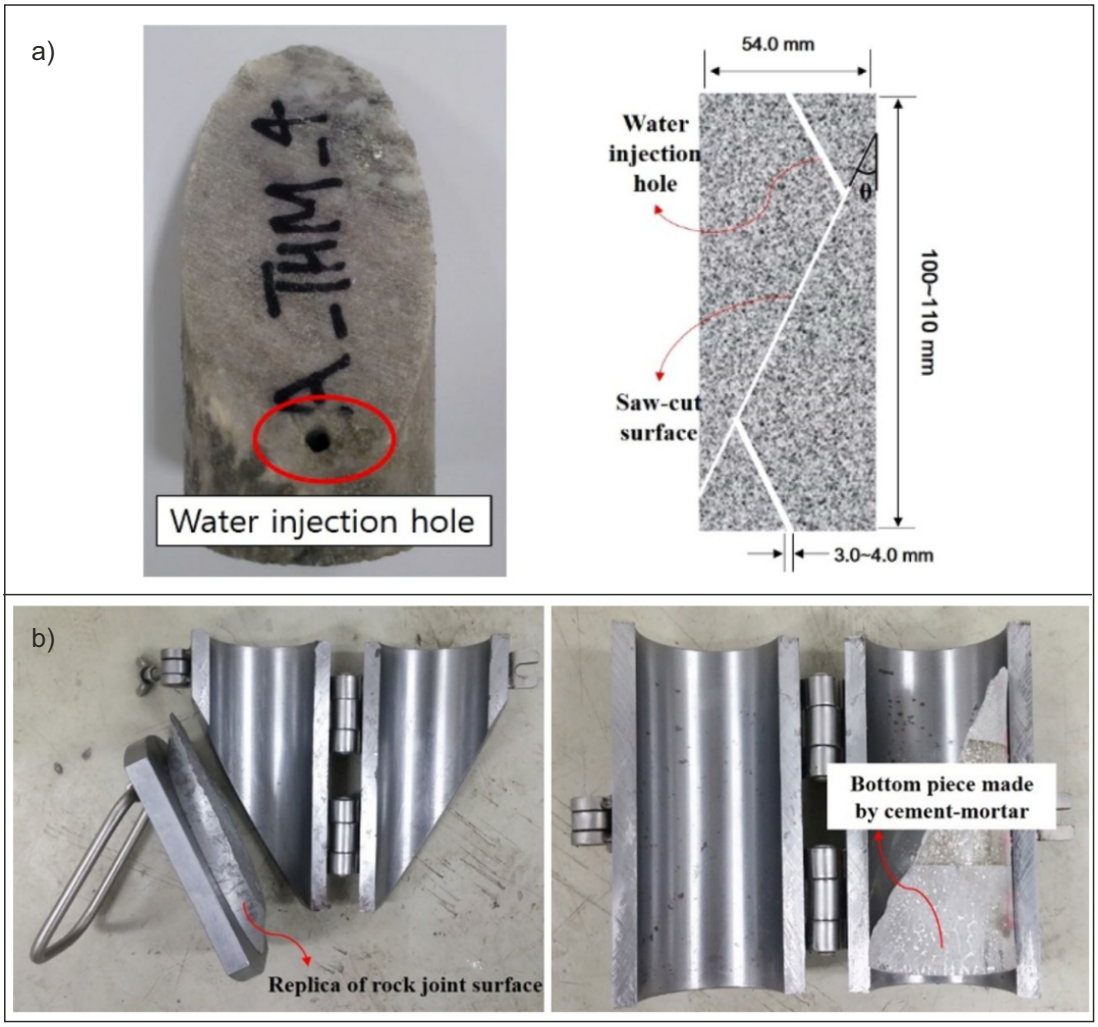

Figure 2.6: Specimen configurations by Kim and Jeon (2019). a) Configuration for sawcut specimens of granite, diorite and sandstone. c) Casting of synthetic specimens with roughnesses cast from aluminium replica discontinuity surfaces.

Another recent study by Zhang et al. (2019) undertook triaxial THM shear experiments on sawcut specimens of sandstone at temperatures up to 120 °C and effective normal stresses up to 10 MPa, under oven dry conditions as well under H_2O and CO_2 saturation. The specimens were thermally loaded, before a confining pressure was applied at 0.01 MPa s^{-1}, followed by shearing at a displacement of 0.3 mm min^{-1}. The shear

strength of the discontinuities were seen to reduce by a maximum of 7.96% at 120 °C under dry conditions, with a smaller reduction in strength occurring under saturation. The thermal loading also resulted in a significantly increased shear displacement at peak shear strength (D_a), with the peak shear displacement being increased by 121.8% at 120 °C under dry conditions. Zhang et al. (2019) attribute this to a reduction in shear strength, and increased peak shear displacement to a reduction in shear stiffness at the asperities on the discontinuity with increasing temperature.

2.7 Numerical modelling

In addition to laboratory testing, this study will use discrete element method (DEM) grain based models (GBM) to further explore and validate laboratory results. This section discusses the developments of GBMs and their applications to thermal and mechanical testing of rocks.

2.7.1 Discrete element modelling of brittle fracturing

Numerical models can be useful tools to predict expected mechanical behaviour of rock and other materials and aid in rock engineering design. Numerical modelling can be divided in to two different approaches, those based on continuum formulations and those based on discontinuous or discrete formulations. Continuum formulations such as finite element method (FEM), finite difference method (FDM), and boundary element method (BEM) are applicable to represent situations where deformations are small and the material being modelled is either free of discontinuities or the discontinuities are numerous and distributed uniformly. In this case, the discontinuities and fracturing are represented through implicit modelling as weakness, which are absorbed within the material by the means of a constitutive model. Discontinuous approaches such as DEM and discontinuous deformation analyses (DDA) are suitable for representing situations where deformations are large, the material being modelled is moderately fractured, and the movement of individual blocks is likely (Jing and Stephansson, 2007), where it is possible to accomplish the explicit simulation of fracturing by the direct representation of discontinuities in models. In DEMs, the discontinuous material can be modelled as a dense assembly of either rigid or deformable blocks that interact at contacts. The

discrete blocks can detach and new contacts be detected (Itasca, 2014a), this allows discontinuities to be simulated at this block scale.

A common limitation of both continuum and discontinuum methods is the inability to capture the creation of new fractures through brittle fracturing. Multiple approaches have been taken to attempt to solve this and blur the line between conventional continuum and discontinuum methods.

Originally developed to simulate the behaviour of non-cohesive materials such as soils (Cundall, 1979), the use of discs (or spheres in 3D) (Potyondy and Cundall, 2004) with cohesive bonds between particles and normal stiffnesses, shear stiffnesses and friction coefficients assigned to the discs contacts (Lisjak et al., 2014) have arguably become the most popular method of grain based modelling, with fracturing occurring through the breaking of these cohesive bonds and fracture propagation occurring through the coalescence of bond breakage. The most common use of this method is the bonded particle model (BPM) within Itasca software Particle Flow Code (PFC2D/3D) (Itasca, 2008).

BPMs in PFC have successfully been used to study fracturing processes (Bahrani et al., 2014; Chiu et al., 2013; Peng et al., 2018), however due to the use of circular (or spherical in 3D) blocks, the behaviour of rocks with complex shaped grains and interlocking structures results in unrealistically low ratios of the simulated unconfined compressive strength (UCS) to the indirect tensile strength (σ_t) (Cho et al., 2007). Multiple studies have attempted to address this issue, with 'clustering' logic (Potyondy and Cundall, 2004), 'clumping' logic (Cho et al., 2007), and the flat-joint model (Potyondy, 2012; Wu and Xu, 2016). However, when simulating rough discontinuities in particle based models, a second order roughness is imparted due to the particle topology within the model, likely to add an artificial strength along discontinuities. An attempt to rectify this was made by Deisman et al. (2008) by introducing the smooth-joint contact model (SJM).

Further studies have shown the importance the geometry of particles play in a GBM, and how the geometry controls the generation of crack extension and shearing forces as fractures develop. Instead of discs or spheres, the Voronoi tessellation technique

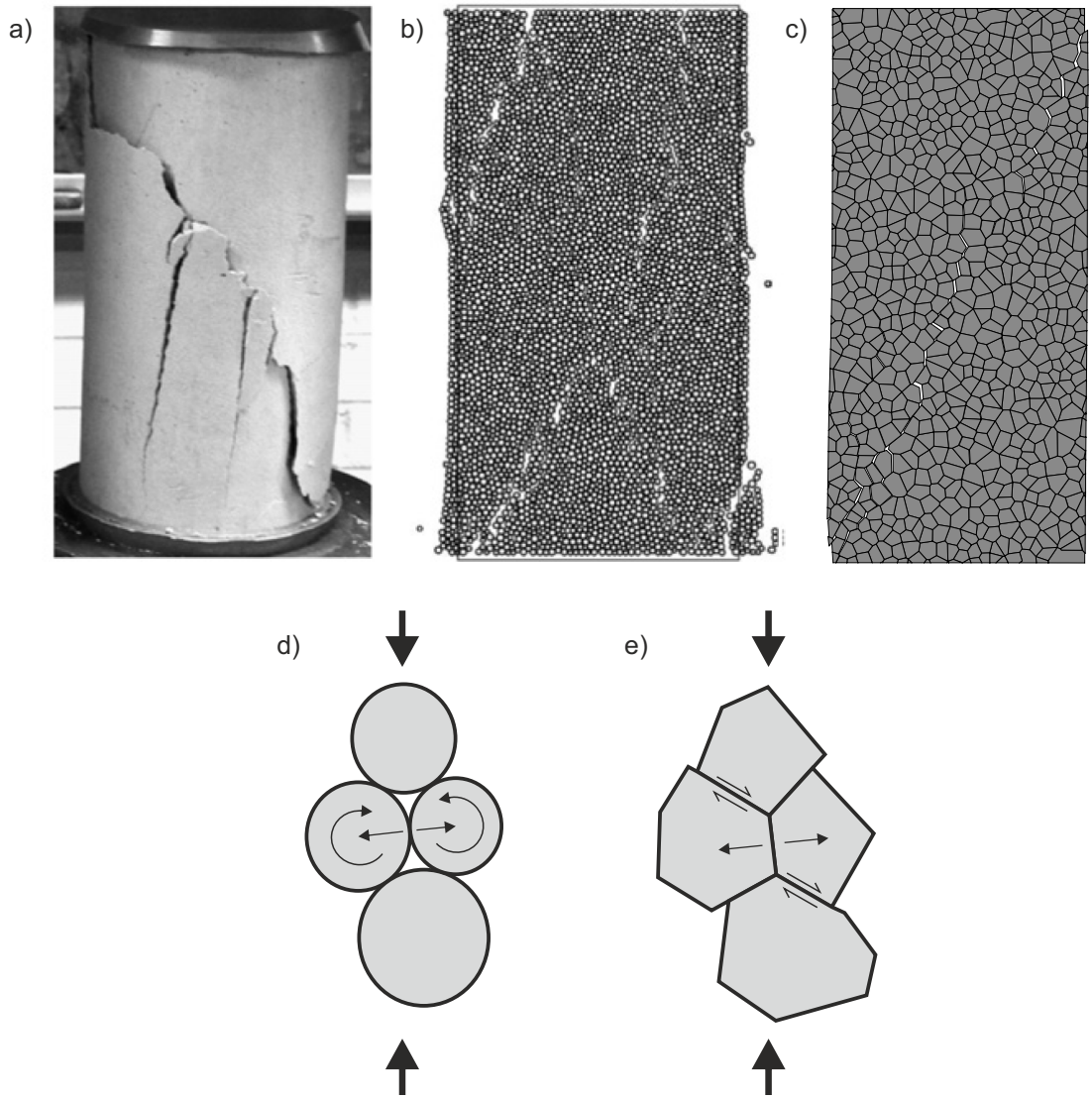

Figure 2.7: a) Formation of shear plane and axial splitting in a specimen post-UCS test. b) Simulation of a UCS test in PFC2D, utilising 'clumping' logic and showing the formation of a shear plane (Cho et al., 2007). c) Simulation of a UCS test in UDEC utilising a Voronoi GBM, showing the formation of a shear failure plane. d) Formation of tensile stresses and rotational moments in disc based BPMs under compressive forces. e) Formation of tensile stresses and shear stresses in Voronoi based GBMs under compressive forces.

has been well accepted for simulating the microstructure of materials (Li et al., 2006; Zhang et al., 2005), and has been implemented in the Itasca software Universal Distinct Element Code (UDEC) (Fig. 2.7c) (Itasca, 2014a). The crystalline or granular

micro-structure of rock is better represented by Voronoi tessellations due to full contact between grains and better interlocking due to the polygonal shapes. In simulations utilising discs, the applied forces translate into tensile stresses at the contacts between discs and rotational moments (Fig. 2.7d), whilst in Voronoi simulations the forces can be resolved into tensile and shearing forces on the grain boundaries (Fig. 2.7e). This is not fundamental when micro-cracks start to form, as micro-cracking in brittle rocks is tension dominated (Diederichs, 2007). However with increasing deviatoric stress, and as yield starts to occur and micro-cracks accumulate and coalesce, shearing becomes dominant, therefore a BPM with circular discs has limited application for the simulation of crack interaction (Diederichs, 2007).

In continuum modelling, the input parameters are derived directly from the mechanical properties measured in laboratory tests. However, for GBMs, the input values of the micro-properties of the model cannot be determined directly from the macro-properties measured in laboratory tests. Instead, the values of the micro-properties assigned to the blocks and their contacts must be determined through a numerical calibration process, in which the emergent macro-properties of the model are compared to the relevant measured response of the material in the laboratory (Potyondy and Cundall, 2004). The grain size, strength and stiffness properties of the Voronoi block assembly, and the strength and stiffness of the block contacts are all altered through a multi-stage parametric analysis of simulated unconfined compression tests, triaxial compression tests and indirect tensile Brazilian disc tests to achieve calibration with the desired lithology over a range of stresses (Christianson et al., 2006; Gao and Stead, 2014; Kazerani et al., 2012). Multiple studies have shown the ability to calibrate Voronoi GBMs to produce realistic macroscopic mechanical behaviour of specimens of various lithologies (granite, diorite, tuff, sandstone) being deformed over a range of stresses within the brittle field (Christianson et al., 2006; Damjanac et al., 2007; Stavrou and Murphy, 2018). The calibration procedure typically calibrates all blocks and contacts to a single set of mechanical properties. Farahmand (2017) applied block and contact properties in percentages relevant to the mineralogy of the lithology being calibrated. However, no study to date has compared the two calibration techniques and their affect on progressive damage and failure mechanisms.

Multiple constitutive models have been implemented to control the block and contact

behaviour within Voronoi GBMs in UDEC, and replicate the mechanical behaviour of different lithologies. Voronoi blocks can be undeformable, or made deformable, with deformable block models including elastic isotropic, Mohr-Coulomb plasticity, strain-hardening, Hoek-Brown and modified Cam-clay. When simulating brittle materials in Voronoi GBMs it is most common to use an elastic or Mohr-Coulomb plasticity model (Itasca, 2014a). A Coulomb slip constitutive model is also most commonly applied to Voronoi contacts, with the option to apply residual properties. Additional constitutive models can be defined, such as the cohesive crack model implemented by Farahmand (2017), designed to better simulate the yielding behaviour of brittle materials due to crack coalescence under increasing deviatoric stress.

Gao and Stead (2014) introduced porosity to a GBM, by deleting blocks to create void space, simulating a sample with 12% porosity. The models showed an increased number of tensile failures in comparison to the same calibrated model with 0% porosity, with tensile micro-cracks nucleating at void boundaries. The pore volume of the sample during deformation was however not tracked, so no information on pore volume changes under deformation (i.e. pore collapse) were obtained. Lu et al. (2013) introduced a single discontinuity in to a GBM, testing a discontinuous specimen in UCS conditions. The model was calibrated to the intact laboratory properties of the Lac du Bonnet granite. A single discontinuity was then introduced to the simulations, but the discontinuity was only introduced as a planar feature within the Voronoi geometry. Contacts along the discontinuity were not assigned different strength or stiffness properties to the Voronoi grains. Changing the orientation of the discontinuity affected the UCS of the specimen, with the biggest strength reduction occurring when $\beta = 30°$, and the highest strength occurring when the discontinuity was perpendicular, with the general UCS vs. β angle fitting the traditional U-shaped curve for the strength behaviour of anisotropic rock (Donath, 1961; Hoek, 1964; McLamore and Gray, 1967). As no strength or stiffness parameters were altered allowing frictional behaviour of the discontinuity to be evaluated, this was a study of anisotropic rather than discontinuous mechanical behaviour.

2.7.2 Grain based thermo-mechanical modelling

Huotari and Kukkonen (2004) carried out PFC 2D simulations to quantify the thermal expansion of the Olkiluoto Mica Gneiss, the host lithology for the Finnish ONKALO spent nuclear fuel repository. Two different simulations were run, one with the same thermal expansion coefficient applied to every particle in the model, and a second with three different thermal expansion coefficients applied in different percentages representing grain scale heterogeneity. The model was then heated from 0° to 50 °C. No mechanical properties were applied to the models, therefore not allowing thermo-mechanical coupling, but thermal expansion was monitored during heating. The modelling produced much larger thermal expansions than theoretical calculations, attributed to the simplification in the grain scale heterogeneity and estimations of mineral percentages.

Lan et al. (2013) replicated the thermo-mechanical loading of the in-situ Äspö Pillar Stability Experiment (APSE) (Andersson, 2007; Andersson et al., 2009) at the Swedish Nuclear Fuel and Waste Management Company's (Svensk Kärnbränslehantering Aktiebolag (SKB)) Äspö Hard Rock Laboratory (HRL) in Sweden. Lan et al. (2013) created a thermo-mechanically coupled tunnel scale GBM in UDEC. A 2D section through the heated pillar was modelled. Thermal and mechanical grain and contact properties were calibrated against mechanical laboratory tests and assigned for four different minerals (Fig. 2.8a). The pillar was then thermally loaded over a 60 day period as in the APSE, whilst thermally induced displacements and stresses were monitored in the simulation. The GBM showed good agreement between the predicted and measured temperatures and displacements, as well as providing new insights into the progressive failure process. Failure initiated with tensile micro-cracking, occurring where thermal grain heterogeneity generated tensile stresses exceeding grain contact tensile strengths. These thermally induced tensile micro-cracks were then seen to propagate following the tangential stresses of the excavation forming partially detached thin slabs of rock (Fig. 2.8b), which were seen in the ASPE as brittle spalling forming v-shaped notches (Andersson, 2007). This study by Lan et al. (2013) showed the ability of a Voronoi based GBM to capture thermo-mechanically induced displacements and provided new insights to the localised stress distribution and micro-cracking in a thermo-mechanically loaded rock mass.

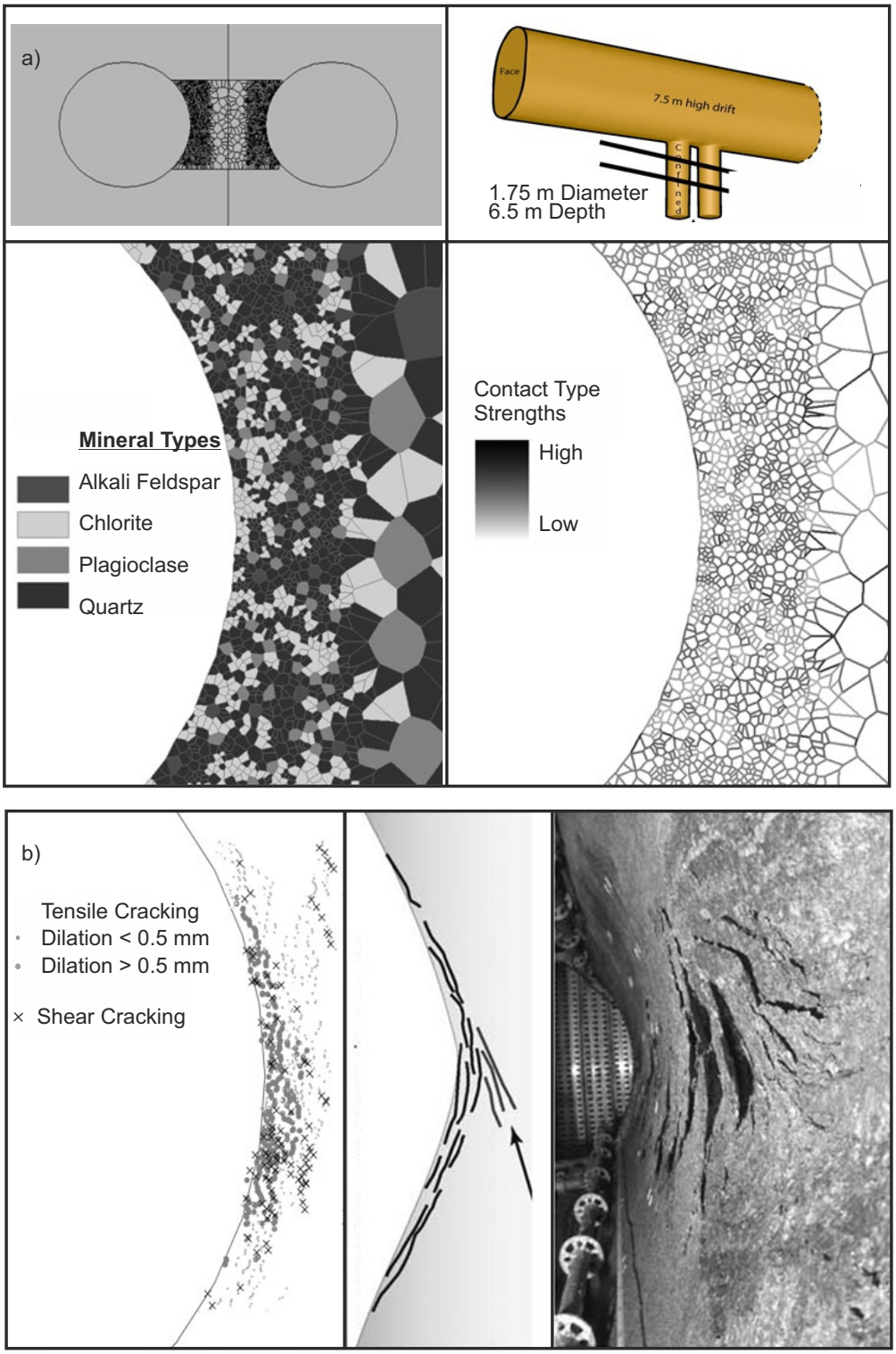

Figure 2.8: a) UDEC GBM model geometry of APSE by Lan et al. (2013), and application of grain properties to GBM. b) The modelled damage after all thermo-mechanical loading at the APSE (Lan et al., 2013) compared with an illustration of observations and a photograph of damage (Andersson, 2007). Figures redrawn after Lan et al. (2013).

The only known study that has introduced thermo-mechanical coupling to a laboratory scale Voronoi GBM was undertaken by Park et al. (2015). The mechanical properties of the Hwangdeung granite were calibrated by simulating laboratory UCS and Brazilian disc indirect tension tests, with mineral percentages taken from X-ray Diffraction (XRD) analysis. Thermal properties were also applied to the Voronoi GBM, before heating the simulations at a rate of 0.4×10^{-5} °C per time step, to temperatures up to 200 °C. UCS and Brazilian disc tests were then carried out at elevated temperatures. No laboratory test data was presented to allow comparison of the mechanical strengths at elevated temperatures, but the model simulations showed the development of displacements due to thermal expansion, and the formation of thermally induced brittle micro-cracking.

2.8 Chapter summary

In this chapter, a literature review was provided on the evolution of the understanding of the brittle deformation of intact rock and discontinuities under mechanical and thermal loading. In addition, a review was provided of research on the thermo-mechanical behaviour of intact rock and discontinuities in the laboratory environment, and in discrete element numerical simulations. As an outcome of this literature review, the following current gaps in knowledge have been identified:

- differences in closure and shear behaviour of rock discontinuities under thermal loading has been shown to occur at a large scale, but is not fundamentally understood at a small (laboratory) scale;
- synthetic materials have successfully been used to examine the fundamental behaviour of rock discontinuities in low stress environments, but have not been validated for use in high stress environments;
- methods for casting discontinuities in synthetic lithologies for shearbox testing in low stress environments have been shown to be achievable and repeatable, but no method exists for repeatedly casting discontinuities in synthetic specimens suitable for triaxial shear testing in higher stress environments; and
- DEM GBMs have been shown to simulate the progressive mechanical failure of

laboratory scale specimens, but thermo-mechanically coupled GBMs capturing the thermo-mechanical behaviour of laboratory specimens has not previously been achieved.

This study will build on the current body of research and attempt to address the above knowledge gaps by:

- creating a synthetic lithology analogous to a real rock lithology suitable for undertaking thermo-mechanical triaxial shear experiments on discontinuities of repeatable topographies (Chapter 4);
- undertake thermo-mechanical laboratory testing at conditions applicable to engineering design on both intact and discontinuous specimens of sandstone (Chapter 5); and
- expand on recent research utilising DEM GBMs to further investigate the thermo-mechanical behaviour of laboratory specimens through thermo-mechanically coupled numerical simulations (Chapter 6).

Chapter 3

Specimen preparation, laboratory apparatus & test methods

3.1 Introduction

In the following chapter, the methods used to undertake specimen processing and preparation of both synthetic specimens in Chapter 4, and real rock specimens in Chapter 5 are outlined. The procedures for undertaking mechanical and thermo-mechanical testing on these lithologies are then described.

3.2 Specimen preparation

Following specimen curing (§ 4.7) all synthetic specimens (Chapter 4), in addition to all natural specimens (Chapter 5) were prepared using the following procedures.

3.2.1 Sawing, coring & grinding

All specimens were prepared according to the dimensions and tolerances outlined in Ulusay (2014). Blocks of dimension stone obtained from the quarries were sawn to a maximum size of 40 x 40 x 20 cm using a diamond sintered circular saw (Fig. 3.1a) to allow further preparation. Blocks were then clamped in place on the table of a pillar drill and specimens prepared for uniaxial and triaxial testing were cored to a diameter of 54 mm using a diamond impregnated coring drill (Fig. 3.1b). Water flush was used to cool the drill bit and remove fines during drilling. Whilst bedding of both the Thornhill Rock and Midgley Grit is massive, bedding orientation can be delineated by the presence of the alignment of minor visible organics. All specimens were cored perpendicular to bedding, to control anisotropic effects.

The ends of the specimens were then trimmed to a length of approximately 120 mm using a diamond sintered circular saw (Fig. 3.1c), providing a length to diameter ratio of between 2.5 and 2:1. Specimens were then locked on to the plate of a grinding machine using v-clamps and a magnetic locking system and the specimen ends were ground flat to an accuracy of ± 0.02 mm, not departing from perpendicularity to the axis of the specimen by more than 0.025 mm in 25 mm using a diamond sintered grinding wheel (Fig. 3.1d), thus preventing an uneven distribution of stress on the specimen ends during experimentation (Hawkes and Mellor, 1970).

Figure 3.1: a) Sawing dimension stone blocks to maximum dimensions of 40 x 40 x 20 cm with diamond sintered circular saw. b) Coring cylindrical specimens at 54 mm diameter with diamond impregnated drill bit. c) Trimming specimen lengths to ≈ 120 mm using a diamond sintered circular saw. d) diamond sintered grinding wheel for grinding specimen ends. e) Inducing discontinuities in specimens at an angle of 30° to 40° by tensile splitting.

Specimens for tensile testing were prepared using the same methods, but specimen dimensions were a diameter of 54 mm and length of approximately 27 mm (Bieniawski and Hawkes, 1978).

3.2.2 Discontinuity creation

For discontinuity testing in triaxial conditions, it is required for the discontinuity to be running through the specimen at 30° to 40° to ensure that the most likely plane of failure is for shear to occur along the discontinuity. Rather than trying to core across

natural discontinuities at the correct angle, it was decided to induce discontinuities in intact specimens by inducing tensile failure, producing a rough discontinuity at the correct angle. Specimens were placed between two metal blades of a hydraulic splitter at the desired angle, and the top blade was then lowered, inducing tensile failure (Fig. 3.1e). Whilst it is recognised that discontinuities induced through tensile splitting are known to produce rougher topographies than naturally forming discontinuities in the same lithology (Vogler et al., 2017), this methodology produced the best repeatability for consistent discontinuity creation, with approximately 7 in 10 specimens splitting to form discontinuities at the correct angle. Occasionally discontinuities formed parallel to bedding despite the angle of the hydraulic splitter blades. This was usually due to the presence of organic material acting as a preferential plane of weakness on which failure occurred. These specimens were discarded.

3.2.3 Laser profilometry

Once discontinuities were created, a laser profilometer was used to obtain a digital representation of the discontinuity topography. A NextEngine 2020i laser profilometer capable of profiling surfaces at up to 100 µm was used (Fig. 4.4a). The laser profilometry produced a triangulated surface for each discontinuity profiled, and a point cloud of data points was extracted from this for further analysis and statistical quantification of the discontinuity roughness as outlined in § 4.4.2.

3.2.4 Oven drying specimens

After preparation and prior to testing, all specimens were oven dried to remove moisture. The International Society for Rock Mechanics (ISRM) suggests oven drying specimens at 105 °C (Ulusay, 2014). However as this study is investigating the thermo-mechanical properties of intact rock and discontinuities at temperatures ranging from ambient room temperature (20 °C) up to 100 °C, it was decided not to oven dry specimens at 105 °C in case irreversible thermal damage occurred when subjecting specimens to this temperature. Instead specimens were oven dried at 40 °C. Vacuum saturated specimens of Thornhill Rock and Midgley Grit were placed in an oven at 40 °C, and removed and weighed every 4 hours until constant mass was achieved (i.e. no more

water was removed from the specimen). Constant mass was achieved after 48 hours, therefore all specimens were oven dried at 40 °C for a minimum of 48 hours going forward. After oven drying, specimens were double sealed in air tight sample bags until ready for testing.

3.3 Characterisation testing

Characterisation testing of synthetic compositions, as well as initial characterisation testing to deduce basic mechanical properties of the Thornhill Rock and the Midgley Grit were undertaken in the Rock Mechanics, Engineering Geology and Geotechnics (RMEGG) laboratory at the University of Leeds. Baseline mechanical data were collected to allow a comparison to be made with thermo-mechanical behaviour (Chapter 5). Additionally, data collected were used as input data for numerical modelling described in Chapter 6.

3.3.1 Strength & stiffness testing

3.3.1.1 Apparatus

A single piece of apparatus was used for both uniaxial and triaxial compression testing in the RMEGG laboratory. A Denison 7227C stiff load frame with axial actuator, which can exert a maximum axial compressive load of 2000 kN was used for both test types (Fig. 3.2). The apparatus works by an actuator piston, powered by a hydraulic ringmain, which raises the bed plate towards the crosshead of the stiff frame, on which the load cell (also rated to 2000 kN) was situated. Hardened steel platens and two hemispherical seats were used above and below the specimen to ensure that the specimen was loaded evenly during each experiment.

For triaxial testing (actually biaxial testing ($\sigma_2 = \sigma_3$)), confining pressure was applied to the specimen using a Hoek cell. This consists of a hollow steel cylinder with threaded removable ends. A urethane rubber sleeve with u-shaped seals was used to create a pressurisation chamber filled with mineral oil. The pressurisation chamber was connected to a manual hydraulic pump. The specimen was inserted into the Hoek cell

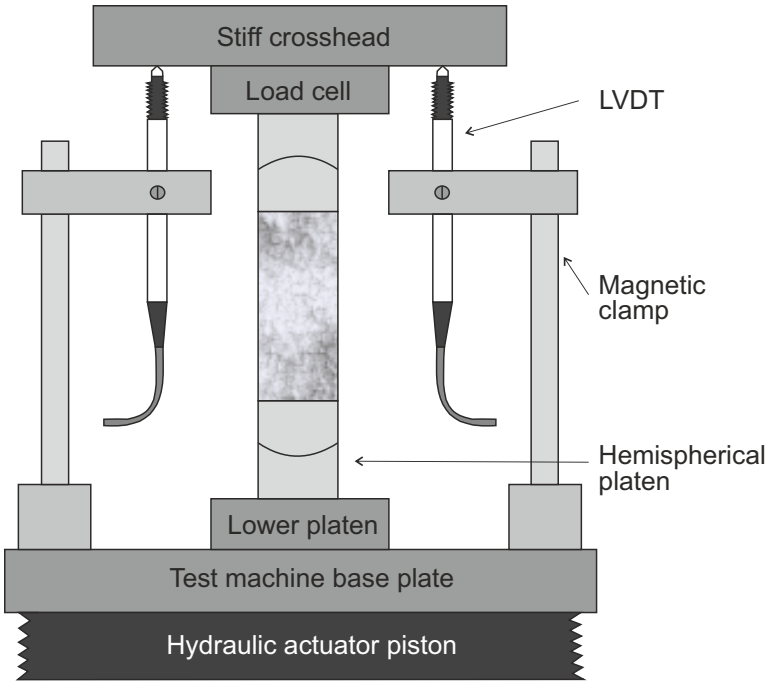

Figure 3.2: Schematic diagram of specimen set up in Denison 7227C load frame for uniaxial compression testing.

allowing confining pressures of up to 70 MPa to be applied.

In addition the apparatus was set up to record auxiliary measurements. Axial displacement was measured using two linearly variable displacement transducers (LVDTs) placed diametrically opposite to each other, and magnetically clamped to measure in an axial orientation. Axial and radial strain could also be measured if required using Vishay strain gauges. These are foil strain gauges, which are bonded directly to the surface of the specimen, typically with two axial and two radial strain gauges applied diametrically opposite each other in the centre of the specimen over 10 mm. The voltage of the LVDTs were calibrated prior to testing using a manual barrel micrometer. The voltage of the load cell was calibrated prior to testing using a proving ring. Readings of axial load and displacement were then logged every second for the duration of each test.

3.3.1.2 Test methods

General test procedures for uniaxial and triaxial testing follow the suggested methods as outlined by the ISRM (Bieniawski and Bernede, 1979; Kalman et al., 1983). After specimens were prepared and oven dried they were loaded in to the apparatus. A small pre-load was then applied to the specimen of 3 kN (1.3 MPa). For uniaxial and triaxial testing, specimens were loaded at a constant axial displacement rate of 0.1 mm min^{-1} until failure. During the initial period of axial loading the confining pressure within the Hoek cell was gradually increased by hand to the desired pressure. Care was taken to apply the pressure as hydrostatically as possible, maintaining a differential stress of just the pre-load prior to then allowing the specimen to deform. For specimens with brittle behaviour, where possible the test was terminated when residual strength was obtained. For specimens tested at higher confining pressures, tests were terminated after peak strength had been obtained and left to run to a maximum of 3% axial strain.

3.4 Additional characterisation testing

In addition to compressional strength and stiffness testing, the following tests were also undertaken to provide inputs for numerical modelling.

3.4.1 Tensile strength

Tensile strength was obtained using the indirect tensile strength test (Brazilian test), following the suggested methods of the ISRM (Bieniawski and Hawkes, 1978). Specimens were prepared as cylinders of 36 mm diameter, and 20 mm length. Following specimen preparation and oven drying, specimens were wrapped in masking tape, and placed diametrically between two hardened steel platens in a MAND 250 kN stiff load frame fitted with a 10 kN load cell. Specimens were loaded at a loading rate of 200 N s^{-1} until failure occurred. The tensile strength (σ_t) of the specimen was then calculated as:

$$\sigma_t = \frac{2P}{\pi r(\text{t})} \qquad \text{(MPa)} \tag{3.1}$$

where P is the load at failure (N), and r and t are the radius and thickness of the test specimen (mm).

3.4.2 Density & porosity

Density and porosity measurements were obtained using saturation and buoyancy techniques on offcuts of cylindrical specimens from specimen preparation, following the suggested methods of the ISRM (Franklin et al., 1981). Specimens were vacuum saturated in de-aired water for 24 hours. Specimens were then weighed to obtain both the saturated-surface-dry mass (M_{sat}), and the saturated-submerged mass (M_{sub}). The sample bulk volume (V) was then calculated as:

$$V = \frac{M_{sat} - M_{sub}}{\rho_w} \tag{3.2}$$

where ρ_w is the density of water. Specimens were then oven dried at 40 °C for 48 hours to obtain the dry mass (M_s), allowing dry density (ρ_d) to be calculated as:

$$\rho_d = \frac{M_s}{V} \tag{3.3}$$

The water volume (V_w) of saturated specimens was then calculated as:

$$V_w = \frac{M_{sat} - M_s}{\rho_w} \tag{3.4}$$

allowing percentage porosity (φ) to be calculated as:

$$\varphi = \frac{V_w}{V} \times 100 \tag{3.5}$$

3.5 Triaxial testing at the British Geological Survey

All of the main testing in this study was undertaken in the Rock Mechanics and Physics Laboratory (RMPL) at the British Geological Survey (BGS), Environmental Science Centre in Keyworth, Nottinghamshire.

3.5.1 Apparatus

Triaxial testing on intact and discontinuous specimens was undertaken in a closed-loop proportional-integral-derivative servo-controlled (PID controlled or three-term controller) stiff load frame capable of maximum axial loads up to 4600 kN, fitted with a confining pressure vessel capable of applying confining pressures up to 140 MPa (Fig. 3.3). The confining cell was fitted with external heater bands utilising cascade control from an internal thermocouple fitted directly next to the specimen and an external thermocouple fitted to a heater band (accurate to ±0.5 °C). Mineral oil was used as a confining medium. A 2600 kN capacity force transducer (accurate to 0.32% of the load) was used to measure the axial load. A spherical seated platen was used between the specimen and the capacity force transducer to prevent eccentric loading.

Specimens were instrumented with two axial extensometers (accurate to ±0.01%). On intact specimens, the axial extensometers were placed diametrically opposite each other over the central 50 mm of the specimen. On discontinuous specimens, the axial extensometers were placed diametrically opposite each other on the long edge of the discontinuity. A circumferential chain extensometer (accurate to ±0.01%) was also fitted to specimens. It was fitted mid-length on intact specimens and mid-discontinuity on discontinuous specimens.

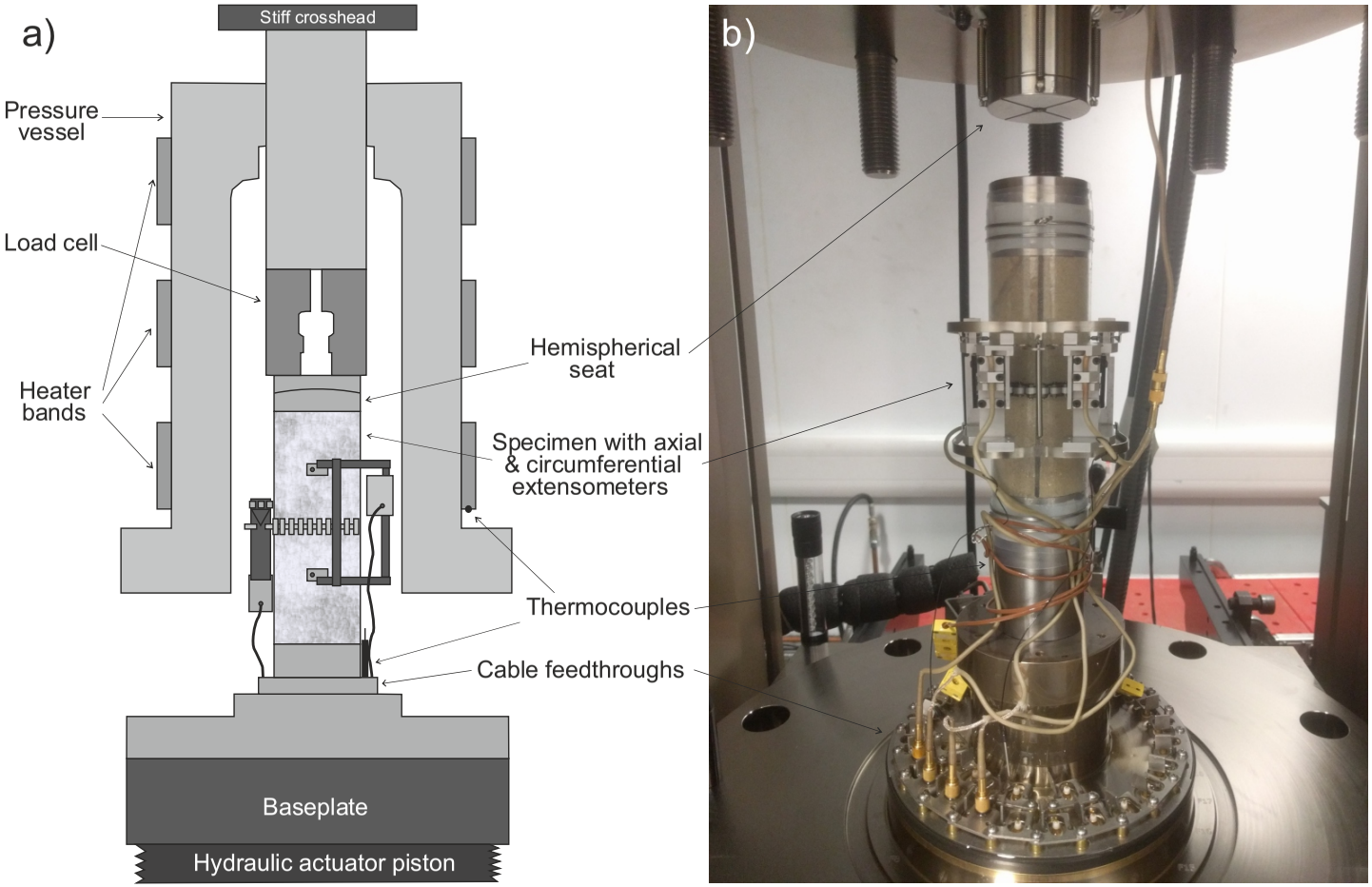

Figure 3.3: a) Schematic diagram of instrumented specimen set up in pressure vessel for triaxial testing. b) Photograph of specimen set up in pressure vessel for triaxial testing.

3.5.2 Specimen assembly

Specimens were placed between two hardened steel platens encased in two layers of 0.5 mm Polytetrafluoroethylene (PTFE) heat shrink tubing and sealed using stainless steel locking wires over self-amalgamating silicone tape to prevent the ingress of confining fluid to the specimen. The extensometers were then fitted directly over the PTFE specimen jacket.

3.5.3 Test methods & procedures

Test procedures for triaxial testing at the BGS were designed to replicate boundary conditions that may be expected in a GDF scenario. All triaxial testing was undertaken using a confining pressure of 5 MPa. Depending on the density of overburden, ground saturation, the regional stress field and the coefficient of lateral earth pressure, this equates to a depth of between 200 and 500 m depth. For testing under thermal loading, the thermal loading was applied prior to the mechanical loading (confining pressure and axial loading). This is equivalent to a GDF scenario in which the storage facility is excavated and likely supported (i.e. the rock mass in the close vicinity of the excavation is unloaded), the waste is then emplaced (i.e. the thermal loading source is introduced), the storage facility is then backfilled (i.e. the mechanical load is replaced on the rock mass).

3.5.3.1 Room temperature intact testing

1. Following preparation, assembly and instrumentation, specimens were loaded in to the pressure vessel;
2. the axial hydraulic actuator piston was manually raised to engage with the base plate of the pressure vessel. The base plate was then manually raised until the specimen was within 1 mm of contact with the capacity force transducer. The axial displacement was zeroed at this point, and 0 mm displacement was maintained by the servo-control;
3. the pressure vessel was lowered and sealed shut;

4. contact was made with the specimen. Firstly a pre-load of 1 kN was applied to the specimen, this was incrementally increased to 2.3 kN (1 MPa on a 54 mm diameter (Ø) specimen), ensuring good specimen contact and no large displacements occurred. Axial and circumferential extensometers were zeroed at this point;

5. the pressure vessel was filled with confining oil;

6. the confining pressure intensifier was raised ensuring enough room remained in confining displacement range for confining pressure to be applied;

7. the test procedure was then initiated and data began logging;

8. the confining pressure was increased to 5 MPa at 1 MPa min^{-1}, whilst maintaining an axial differential pre-load of 1 MPa;

9. once all strains were stable at hydrostatic stress, axial loading was initiated. Axial loading was undertaken in axial strain control at $5 \times 10^{-6}\,\mathrm{s}^{-1}$ controlled directly from the axial extensometers;

10. when the specimen began to yield, loading control was switched to circumferential strain control to better control the radial dilation of the specimen and capture the failure process. Circumferential extension control was undertaken at $1 \times 10^{-3}\,\mathrm{mm\,s}^{-1}$;

11. deformation was continued until 2 mm circumferential strain occurred;

12. the specimen was unloaded axially at $0.01\,\mathrm{mm\,s}^{-1}$ back to a hydrostatic pressure of 5 MPa. The confining pressure was then removed at 1 MPa min^{-1}; and

13. the pressure vessel was emptied of confining oil, the pressure vessel was opened and the specimen was removed.

3.5.3.2 Elevated temperature intact testing

The initial procedure was identical to the room temperature procedure as outlined in points 1 to 5 in § 3.5.3.1, followed by:

6. the pressure vessel was wrapped in thermally insulating blankets;

7. the confining pressure intensifier was raised to its maximum limit. Thermal expansion of the confining oil under heating results in the confining displacement retracting to account for the additional volume. Raising the confining pressure intensifier to its maximum limit allows room for the confining displacement to retract during heating;

8. a small initial confining pressure of 0.5 MPa was applied whilst maintaining an axial differential pre-load of 1 MPa;

9. the test procedure was then initiated and data began logging;

10. the temperature was increased at $1.5\,^{\circ}\mathrm{C\,min^{-1}}$ to the desired thermal load of either 50 °C, 75 °C or 100 °C. For tests above 50 °C, the confining pressure intensifier required manual repriming during heating due to the thermal expansion of the confining oil. A loading rate of $1.5\,^{\circ}\mathrm{C\,min^{-1}}$ ensures the specimen is not thermally shocked, and ensures a low temperature gradient across the specimen;

11. based on a thermal conductivity (k) of $2.3\,\mathrm{W\,m^{-1}\,K^{-1}}$, density ($\rho$) of $2250\,\mathrm{kg\,m^{-3}}$ and specific heat capacity (c_p) of $700\,\mathrm{J\,g^{-1}\,K^{-1}}$, thermal diffusivity ($\kappa$) can be calculated as:

$$\kappa = \frac{k}{\rho \cdot c_p} \tag{3.6}$$

κ of specimens is given as approximately $1.4 \times 10^{-6}\,\mathrm{m^2\,s^{-1}}$. Specimen radius ($r$) is 2.7×10^{-2} m, therefore the time constant for temperature equilibrium (r^2/κ) (Wang et al., 2013), is approximately 900 s. To ensure thermal equilibrium across the pressure vessel and the specimen, temperature and pre-loads were held constant for 30 min;

12. the confining pressure was increased to 5 MPa at $1\,\mathrm{MPa\,min^{-1}}$, whilst maintaining an axial differential pre-load of 1 MPa;

13. once all strains were stable at hydrostatic pressure, axial loading was initiated. Axial loading was undertaken in axial strain control at $5 \times 10^{-6}\,\mathrm{s^{-1}}$ controlled directly from the axial extensometers;

14. when the specimen began to yield, loading control was switched to circumferential strain control to better control the radial dilation of the specimen and

capture the failure process. Circumferential extension control was undertaken at $1 \times 10^{-3}\,\mathrm{mm\,s^{-1}}$;

15. deformation was continued until 2 mm circumferential extension occurred;
16. the specimen was unloaded axially at $0.01\,\mathrm{mm\,s^{-1}}$ back to a hydrostatic pressure of 5 MPa. The confining pressure was then removed at $1\,\mathrm{MPa\,min^{-1}}$;
17. the pressure vessel was left to passively cool back to ambient temperature, typically taking 18 hours;
18. the pressure vessel was emptied of confining oil, the pressure vessel was opened and the specimen was removed.

3.5.3.3 Discontinuity testing

Procedures for discontinuity testing were identical to that for testing of intact specimens, with the exception of not switching from axial strain control to circumferential strain control during deformation. As failure in the discontinuous specimens was in shear along the discontinuity, deformation control was maintained in axial strain control to control the shear displacement on the discontinuity. Discontinuities were sheared until residual shear strength was reached or until a maximum of 4% axial strain.

3.5.3.4 Data logging

Throughout all intact and discontinuity testing, the following raw data was logged at both 1 s intervals, and at every 250 N change in axial force, allowing any sudden changes in load or deformational behaviour to be captured:

- time;
- axial force;
- axial stress[1];
- axial displacement;
- confining pressure;
- confining displacement;
- axial extension A & B;
- circumferential extension;

[1] Based on a specimen diameter of exactly 54 mm. Recalculated from axial force using individual specimen dimensions during post-processing.

- volumetric strain[1];
- temperature.

3.5.4 Tuning & calibration

Calibration of the servo-controller, pressure vessel, hydraulic system, heating system and all associated ancillary measurement apparatus (e.g. extensometers) was carried out annually by the manufacturer (MTS Systems Corporation) to American Society for Testing & Materials (ASTM) requirements against known standards, and was carried out three times in the duration of this study.

Tuning of the PID control channels used during deformation (axial force, axial strain, and circumferential strain) was carried out for each lithology tested to provide the best response of the closed-loop servo-control. Tuning was carried out for each channel in turn by loading specimens to approximately 6% of UCS in a control channel, and then pulsing the load ±3% with a square wave signal every second whilst adjusting the feedback gain variables (P-gain and I-gain) until the best fit between the command signal and servo-control response was achieved. Tuning was also possible during testing if required.

3.5.5 Dummy testing

In addition to manufacturer calibration and tuning, testing of the calibration and thermal loading procedure was undertaken on dummy specimens of aluminium. Aluminium alloy 2011-t3 (properties in Table 3.1) was milled to create cylindrical specimens 120 mm in length by 54 mm diameter. Specimens were assembled as previously outlined in § 3.5.2.

Firstly a mechanical load test within the linearly elastic region of the aluminium's strength was undertaken. The specimen was loaded in axial strain control at $5 \times 10^{-6}\,\mathrm{s}^{-1}$ up to 100 kN and back again. The specimen showed perfectly linearly elastic behaviour. Young's modulus (E) and Poisson's ratio (ν) were then calculated from the axial stress

[1] Calculated from axial and circumferential strains directly from extensometer readings.

Physical property	Value
Density (ρ)	$2830\,\mathrm{kg\,m^{-3}}$
Young's modulus (E)	$70\,\mathrm{GPa}$
Poisson's ratio (ν)	0.35
Thermal conductivity (k)	$151\,\mathrm{W\,m^{-1}\,K^{-1}}$
Coefficient of linear thermal expansion (α_L)	$2.29 \times 10^{-5}\,\mathrm{K^{-1}}$

Table 3.1: Published physical properties of 2011-t3 alloy aluminium.

(σ_a) (calculated from the axial force and the specimen dimensions) and extensometer data as:

$$E = \frac{\sigma_a}{\varepsilon_a} \tag{3.7}$$

$$\nu = -\frac{\varepsilon_d}{\varepsilon_a} \tag{3.8}$$

where ε_d is the diametral strain from the circumferential extensometer, and ε_a is the axial strain from the axial extensometers. Results from this experimental loading test give $E = 70.24\,\mathrm{GPa}$, and $\nu = 0.29$ for the aluminium alloy. E is shown to be identical to the published value of 70 GPa (within the precision of the reported published value), showing that the axial extensometers accurately obtain the axial deformation of the aluminium under linear elastic loading, despite the specimen being encased in two layers of PTFE. $\nu = 0.29$ is slightly lower than the published value of 0.35, suggesting less circumferential deformation occurred than would be expected, this could be due to the milling of the aluminium rod, or more likely due to slack in the circumferential chain resulting in not all of the circumferential deformation being obtained by the extensometer.

Overall, this dummy testing demonstrated that at room temperature the manufacturer's calibration of the capacity force transducer and extensometers produce good results for obtaining strength and stiffness properties of a test material with known published properties.

In addition, aluminium dummy testing was undertaken of the thermal loading procedure for elevated temperature testing (points 1 to 5 of § 3.5.3.1 followed by points 6 to 11 of § 3.5.3.2) to gauge the behaviour of the servo-controlled triaxial rig at elevated temperatures and analyse the behaviour of the extensometers under thermal loading. Vishay strain gauges measure the change in electrical resistance as the foil is deformed, therefore also measuring the strain of the gauge itself under thermal loading. In comparison, axial and circumferential extensometers work with the resistive-type foil strain gauges bonded between a reference leg and a moveable leg to create a Wheatstone bridge. As the reference leg from which the deformation is calculated also undergoes thermal expansion, the extensometers should be rated to obtain strain measurements at elevated temperatures.

The theoretical thermal expansion of the aluminium specimen was calculated from the published coefficient of linear thermal expansion (α_L) as:

$$\varepsilon = \frac{\Delta L}{L} = \alpha_L \Delta T \tag{3.9}$$

where L is the original specimen length, ΔL is the change in specimen length, and ΔT is the change in temperature. The theoretical thermal expansion was compared with the thermal expansion obtained by the axial and circumferential extensometers during the thermal loading test, as well as the axial displacement of the axial ram of the triaxial rig whilst maintaining a pre-load of 1 MPa (Fig. 3.4).

For the first 1000 s of heating, a lag is observed between the heating command at 1.5 °C min^{-1} and the heating of the specimen measured from the thermocouple within the triaxial pressure vessel next to the specimen. This is due to the initial heating of the steel pressure vessel and mineral oil confining fluid prior to heating of the specimen. Heating then occurs at a slightly slower rate than the heating command of 1.1 °C min^{-1} to approximately 80 °C before the servo-control feedback reduces the heating rate and plateaus to 100 °C after approximately 2.5 h of heating.

The axial linear thermal expansion measured on the axial extensometers (Fig. 3.4a) shows an additional lag of approximately 1000 s to the heating curve. This is due to

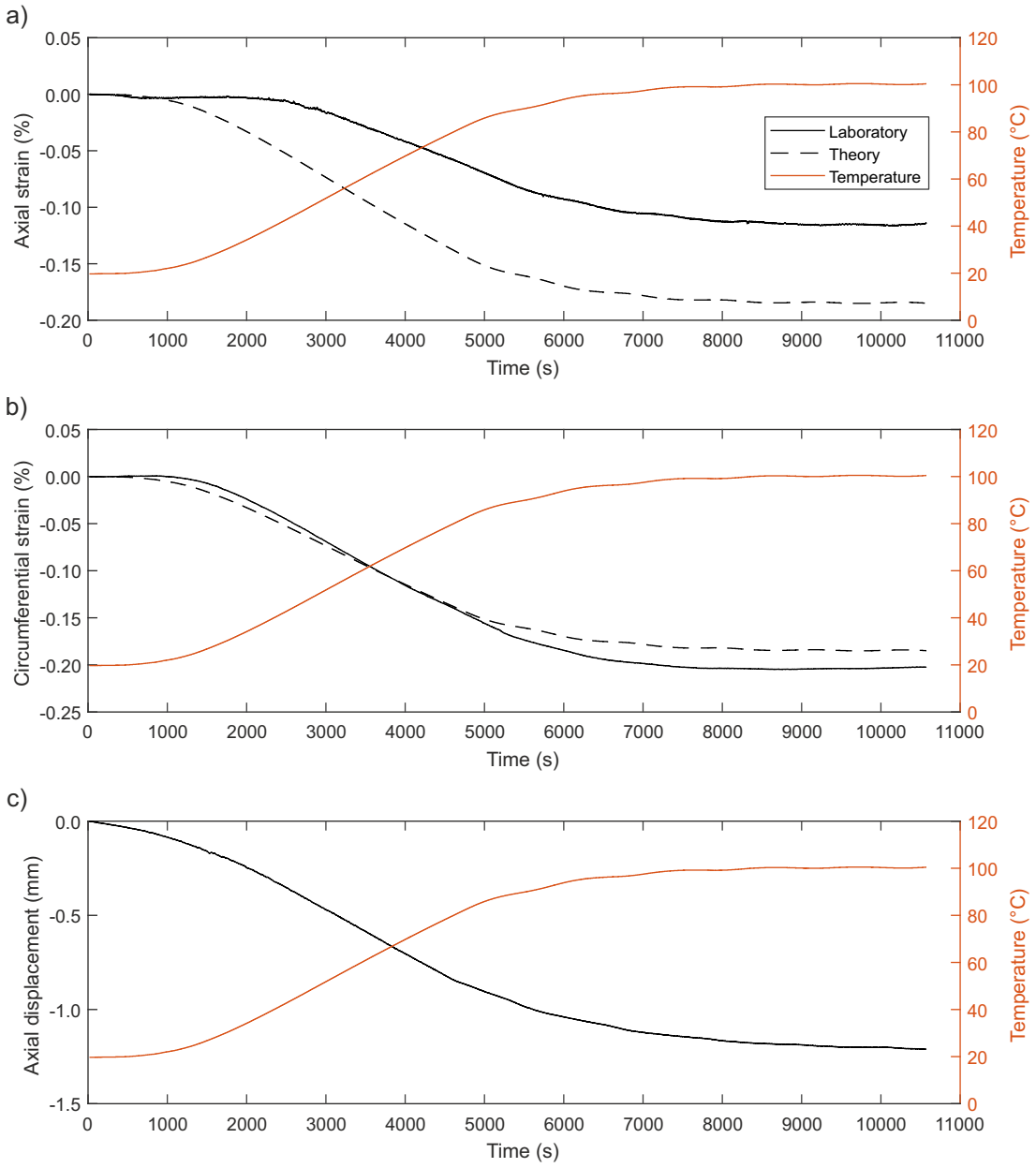

Figure 3.4: a) Theoretical axial thermal expansion of aluminium specimen (based on coefficient of linear thermal expansion of 2011-t3 alloy of $2.29 \times 10^{-5}\,\mathrm{K}^{-1}$) with heating from 20 to 100 °C, compared to axial thermal expansion observed in the laboratory heating test from axial extensometers. b) Theoretical circumferential thermal expansion of aluminium specimen (based on coefficient of area thermal expansion of 2011-t3 alloy of $4.58 \times 10^{-5}\,\mathrm{K}^{-1}$) with heating from 20 to 100 °C, compared to circumferential thermal expansion observed in the laboratory heating test from the circumferential extensometer. c) Axial displacement of the axial ram caused by axial thermal expansion during the laboratory heating test from 20 to 100 °C.

the thermal diffusivity of the aluminium resulting in additional time for the specimen to heat to the temperature of the surrounding confining fluid. After the initial lag, the axial linear thermal expansion is less than the theoretical axial thermal expansion. This may be a result of increased ductility of the PTFE jacketing with increased temperature resulting in slipping of the specimen within the PTFE jacket, or slipping of the extensometers on the PTFE jacket, subsequently not all of the axial thermal expansion is measured. However, this error may be minimised with rock specimens due to increased friction between the specimen and the PTFE jacket compared with aluminium specimens. If the axial extensometers are also unable to adequately measure the axial thermal expansion of rock specimens during thermal loading, this will limit the interpretation of thermo-mechanical laboratory tests, and it will not be possible to assess the potential thermal closure of discontinuities during thermo-mechanical laboratory testing. The area thermal expansion (α_A (where $\alpha_A = 2\alpha_L$)) obtained from the circumferential strain gauge (Fig. 3.4b) fits very closely with the theoretical area thermal expansion. The axial displacement of the axial hydraulic ram shows significant displacement during heating to maintain the 1 MPa axial pre-load (Fig. 3.4c).

This displacement accounts for the thermal expansion of the platens, load cell and pressure vessel, in addition to the thermal expansion of the specimen, and therefore can not be used to calculate specimen deformation during thermally loaded tests.

3.6 Chapter summary

In this chapter the methods used to undertake specimen processing and preparation were described. The methods contained in this chapter are applicable to both the synthetic specimens developed in Chapter 4 and rock specimens tested throughout Chapter 5.

Chapter 4

Synthetic rock development & testing

4.1 Introduction

Investigating the mechanics of discontinuities under different temperatures and stresses, in particular, looking at the effects of varying discontinuity topography and the potential changes in discontinuity mechanics with increasing temperature, is complicated by a large number of variables influencing the process. These variables include: rock strength, discontinuity wall strength, specimen micro-heterogeneity (e.g. mineralogy, grain size, grain shape, anisotropy), discontinuity roughness, and boundary conditions. Due to the heterogeneity of rock, every specimen will have a unique set of these properties. Synthetic materials have been used extensively in rock discontinuity mechanics to overcome this, where the preparation of identical synthetic specimens with the same topographical and mechanical characteristics reduces the number of variables influencing the discontinuity behaviour. This allows fundamental behaviour to be defined through the testing of identical discontinuities under varying conditions.

In this chapter, a new methodology utilising 3D printing to create moulds with representative topographies, which synthetic discontinuity specimens can be cast from, is presented. In addition, the intact mechanical properties and suitability of different synthetic compositions is explored.

Raw data from laboratory testing undertaken as part of this chapter is available to download from the National Geoscience Data Centre:

https://dx.doi.org/10.5285/ae62bf20-042c-4c65-8a51-5683b8bef2f0

In addition, summarised parameters from the laboratory testing are tabulated in Appendix A.

4.2 Creation of discontinuous specimens

A number of different materials have previously been used for the construction of moulds to be used as negatives for casting. Materials include silicon rubber (Chrysanthakis and Barton, 1990), silicon elastomer (Gentier et al., 2000) and Vinamold

rubber (Grasselli, 2001; Papaliangas, 1996). All of the above compounds are used to create moulds by fixing a real rock discontinuity in to a square or rectangular steel frame, liquefying the moulding material by heating and then pouring the liquid moulding material over the real discontinuity and allowing to cool. Once cooled, the moulding material can be removed from the discontinuity creating a negative in to which a synthetic mixture can be cast to reproduce the discontinuity. This methodology works well for the creation of synthetic discontinuities for shearbox testing where the discontinuity is cast parallel to the square frame of the mould (Fig. 2.4a). For triaxial testing, the discontinuity is required to be cast through a cylindrical specimen orientated at an angle in the range of 30° to 45° dependent on the friction angle of the material. This is done so that shear displacement along the discontinuity is the most likely mode of failure during testing (Fig. 2.4d). Creating a synthetic specimen with a discontinuity running at an angle through the mould using a hot set moulding material presents challenges, therefore a new method utilising 3D printing has been devised.

3D printing or additive manufacturing, allows the generation of 3D solid objects directly from computer aided design (CAD) files. Multiple 3D printing technologies exist, but the most common is a fused deposition modelling process, which works through depositing a binder material, ranging from general purpose plastics such as acrylonitrile butadiene styrene (ABS) or polylactic acid (PLA) to resins, rubbers, various metallic alloys or even sand grains. The binder material is deposited from a printer head, which is able to move in three dimensions, and the object is built in a layer by layer process. Printing resolution is dependent on the binding material and the object design, but resolutions in the order of hundreds of microns can typically be achieved. As the technology has advanced and become more accessible over the last decade, 3D printing has found its place in many disciplines including medicine, engineering and education. Jiang et al. (2016a) and Jiang et al. (2016b) have recently utilised 3D printing in rock mechanics to study mechanical behaviour in laboratory uniaxial compression testing and the effects of discontinuity topography on shear behaviour in laboratory shearbox testing. Both of these studies use 3D printing to replace previous methods for producing synthetic specimens in laboratory testing. Here, instead the 3D printing is merely used to generate a negative mould for casting, replacing the hot set methodology, rather than 3D printing the synthetic specimen itself.

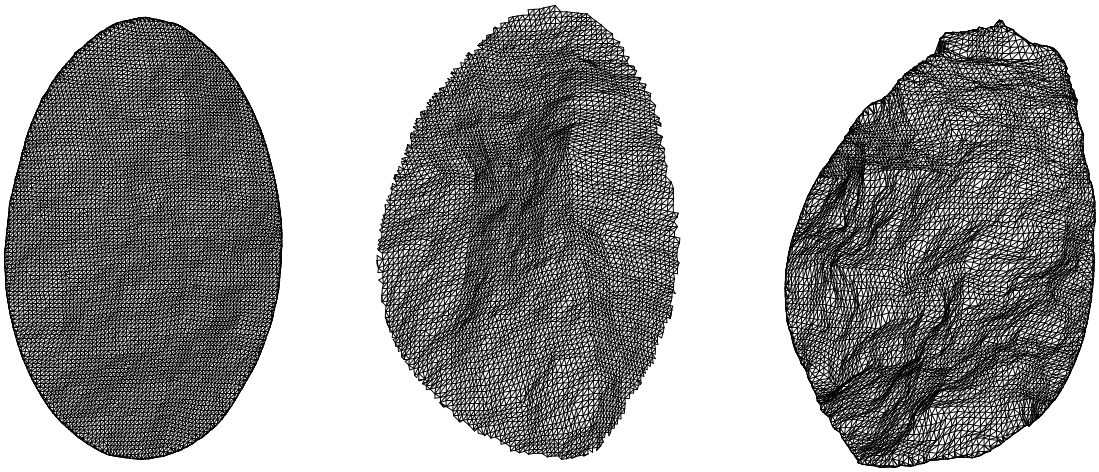

Figure 4.1: Three different modelled roughnesses equivalent to *JRC* 2 to 4 (*Surface 1*), *JRC* 10 to 12 (*Surface 2*) and *JRC* 16 to 18 (*Surface 3*).

The discontinuity planes were modelled fractally in 3D graphics software Blender^{TM} to create three different discontinuity surfaces of different roughnesses (referred to as "*Surface 1*", "*Surface 2*" and "*Surface 3*") (Fig. 4.1)A planar surface was generated in Blender^{TM}, and subdivided into a 0.1 mm regular quad mesh. A fractal dimension between 0 and 1 was applied to the mesh for each surface to add roughness. The roughnesses were quantified statistically (§ 4.4.2), and correlated to a *JRC* value for each surface. Once modelled, the inverse of each discontinuity was also modelled to allow creation of two half specimens, which fit together along the discontinuity plane. The two discontinuity surfaces were built in to cylinders of 54 mm diameter and 1500 mm height, running at a 40° angle from the vertical through the model, ready for 3D printing. 3D printing of the moulds was completed in 200 µm layers of ABS plastic at 25% fill using a Lulzbot Taz 5 3D printer (Fig. 4.2). Prior to specimens being cast, the ABS moulds were coated with a mould release agent to aid the removal of the specimens once cured. Specimens were then cured as described in § 4.7.4. After curing, specimens were further prepared (§ 3.2.1), laser profiled (§ 3.2.3) and oven dried (§ 3.2.4) before being sealed and stored at room temperature prior to testing.

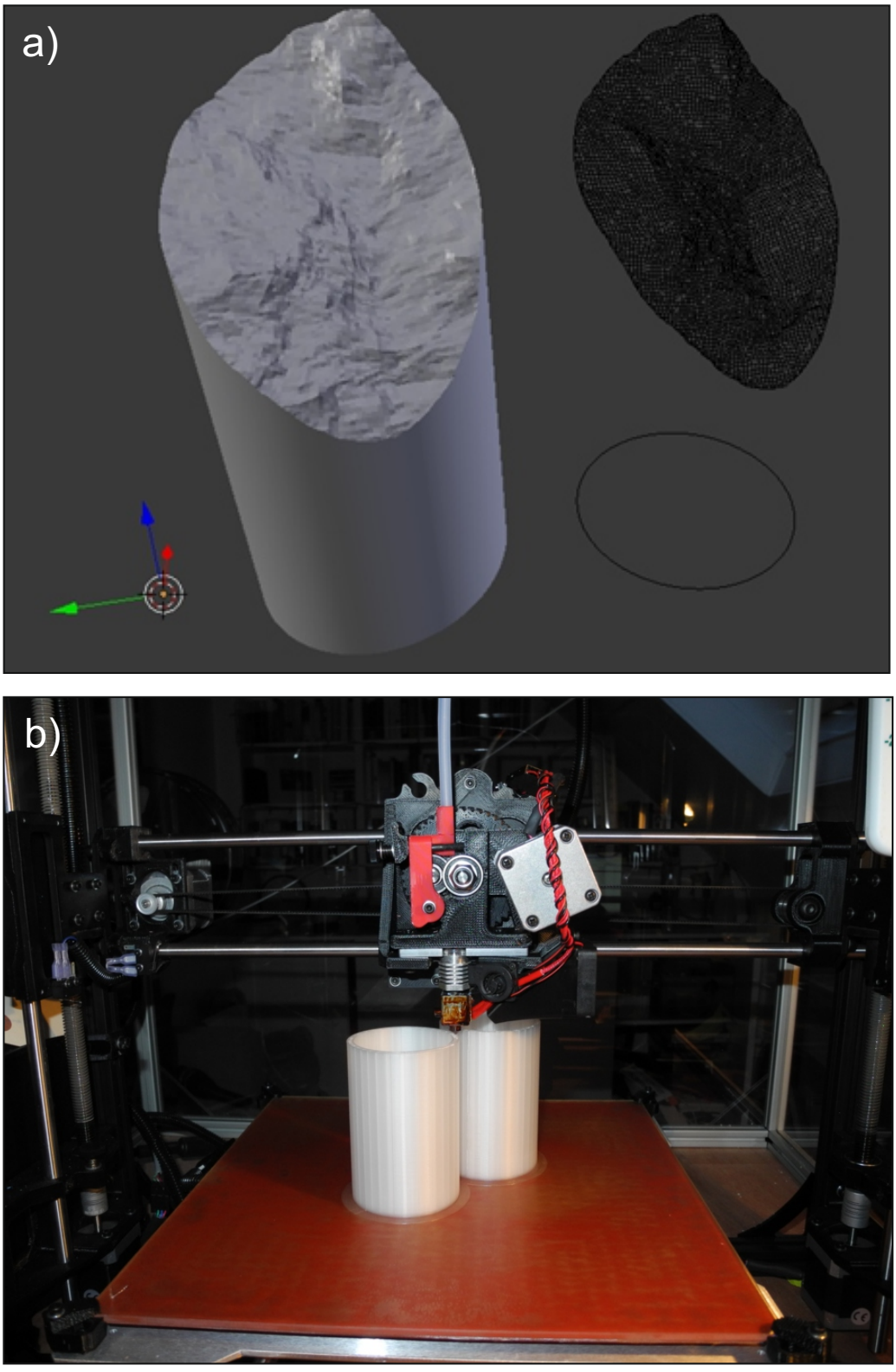

Figure 4.2: a) 3D model of the mould created for 3D printing with discontinuity at 40° through the mould. Roughness shown is *Surface 2* with *JRC* of 10 to 12. b) 3D printing in process.

4.3 Discontinuous specimen creation

After curing, all specimen ends were sawn to give a complete specimen length (i.e. two half specimens) to diameter ratio of between 2.5 and 2:1 (ISRM, 1978). The ends were then ground flat to 0.02 mm, not departing from perpendicularity to the axis of the specimen by more than 0.025 mm in 25 mm (Ulusay, 2014). Specimens were then photographed and each discontinuity scanned using a Nextengine 2020i 3D desktop laser profilometer at 40,000 points cm^{-2}, and dimensional accuracy of $\pm$ 100 µm. This allows for quantification of the discontinuity topography as well as ensuring conformity and consistency between specimens. All specimens were then oven dried at 40 °C for a minimum of 48 h before being sealed and stored at room temperature prior to testing.

4.4 Roughness quantification

4.4.1 Theory

The measurement and the quantification of discontinuity roughness is a fundamental issue in rock mechanics, discontinuity roughness has significant influences on mechanical properties. The first problem lies in the measurement of discontinuity roughness. Numerous technologies exist and have been implemented for measuring discontinuity roughness in both the laboratory and in-situ environments. These are easily divided in to two categories: those requiring physical contact with the specimen surface e.g. profile (Barton) combs (Barton and Choubey, 1977), needle profilometers (Morelli, 2014), and shadow profilometry (Maerz et al., 1990), and those not requiring physical contact with the specimen surface e.g. laser profilometry (Tatone, 2009), high resolution photogrammetry (Ogilvie et al., 2002), optical triangulation systems and advanced topometric scanners (Grasselli, 2001). All measuring devices, regardless of methodology, will have some form of sampling limitation, namely the minimum possible spacing between discrete data points that it is possible to obtain (e.g. the sampling resolution of a profile comb can not be greater than the diameter of the comb pins). Correct selection of the sampling interval is important with consideration to the scale effect on rock joints. Rock discontinuity roughness is often defined as a measure of the small scale unevenness on top of the larger scale waviness of the discontinuity surface relative

to the mean plane. This means that when a larger sampling interval is used, discontinuity roughnesses generally tend to be smoother, and information about the small scale unevenness is lost. Conversely, when examining small scale discontinuities at high resolution data noise can add additional variations and increase the discontinuity roughness (Chae et al., 2004). Rock mechanics laboratory tests are typically carried out on specimens less than 100 mm in size and it has been shown that the size of the asperities damaged in shearing are in the order of millimetres (Grasselli et al., 2002). Yong et al. (2018) studied sampling intervals using Fourier series and calculated the maximum sampling intervals acceptable for characterising the roughness of different sized specimens. It was found that a sampling interval of 0.5 mm or less was acceptable for characterising all roughnesses within the joint roughness coefficient (JRC) scale on specimens of 100 mm in length.

Regardless of measurement methodology this provides a number of discrete data points, which can then be analysed quantitatively. Empirical, statistical and fractal methods exist to quantify discontinuity roughness (Barton and Choubey, 1977). There has been criticism of empirical methods. The most common method for quantification of discontinuity roughness through JRC is for the roughness profile to be visually compared to ten standard profiles, therefore an amount of subjectivity is introduced through the method (Beer et al., 2002). There has also been further criticism of the JRC method as the measurement is typically conducted on a small number of profiles across the discontinuity. Ferrero (1999) showed that 20 different profiles chosen randomly on one discontinuity could be given a range of JRC values from 8 to 20.

Due to the importance of scale effects, there have been multiple studies investigating the applicability of fractal models as a method to characterise discontinuity roughness. The fractal dimension (D) is a description of the degree of variation in a curve, a surface or of a volume from a plane (Mandelbrot, 1967). D has a minimum value of 1 for a smooth profile and a maximum value of 2 for a very rough profile (Mandelbrot, 1983). Fractals can be described as either being self-similar or self-affine. A self-similar fractal has the same statistical properties irrelevant of its scale, however a self-affine fractal only maintains its statistical properties if it is scaled differently in different directions (Fig. 4.3) (Fardin et al., 2001). Brown and Scholz (1985) and Den Outer et al. (1995) analysed a number of natural rock surfaces over a range of spatial scales and found that

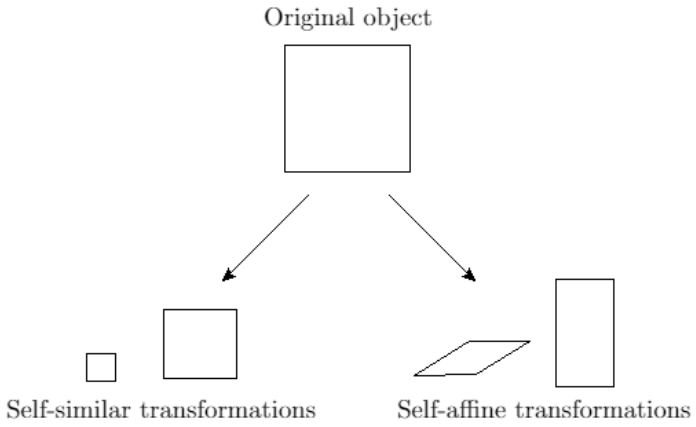

Figure 4.3: The difference between the scaling of self-affine and self-similar fractals.

the fractal dimension varied with spatial scale, concluding that discontinuity roughness could be considered by self-affine fractals.

There have been various methods for quantifying discontinuity roughness using self-affine fractals, including box counting (Kulatilake et al., 1995), divider (Lee et al., 1990), line scaling (Kulatilake et al., 1997), roughness length (Kulatilake and Um, 1999), and variogram methods (Ferrero, 1999). It has since been considered that the application of divider and box counting methods to self-affine fractals is not representative (Kulatilake et al., 1995). However, the line scaling, roughness length, spectral and variogram methods are all suitable to apply to self-similar profiles. Kulatilake et al. (1998) investigated the accuracy of the variogram method further, coupled with work by Kulatilake et al. (2006) who investigated the possible anisotropy in discontinuity roughness using a highly refined variogram technique. Kulatilake et al. (1997) investigated the line scaling method, Kulatilake and Um (1999) investigated the roughness-length method and Shirono and Kulatilake (1997) investigated the accuracy of the spectral method. Both the variogram technique (Kulatilake et al., 1998) and the modified divider method (Ge et al., 2014; Kulatilake et al., 2006) have been shown to produce the best results for discontinuity roughness, which agree with intuitive visual observations, and due to their foundation on self-affine fractals, both methods can be applied at any scale, from laboratory to outcrop (Ge et al., 2014).

Various statistical parameters can be used to quantify discontinuity roughness such as autocorrelation functions average roughness angle, centreline average values, mean square first derivative, mean square roughness height, percentage excess of distance, root mean square first derivative (Z_2), root mean square second derivative (Z_3), root mean square roughness height (RMS), roughness profile indexes (R_p) and structure function (SF). Tse and Cruden (1979) looked at all statistical parameters and found that Z_2 and R_p could be correlated well with *JRC* values. Statistical and fractal methods are then typically correlated back to the empirical *JRC* classification proposed by Barton (1973). The *JRC* method is widely used in research and industry, having been adopted by the ISRM (1978), and allowing inputs of discontinuity roughness in to multiple discontinuity shear strength criterion and multiple rock mass classification systems.

4.4.2 Data gathering and processing

In this study, a NextEngine 2020i laser profilometer capable of profiling surfaces at up to 100 µm resolution was used (Fig. 4.4a). The laser profilometry produced a point cloud of data points that could be analysed. The best fit plane through the 3D point cloud was created before being aligned so that the y plane was equal to zero along the plane (Fig. 4.5a). Ten 2D profiles were then created at 5 mm regularly spaced intervals across each discontinuity surface in the direction of shearing, expressed by x and z co-ordinate pairs (Fig. 4.5b). The sampling interval for each profile was then reduced to 0.5 mm for quantification, for reasons described in § 4.4.1 and to allow direct comparison with *JRC* values derived in previous studies that processed discontinuity roughness data using the same sampling interval (Tatone and Grasselli, 2010; Tse and Cruden, 1979; Yu and Vayssade, 1991).

To allow comparison with the largest number of other studies, it was chosen to use statistical methods to quantify discontinuity roughness, with Z_2 and R_p calculated for each discontinuity profile (Eq. 4.1 and 4.2 respectively), which are known to correlate well with *JRC* (Miller et al., 1990; Tse and Cruden, 1979; Yu and Vayssade, 1991).

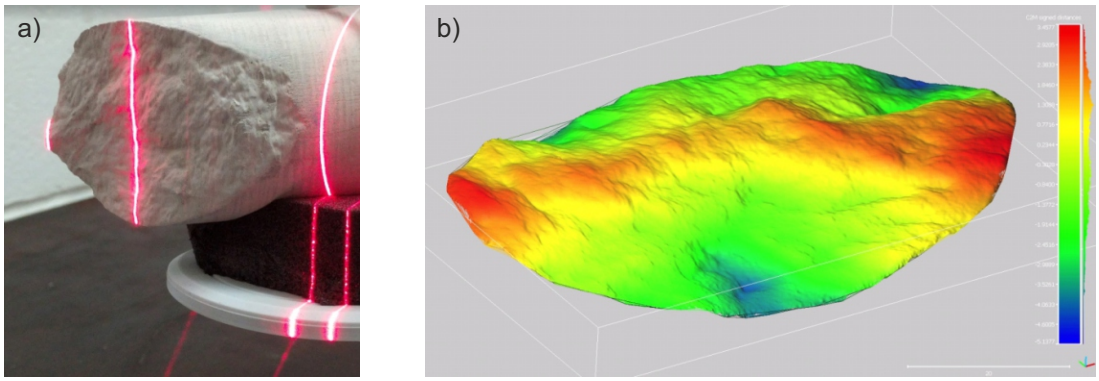

Figure 4.4: a) Specimen being laser profiled with NextEngine 2020i. b) Resultant point cloud data of specimen roughness from laser profilometry.

$$\mathrm{Z}_2 = \left[\frac{1}{L}\int_{x=0}^{x=L}\left(\frac{dy}{dx}\right)^2 dx\right]^{\frac{1}{2}} = \left[\frac{1}{L}\sum_{i=1}^{n-1}\frac{(y_{i+1}-y_i)^2}{x_{i+1}-x_i}\right]^{\frac{1}{2}} \tag{4.1}$$

$$\mathrm{R}_p = \frac{\sum_{i=1}^{n-1}\left[(x_{i+1}-x_i)^2+(y_{i+1}-y_i)^2\right]^{\frac{1}{2}}}{L} \tag{4.2}$$

Many relationships between Z_2 and JRC have previously been proposed based on digitising the original profiles of Barton and Choubey (1977) at 0.5 mm sampling intervals, and plotting the JRC values against Z_2 values before taking the best fit line between the points (Eqs. 4.3 to 4.6, Fig. 4.6a) (Jang et al., 2014; Tatone and Grasselli, 2010; Tse and Cruden, 1979; Yu and Vayssade, 1991).

$$JRC = 32.2 + 32.47 \log \mathrm{Z}_2 \tag{4.3}$$

$$JRC = 61.79\mathrm{Z}_2 - 3.47 \tag{4.4}$$

$$JRC = 51.85(\mathrm{Z}_2)^{0.60} - 10.37 \tag{4.5}$$

$$JRC = 51.16(\mathrm{Z}_2)^{0.531} - 11.44 \tag{4.6}$$

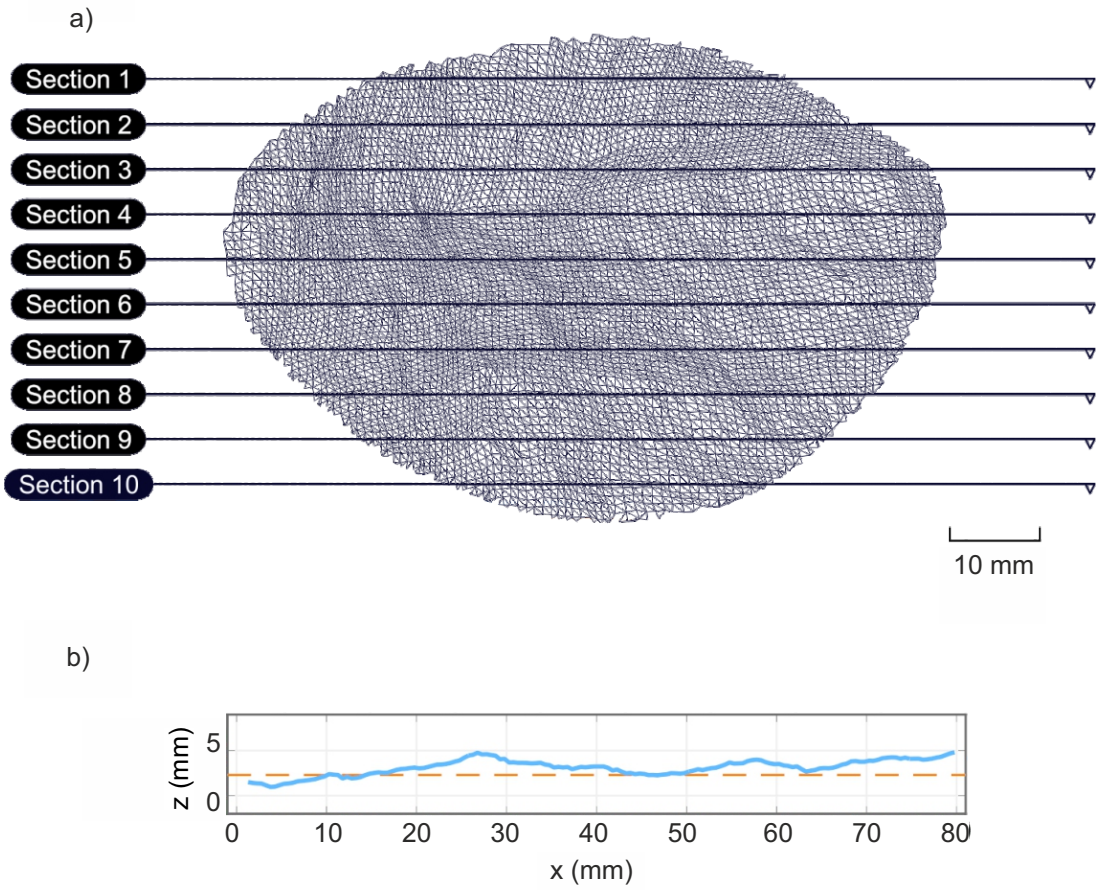

Figure 4.5: a) 3D triangulated surface of discontinuity surface from laser profilometry with point cloud data extracted and ten 2D cross sections across the surface at 5 mm intervals in the direction of shearing. b) Profile view of cross section 5 (note that the red dashed line represents the best fit plane of the 3D surface used to orient the y plane rather than the best fit line of the cross section).

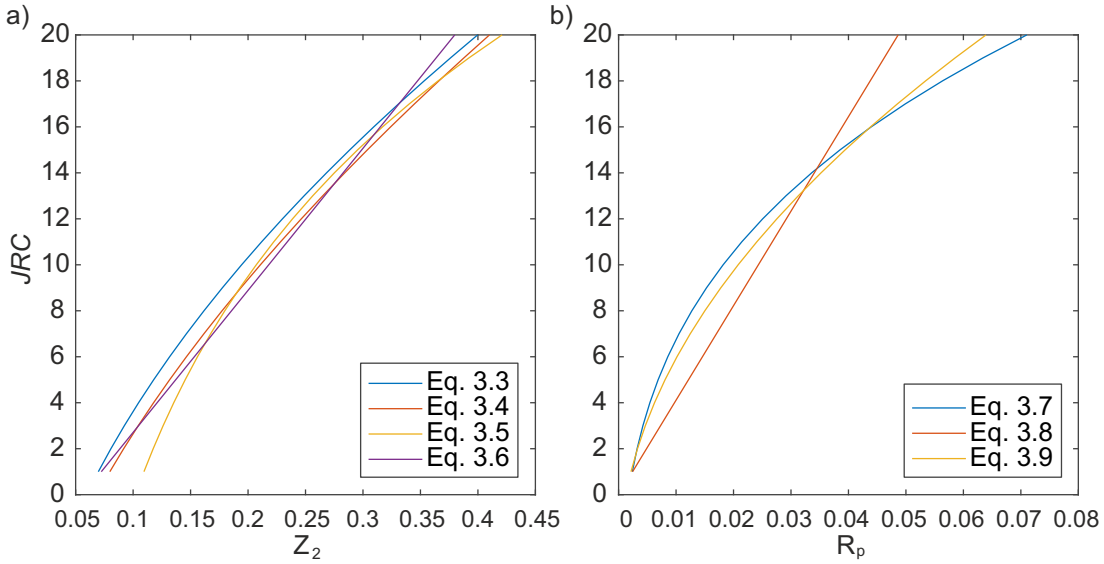

Figure 4.6: Proposed correlations between a) Z_2, b) R_p and *JRC*.

R_p has widely been used to analyse the roughness of various materials. R_p values start at 1, therefore $R_p - 1$ values are typically used in rock mechanics studies for convenience. Multiple relationships between R_p and *JRC* have also previously been proposed (Eqs. 4.7, 4.8 and 4.9, Fig. 4.6b)(Jang et al., 2014; Maerz et al., 1990; Yu and Vayssade, 1991).

$$JRC = 411.1(R_p - 1) \tag{4.7}$$

$$JRC = 92.07\sqrt{R_p - 1} - 3.28 \tag{4.8}$$

$$JRC = 65.9(R_p - 1)^{0.302} - 9.65 \tag{4.9}$$

Using a subjective visual comparison with *JRC* profiles originally proposed by Barton and Choubey (1977), Eq. 4.4 and Eq. 4.8 were found to best correlate Z_2 and R_p values to *JRC* values for the data in this study.

4.5 Repeatability of discontinuous specimen creation

The major advantage of synthetic replica discontinuities is the ability to create multiple identical specimens for testing under different conditions. Therefore it is paramount to ensure the reliability and repeatability of the specimen creation methodology. Five specimens were cast from each of the three surface moulds, before being cured and prepared as described in § 4.2. The surfaces of these specimens were then quantified as described in § 4.4. A comparison of each of the ten sections from each specimen was then made to the relevant section on all other specimens with that surface, as well as the mould from which the specimens were cast.

A comparison of the roughnesses of the specimens and the moulds is shown in Fig. 4.7. The increase in roughness across the three modelled surfaces can be seen, but a larger variation in roughness between sections across the same surface can also be seen with increasing roughness, with little variation seen in the sections of *Surface 1* compared to *Surface 3*. For *Surface 2* and *Surface 3*, the specimens do not acquire all of the detailed roughness of the moulds from which they were cast, resulting in consistently lower Z_2 and R_p values than the values of the moulds. Also a greater loss of roughness between the casts and the mould is observed in *Surface 3* than *Surface 2*. Not all of the roughness from the mould being obtained in the casts is likely to occur due to a combination of coating the mould in a release agent prior to casting the specimen, the viscosity of the synthetic material when casting and also the grain size of the synthetic material, which could in places be larger than the resolution of the 3D printed mould. The loss of roughness is less visible in *Surface 1*, and the roughness of the cast occasionally appears greater than the roughness of the mould. This likely occurs due to the small fluctuations in roughness being very close to both the resolution of the laser profilometer and the step height of the 3D printing. Nonetheless, visual comparison of the data shows there is good repeatability in producing surfaces with repeatable topographies (Fig. 4.8).

A single factor analysis of variance (ANOVA) was undertaken on the Z_2 and R_p values derived from each section of the surfaces to confirm visual comparisons (Table 4.1). All F-values (the variation between specimen means divided by the variation within the specimens) are shown to be significantly less than the critical F-value for a

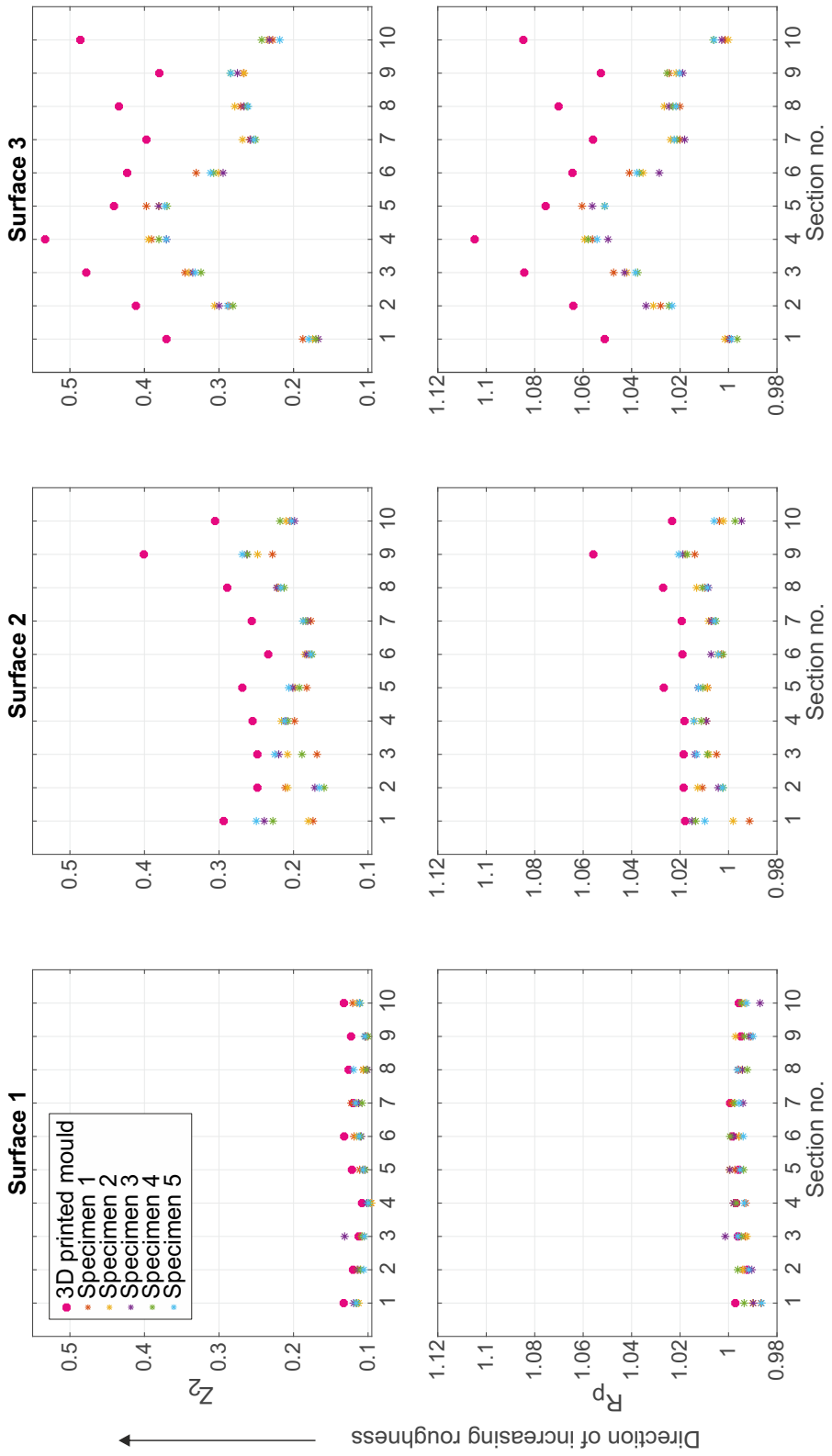

Figure 4.7: Comparison of roughness statistics Z_2 and R_p between 3D printed moulds and specimens cast from the moulds.

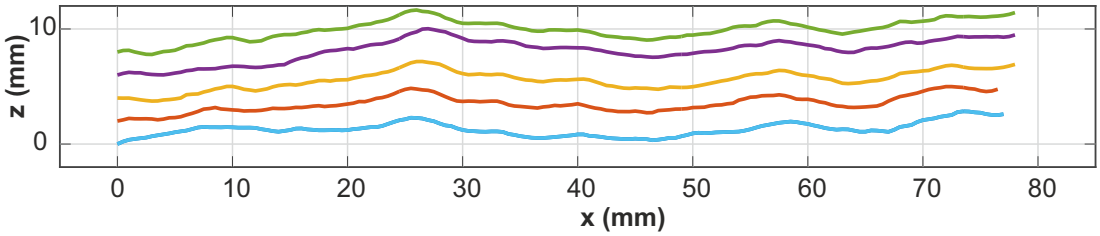

Figure 4.8: Visual comparisons of Section 5 processed from five different specimens cast from mould containing *Surface 2*. Sections have been separated rather than stacked for visual comparison.

Dataset analysed	ANOVA result
Surface 1 Z_2 values	F(4,45) = 0.8089, p = 0.526
Surface 1 R_p values	F(4,45) = 0.6815, p = 0.608
Surface 2 Z_2 values	F(4,45) = 0.6131, p = 0.655
Surface 2 R_p values	F(4,45) = 0.5024, p = 0.734
Surface 3 Z_2 values	F(4,45) = 0.0457, p = 0.996
Surface 3 R_p values	F(4,45) = 0.0335, p = 0.998

Table 4.1: Results of single factor analysis of variance, assessing the repeatability of cast specimen creation from three different roughness moulds.

0.05 significance level (2.124). p-values are all shown to be significantly greater than 0.05. Therefore, both F-values and p-values show no statistically significant differences between group means. F-values are lower and p-values are greater with increasing roughness, confirming visual comparisons that repeatability of the casts improves with increasing roughness.

4.6 Desirable synthetic rock properties

The aim of this study is to increase the understanding of the small scale thermo-mechanical behaviour of discontinuities. Of particular interest is the behaviour of discontinuities in lower strength sedimentary lithologies, which are outlined by RWM as one of the generic host lithologies for a potential GDF for HLW in the UK. Therefore the aim of the synthetic lithology for use in this study is to replicate the mechanical (both strength and elastic) properties of a lower strength sedimentary lithology, defined in the Quintessa report by Metcalfe et al. (2015) on behalf of RWM as:

- bulk dry density: 1900 to 2500 $\mathrm{kg\,m^{-3}}$;
- uniaxial compressive strength (UCS): 12.5 to 100 MPa;
- Young's modulus (E): 12.5 to 100 MPa; and
- Poisson's ratio (ν): 0.16 to 0.45.

For this study, it was therefore decided to attempt to use a single aggregate, which when mixed with a binding agent (and water) would give a synthetic material with these properties, whilst also having adequate workability to allow specimen preparation, have good reproducibility, and ability to conform to the rough topography of moulds to create specimens for discontinuity testing. Due to the desire to apply thermal as well as mechanical loads to the specimens, it was decided to avoid glass, plastics, or resins and use an aggregate with cementitious binding material as having the closest thermal properties to a lower strength sedimentary lithology. In addition to having mechanical properties representative of a lower strength sedimentary lithology, the synthetic lithology needs to have a consistency that allows good workability and be able to conform to the specimen moulds, whilst keeping density high enough and porosity low enough to maintain mechanical properties. The different constituents of a suitable synthetic lithology, the constituent ratios and the curing conditions required to produce a synthetic lithology suitable to represent a lower strength sedimentary lithology are discussed in the following sections.

4.7 Synthetic constituents

4.7.1 Binding material

In this study, it was chosen to use a granular aggregate with a cementitious binding agent suitable for the replication of a lower strength sedimentary rock. Strong, pure plaster based materials such as *Hydrostrone* (Huang et al., 1993; Kutter and Otto, 1990; Tatone, 2014), plaster (Huang and Doong, 1990) and *DieKeen* (Handanyan et al., 1990) have been used previously as binding agents. However, cement was chosen over plaster as the binding material due to its stability in water allowing for tests in saturated conditions if wished. Another advantage is the lack of a need for oven curing, key for thermo-mechanical testing. Initial compositions were trialled with Ordinary Portland cement, but with long curing times of 28 days required to reach 87% of peak strength (Zhang et al., 2014) (Fig. 4.9a) and low Young's modulus (E), a cement with more desirable properties was required.

Calcium aluminate cement (CAC), also commonly sold as High Alumina Cement (HAC) within the UK, was first developed by Lafarge in the 1920s. It was popular within the refractory industry in the 1950s to 1970s for applications such as pre-cast beams and structural concrete due to it developing strength rapidly. CAC is prone to crystalline rearrangement when exposed to water for long periods of time (decades), which resulted in several structural failures within the industry. CAC is therefore no longer used for structural concrete. It is, however, still readily available and as crystalline rearrangement occurs on a time scale much longer than of interest to this project it has been chosen as a potential cementitious binding agent in the synthetic rock due to its fast curing properties, and rapid gain of strength. It gains strength so rapidly that within 24 hours of curing the compressive strength of the cement can be as high as 90% of the ultimate strength (Neville, 1975). Test data on the effect of curing time is shown in Fig. 4.9b showing that after 7 days of curing, the cement has obtained 98% of the strength at 28 days. It is also advantageous over Ordinary Portland cement due to its low porosity.

The principal mineralogical phase is monocalcium aluminate ($CaOAl_2O_3$). The nature of the hydrates formed is temperature dependent. For hydration below 25 °C two

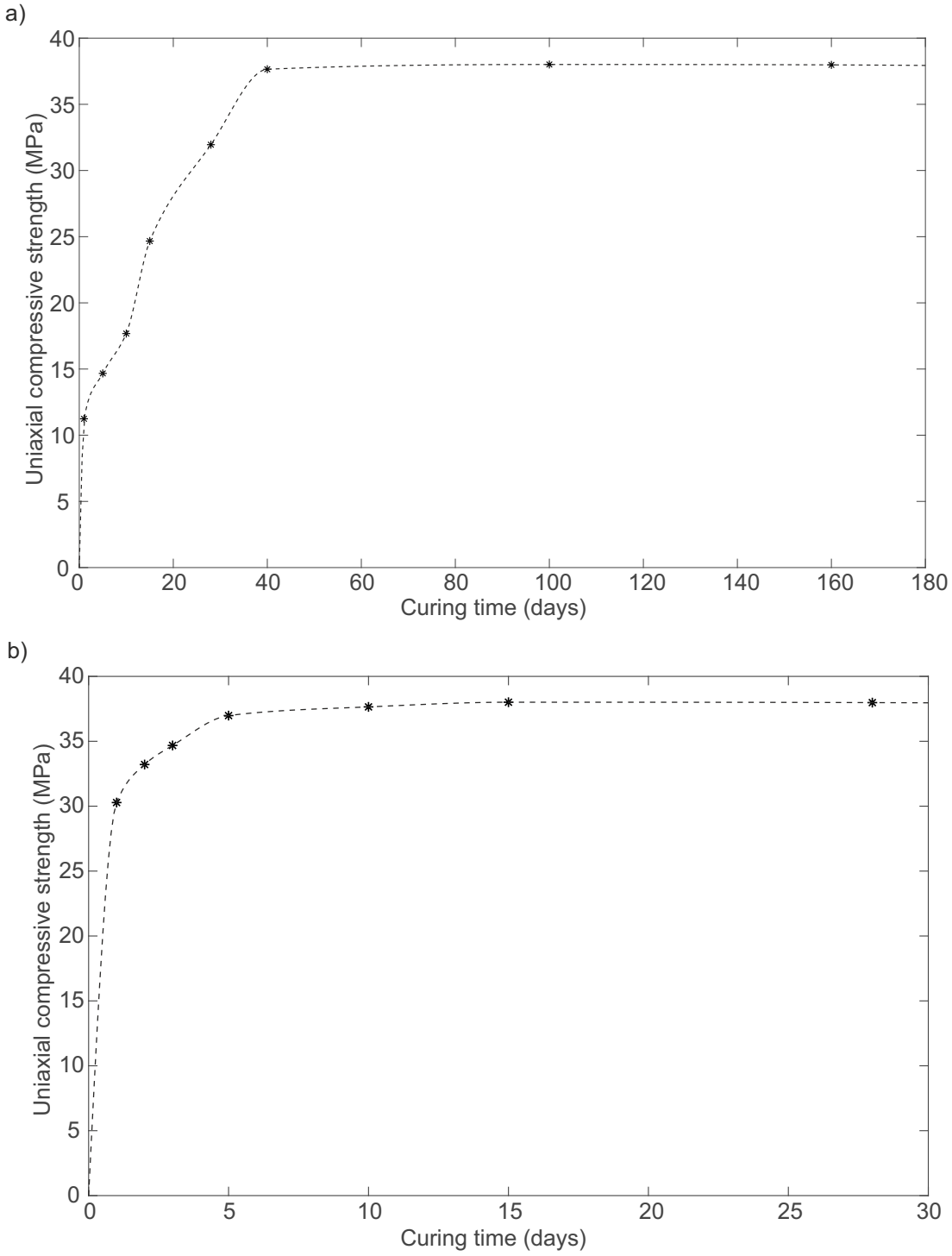

Figure 4.9: a) Increasing unconfined compressive strength of Ordinary Portland cement with increased curing time. b) Increasing unconfined compressive strength of calcium aluminate cement with increased curing time.

metastable hexagonal aluminates form:

$$CaO.Al_2O_3\ 10H_2O$$

$$2CaO.Al_2O_3\ 8H_2O$$

These hydrates undergo crystalline rearrangement over time to a cubic stable form:

$$3(CaO.Al_2O_3.10H_2O) \longrightarrow 3CaO.Al_2O_3.6H_2O + 2(Al_2O_3.3H_2O) + 18H_2O$$

$$3(2CaO.Al_2O_3.8H_2O) \longrightarrow 2(3CaO.Al_2O_3.6H_2O) + Al_2O_3.3H_2O + 9H_2O$$

This crystalline rearrangement takes decades at a temperature of 20 °C, but happens more readily at increased temperature and results in increased porosity, reducing the strength. In the laboratory environment at room temperature, the conversion has no effect on strength if the material is used in less than a year (Neville, 1975), however this could be problematic if the conversion process is accelerated at elevated temperatures. CAC has a lower porosity than Ordinary Portland cement as it combines with a higher proportion of the water in the hydration reaction reducing the amount of free water, which forms voids (Neville, 1975).

In addition to cement as a binder, metakaolin (MK) is a dehydroxylated form of the clay mineral kaolinite obtained by calcinating kaolinitic clay at between 500 and 800 °C. MK is traditionally used in the construction industry to reduce the clinker factor of cements, producing a more sustainable material with increased workability and lower heat of hydration resulting in a lower tendency to crack when curing. Whilst MK is not itself a cement, it is pozzolanic when mixed with cement and water, and can lower porosity whilst maintaining good strength (Sabir et al., 2001). MK was therefore trialled as a substitute for a portion of the cement in some compositions in an attempt to represent a lower strength sedimentary lithology.

4.7.2 Aggregates

The following considerations were taken into account when selecting potential aggregates for use in this study:

- the size of the aggregate should be representative of the grain size of a natural lower strength sedimentary lithology. Accounting for specimen size, an aggregate size of less than 1 mm was selected. All aggregates were sieved so that 100% passed the 1 mm sieve. A grain size distribution chart for each aggregate is presented in Fig. 4.10;
- angular aggregates should give a higher strength and lower porosity in comparison to more rounded aggregates, and are more representative of constituent grains in lower strength sedimentary lithologies;
- well graded aggregates should provide better workability when casting; and
- aggregates with fines will reduce workability and require additional water, potentially increasing porosity, reducing the strength and increasing the need for compaction by vibration to remove air bubbles.

A number of aggregates including builders sand, sharp sand, pure silica sand and andalusite were investigated as possible aggregates. Andalusite (Al_2SiO_5) consists of prismatic crystals with square cross section, and has a hardness of 6.5 to 7.5 (Mohs scale). It is white, grey or pink in colour with a dull vitreous lustre. It is commonly extracted from metamorphosed shales and pegmatites and used in the refractory industry. Silica sand is primarily a quartz sand (SiO_2) with minor amounts of minerals such as feldspar, micas and clays. It is a well graded, well sorted, fine grained sand with a density of $2650\,\mathrm{kg\,m^{-3}}$, and buff in colour. Builders sand and sharp sand are both sands commonly used in the construction industry. They are both poorly sorted with very similar grain size distributions (Fig. 4.10), but sharp sand typically has a more angular grain shape than builders sand.

4.7.3 Constituent ratios

The properties of the synthetic rock vary with both the ratio of the cementitious material to the aggregate (c/a) and the cementitious material to water ratio (w/c). A range

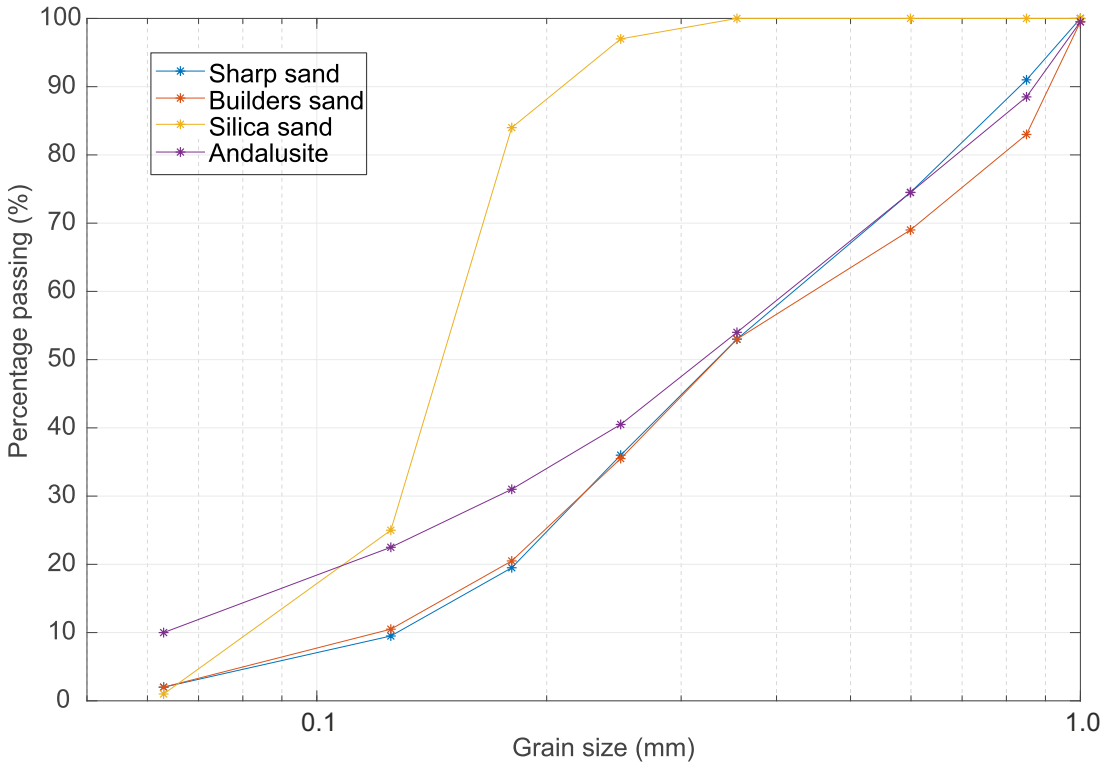

Figure 4.10: Grain size distribution of different aggregates trialled in the creation of a synthetic lithology.

of both c/a and w/c were trialled. The ideal ratios would have low enough viscosity to produce a workable mix and be able to conform to the roughness of the specimen moulds, producing representative discontinuity specimens, but also have mechanical properties representative of a lower strength sedimentary lithology.

4.7.4 Curing conditions

The conditions under which cementitious materials cure are known to affect their mechanical properties. It is therefore important to maintain constant curing conditions for all specimens. Throughout this study, all specimens were mixed manually in batches and poured in to moulds before being vibrated for one minute with a dentist's vibrating table to remove entrapped air bubbles and ensure uniform consistency. It was found that vibrating the specimens for any longer created convection currents in the specimens resulting in anisotropy. Specimens were left to cure in the moulds at room temperature for 24 hours before being removed from the moulds, this allowed time for the specimen to cure enough to obtain the shape of the mould, and harden enough to not be damaged during mould removal. Initially specimens were left to cure in room conditions, but due to the importance of humidity during chemical curing, fluctuations in the room's atmosphere affected the curing process. Submerged curing was therefore used to better control the curing environment. Specimens were submerged and vacuum saturated, ensuring sufficient water for complete chemical curing of the cement, and were left to cure submerged at room temperature for the desired duration for that cement. Ordinary Portland cement requires 28 days curing to gain strength (Fig. 4.9a), and CAC requires 7 days curing to gain strength (Fig. 4.9b). Therefore specimens were cured for these durations as a minimum, and tested as closely to these timings as reasonably possible.

4.8 Intact properties of different synthetic compositions

4.8.1 Introduction

When the methodology for casting intact specimens had been deduced, and the most repeatable curing conditions confirmed, different binder and aggregate combinations were

trialled to create compositions with varying cement:aggregate (c/a) and water:cement (w/c) ratios. Many compositions had poor workability and did not conform to the moulds sufficiently, resulting in specimens with voids or obvious textural anisotropy. Other specimens had very low density or broke during specimen preparation, these compositions were discarded. 20 different compositions with good workability were prepared and tested to gain mechanical properties.

4.8.2 Strength & stiffness in uniaxial compression

Table A.1 in Appendix A outlines the constituents and mechanical properties of compositions that were tested as intact specimens to try and achieve the desired synthetic rock properties of a lower strength sedimentary lithology (§ 4.6). Preliminary testing was carried out in the RMEGG laboratory at the University of Leeds using the apparatus and methodologies outlined in § 3.3. When tested in uniaxial compression, some compositions either crumbled as soon as axial loading was initiated on the specimen, or did not reach a UCS of at least 12.5 MPa required to represent a lower strength sedimentary lithology. Other compositions produced the required UCS and E, but did not fail in a brittle manner with axial splitting or a shear plane (Fig. 4.11a), and instead underwent a ductile strain hardening behaviour post failure (Fig. 4.11c), or a quasi-brittle failure (Fig. 4.11b) with a slow reduction in strength with increasing strain and the lack of formation of a macroscopic failure plane. Quasi-brittle or ductile behaviour is not representative of a lower strength sedimentary lithology under these low stress conditions; therefore no further testing was undertaken on these compositions.

Generally, whilst increasing the w/c ratio increases the workability of the specimens during casting, it results in lower strength specimens. Compositions containing sharp sand typically behaved in a more brittle manner than the same composition with builder's sand, likely due to the increased angularity of the aggregate grains. Compositions using silica sand commonly behaved in a quasi-brittle manner, likely due to the poor grain size distribution of the silica sand. Unexpectedly, the compositions using andalusite aggregate also behaved in a quasi-brittle manner, even though andalusite shows a similar grain size distribution to sharp and builder's sand, and individual grains are known to have a fibrous structure.

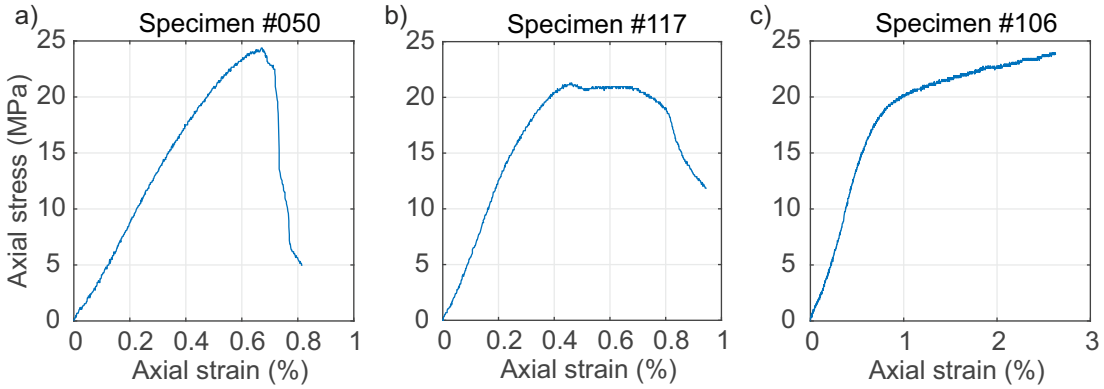

Figure 4.11: a) Axial stress strain plot for Specimen #050, displaying brittle behaviour, with a stress drop immediately after peak stress and axial splitting occurring within the specimen. b) Axial stress strain plot for Specimen #117, displaying quasi-brittle behaviour, with a gradual failure after peak stress and no visible macroscopic failure. c) Axial stress strain plot for Specimen #106, displaying ductile strain hardening behaviour, with strengthening occurring with increasing strain.

4.8.3 Strength & stiffness in triaxial compression

Two compositions produced strengths and stiffnesses representative of a lower strength sedimentary lithology and failed in a brittle manner with the formation of a shear plane or axial splitting. These two compositions (Table 4.2) were tested further under triaxial conditions in the RMPL at the BGS using the apparatus and following the procedures outlined in § 3.5. Further details on the additional testing is provided in Table A.2 in Appendix A. Both compositions had uniaxial compressive strengths between 25 and 30 MPa. Hoek et al. (2002) proposed that to determine the strength of a lithology over a range of stresses, and to allow a failure envelope to be created for that lithology, at least three triaxial tests at confining pressures ranging from 0 to 50% of the uniaxial compressive strength should be undertaken. Therefore, in addition to the UCS testing, triaxial testing was undertaken on the two compositions at confining pressures of 5, 10 and 15 MPa. These confining pressures are also representative of the in-situ stresses that may be experienced in a GDF at depths up to 1 km. Even if in-situ stresses in a GDF scenario were lower than these confining pressures, there is potential for much higher localised stresses to occur at discontinuity surfaces (Brown and Scholz, 1985; Tabor, 1975; Thomas and Sayles, 1977). As this study is focussed on discontinuity behaviour, it is therefore also important to understand the intact properties at these stresses.

Constituent ratios[1]				Curing time
Binder	Aggregate	H_2O	Metakaolin	
2.40 (Portland cement)	4.00 (Sharp sand)	3.00	1.00	28 days
1.00 (CAC)	0.25 (Sharp sand)	0.43	0.00	7 days

Table 4.2: Two compositions tested under triaxial conditions for further characterisation of elastic and strength properties.

The composition using CAC as a binding agent (Table 4.2) was tested at a confining pressure of 5 MPa, loaded at an axial strain rate of $5 \times 10^{-6}\,s^{-1}$, as per the procedure outlined in § 3.5.3.1. A peak stress of 51.25 MPa was obtained, E of 11.99 GPa and ν of 0.43. Although the composition behaved in a brittle manner in UCS, at this low confining pressure of 5 MPa, the specimen behaved in a quasi-brittle manner (observed in the very high ν of 0.43), absorbing additional axial strain without a drop in stress until the test was terminated at 4.5% axial strain (Fig. 4.12a). Quasi-brittle behaviour occurs due to substantial sub-critical crack growth prior to failure (Ma and Huang, 2018), leading to an early yielding and ductile behaviour and accommodating much larger amounts of axial strain than would normally be witnessed at these low confining pressures in a lower strength sedimentary lithology. As the CAC composition displayed non-representative quasi-brittle behaviour at the low confining pressure of 5 MPa, it was not tested further at 10 and 15 MPa. The triaxial test with a confining pressure of 5 MPa was, however, repeated on another specimen of the same CAC composition (Specimen #093), but a pre-consolidation phase was applied to the specimen prior to the triaxial test to attempt to consolidate the specimen and produce a more brittle behaviour. The pre-consolidation phase consisted of hydrostatically ($\sigma_1 = \sigma_2 = \sigma_3$) loading the specimen to 20 MPa at 1 MPa min^{-1}, holding the specimen under a hydrostatic pressure of 20 MPa for one hour, prior to unloading the specimen again at 1 MPa min^{-1}. The triaxial test was then undertaken using an identical procedure to Specimen #088. The pre-consolidation phase did not make a difference to the mechanical behaviour of the specimen, with a peak stress of 50.64 MPa, E of 11.37 GPa and ν of 0.43, again failing in a quasi-brittle manner at low confining pressure. Therefore no further mechanical testing was undertaken of this CAC composition as it was not deemed representative of a lower strength sedimentary lithology.

[1] Constituent ratios are provided as ratios by weight.

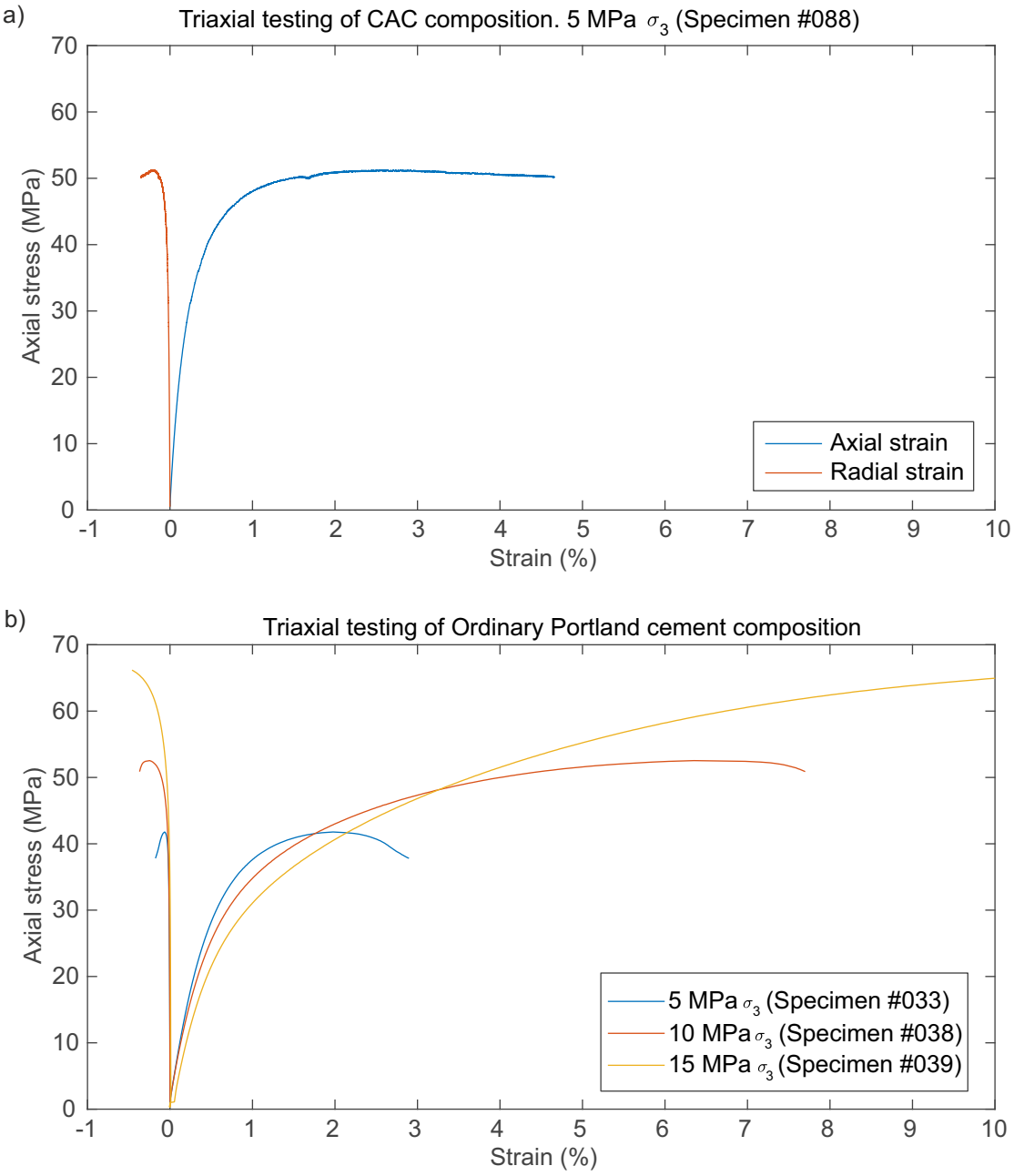

Figure 4.12: a) Axial and radial stress strain plot of triaxial test on CAC composition (Specimen #088) at a confining pressure of 5 MPa. b) Axial and radial stress strain plots of triaxial tests undertaken on Ordinary Portland cement composition specimens at confining pressures of 5, 10 and 15 MPa.

The composition using Ordinary Portland cement as a binding agent (Table 4.2) was tested at confining pressures of 5, 10 and 15 MPa (Fig. 4.12b), loaded at an axial strain rate of $5 \times 10^{-6}\,s^{-1}$, as per the procedure outlined in § 3.5.3.1. At a confining pressure of 5 MPa, the Ordinary Portland cement composition failed in a more brittle manner than the CAC composition, but still showed a progression to quasi-brittle behaviour at low confining stress from the brittle behaviour that was observed in UCS. At 10 MPa confining pressure, the Ordinary Portland cement composition showed a completely quasi-brittle behaviour, with a drop in axial stress not occurring until 8% axial strain, and at 15 MPa confining pressure, further ductile behaviour was observed, with the specimen still strain hardening when the test was terminated at 10% axial strain. Fig. 4.13 shows the three Ordinary Portland cement specimens after testing, with the formation of undulating failure zones rather than distinct shear planes, as well as the increasing axial shortening that occurred with increasing confinement to reach the same stage of failure plane formation.

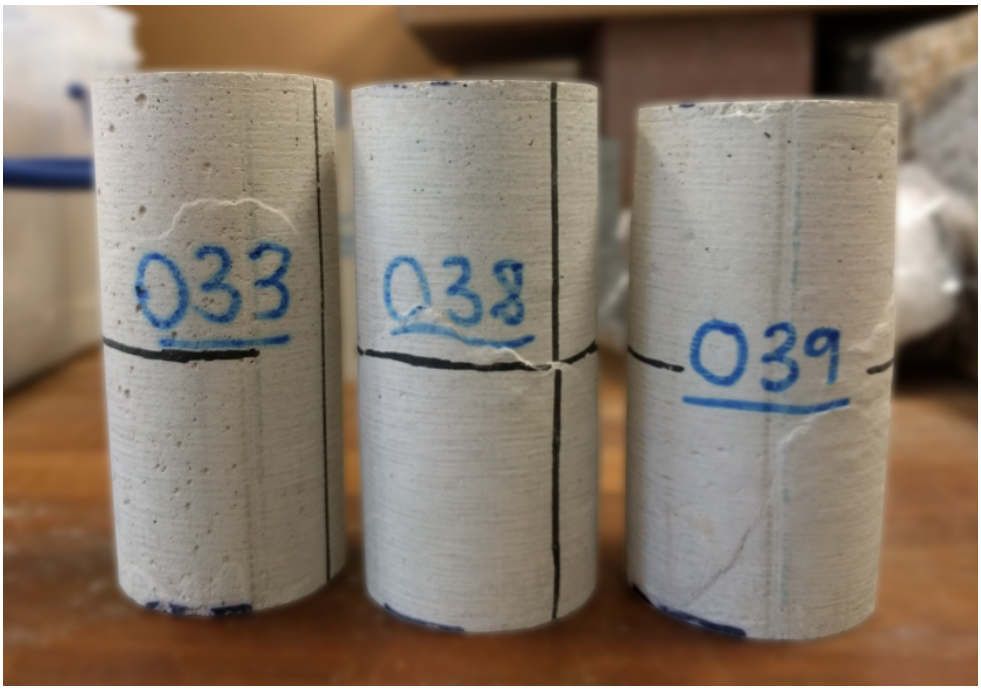

Figure 4.13: Three specimens of Ordinary Portland cement composition (Table 4.2) after testing under triaxial conditions. Specimen #033 at 5 MPa σ_3. Specimen #038 at 10 MPa σ_3. Specimen #039 at 15 MPa σ_3.

4.8.4 Optical microscopy

Polished thin sections were made from specimens of the two compositions in Table 4.2. Specimens were blue epoxy impregnated under vacuum prior to sectioning, and were double polished to 30 µm. Both compositions show the sharp sand aggregate of predominantly angular quartz and feldspar grains supported by the matrix of cementitious binder, however, the CAC binder has a larger grain size than the Ordinary Portland cement (Fig 4.14). Due to the blue epoxy impregnation of the specimens, pore spaces are seen as blue circular voids. Thin sections of the Ordinary Portland cement composition were made from an undeformed specimen as well as from specimens after triaxial testing at confining pressures of 5 and 10 MPa. The specimen deformed at a confining pressure of 5 MPa shows the formation of brittle fractures through the aggregate grains of quartz and feldspar (Fig. 4.14b), whilst the specimen deformed at a confining pressure of 10 MPa shows fractures predominantly skirting around the grains of aggregate and propagating through the cementitious matrix (Fig. 4.14c). This is concordant with the transition to quasi-brittle and ductile behaviour seen in the stress strain data at these relatively low stresses, with brittle deformation occurring through the matrix and aggregate grains at low confining pressures, and a transition to ductile deformation through the cementitious matrix at higher confining pressures. All specimens show considerably more cementitious matrix than would be expected in a lower strength sedimentary lithology, which is the underlying cause of the increasingly ductile behaviour.

4.8.5 Scanning electron microscopy (SEM)

Polished thin sections were carbon coated to approximately 25 µm thickness using an EMITECH K950 carbon evaporation coater. This conductive layer provided a pathway for the negatively charged electrons in the beam to reach Earth via the SEM stage. Although geological specimens are rarely damaged by the electron beam, charging of non-conductive areas present on the specimen surface produce artefacts that affect image quality. SEM analysis was performed using a LEO 435VP variable pressure digital scanning electron microscope at the BGS. The instrument was used in conventional high vacuum mode. The SEM was equipped with a KE Developments four-quadrant (4 diode type) solid state detector for backscattered electron imaging (BSEM). Phase/mineral

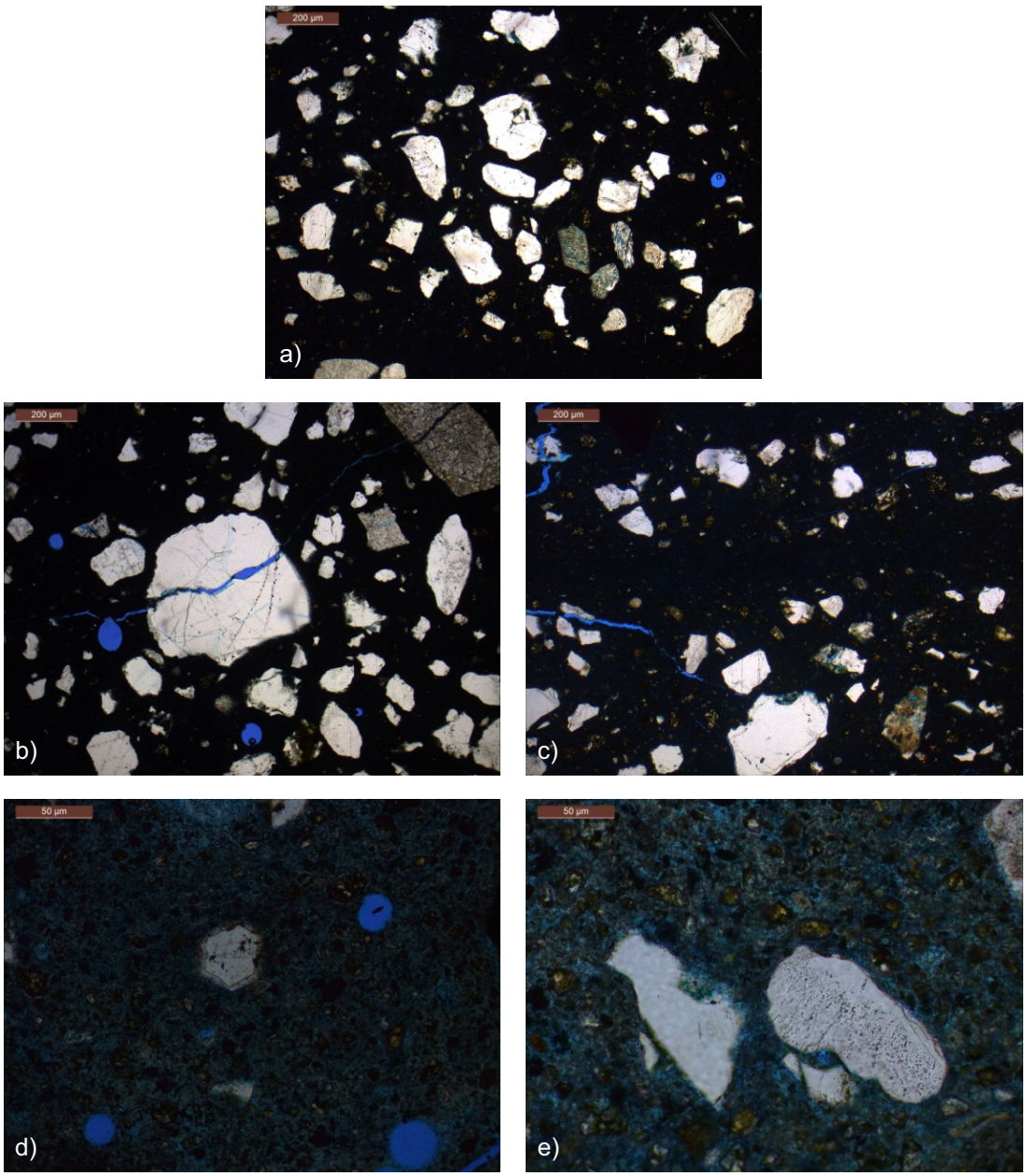

Figure 4.14: Optical microscopy of synthetic compositions tested under triaxial conditions. a) Undeformed Ordinary Portland cement (Specimen #056). b) Ordinary Portland cement after triaxial testing at 5 MPa σ_3 (Specimen #051). c) Ordinary Portland cement after triaxial testing at 10 MPa σ_3 (Specimen #038). d) Undeformed CAC (Specimen #099). e) CAC after triaxial testing at 5 MPa σ_3 (Specimen #088).

identification was aided by qualitative observation of energy-dispersive X-ray spectra recorded simultaneously during SEM observation, using an Oxford Instruments INCA energy-dispersive X-ray microanalysis (EDXA) system.

SEM analysis of undeformed Specimen #056 again shows the aggregate grains of quartz and feldspar supported by the matrix of the Ordinary Portland cement binder (Fig. 4.15b), but the higher resolution imaging allows further analysis of the matrix compared with optical microscopy. Individual minerals can be seen randomly orientated within the fine grained cementitious matrix. Spot EDXA analysis (Fig. 4.15a) shows the matrix to be made up of calcium silicates and calcium aluminates as well as high density, light coloured, flowery areas likely to be the rehydrated metakaolin. The specimen deformed in triaxial conditions at a confining pressure of 5 MPa (Specimen #051) again shows brittle deformation, with fractures propagating through grains of quartz aggregate as well as the matrix (Fig. 4.15c), whilst the specimen deformed at a confining pressure of 10 MPa (Specimen #038) shows fractures undulating around aggregate grains and propagating purely through the matrix (Fig. 4.15d). Additionally, the specimen deformed at 10 MPa confining pressure shows linear bands of cementitious rich material (Fig. 4.15e). Aggregates and lighter coloured, higher density minerals within the matrix are absent from these bands. In addition the needle shaped calcium aluminates are often aligned within the bands. It is possible that these bands are pathways for ductile deformation in the specimen, with grain comminution accounting for the lack of high density minerals. However, there are no obvious textural effects to suggest grain comminution has occurred and the bands have formed due to the mechanical deformation. It is also possible that the cementitious rich bands are relic structures from the curing process with improper mixing causing heterogeneity, and the bands have been exploited as weaker layers to accommodate ductile deformation, although these structures are not observed in other specimens of the same batch.

4.8.6 Summary of different synthetic compositions

Testing of many different intact cementitious compositions in uniaxial compression has shown that it is possible to create multiple brittle compositions in these low stress environments, which might have strengths and stiffnesses comparable to a lower strength

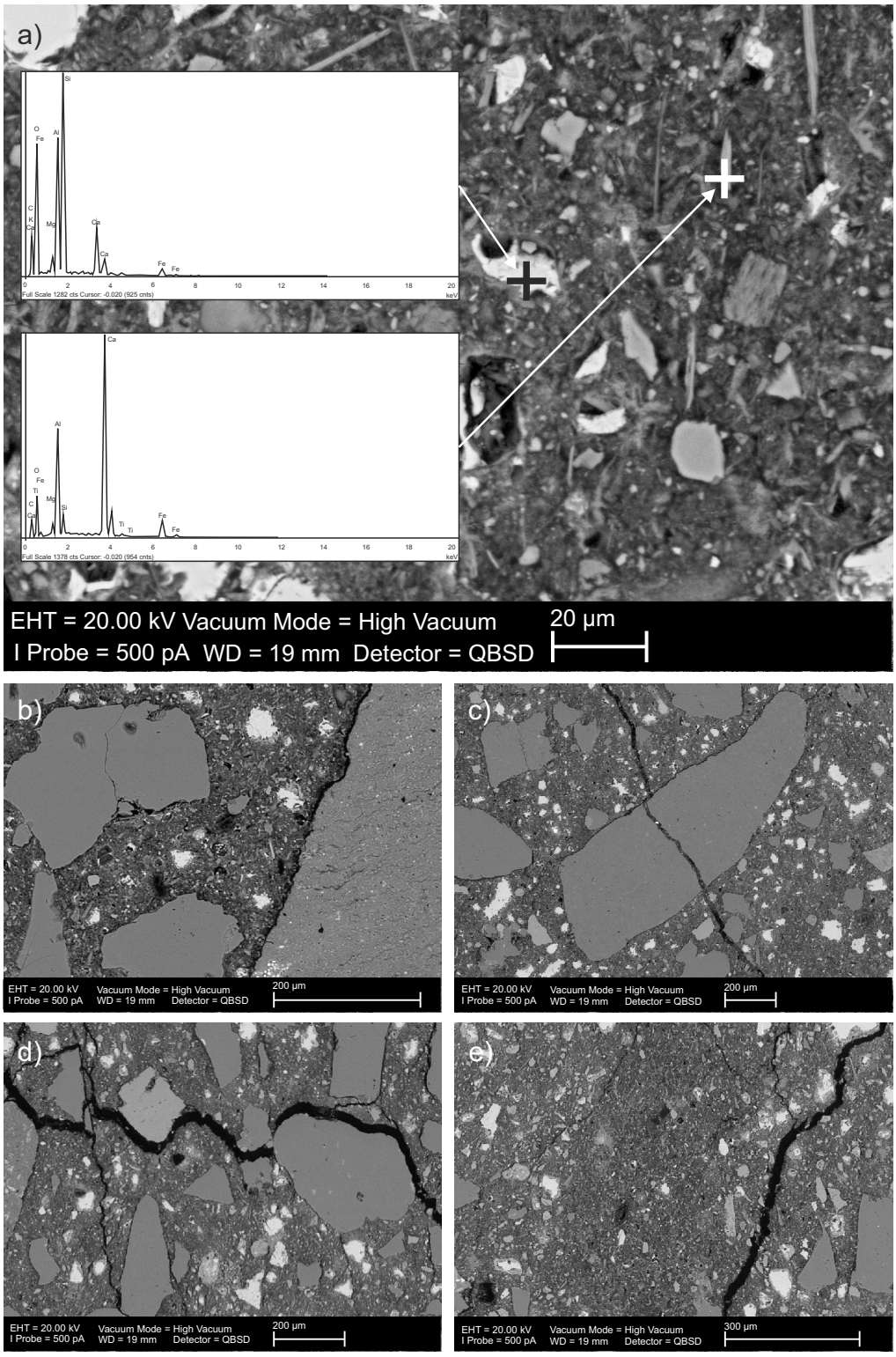

Figure 4.15: SEM images of Ordinary Portland cement composition (Table 4.2) after testing under triaxial conditions. a) Undeformed (Specimen #056) with two EDXA spectra showing mineral identification for areas under the crosshairs. b) Undeformed Specimen #056. c) Specimen #051 after triaxial testing at 5 MPa σ_3. d) and e) Specimen #038 after triaxial testing at 10 MPa σ_3.

sedimentary lithology. However, testing of these compositions in higher stress environments (laboratory triaxial testing) shows that the compositions undergo a brittle to ductile transition at lower stresses than might be expected in a lower strength sedimentary lithology. Whilst compositions made with a CAC binder require less curing, they undergo the brittle to ductile transition at even lower stresses than the same composition with an Ordinary Portland cement binder. Therefore, whilst it is realised that an Ordinary Portland cement composition specimen may not be completely representative of a lower strength sedimentary lithology, it is the most representative composition that has been created in this study, and was therefore selected to be used to create a methodology for casting discontinuous specimens. All synthetic compositions require a significant ratio of binder to aggregate to allow satisfactory workability and to be able to conform to the moulds. However, this high binder to aggregate ratio results in quasi-brittle behaviour occurring due to failure through the matrix, rather than brittle fracturing of the aggregate.

4.9 Chapter summary

In this chapter, a new methodology was presented for creating synthetic discontinuity specimens. The methodology, which utilises 3D printing to create moulds for casting specimens, was shown to produce repeatable discontinuity topographies, potentially allowing for the fundamental behaviour of discontinuities to be defined by removing natural heterogeneity and allowing the testing of identical topographies under varying conditions.

In addition, the mechanical behaviour of different cementitious compositions as analogues to lower strength sedimentary lithologies was explored. Significant previous work has been carried out within the rock mechanics community utilising synthetic lithologies to represent real rock lithologies. In this study, it was found that cementitious compositions can be created with representative behaviour of lower strength sedimentary lithologies in low stress environments. However, at higher stresses, cementitious compositions start to transition from brittle behaviour to quasi-brittle and ductile behaviour at much lower stresses than a lower strength sedimentary lithology may display. In near surface engineering scenarios with low stress environments, such as slope stabil-

ity problems, using a cementitious analogue may be applicable. However, even in these environments, localised stresses at the small scale, such as at an asperity level on a discontinuity, may still be relatively high, and failure mechanisms at the micro-scale may not be representative even in these apparent low stress environments. Further to this, cementitious analogues are certainly unlikely to be representative of rock lithologies in high stress environments such as the scenario of a GDF. It is recognised that there are many potential synthetic materials that could be used to replicate the mechanical behaviour of rock, and similarly a range of different mechanical behaviours exhibited by different lithologies. Consideration and justification of the behaviour of synthetic constituents should therefore be given prior to selection for use in rock mechanics and discontinuity mechanics studies, and workers should consider carefully whether the constituents selected will adequately replicate the behaviour of the desired natural lithology in the required stress environment.

If a synthetic composition can be created that is representative of the desired natural lithology under the required stress environment, then the new methodology for casting synthetic specimens shows promise to allow fundamental discontinuity behaviour to be studied, with discontinuity angle and topography being closely controlled. To achieve a suitable synthetic composition utilising an aggregate and cementitious binder, the most important area for future work would be in the ratio of aggregate to binder. If a higher aggregate to binder ratio could be achieved, which would allow increased grain support, rather than matrix support then brittle behaviour at higher stresses would be likely. It would be important however, to ensure that increasing the aggregate to binder ratio would not affect the ability of the synthetic composition to be cast reliably and repeatedly and undergo uniform curing.

Chapter 5

Thermo-mechanical laboratory testing

5.1 Introduction

Synthetic rocks were developed and tested to control the variability of intact strength and stiffness, and discontinuity topography between specimens, allowing fundamental behaviour to be determined (Chapter 4). It was not possible to create a synthetic lithology representative of a lower strength sedimentary lithology, therefore real rocks have instead been used. In this chapter, the results of thermo-mechanical laboratory triaxial testing on intact and discontinuous specimens of two sedimentary lithologies are presented and discussed. The testing follows methods and procedures outlined in Chapter 3.

Raw data from laboratory testing undertaken as part of this chapter is available to download from the National Geoscience Data Centre:

https://dx.doi.org/10.5285/ae62bf20-042c-4c65-8a51-5683b8bef2f0

In addition, summarised parameters from the laboratory testing are tabulated in Appendix B along with photographs of every specimen after testing.

5.2 Rock lithologies

Two different lithologies, the Thornhill Rock and Midgley Grit, were used throughout this study. The following section outlines basic geological information for these two rocks, including their geological histories and where and how they were obtained. Initial attempts to use a lithology better aligned to a "lower strength sedimentary" rock (both the Whitby Mudstone and Redcar Mudstone were trialled,) encountered significant problems during sample preparation and discontinuity creation, and it was not possible to gain enough specimens for testing. The Thornhill Rock and Midgley Grit were therefore selected for testing due to their mechanical properties, homogeneity and availability. Both lithologies are also similar mineralogically, but differ in grain size. This results in different discontinuity roughness, allowing the effect of roughness to be examined under thermo-mechanical loading.

5.2.1 Thornhill Rock

The Thornhill Rock (local building stone name: Woodkirk Sandstone) is a *c.* 40 m thick unit, comprising thick beds of cross-bedded fine-grained silica cemented sandstone locally split with thin coal measures and mudstone. It belongs to the Pennine Middle Coal Measures Formation, which is Westphalian (Carboniferous) in age (313 to 304 Ma) (Fig. 5.1). The Pennine Middle Coal Measures were formed as part of the Pennine Basin, an equatorial tropical basin with large subsiding river deltas draining from a land mass to the east (Stone et al., 2010). Following deposition, Variscan tectonics of the late Carboniferous and early Permian deformed earlier Carboniferous rocks into gentle folds and produced faulting. Uplifted areas were then eroded and the Westphalian beds were preserved in synclines, forming the present day coalfields (Stone et al., 2010). The Pennine Middle Coal Measures were mined throughout the 1900s in West Yorkshire for bituminous coal, and are still quarried to date for building stone.

Thornhill Rock used in this study was obtained as blocks of dimension stone of buff coloured fine-grained sandstone approximately $40 \times 40 \times 40$ cm from Britannia Quarry, operated by Calder Masonry at Rein Road, Morley, Leeds, West Yorkshire, LS27 0SW (53°43'55" N 1°35'49" W).

Characterisation testing of the Thornhill Rock was undertaken following procedures outlined in § 3.3 and § 3.4. 10 specimens were tested in uniaxial compression, eight specimens were tested in triaxial compression, and seven specimens were tested in indirect tension. The density and porosity of all specimens was calculated prior to destructive testing. Data from each test are tabulated in Table B.1 and B.2 of Appendix B.

Young's modulus (E) and Poisson's ratio (ν) were calculated at 50% peak stress from strain gauge data in the uniaxial compression testing using Eq.'s 3.7 and 3.8, respectively. Bulk modulus (K) and shear modulus (G) were calculated from the Young's modulus and Poisson's ratio according to Hooke's law as:

$$K = \frac{E}{(3 \times (1 - 2\nu)} \tag{5.1}$$

$$G = \frac{E}{(2 \times (1 + \nu)} \tag{5.2}$$

Triaxial tests were undertaken at confining pressures of 4, 8 and 12 MPa. The Mohr-Coulomb failure envelope (Eq. 2.2) for the Thornhill Rock was then calculated from the laboratory data, providing a friction angle (ϕ) and cohesion (c). The generalised Hoek-Brown failure criterion (Hoek et al., 2002) was also fitted to the laboratory data. The generalised Hoek-Brown failure criterion is given by:

$$\sigma_1^{'} = \sigma_3^{'} + \mathrm{UCS}\left(m_i \frac{\sigma_3^{'}}{\mathrm{UCS}} + s\right)^a \tag{5.3}$$

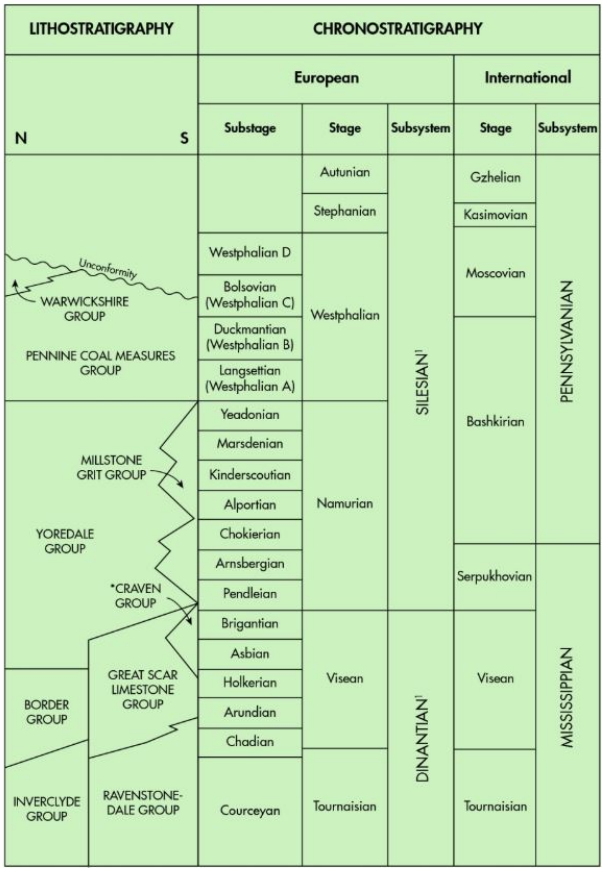

Figure 5.1: Stratigraphical classification of the Carboniferous rocks of northern England (Stone et al., 2010).

where $\sigma_1^{'}$ and $\sigma_3^{'}$ are the major and minor effective principal stresses at failure, m_i is the Hoek-Brown material constant for intact rock, and s and a are constants where $s = 1$ and $a = 0.5$ for intact rock. Summarised properties from the characterisation testing are tabulated in Table 5.1.

Property	Unit	Thornhill Rock	Midgley Grit
Density (ρ)	$\mathrm{kg\,m^{-3}}$	2250.00	2220.00
Porosity (φ)	-	15.5 %	13.7 %
Unconfined compressive strength (UCS)	MPa	50.80	37.80
Young's modulus (E)	GPa	8.70	9.50
Poisson's ratio (ν)	-	0.22	0.21
Bulk modulus (K)	GPa	5.18	5.46
Shear modulus (G)	GPa	3.57	3.93
Tensile strength (σ_t)	MPa	4.20	1.92
Hoek-Brown material constant ($\mathrm{m_i}$)	-	24.70	19.22
Hoek-Brown material constant (s)	-	1.00	1.00
Hoek-Brown variable coefficient (a)	-	0.50	0.50
Cohesion (c)	MPa	9.63	7.32
Friction angle (ϕ)	°	49.73	47.20

Table 5.1: Properties obtained from baseline characterisation testing of the Thornhill Rock and Midgley Grit.

Four visits were made to Britannia Quarry to obtain blocks of Thornhill Rock for sampling. Although visually similar in terms of colour and grain size, blocks could have been quarried from different units of Thornhill Rock within the quarry, resulting in a batch effect when testing the thermo-mechanical properties. To confirm if mineralogical differences occurred between batches, specimens from Batch 2, 3 and 4 were scheduled for quantitative X-ray diffraction (XRD) to provide whole rock mineral percentages (Fig. 5.2a). XRD analysis shows the Thornhill Rock predominantly contains quartz (55 to 65%), in addition to alkali and plagioclase feldspars, as well as minor constituents of chlorite, kaolinite, siderite, microcline and jarosite. XRD analysis also confirms that there are mineralogical differences between batches, with Batch 4 containing approximately 5% less quartz than other batches, replaced by microcline and

kaolinite. The mineralogy of Batch 2 and 3 is however seen to be broadly similar. In addition to mineralogical differences, there is potential for different batches to have been exposed and de-stressed for different periods of time, and excavated using different methods. To account for this batch effect, all results on intact and discontinuous thermo-mechanical testing of the Thornhill Rock are separated in to batches.

5.2.2 Midgley Grit

The Midgley Grit is a coarse-grained sandstone (locally termed as a Gritstone). The Midgley Grit is a *c.* 25 m thick unit within the Millstone Grit Group in West Yorkshire, UK. Namurian (Carboniferous) in age (326 to 313 Ma), and underlying the Pennine Coal Measures. Whilst the "Millstone Grit" is used to describe the Namurian succession of Yorkshire, the lithological assemblage is different from the type area for the Millstone Grit in Derbyshire, and more closely follows the depositional setting of the Yoredale Group (Fig. 5.1), except for the absence of limestone beds (Stone et al., 2010). The Millstone Grit Group of West Yorkshire formed as large fining upwards successions of channel-fill coarse-grained sandstone bodies within wider mixed shelf-deltaic sequences (Stone et al., 2010). Following deposition, the Millstone Grit Group underwent similar orogenic processes to the overlying coal measures throughout the late Carboniferous. The Millstone Grit further south (in Derbyshire) is famous for its use as millstones in watermills throughout the Peak District, the Millstone Grit Group of Yorkshire has also been quarried since the 13th century and is still quarried to date as building stone and aggregate.

Specimens used in this study were obtained as blocks of dimension stone of yellow to buff coloured coarse-grained sandstone approximately 30 × 30 × 30 cm from Black Hill Quarry operated by Mone Bros at Kings Road, Leeds, West Yorkshire, LS16 8BG (53°52'30" N 1°35'21" W).

Characterisation testing of the Midgley Grit was undertaken in line with the characterisation testing of the Thornhill Rock (§ 5.2.1). Three specimens were tested in uniaxial compression, nine specimens were tested in triaxial compression, with three tests undertaken at each confining pressure of 5, 10 and 15 MPa. Seven specimens were tested in indirect tension. The density and porosity of all specimens was calculated

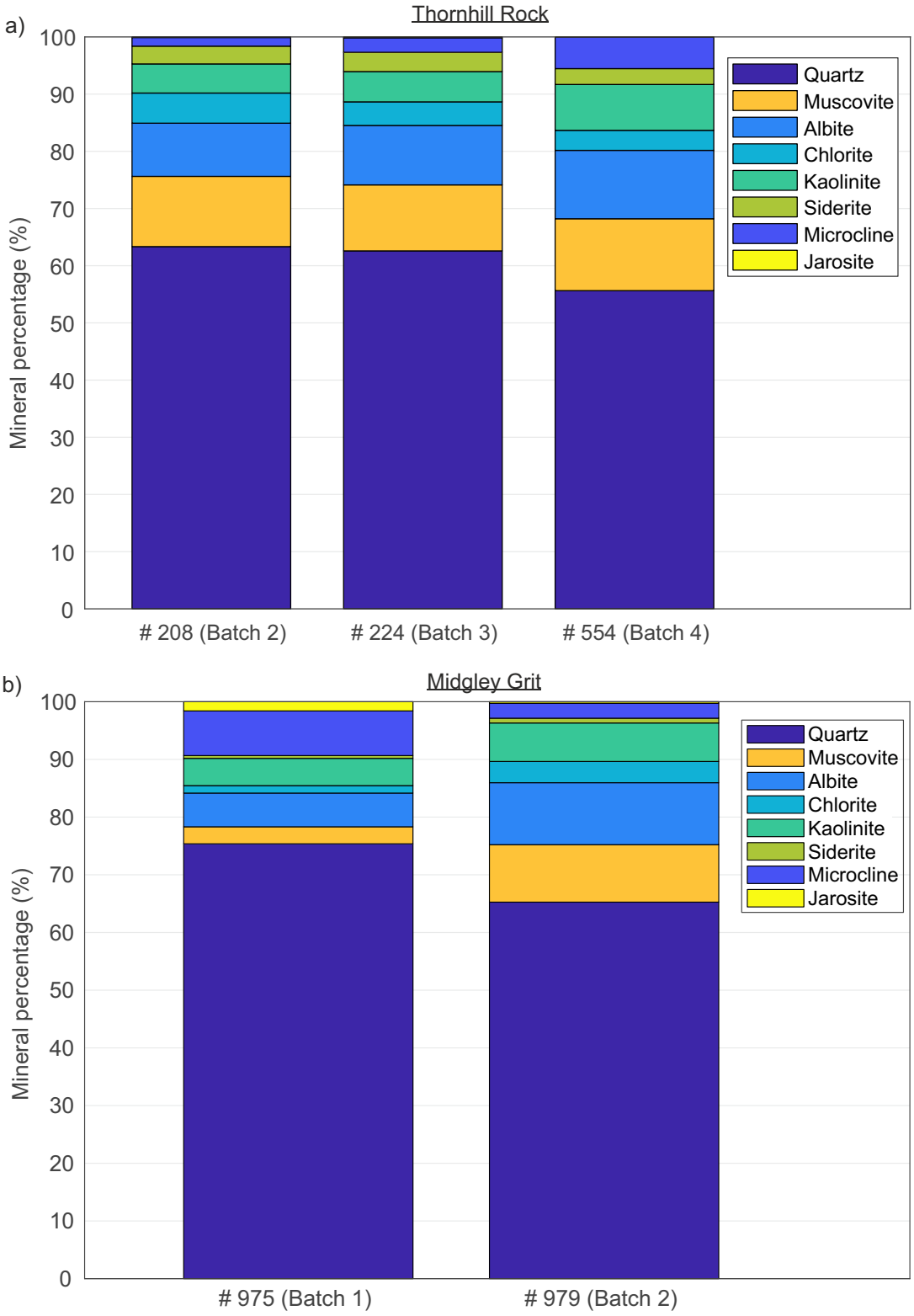

Figure 5.2: a) Bulk mineral percentages for different batches of Thornhill Rock obtained from quantitative X-ray diffraction (XRD) analysis. b) Bulk mineral percentages for different batches of Midgley Grit obtained from quantitative XRD analysis.

prior to destructive testing. Data from each test are tabulated in Table B.3 and B.4 of Appendix B, and baseline properties for the Midgley Grit from the characterisation testing are tabulated in Table 5.1.

As with the Thornhill Rock, in the duration of this study two batches of Midgley Grit were obtained as dimension stone from Black Hill Quarry. Quantitative XRD analysis has been undertaken on a specimen from each batch (Fig. 5.2b) to provide whole rock mineral percentages. The Midgley Grit contains considerably more quartz than the Thornhill Rock (65 to 75%), and more microcline feldspar, with the same minor constituents, but in smaller ratios. A batch effect is also observed in the Midgley Grit, with Batch 2 containing less quartz and microcline feldspar than Batch 1, replaced by minor constituents of muscovite, plagioclase feldspar and siderite. To account for this batch effect, all results on intact and discontinuous thermo-mechanical testing of the Midgley Grit are separated in to two batches.

5.3 Intact thermo-mechanical testing

Triaxial testing on intact specimens of Thornhill Rock and Midgley Grit were undertaken at room temperature, as well as at elevated temperatures of 50 °C, 75 °C and 100 °C. Test methods and procedures are outlined in § 3.5.3.1. This section presents and discusses the results.

The raw data from each test were processed, separating the thermal loading and mechanical loading portions of each test. The data from the thermal loading were checked to ensure the constant axial stress of 1 MPa (Fig. 5.3c) and constant confining pressure of 0.5 MPa (Fig. 5.3d) were maintained during heating. The data from the mechanical loading were checked to ensure that the temperature and confining pressure were held constant throughout the duration of the test (Fig. 5.4d & e). It was also confirmed that the specimen was deformed under constant axial strain for the initial portion of the test and that the axial extensometers worked as a pair (Fig. 5.4g showing constant axial deformation for the first $\approx$ 1400 s). The procedure then switched to constant circumferential strain control (Fig. 5.4c). Provided these procedural elements were followed

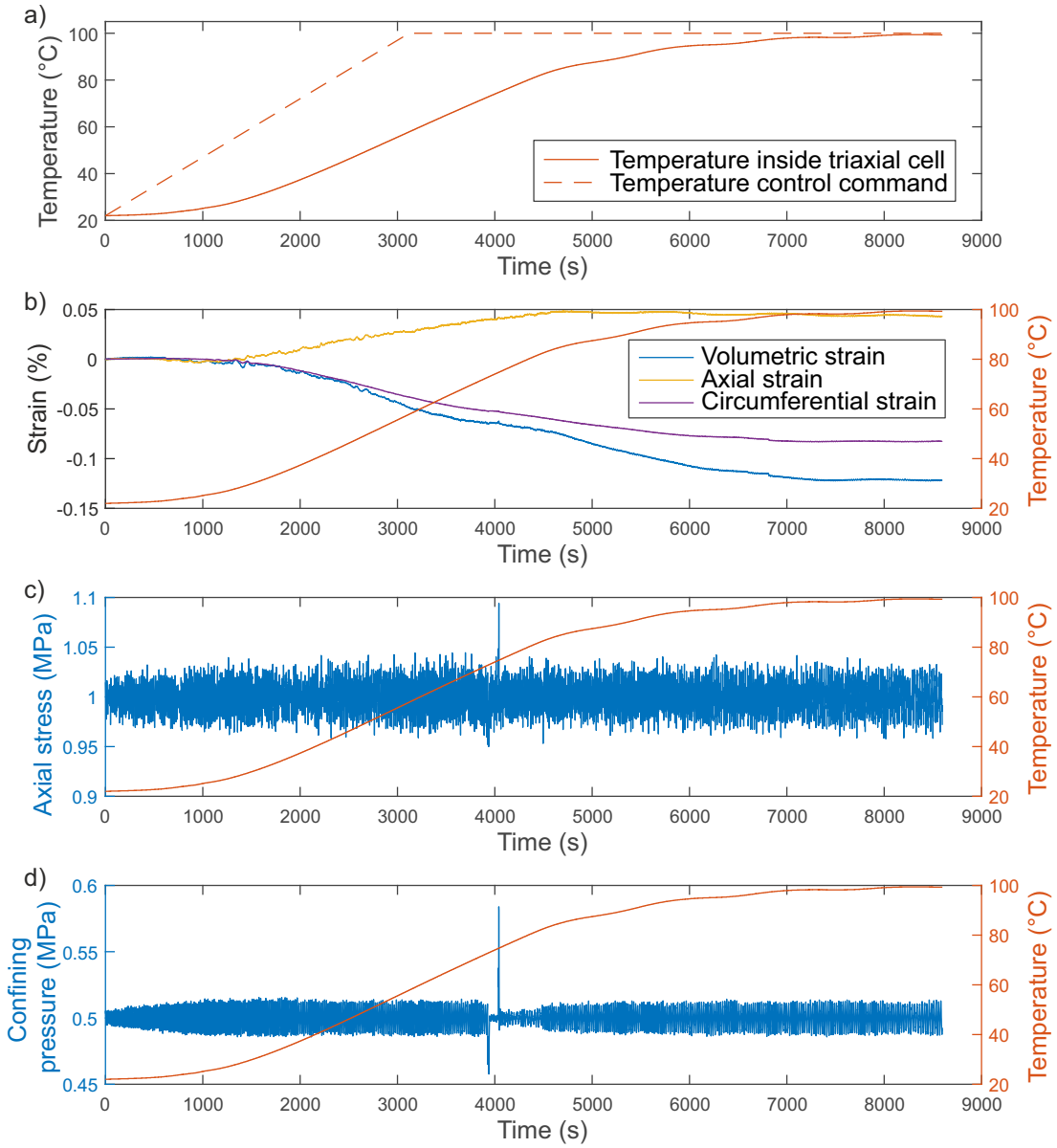

Figure 5.3: a) Heating of specimen within the triaxial pressure vessel based on data from the thermocouple placed directly next to the specimen, compared to the 1.5 °C min^{-1} heating command. b) Volumetric, axial and circumferential deformation of the specimen during heating due to thermal expansion. c) Constant axial stress of 1 MPa maintained during thermal loading. d) Constant confining pressure of 0.5 MPa maintained during thermal loading (example data from Specimen #562, tested at 5 MPa σ_3 and 100 °C).

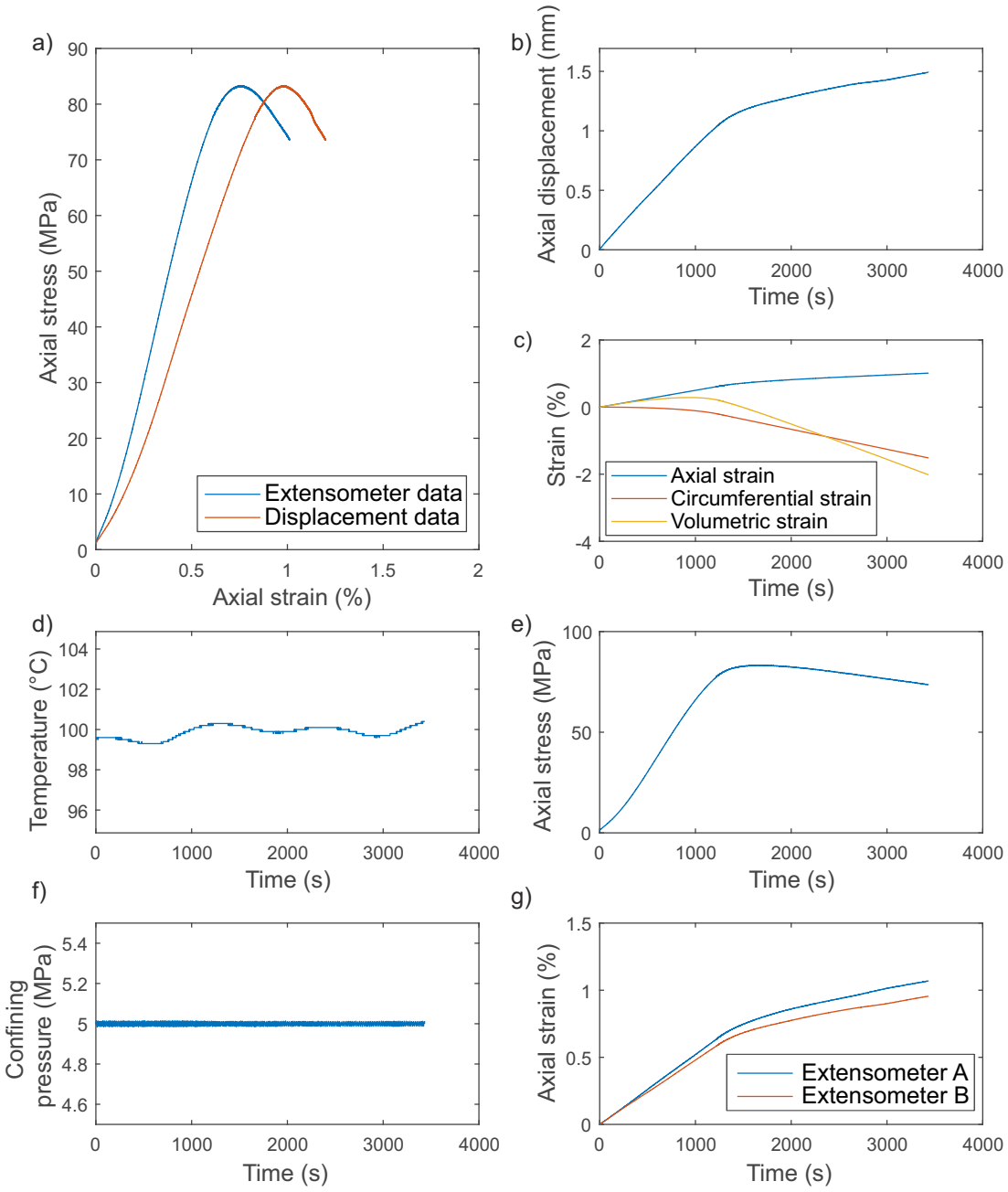

Figure 5.4: Data plots of logged raw data for mechanical loading portion of test (example data from Specimen #562, tested at 5 MPa σ_3 and 100 °C). Further details in § 3.5.3.4.

correctly and the specimen was recovered from the triaxial pressure vessel without the ingress of confining oil, the test was deemed successful.

Young's modulus (E) (tangential modulus) and Poisson's ratio (ν) were calculated from the mechanical loading for each specimen (Jaeger et al., 2007; Ulusay, 2014) at 50% of peak stress (Fig. 5.5a) by solving simultaneously according to Hooke's law as:

$$\begin{aligned} \varepsilon_a &= \frac{(\sigma_1 + \sigma_3) - (2 \times \nu \times \sigma_3)}{E} \\ \varepsilon_d &= \frac{\sigma_3 - (\nu \times (\sigma_1 + 2\sigma_3))}{E} \end{aligned} \tag{5.4}$$

where ε_a and ε_d are the axial and diametral strains respectively, obtained from the axial extensometers and circumferential chain extensometer on the specimen. The volumetric strain ($\varepsilon_v = \Delta V/V$) of each specimen was then calculated as:

$$\frac{\Delta V}{V} \approx \varepsilon_a + 2\varepsilon_d \tag{5.5}$$

The crack damage (CD) threshold for each specimen was taken at the point of maximum volumetric compaction (Fig. 5.5b), and the crack initiation (CI) threshold was calculated using the lateral strain response method (Nicksiar and Martin, 2012) (Fig. 5.5c & d).

For the thermal loading of all specimens, and concordant with the aluminium dummy testing (§ 3.5.5, Fig. 3.4), a lag is observed in the first 1000 s between the heating command at 1.5 °C min^{-1} and the heating of the specimen measured from the thermocouple within the triaxial pressure vessel next to the specimen (Fig. 5.3a). This is due to the initial heating of the steel pressure vessel and mineral oil confining fluid prior to heating of the specimen itself. Heating then occurs at a slightly slower rate (1.1 °C min^{-1}) than the heating command (1.5 °C min^{-1}), before the servo-control feedback reduces the heating rate and it plateaus to the desired temperature. Due to the calibration of the feedback on the temperature servo-controller, all tests undertaken at 50 °C overshot the target temperature and were actually undertaken in the region of 52 to 60 °C. All thermally loaded tests above 50 °C show a peak in the confining pressure

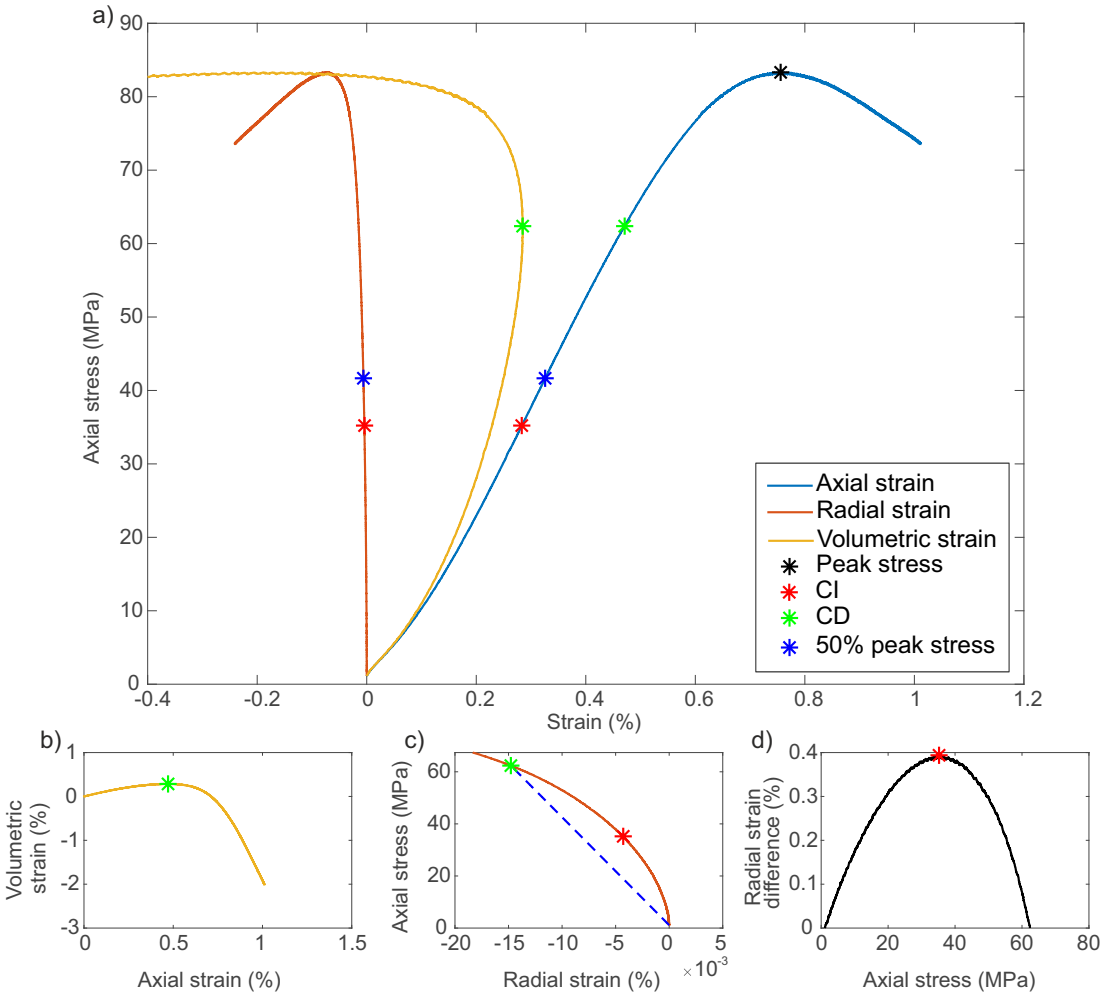

Figure 5.5: a) Axial, radial, and volumetric strain vs. axial (differential) stress plot, showing the peak stress, crack initiation (CI) and crack damage (CD) thresholds, as well 50% peak stress at which E and ν are calculated. b) CD threshold calculated as the point of maximum volumetric compression. c) & d) Calculation of the CI threshold, following the lateral strain response method (Nicksiar and Martin, 2012). (Example data from Specimen # 562, tested at 5 MPa σ_3 and 100 °C).

and axial stress during heating (≈ 4000 s on Fig. 5.3c & d) of approximately 0.1 MPa, which is due to manual repriming of the confining pressure intensifier, necessary due to the thermal expansion of the confining oil.

Fig. 5.3b shows example deformation due to thermal expansion of a specimen heated to 100 °C. As with the aluminium dummy testing, the axial extensometers do not pick up the thermal expansion of the specimen, and instead record compaction during the heating phase. This may be as a result of increased ductility of the PTFE jacket, with increased temperature resulting in slipping of the specimen within the PTFE jacket, or slipping of the extensometers on the PTFE jacket. However, the circumferential strain recorded from the circumferential chain extensometer, shows dilation throughout heating (as expected due to thermal expansion, and as was accurately recorded during aluminium dummy testing). Isotropic thermal expansion is therefore assumed and the circumferential extensometer deformation (ε_c) is used to calculate the linear thermal expansion coefficient (α_L) for each specimen as:

$$\alpha_L = \frac{\varepsilon_c}{\Delta T \pi} \tag{5.6}$$

where ΔT is the change in temperature.

5.3.1 Thornhill Rock

15 thermo-mechanical triaxial tests were undertaken across two batches of Thornhill Rock. Full results are tabulated in Table B.5 of Appendix B.

All specimens of Thornhill Rock subjected to thermal loading under pre-load conditions of 1 MPa axial stress and 0.5 MPa confining pressure displayed similar deformation, with linear thermal expansion coefficients ranging from $1.53 \times 10^{-6}\,\mathrm{K}^{-1}$ to $5.08 \times 10^{-6}\,\mathrm{K}^{-1}$ (mean $= 3.42 \times 10^{-6}\,\mathrm{K}^{-1}$, standard deviation ($s$) $= 0.84 \times 10^{-6}\,\mathrm{K}^{-1}$).

The axial and radial stress-strain curves for the mechanical loading portion of tests for eight specimens from Batch 4 tested at 5 MPa confining pressure and temperatures of 20 °C, 50 °C, 75 °C and 100 °C are shown in Fig. 5.6. The stress-strain curves for

all temperatures display typical compressive brittle behaviour (Hoek and Bieniawski, 1965). The repeat tests at each temperature show good repeatability, as expected from such homogeneous specimens. The stress-strain curves show a clear reduction in peak strength with increasing thermal loading. The peak strength is seen to reduce by approximately 17% between testing at room temperature and at 100 °C. Both tests undertaken at 50 °C show a more brittle failure than other tests, with a sudden stress drop directly after obtaining peak strength and a reduction to residual strength. No explanation can be offered for the occurrence of this behaviour at 50 °C and not at other temperatures, as all specimens were tested to the same amount of circumferential strain.

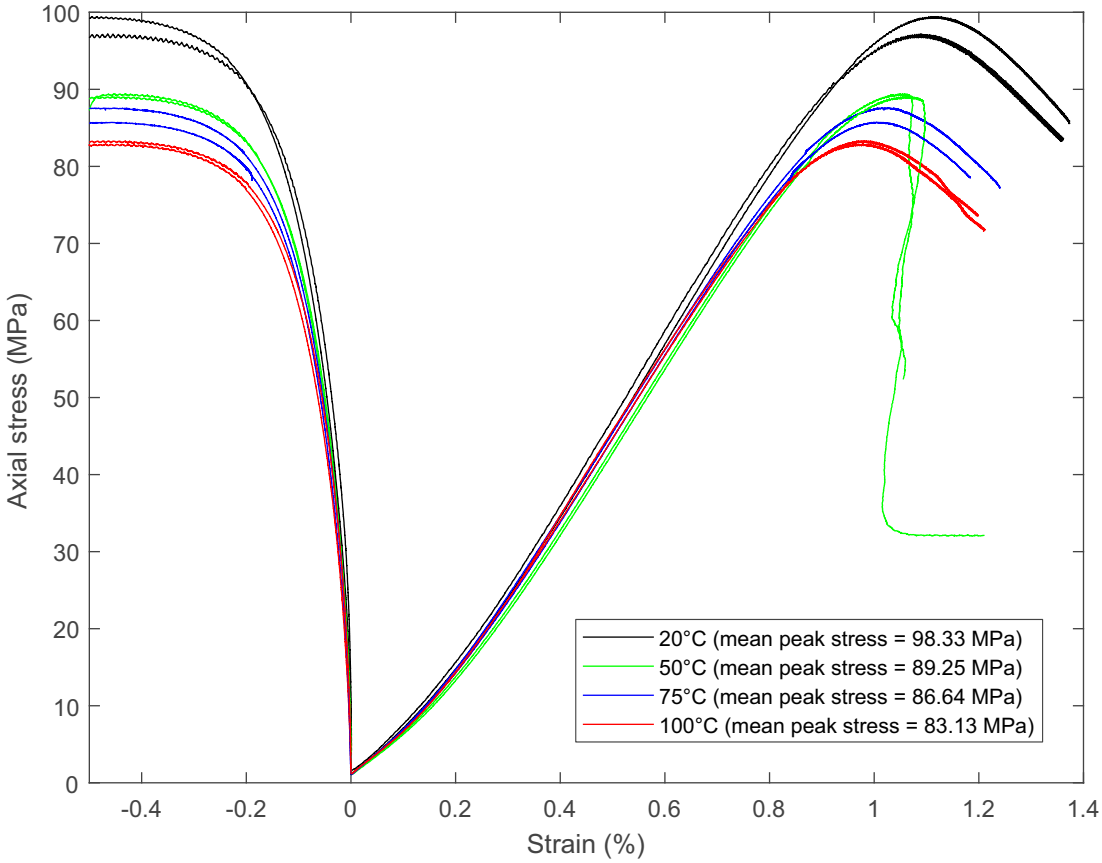

Figure 5.6: Axial stress vs. radial and axial strain data for triaxial tests on intact specimens of Thornhill Rock (Batch 4), carried out at 5 MPa σ_3 and temperatures of 20 °C, 50 °C, 75 °C and 100 °C.

Photographs of specimens after testing (Fig. 5.7) show the formation of a single shear plane fracture at all temperatures tested. The shear plane did not develop well in the tests undertaken at 100 °C (Fig. 5.7d), and the shear plane at 50 °C is not distinctly different from 20 °C or 75 °C, despite the large stress drop post-peak. All developed fractures are very planar, with little undulation or lobing, and form at angles between 18° and 28° from the vertical. It is important to note the ingress of oil to some specimens (Fig. 5.7b & d). This typically occurred at elevated temperatures as the PTFE jacket became more ductile, allowing ingress of oil to the specimen from the platens. However, the specimens are not saturated, suggesting that the oil ingress occurred after the confining pressure had been removed during unloading. Consequently this is not thought to affect the thermo-mechanical behaviour observed in the experiments.

Although Batch 3 is weaker than Batch 4, the same relative decrease in peak strength is observed with increasing temperature (Fig. 5.8a), with a 17% decrease in strength observed between room temperature and 100 °C. Neither batch show a significant variation in Young's modulus with temperature (Fig. 5.8b), but in both batches an increase in Poisson's ratio is observed with increasing temperature (Fig. 5.8d). As no significant variation is seen in the Young's modulus, the increasing Poisson's ratio with temperature must be due to increasing radial dilation, which can be seen in Fig. 5.6. Both batches of Thornhill Rock show decreasing CI and CD stresses with increasing temperature (Fig. 5.8c & e), and the reductions in CI and CD with temperature correlate consistently with the reduction in peak strength for both batches. The mean CI for all specimens is 41.6% of the peak stress (min. = 39.2%, max. = 43.7%, s = 1.2%), and the mean CD for all specimens is 74.8% of the peak stress (min. = 71.6%, max. = 77.0%, s = 1.5%).

5.3.2 Midgley Grit

Three thermo-mechanical triaxial tests were undertaken on intact Midgley Grit. Full results are tabulated in Table B.6 of Appendix B.

A more limited suite of testing was undertaken on the Midgley Grit than the Thornhill Rock due to specimen availability, with only a single test undertaken at 20 °C, 50 °C

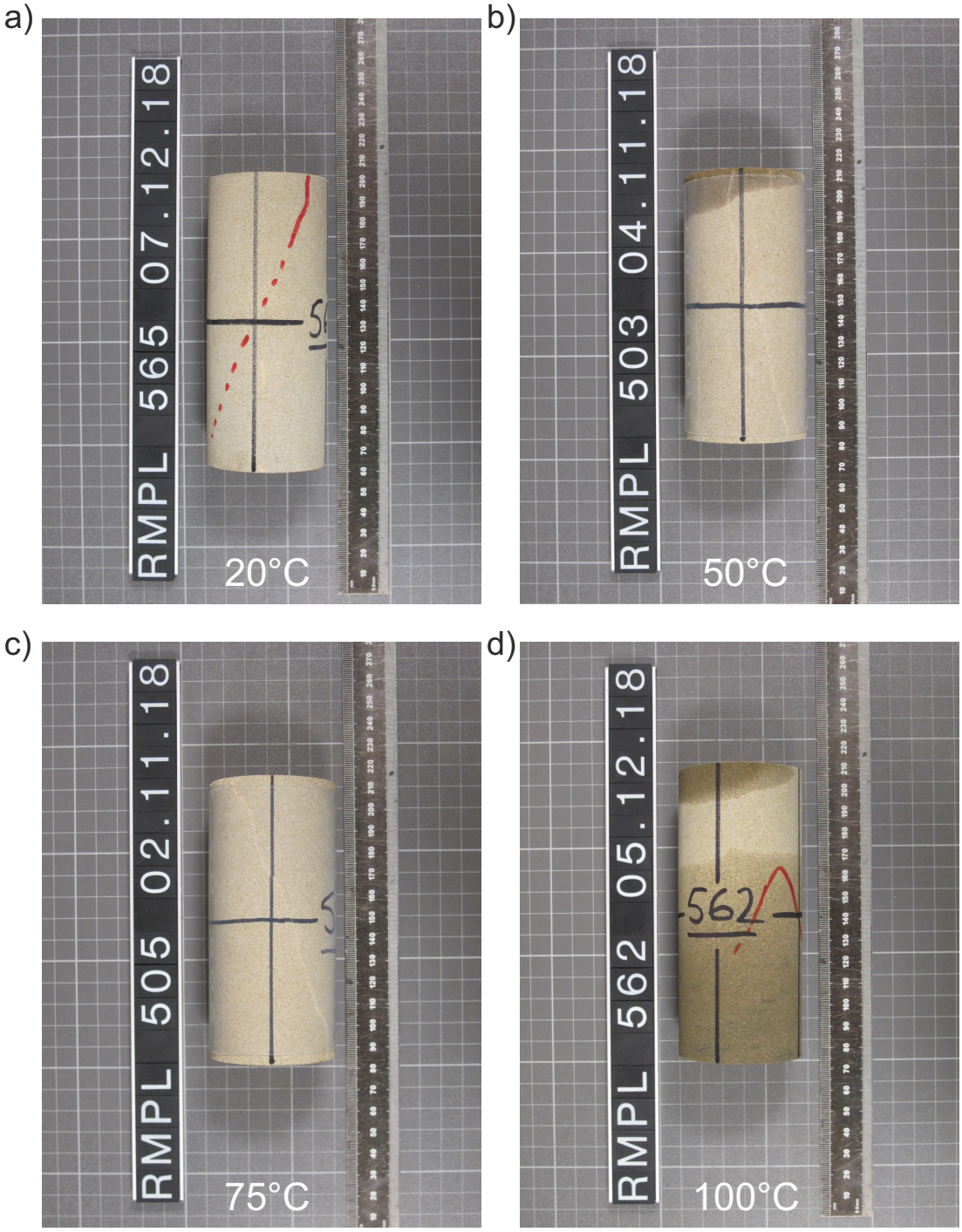

Figure 5.7: Photographs of specimens of intact Thornhill Rock (Batch 4) after thermo-mechanical triaxial testing, all tests were undertaken at 5 MPa σ_3, under constant axial strain control ($5 \times 10^{-6}\,\mathrm{s}^{-1}$) until yield, then constant circumferential extension control ($1 \times 10^{-3}\,\mathrm{mm\,s}^{-1}$) and terminated at 2 mm circumferential extension. Note slight oil ingress in to specimens a) & d).

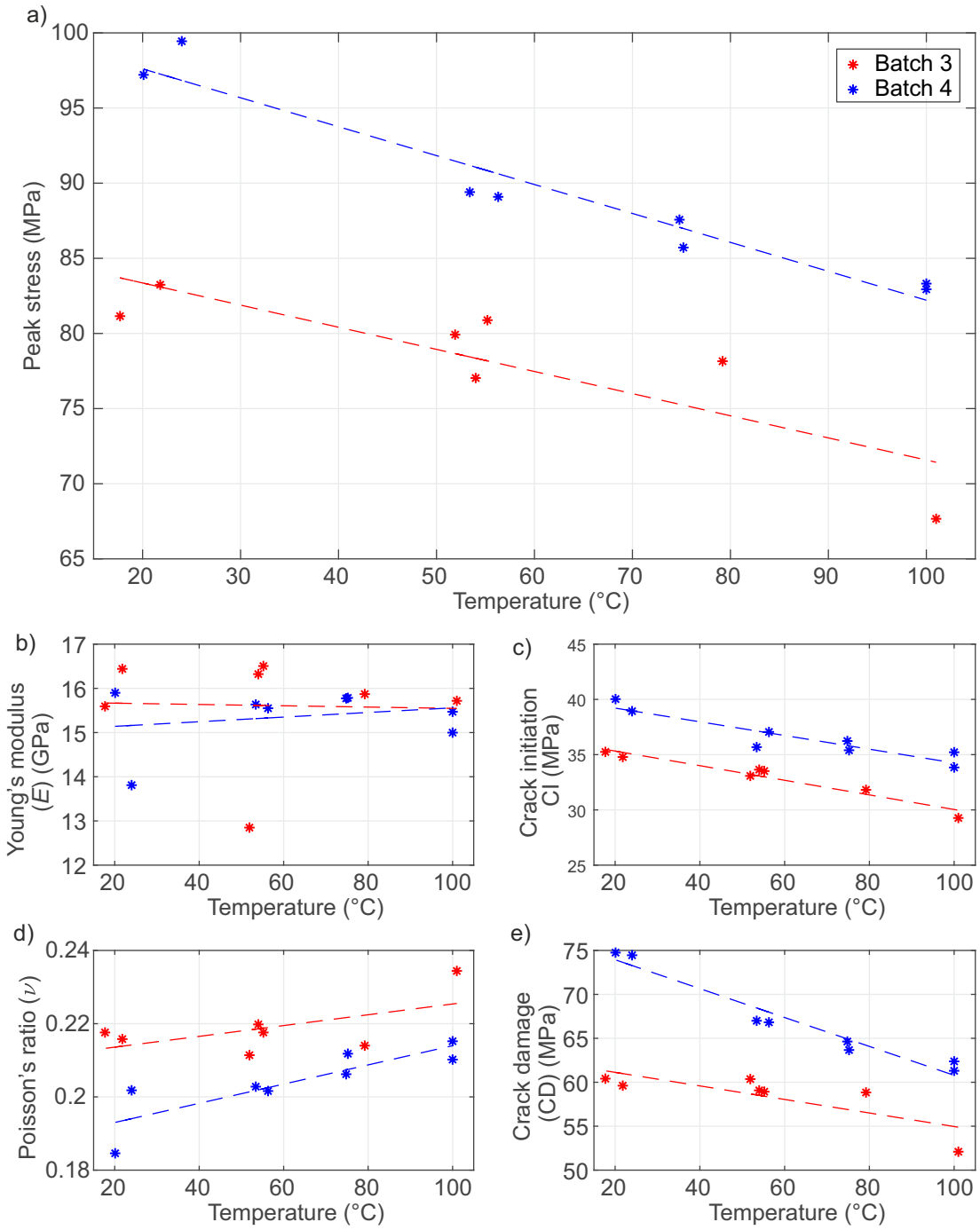

Figure 5.8: Plots of peak stress, Young's modulus, Poisson's ratio, crack initiation threshold stress and crack damage threshold stress vs. temperature for thermo-mechanical triaxial testing on intact specimens of Thornhill Rock. Dashed lines represent linear least squares regression of the data.

and 100 °C. The two specimens of Midgley Grit subjected to thermal loading under pre-load conditions of 1 MPa axial stress and 0.5 MPa confining pressure displayed similar deformation, with calculated linear thermal expansion coefficients of $1.22 \times 10^{-6}\,\mathrm{K}^{-1}$ and $1.38 \times 10^{-6}\,\mathrm{K}^{-1}$.

The axial and radial stress-strain curves for the mechanical loading portion of the three tests undertaken at 5 MPa confining pressure and temperatures of 20 °C, 50 °C and 100 °C are shown in Fig. 5.9a. All specimens again show typical brittle behaviour, and a reduction in peak strength is seen with increasing thermal loading. The peak strength is seen to reduce by approximately 7% between testing at room temperature and at 100 °C (Fig. 5.10a). All tests were terminated at 2 mm circumferential extension, but whilst all peak strengths occur after a similar amount of axial strain, considerably more axial strain is observed with increasing thermal loading post-peak. All specimens formed single shear fracture planes (photographs in Fig. 5.9b to d) at angles between 28° and 30°. As well as a reduction in peak strength with increased thermal loading, a reduction in also seen in the CI and CD thresholds (Fig. 5.10c & e). The reduction in CI and CD is consistent with the reduction in peak strength. The mean CI for all specimens is 42.9% of the peak stress (min. = 40.2%, max. = 44.7%, s = 1.9%), and the mean CD for all specimens is 73.5% of the peak stress (min. = 71.7%, max. = 74.8%, s = 1.3%). A slight decrease in Young's modulus (Fig. 5.10b), and an increase in Poisson's ratio (Fig. 5.10d) is observed with increasing thermal loading.

5.3.3 Discussion

All specimens of Thornhill Rock and Midgley Grit show brittle deformation and the formation of a single shear plane, regardless of the differences in thermal loading prior to mechanical testing. Both the Thornhill Rock and the Midgley Grit show a reduction in peak strength with increased thermal loading, evident at just 50 °C, and considerable at temperatures of 100 °C. This reduction in strength under thermal loading can be attributed to thermal micro-cracking. Both the Thornhill Rock and Midgley Grit show bulk linear thermal expansion coefficients from thermal loading ranging from 1.22×10^{-6} to $5.08 \times 10^{-6}\,\mathrm{K}^{-1}$. It is unlikely that this thermal expansion is isotropic within the granular structure of the specimens, but instead will occur heterogeneously with mineralogical differences in the specimens causing localised stress concentrations.

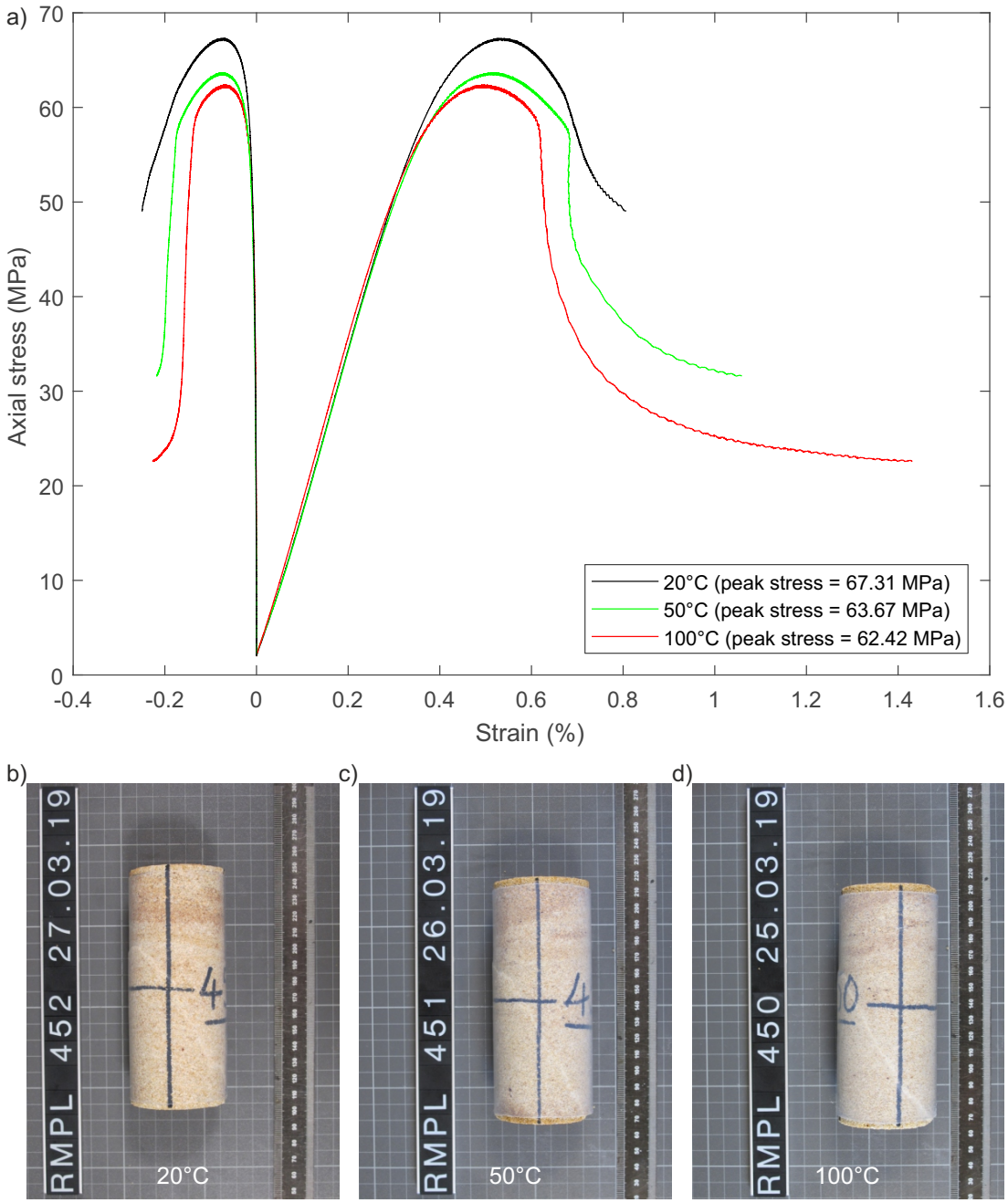

Figure 5.9: a) Axial stress vs. radial and axial strain data for triaxial tests on intact specimens of Midgley Grit, carried out at 5 MPa σ_3, under constant axial strain control ($5 \times 10^{-6}\,s^{-1}$) until yield, then constant circumferential extension control ($1 \times 10^{-3}\,mm\,s^{-1}$) and terminated at 2 mm circumferential extension. Tests undertaken at temperatures of 20 °C, 50 °C and 100 °C. b) to d) Photographs of specimens of intact Midgley Grit after thermo-mechanical triaxial testing.

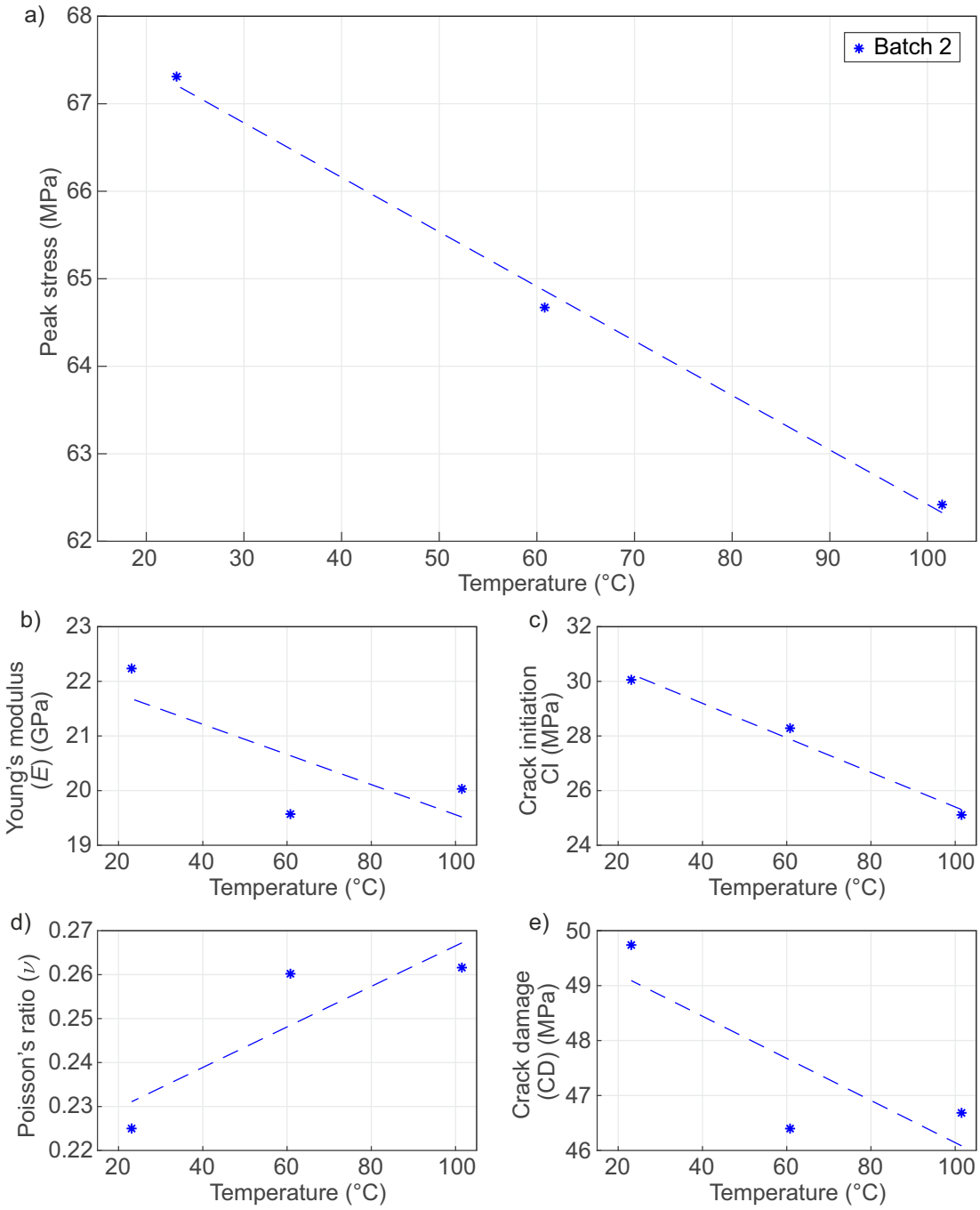

Figure 5.10: Plots of peak stress, Young's modulus, Poisson's ratio, crack initiation threshold stress and crack damage threshold stress vs. temperature for thermo-mechanical triaxial testing on intact specimens of Midgley Grit. Dashed lines represent linear least squares regression of the data.

These localised stresses are large enough to induce inter-granular tensile micro-cracking (Fredrich and Wong, 1986), causing a strength reduction of up to 17% between room temperature and 100 °C. The crack initiation and crack damage thresholds are also seen to reduce with increasing thermal loading, with the crack initiation threshold consistently occurring at approximately 42% of the peak stress for the Thornhill Rock, and at approximately 43% of the peak stress for the Midgley Grit. This suggests that the weakening is occurring prior to mechanical loading due to thermal micro-cracking during the thermal loading phase of the experiments.

An increase in Poisson's ratio is observed in both lithologies with increasing thermal loading, however, with little change observed in Young's modulus, this must occur due to increased radial deformation. The pre-load mechanical conditions applied during thermal loading are not hydrostatic, with an additional 1 MPa axial differential stress applied in addition to the 0.5 MPa hydrostatic stress. It is therefore likely that tensile micro-cracking will preferentially occur parallel to the axial load, causing increased radial deformation.

The Thornhill Rock shows a greater reduction in strength with increasing thermal loading than the Midgley Grit. This correlates with the Midgley Grit having a lower bulk linear thermal expansion coefficient during the thermal loading phase, therefore likely to induce less thermal micro-cracking. The reduced thermal expansion coefficient of the Midgley Grit in comparison to the Thornhill Rock is unexpected. XRD analysis shows that the Midgley Grit contains a greater percentage of quartz than the Thornhill Rock (65 to 75% in the Midgley Grit compared to 55 to 63% in the Thornhill Rock). Quartz has a relatively high linear thermal expansion coefficient of $1.60 \times 10^{-5}\,\mathrm{K}^{-1}$ (Park et al., 2015). The Midgley Grit does however also typically have a higher percentage of microcline in comparison to the Thornhill Rock, which has a relatively low linear thermal expansion coefficient of $0.53 \times 10^{-5}\,\mathrm{K}^{-1}$ (Siegesmund et al., 2018). In addition to the mineralogy, it is likely that the differences in grain size, porosity and strength of the cement between grains will affect the thermal expansion of the different lithologies, and the degree of thermally induced micro-cracking.

Polished thin sections were made from intact specimens of Thornhill Rock after thermo-mechanical triaxial testing (specimens #565, #503, #505 and #562). Specimens were

blue epoxy impregnated under vacuum prior to sectioning, and were sectioned across the developed shear plane. All four specimens that were sectioned had been mechanically loaded to 2% circumferential strain, but thermally loaded to different temperatures. However, no differences could be seen between the damage within the sections under optical microscopy. It was hypothesised that thermal loading would cause micro-cracking damage throughout the specimens, with no preferred orientation. Later mechanical loading then may cause further micro-cracking, with damage accumulated and concentrated around the shear plane. However, no gradation in micro-cracking across the specimens thermally loaded to 20 and 100 °C could be determined, or a difference in the micro-cracking between specimens in general. It is possible that the thermal damage has been over-printed by the mechanical damage, as the thermally induced micro-cracks will have acted as initiation points for further mechanically induced micro-cracking. It is also possible that other mechanisms of damage accumulation could be occurring. The porosity of the Thornhill Rock is approximately 15%. The re-alignment of quartz grains and pore collapse could be alternative mechanisms of progressive damage (Dunn et al., 1973). Additional laboratory testing including hydrostatic pore collapse tests and permeability measurements to assess the evolving permeability of specimens during deformation would be useful to examine this hypothesis.

5.3.4 Time dependent behaviour testing

Due to the thermal loading control rate of 1.5 °C used for all thermo-mechanical loading tests, specimens tested at higher temperatures are subjected to mechanical pre-loads for a substantially longer period of time than tests undertaken at room temperature. To ensure that the apparent strength reduction with increasing thermal loading is not in fact due to mechanical creep through stress corrosion cracking (Baud and Meredith, 1997; Lockner, 1993; Main, 2000), a time dependent creep test was undertaken on an intact specimen of Thornhill Rock. The specimen was prepared and assembled (§ 3.2 and § 3.5.2), and subjected to the pre-load conditions used for all thermo-mechanical testing of 1 MPa axial stress and 0.5 MPa confining pressure. These stress conditions were maintained for 3 hours whilst monitoring the axial strain of the specimen. If the specimen was to develop primary creep behaviour, it would be expected that the specimen would deform under these constant stress conditions, observed as increasing

axial strain with time. Fig. 5.11a shows the axial strain recorded under the pre-load conditions for the 3 hour duration. A small amount of axial strain is observed within the first hour of the test, but this is extremely minimal ($< 0.001\,\%$), and is likely due to the warming and stabilisation of the electronics in the servo-control system. Beyond this, no deformation is observed. It can therefore be concluded that the trends observed with increasing thermal loading discussed within this section occur due to the thermal loading alone and not due to biases in the laboratory procedures.

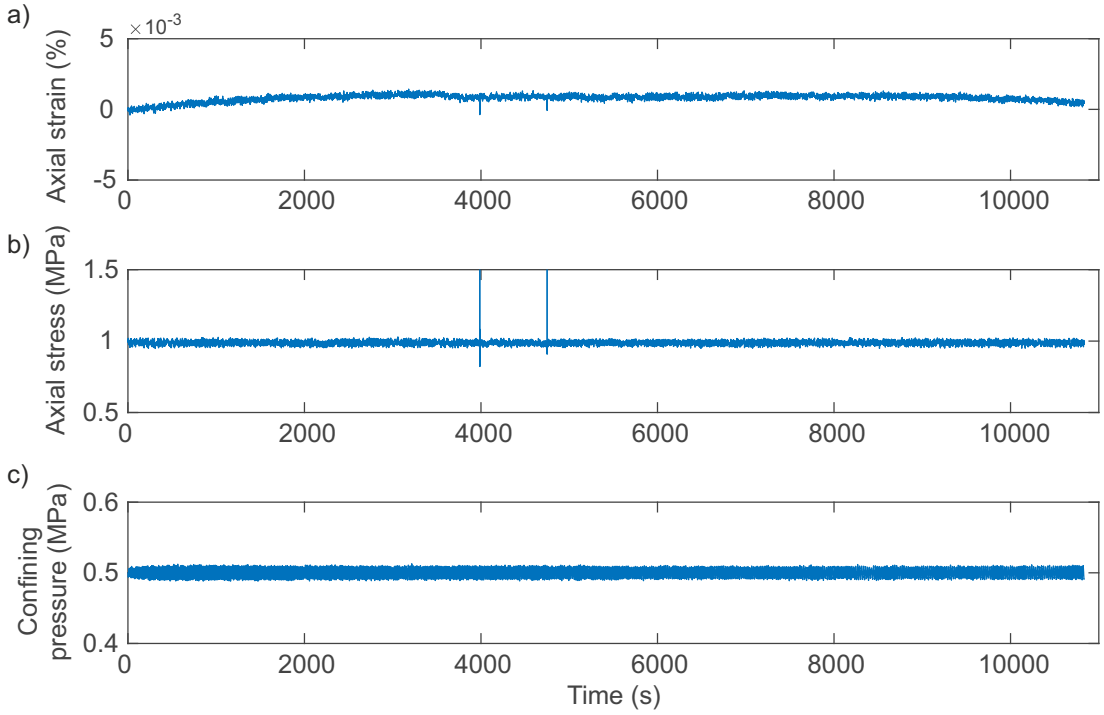

Figure 5.11: Axial strain, axial stress and confining pressure plots vs. time, for time dependent test undertaken on a specimen of Thornhill Rock.

5.4 Thermo-mechanical testing of discontinuities

In addition to triaxial testing on intact specimens of Thornhill Rock and Midgley Grit, thermo-mechanical triaxial testing was undertaken on specimens of both lithology with a pre-existing discontinuity already present (§ 3.2.2), allowing the thermal closure and shear behaviour to be examined. Test methods and procedures are outlined in § 3.5.3.3. This section presents and discusses the results.

As with the intact testing, the raw data from each test was processed, separating the thermal loading and mechanical loading portions of each test. The data from thermal loading were checked to ensure the mechanical pre-load conditions were maintained during heating. The data from the mechanical loading were checked to ensure that the temperature and confining pressure were maintained for the duration of the test, and the specimen was deformed in constant axial strain for the duration of the test. Provided these procedural elements were followed correctly and the specimen was recovered from the triaxial pressure vessel without the ingress of confining oil, the test was deemed successful.

5.4.1 Data interpretation method

By inducing a discontinuity in specimens through tensile failure at an angle ($\beta \approx 30°$ from vertical), the most common method for failure under axial loading is shear failure along this pre-existing discontinuity. Rather than assessing the data in terms of principal stresses as for intact specimens, it is therefore essential to instead examine the data in the resolved shear and normal stresses as a function of shear displacement along the discontinuity. The procedures outlined by Wong (1982b) and Ohnaka et al. (1997) were followed to rotate stresses and remove the elastic deformation of both the intact specimen material and the triaxial rig. This allows evaluation of just the shear behaviour of the discontinuity. Resolved shear stress (τ) and normal stress (σ_n) were calculated as:

$$\tau = \frac{(\sigma_1 - \sigma_3)\sin 2\beta}{2} \tag{5.7}$$

$$\sigma_n = \sigma_3 + \frac{(\sigma_1 - \sigma_3)(1 - \cos 2\beta)}{2} \tag{5.8}$$

The apparent slip (D_{app}) along the discontinuity was then evaluated from the relation:

$$D_{app} = \frac{\varepsilon_a(l)}{\cos\beta} \tag{5.9}$$

where $\varepsilon_a(l)$ was used to calculate the change in length of the specimen from axial extensometers, rather than the axial load actuator displacement, which is affected by the

elastic deformation and thermal expansion of the loading platens. D_{app} includes the elastic deformation of the intact specimen material itself (D_{el}) as well as the inelastic response caused by shear displacement. The elastic deformation was therefore subtracted to give just the shear displacement of the discontinuity (D) (Fig. 5.12) using:

$$D = D_{app} - D_{el} = D_{app} - \frac{(\tau + a)}{b} \tag{5.10}$$

where a and b are constants and the linear line is represented by the equation:

$$\tau = b(D_{el}) - a \tag{5.11}$$

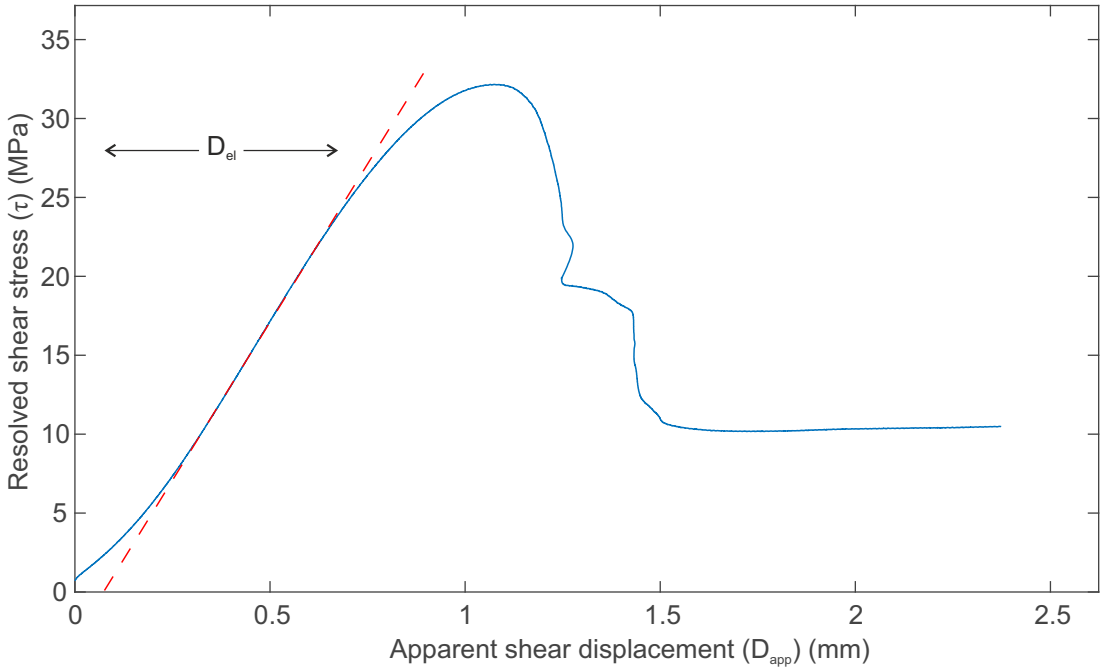

Figure 5.12: Resolved shear stress (τ) against apparent shear displacement (D_{app}) for Specimen #554. The red dashed line represents the elastic component (D_{el}) of the specimen deformation.

Fig. 5.13 shows a corrected shear stress (τ) vs. shear displacement (D) plot, showing the displacement dependent constitutive relation for shear on a discontinuity. As is common with laboratory shear experiments it is found that shear stress initially increases with an increase in shear displacement. After a peak shear stress (τ_p) is obtained, τ degrades with ongoing shear displacement until a residual shear stress (τ_r) is obtained. In

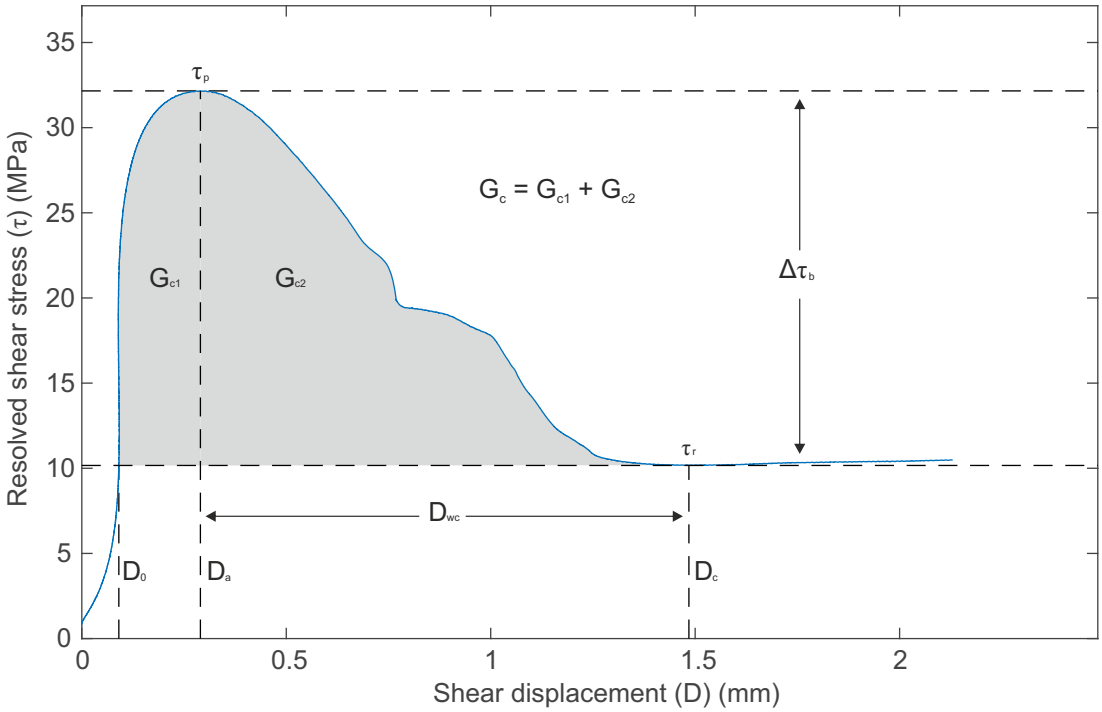

Figure 5.13: Resolved shear stress (τ) against shear displacement (D) for Specimen #554, illustrated with parameters derived for different amounts of shear stress and shear displacement.

addition, it is possible to obtain the parameters as annotated on Fig. 5.13. D_a is the shear displacement at τ_p. D_c is the shear displacement at which τ_r is reached. D_0 is the shear displacement at which the shear stress intersects with an extrapolation of τ_r. $\Delta\tau_b$ is the shear stress drop between τ_p and τ_r, and D_{wc} is the shear displacement between τ_p and obtaining τ_r. The shaded region (G_c) is the fracture energy, given by:

$$G_c = \int_{D_0}^{D_c} [\tau(D) - \tau_r] dD \tag{5.12}$$

This can be further divided in to the energy required to reach macroscopic shear failure at τ_p as G_{c1}, and the additional energy required during shear displacement to obtain τ_r as G_{c2}, given by:

$$G_{c1} = \int_{D_0}^{D_a} [\tau(D) - \tau_r] dD \tag{5.13}$$

$$G_{c2} = \int_{D_a}^{D_c} [\tau(D) - \tau_r] dD \tag{5.14}$$

5.4.2 Thornhill Rock

16 discontinuous thermo-mechanical triaxial tests were undertaken across four batches of Thornhill Rock. Full results are tabulated in Table B.7 of Appendix B.

Laser profilometry was undertaken on each discontinuity prior to testing, allowing the roughness to be quantified (§ 4.4.2). Fig. 5.14a shows the *JRC* values for all discontinuous specimens of Thornhill Rock. Batch 1 shows a slightly reduced roughness (mean *JRC* of between 7 and 9), but all other batches show very similar roughnesses, with mean *JRC* values between 10 and 12. This shows that whilst it is not possible to undertake testing of identical discontinuities under different thermal and mechanical loads, inducing the discontinuities through tensile splitting produces repeatable roughness, controlled by the grain size of the rock, despite individual differences in topography of each discontinuity.

Shear stress vs. shear displacement curves for the eight specimens from Batch 4 tested at 5 MPa confining pressure and temperatures of 20 °C, 50 °C, 75 °C and 100 °C are shown in Fig. 5.15. All specimens show typical shear behaviour, with an initial increase in shear stress with a small amount of discontinuity closure, until a peak shear stress is obtained. Shear displacement then occurs along the discontinuity until a residual shear strength is obtained.

Different shear parameters are plotted against temperature for all three batches of specimens in Fig. 5.16. All batches show an initial increase in peak shear strength (τ_p) (Fig. 5.16a) between room temperature and 50 °C, with an increase in peak shear strength of between 14 and 33%. A reduction in peak shear strength is then observed with further thermal loading to 75 and 100 °C, with the reduction in strength differing between batches. By thermal loading to 100 °C, peak shear strength returns back to similar strengths observed at room temperature. Little change is observed in residual shear strength (τ_r) with thermal loading, meaning that the stress drop between peak

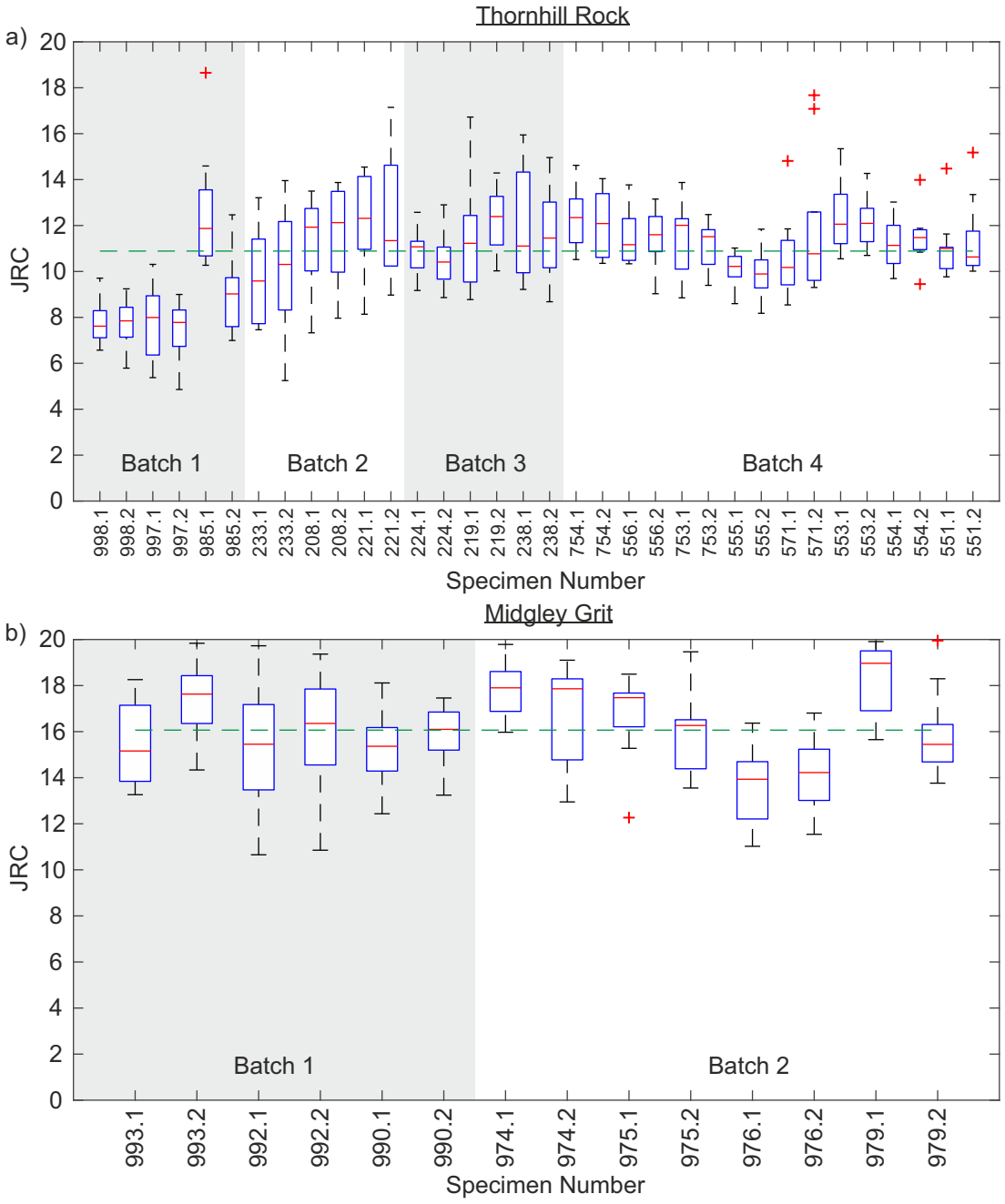

Figure 5.14: a) Joint Roughness Coefficient (JRC) values for discontinuous specimens of Thornhill Rock. b) JRC values for discontinuous specimens of Midgley Grit. Roughness data for both lithologies was obtained as point cloud data from laser profilometry, analysed statistically as 2D profiles parallel to the shearing direction, and correlated from Z_2 to JRC using the relationship proposed by Yu and Vayssade (1991). On each box, the central red mark indicates the median. The bottom and top edges of the box indicate the 25^{th} and 75^{th} percentiles respectively. The whiskers extend to the most extreme data points not considered outliers, and outliers are plotted individually as '+' (outliers are values 1.5 times greater than the interquartile range). The green dashed line represents the mean roughness value of all profiles for that rock type.

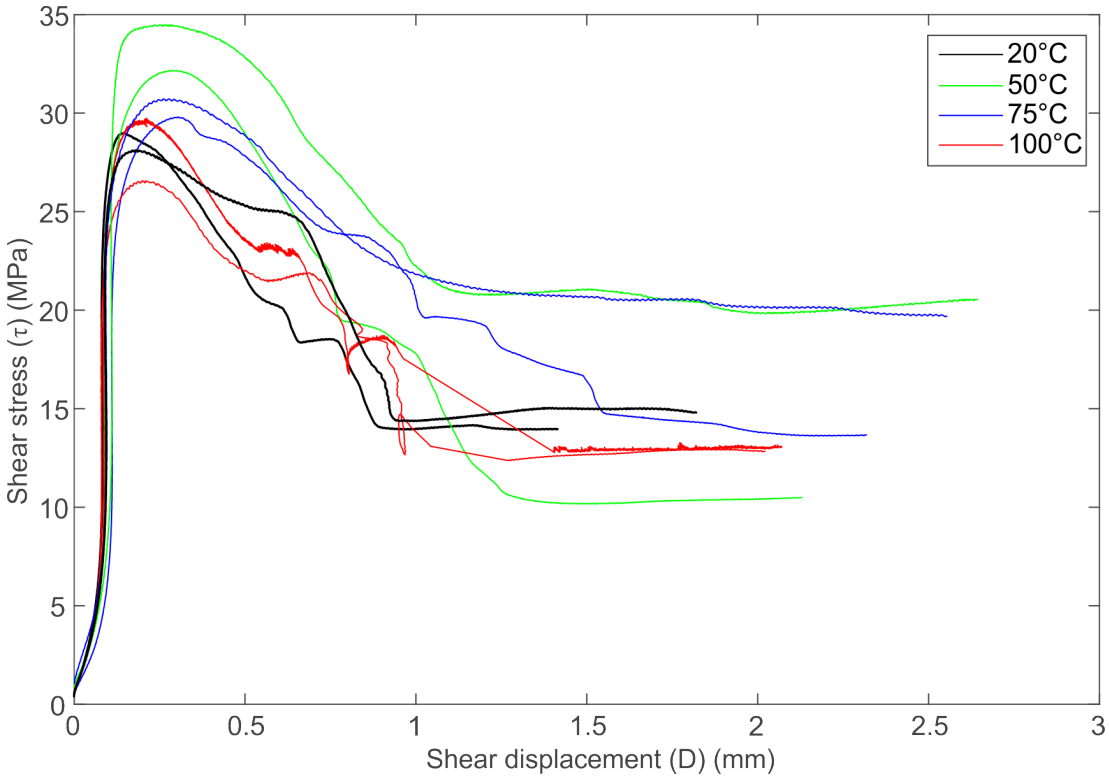

Figure 5.15: Shear stress vs. shear displacement data for thermo-mechanical triaxial tests on discontinuous specimens of Thornhill Rock (Batch 4), carried out at 5 MPa σ_3 and temperatures of 20 °C, 50 °C, 75 °C and 100 °C.

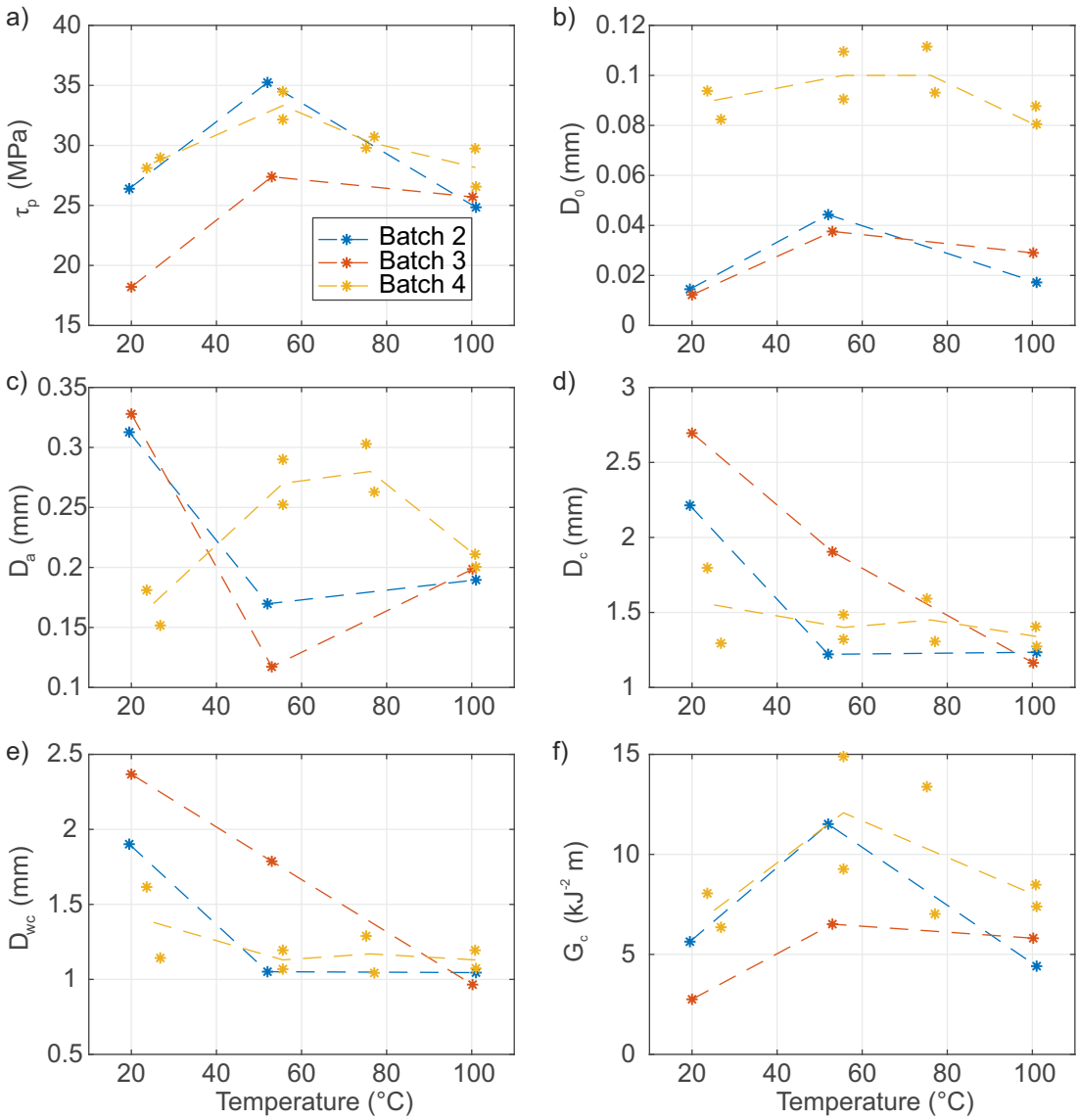

Figure 5.16: Shear parameters (outlined on Fig. 5.13) vs. temperature for elevated temperature triaxial testing on discontinuous specimens of Thornhill Rock. a) Peak shear strength (τ_p). b) Shear displacement at which the shear stress intersects with an extrapolation of the residual shear stress (D_0). c) Shear displacement at peak shear strength (D_a). d) Shear displacement at residual shear strength (D_c). e) Shear displacement between peak and residual shear strengths (D_{wc}). f) Fracture energy (G_c). The dashed line for Batch 4 is plotted as the mean of the two specimens tested at each temperature.

and residual shear strengths ($\Delta\tau_b$) is controlled by the change in peak shear strength. The shear displacement at peak shear strength (D_a) (Fig. 5.16c) shows a decrease from room temperature to 50 °C for Batch 2 and 3, followed by an increase again at 100 °C. However, the opposite trend is observed for Batch 4, with an increase in D_a from room temperature to 50 °C and 75 °C, before a reduction D_a at 100 °C. Both the shear displacement at which residual shear strength is reached (D_c) (Fig. 5.16d), and the shear displacement occurring between peak and residual shear strengths (D_{wc}) (Fig. 5.16e), are seen to reduce with increasing thermal loading. A greater reduction is seen in Batch 2 and 3 than in Batch 4. The fracture energy (G_c) (Fig. 5.16f) required to shear each specimen follows the same trend as the peak shear strength with thermal loading, with an increase in required energy between room temperature and 50 °C, followed by a decrease in required energy with further thermal loading up to 100 °C. Batch 3 and 4 show very similar absolute values for all shear parameters, whilst Batch 4 shows similar trends for all parameters except D_a, it typically shows reduced effects of thermal loading.

Photographs of specimens after testing (Fig. 5.17a) show shear displacement occurred along the discontinuities in most specimens, however, in five specimens the pre-existing discontinuity became locked and a new fracture formed (Fig. 5.17b). This typically occurred in specimens where the discontinuity angle (β) was greater than 30° and the new fracture occurred at a steeper angle. The formation of a new fracture occurred in these cases due to the applied stress field, with the most likely plane of failure occurring at $\beta = 45 - \phi/2$ (Jaeger et al., 2007). It is therefore assumed that the formation of a new fracture occurs due to the stress field and most likely plane of failure. Where this occurred, stresses were resolved and the specimen was analysed for the displacement occurring on this new fracture plane. All sheared discontinuities showed the formation of gouge material and slickensides (Fig. 5.17c).

5.4.3 Midgley Grit

Six thermo-mechanical discontinuity triaxial tests were undertaken from a single batch of Midgley Grit. Full results are tabulated in Table B.8 of Appendix B. Tests were undertaken at 5 MPa confining pressure, and temperatures of 20 °C, 50 °C and 100 °C.

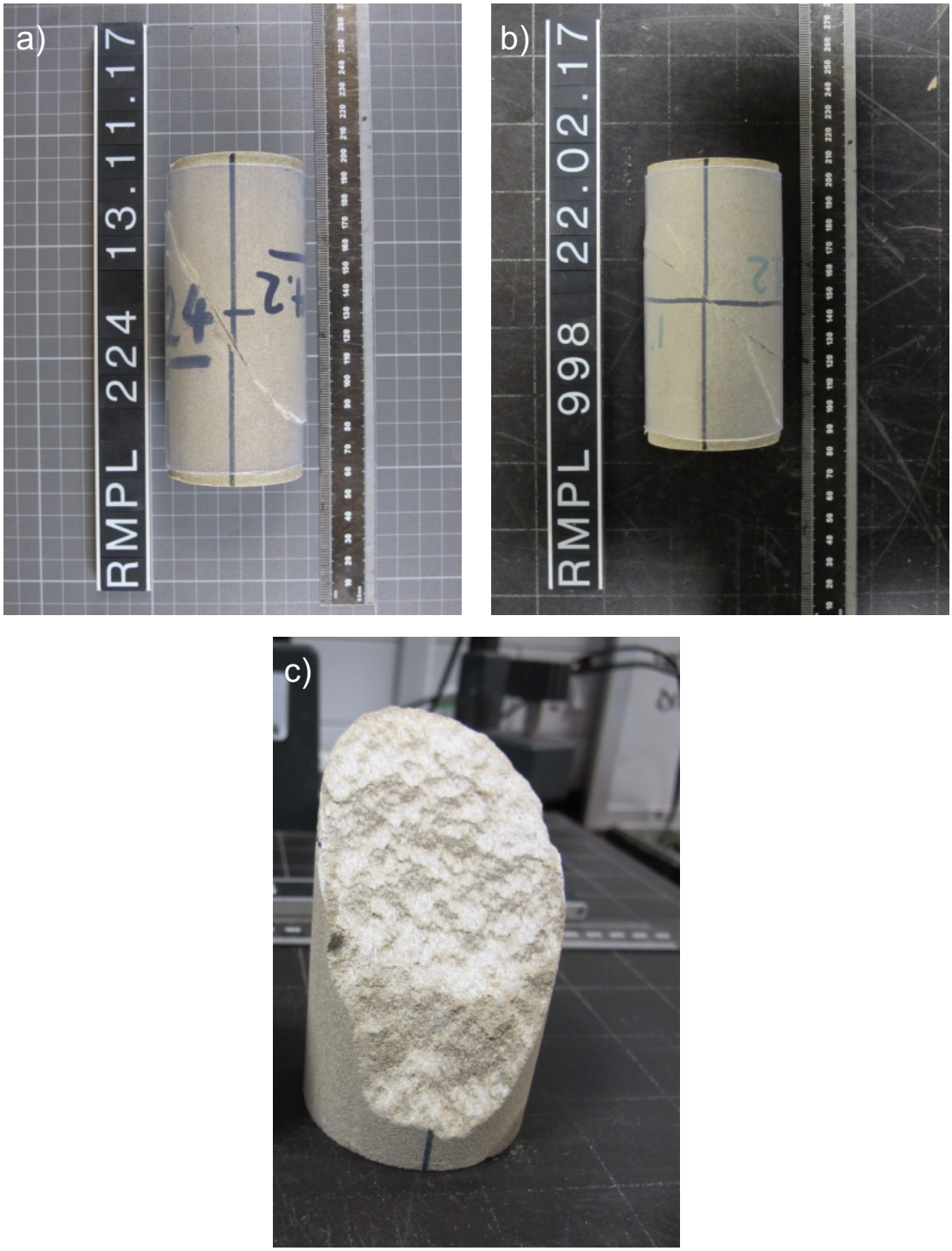

Figure 5.17: Photographs of discontinuous specimens of Thornhill Rock after thermo-mechanical triaxial testing. a) A specimen that sheared along the pre-existing discontinuity. (Specimen # 224, Batch 3, tested at 5 MPa σ_3 and 50 °C). b) A specimen that sheared along a newly formed higher angle fracture rather than the pre-existing discontinuity (Specimen # 998, Batch 1, tested at 5 MPa σ_3 and 50 °C). c) Gouge material and slickensides formed on the discontinuity surface of a sheared specimen (Specimen # 233, Batch 2, tested at 5 MPa σ_3 and 20 °C).

Laser profilometry was again undertaken on each discontinuity prior to testing to allow roughness quantification. Fig. 5.14b shows the *JRC* values for all discontinuous specimens of Midgley Grit. Both batches show similar roughness, with mean *JRC* values between 16 and 18.

Different shear parameters are plotted against temperature in Fig. 5.18. An increase in mean peak shear strength (τ_p) is observed between room temperature and 50 °C for the two specimens (Fig. 5.18a), although the spread in the data is large. With further thermal loading to 100 °C, a considerable reduction in peak shear strength is observed. Again, little change is observed in residual shear strength (τ_r) with thermal loading. The shear displacement extrapolated back from the point at which residual shear strength is reached (D_0) displays the same trend (Fig. 5.18b), with an initial increase in displacement with thermal loading from room temperature to 50 °C, followed by a reduction in displacement with increasing thermal loading to 100 °C. The mean shear displacement required to reach peak shear strength (D_a) for the two tests undertaken at each temperature increases with thermal loading from room temperature to 100 °C (Fig. 5.18c), however, the range in the data is large, producing large uncertainty (D_a at 50 °C: mean = 0.278 mm, s = 0.092 mm). As with the Thornhill Rock, the shear displacement at which residual shear strength is reached (D_c) decreases with thermal loading from room temperature to 100 °C (Fig. 5.18d). Shear displacement at D_c is an order of magnitude greater than at D_a. This therefore controls the trend for the amount of shear displacement occurring between the peak and residual shear strengths (D_{wc}), which also decreases with thermal loading from room temperature to 100 °C (Fig. 5.18e). The mean fracture energy required to initiate and reach residual shear strength shows a slight decrease with increasing thermal loading from room temperature to 100 °C (Fig. 5.18f). Again there is large uncertainty between the results of the two specimens tested at both 20 °C and 100 °C.

As with specimens of Thornhill Rock, the majority of discontinuous Midgley Grit specimens sheared along the pre-existing discontinuity. However, in some specimens the pre-existing discontinuity became locked and a new fracture formed. This either occurred where the pre-existing discontinuity was at a relatively low angle ($\beta > 30°$), with the new fracture forming much steeper, or occurred where the existing discontinuity was particularly rough, with new fractures propagating linearly from the original

discontinuity, increasing the planarity. Where new fractures formed, stresses were resolved on to this new fracture plane. All sheared specimens of Midgley Grit formed gouge material and slickensides on the surfaces of the discontinuities.

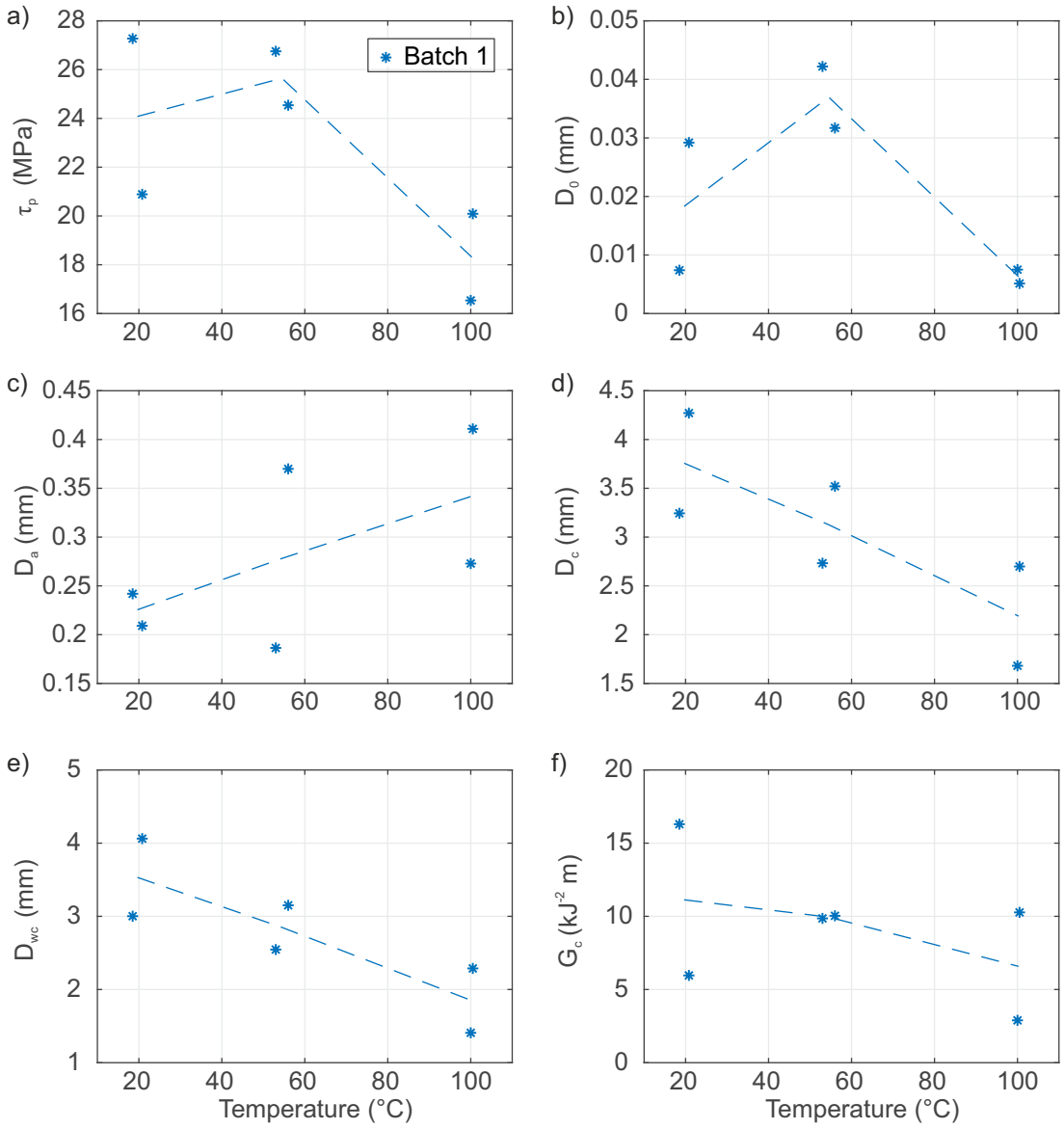

Figure 5.18: Shear parameters (outlined on Fig. 5.13) vs. temperature for elevated temperature triaxial testing on discontinuous specimens of Midgley Grit. a) Peak shear strength (τ_p). b) Shear displacement at which the shear stress intersects with an extrapolation of the residual shear stress (D_0). c) Shear displacement at peak shear strength (D_a). d) Shear displacement at residual shear strength (D_c). e) Shear displacement between peak and residual shear strengths (D_{wc}). f) Fracture energy (G_c). The dashed line is plotted as the mean of the two specimens tested at each temperature.

5.4.4 Roughness evolution

All discontinuous specimens were scanned with a laser profilometer prior to testing, allowing quantification of the surface topography (Fig. 5.14). All specimens that did not suffer any oil ingress during unloading and specimen removal were also laser profiled after shearing. It was not possible to re-profile specimens with oil ingress due to the mineral oil affecting the laser reflectance. For all specimens of both rock types, a reduction in roughness is observed after shearing. This is expected due to the shearing of asperities on the discontinuity surface, and is corroborated by the formation of slickensides and gouge material on the discontinuity surfaces (Fig. 5.17c). Specimens of Thornhill Rock saw a mean reduction in *JRC* of 2.2, and specimens of Midgley Grit saw a mean reduction in *JRC* of 2.4. Although the greater grain size of the Midgley Grit results in a greater initial natural discontinuity roughness, shearing to residual shear strength does not result in a greater reduction in discontinuity roughness. No correlation was found in either lithology between the degree of reduction in discontinuity roughness and the temperature of testing (Fig. 5.20). This suggests the thermal loading only affects the initial interlocking of the discontinuity surfaces and strength of the intact material, and once shearing is initiated, the thermal loading does not affect the frictional properties of the asperities on the discontinuity surfaces.

In addition to comparing the quantified roughness, a comparison of the laser profilometry point cloud data was undertaken for two specimens of each rock type. The open source free software CloudCompare v2.9 (EDF, 2011) was used to first align and then compute differences between the discontinuity surfaces before and after shearing. An iterative closest point (ICP) method was used to minimise the differences in distance between the two surfaces. The Multiscale Model to Model Cloud Comparison (M3C2) technique (Lague et al., 2013) was then used to compute the local distance between the two point clouds along the normal surface direction, allowing tracking of the 3D variations in surface orientation.

Aligning the two point clouds using the ICP method relies on having reference points available in the point cloud, or in this case, unchanged areas of the surface. As the whole surface has been sheared, this is extremely difficult and introduces some uncertainty in the alignment. There is potential for disaggregation to have occurred to parts

of the sheared surface during the unloading of the specimen after testing and transportation for laser profilometry. However, differences in the discontinuity surfaces before and after shearing are still evident. Specimen #753 is representative of all specimens for which M3C2 analysis was undertaken and is presented in Fig. 5.19. The tip of the discontinuity broke off during shearing (blue area at right edge of specimen), but otherwise, small changes in roughness can be seen across the specimen. Various areas that were previously high points on the surface (greens areas on Fig. 5.19) have had material removed to leave topographical lows in the M3C2 surface, and these correlate with eroded and slickensided areas when examining the specimen. Typically, the topographical lows are succeeded further down-shear by topographically high areas (red areas on Fig. 5.19), correlating to the deposition of gouge material.

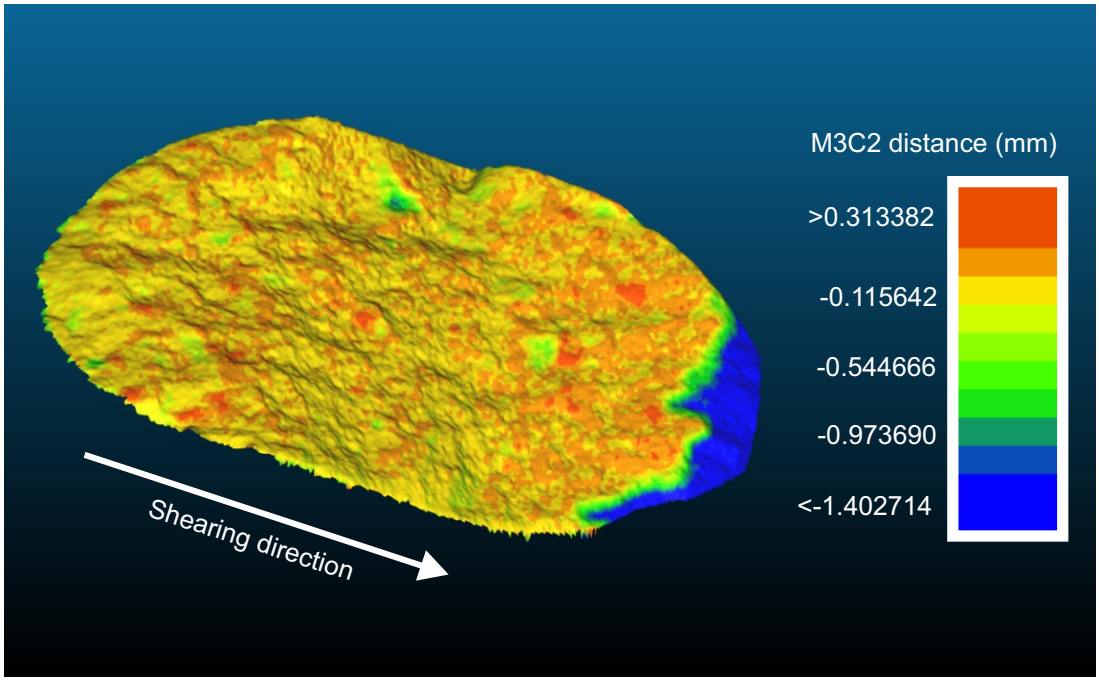

Figure 5.19: Multiscale Model to Model Cloud Comparison (M3C2) of laser profilometry point cloud data from Specimen #753 before and after triaxial shear experiment undertaken at 5 MPa σ_3 and 75 °C.

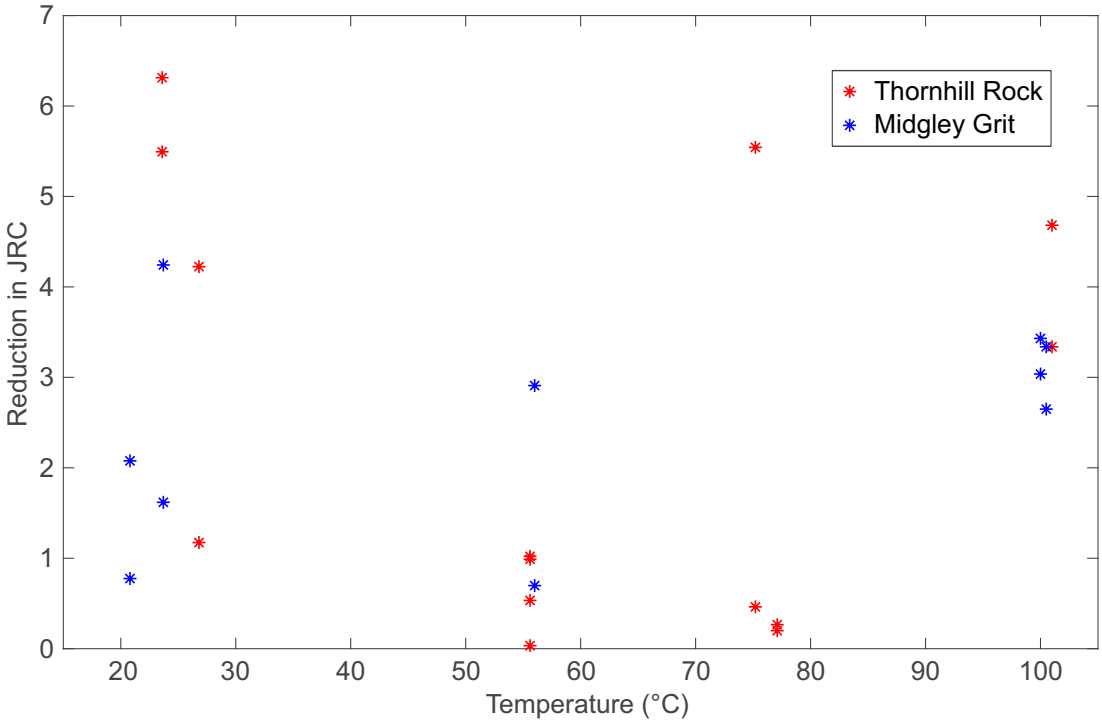

Figure 5.20: The difference between Joint Roughness Coefficient (JRC) values for discontinuous specimens before and after thermo-mechanical triaxial shear experiments. Roughness data was obtained as point cloud data from laser profilometry, analysed statistically as 2D profiles parallel to the shearing direction, and correlated from Z_2 to JRC using the relationship proposed by Yu and Vayssade (1991).

5.4.5 Discussion

Both lithologies show an increase in peak shear strength with thermal loading from room temperature to 50 °C and show a reduction in peak shear strength with continuing thermal loading to 100 °C. This differs from the intact specimens of both lithologies, which show a reduction in peak strength with all thermal loading from room temperature, that is interpreted to occur due to thermal micro-cracking induced by heterogeneous mineralogical thermal expansion during thermal loading. Although the surfaces of the discontinuities induced into specimens prior to testing were induced by tensile splitting, and matching surfaces were placed back together during specimen preparation for the start of the test, there will be an inevitable degree of mismatch at the micro-scale. The increase in peak shear strength of discontinuous specimens with thermal loading from room temperature to 50 °C suggests that the thermal expansion of the specimen up to 50 °C causes thermal closure of the discontinuity. This reduces the degree of mismatch, creates better interlocking of the discontinuity surfaces and increases the shear strength (Fig. 5.22). Thermal micro-cracking of the intact rock surrounding the discontinuity due to heterogeneous mineral expansion may still occur, but may be reduced due to expansion into and closure of the discontinuity being able to occur.

The absolute increase in peak shear strength varies between lithologies and batches, and is likely to be dependent on the exact roughness topography and amount of thermal closure able to occur on each individual discontinuity. With thermal loading above 50 °C to 75 °C and 100 °C, a reduction in peak shear strength is observed in both lithologies. This reduction in strength is greater in the Midgley Grit than the Thornhill Rock, which is the opposite trend to testing of intact specimens, where the Thornhill Rock exhibited greater thermal expansion and hence greater thermally induced micro-cracking. It can be postulated that this shear strength reduction occurs with increased thermal loading due to maximum thermal closure occurring on the discontinuity at some point between 50 °C and 75 °C, with additional thermal loading then inducing thermal micro-cracking both in the intact material, as well as at asperities on the discontinuity, causing a strength reduction, as is observed with intact specimens. For this strength reduction to be greater in the Midgley Grit than the Thornhill Rock, maximum thermal closure would have to be achieved at a lower temperature, which

could occur due to the increased discontinuity roughness. Changes in the residual shear strength are negligible for both rock types (Fig. 5.15), regardless of the thermal loading (Fig. 5.21), which further substantiates the suggestion that thermal loading only affects the initial interlocking of the discontinuity surfaces and strength of the intact material. Once shearing is initiated, the thermal loading does not affect the frictional properties of the asperities on the discontinuity surfaces, meaning there is no correlation between thermal loading and reduction in *JRC* (Fig. 5.20).

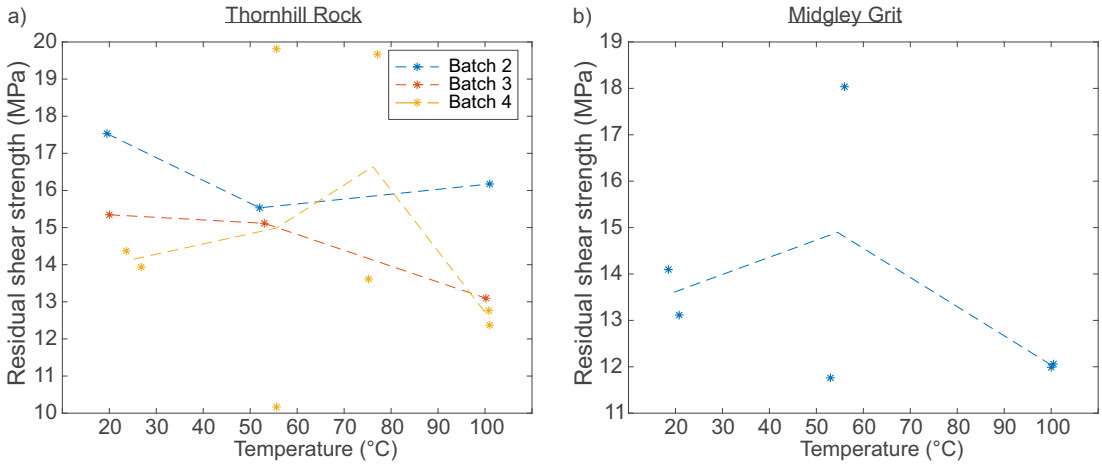

Figure 5.21: a) Residual shear strength vs. temperature for elevated temperature triaxial testing on discontinuous specimens of Thornhill Rock. b) Residual shear strength vs. temperature for elevated temperature triaxial testing on discontinuous specimens of Midgley Grit.

The shear displacement at which the shear stress intersects with an extrapolation of τ_r (D_0) directly correlates with the trends for peak shear strength with thermal loading. D_0 of Batch 4 for the Thornhill Rock is significantly higher than the other two batches, even though the roughness of the discontinuities is very similar and no difference was observed between the linear thermal expansion coefficients of the batches in intact testing. The peak strength of Batch 4 is, however, known to be slightly higher than other batches when tested as intact specimens, and XRD analysis shows the batch to have a lower quartz content. With the aforementioned exception of Batch 4 of the Thornhill Rock, the values of D_0 for the Thornhill Rock and the Midgley Grit are very similar, suggesting that the differences in grain size and discontinuity roughness have negligible effects.

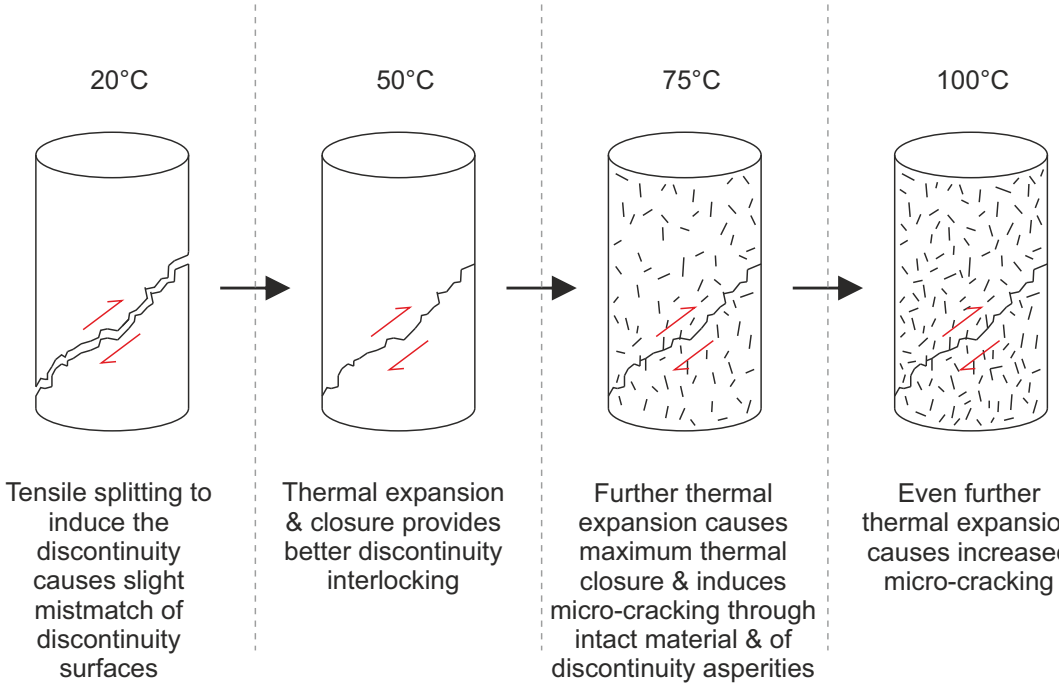

Figure 5.22: Schematic diagram of proposed thermo-mechanical behaviour of discontinuous specimens of Thornhill Rock and Midgley Grit.

The fracture energy (G_c) required to initiate shear, reach peak shear stress and shear until residual shear strength is obtained also correlates with the peak shear strength for the Thornhill Rock, with greater fracture energy required to shear specimens with a higher shear strength. Comparing peak shear strength to required fracture energy, the coefficients of determination (R^2) for Batch 2 and Batch 3 are 0.99 and 1.00 respectively. However, the poor correlation for Batch 4 ($R^2 = 0.17$) brings the R^2 for all batches down to 0.57. The fracture energy with thermal loading does not follow the same trend for the Midgley Grit specimens, but there is large scatter, and therefore large uncertainty in the fracture energies obtained from testing on the Midgley Grit.

The displacement required to reach residual shear strength (D_c), and the displacement occurring between peak and residual shear strength (D_{wc}), both decrease with increasing thermal loading for both lithologies. It is expected that D_c and D_{wc} would reduce with decreasing peak shear strength at 75 and 100 °C, as thermally induced micro-cracking within the specimen and on the discontinuity surface cause reduced strength of the asperities on the discontinuity surface, and less shear displacement is required to reach the residual shear strength. It might also be expected that D_c and D_{wc} should initially increase from room temperature to 50 °C with the increase in peak shear strength, but this is not the case and the inverse is actually observed. It can be postulated that the thermal closure of the discontinuity causes this reduction in the required shear displacement as is observed in D_a of Batch 2 and 3 of the Thornhill Rock.

The thermo-mechanical behaviour of all tested specimens of discontinuous Thornhill Rock and Midgley Grit suggest that maximum thermal closure of the discontinuities occur at between 50 °C and 75 °C. Whilst the Thornhill Rock and Midgley Grit are similar mineralogically, the increased grain size produces increased discontinuity roughness. Due to the more limited testing undertaken on the Midgley Grit, it is hard to deduce whether this increased roughness affects the temperature at which maximum thermal closure occurs, but it might be expected that the temperature at which maximum closure occurs will depend on the discontinuity roughness, and thermal expansion coefficients of the minerals. The degree of strength reduction thereafter is also likely to be mineralogy dependent, controlled by the mineral heterogeneity and hence the heterogeneity of thermal expansion as well as the strength of grain contacts.

5.5 Multi-stage temperature testing

As previously discussed, because it was not possible to create a synthetic lithology that was mechanically representative of a lower strength sedimentary lithology, every thermo-mechanical shear experiment on a discontinuous specimens of rock has a different discontinuity roughness, adding uncertainty to the fundamental thermo-mechanical behaviour. Multi-stage temperature testing was therefore undertaken on two discontinuous specimens of Thornhill Rock to allow the effects of three different thermal loads to be examined on a single discontinuity surface. The two multi-stage temperature methods used differ in the mechanical loading and deformation control applied during thermal loading, simulating differing boundary conditions in different geological scenarios. The methods, results, and effects of the differing mechanical loading during thermal loading are presented and discussed in this section.

5.5.1 Multi-stage temperature test methods

5.5.1.1 Method one - constant strain

An initial axial pre-load of 2.3 kN (1 MPa) was applied to ensure a stable contact and alignment of the platens. The confining pressure vessel was then closed and filled with mineral oil confining fluid. The axial pre-load was maintained whilst the confining pressure was applied at 1.0 MPa min^{-1} to 5.0 MPa. Once stable, axial loading was initiated in constant axial strain rate control at a rate of $5.0 \times 10^{-6}\,\text{s}^{-1}$. Deformation continued beyond peak stress until residual strength was reached (A to B on Fig. 5.23a).

At this point the specimen was held in axial strain control (i.e. the servo-control adjusted the axial load in order to maintain constant displacement on the axial extensometers). Whilst held in axial strain control, the rig was heated at 1.5 °C min^{-1} to 50 °C (B to C on Fig. 5.23a). The cascade temperature control overshot to 55 °C before stabilising. The specimen was then left for approximately 1 hour allowing thermal equilibrium to be reached throughout the confining fluid and the specimen. Once thermal equilibrium was reached, deformation continued at the same constant axial strain rate (C to D on Fig. 5.23).

The specimen was then held in axial strain control again whilst the rig was heated at 1.5 °C min^{-1} to 100 °C (D to E on Fig. 5.23a). After being left for a further hour to reach thermal equilibrium, the specimen was then deformed again as described above (E to F on Fig. 5.23a). The specimen was then unloaded before being left to cool passively. The axial load (differential), axial stress, axial load actuator displacement, confining pressure, confining pressure actuator displacement, axial strain, circumferential strain and temperature were monitored for the duration of the test at sampling rates of 1 s and 500 N.

5.5.1.2 Method two - unloading and constant stress

The pre-load condition setup was identical to the procedure outlined in the first paragraph of § 5.5.1.1. Once residual strength was reached (B on Fig. 5.23b), the specimen was unloaded at 0.5 kN s^{-1} to the pre-load conditions of 5 MPa confining pressure and 1 MPa differential axial stress (B to C on Fig. 5.23b). These loads were maintained constant and the specimen was free to deform whilst the rig was heated at 1.5 °C min^{-1} to 50 °C. The cascade temperature control overshot to 55 °C before stabilizing. The specimen was then left under these conditions for approximately 1 hour allowing thermal equilibrium to be reached. The specimen was then loaded again in constant axial strain rate control at a rate of 5.0×10^{-6} s^{-1} for 1% axial strain (D to E on Fig. 5.23b). The specimen was then unloaded at 0.5 kN s^{-1} and pre-loads maintained whilst the rig was heated at 1.5 °C min^{-1} to 100 °C (E to G on Fig. 5.23b). After being left for a further hour to reach thermal equilibrium, the specimen was re-loaded in constant axial strain rate control at a rate of 5.0×10^{-6} s^{-1} for a final 1% of axial strain (G to H on Fig. 5.23b). The specimen was then unloaded before being left to cool passively. The same parameters were recorded for the duration of the test at the same sampling rates as in method one (§ 5.5.1.1).

5.5.2 Results & discussion

The two methods differ from beyond residual shear strength being obtained (B on Fig. 5.23a and 5.23b), and the specimens are clearly affected by the differing methods.

In method one, the specimen was held in constant axial strain control during heating.

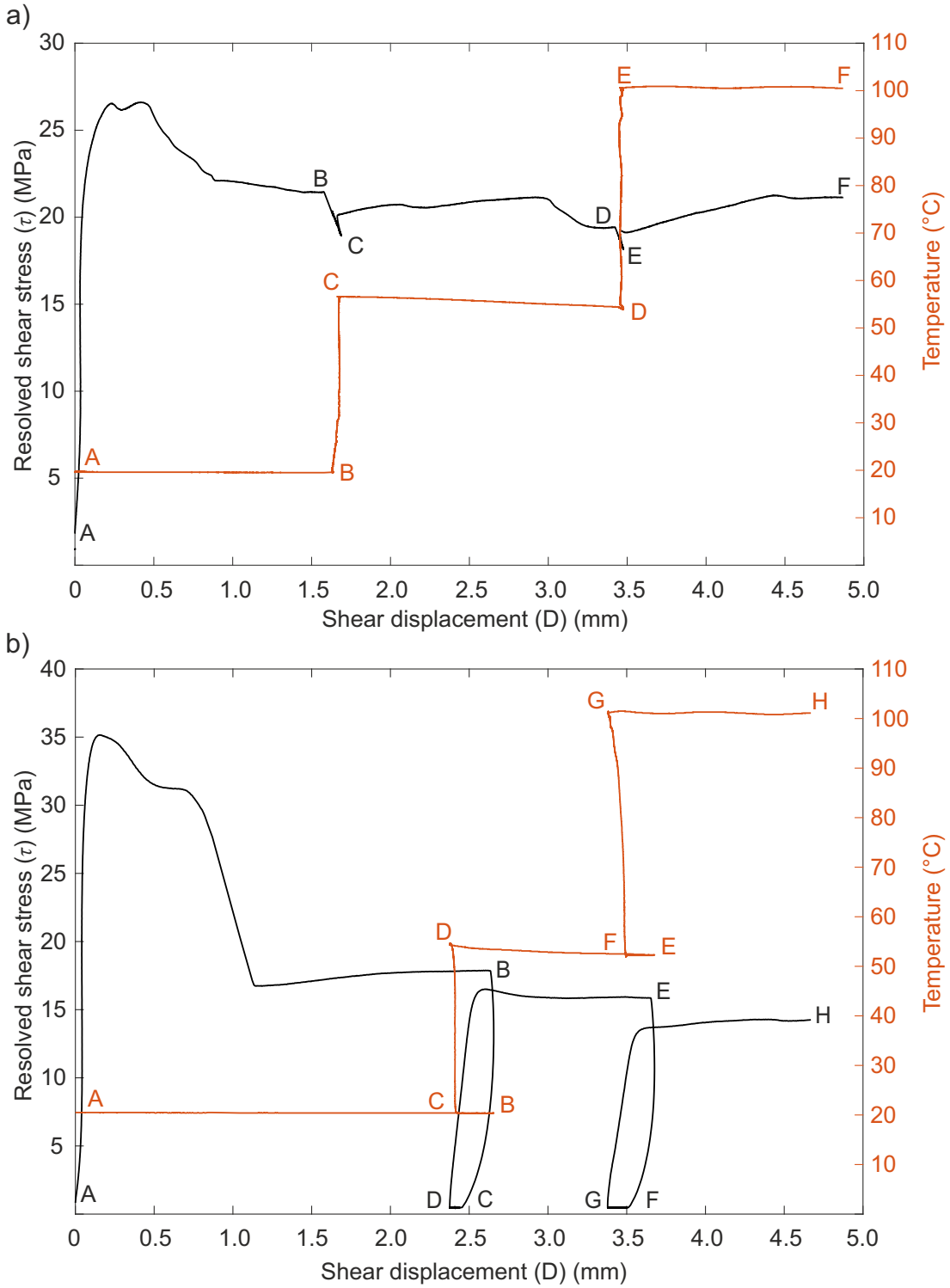

Figure 5.23: a) Plot of resolved shear stress (τ) against shear displacement (D) for method one, with the specimen held in constant axial strain during heating. b) Plot of resolved shear stress (τ) against the shear displacement (D) for method two, with the specimen unloaded to 5 MPa confining pressure, and 1 MPa axial (differential) stress during heating. Letters refer to the different stages of testing as outlined in §'s 5.5.1.1 & 5.5.1.2 and referred to throughout § 5.5.

It was therefore unable to deform in an axial orientation, as the servo-control of the triaxial rig counteracted the thermal expansion of the specimen by adjusting the axial load, and hence also the resolved shear stress (B to C on Fig. 5.23a). In method two, the specimen was unloaded upon reaching residual shear strength to pre-load conditions of 5 MPa confining pressure and 1 MPa axial (differential) stress (C on Fig. 5.23b). It was then free to deform under constant load conditions during heating (C to D on Fig. 5.23b). During heating from 20 °C to 55 °C, axial and circumferential dilation occurred due to thermal expansion of the specimen (Fig. 5.24d to 5.24f).

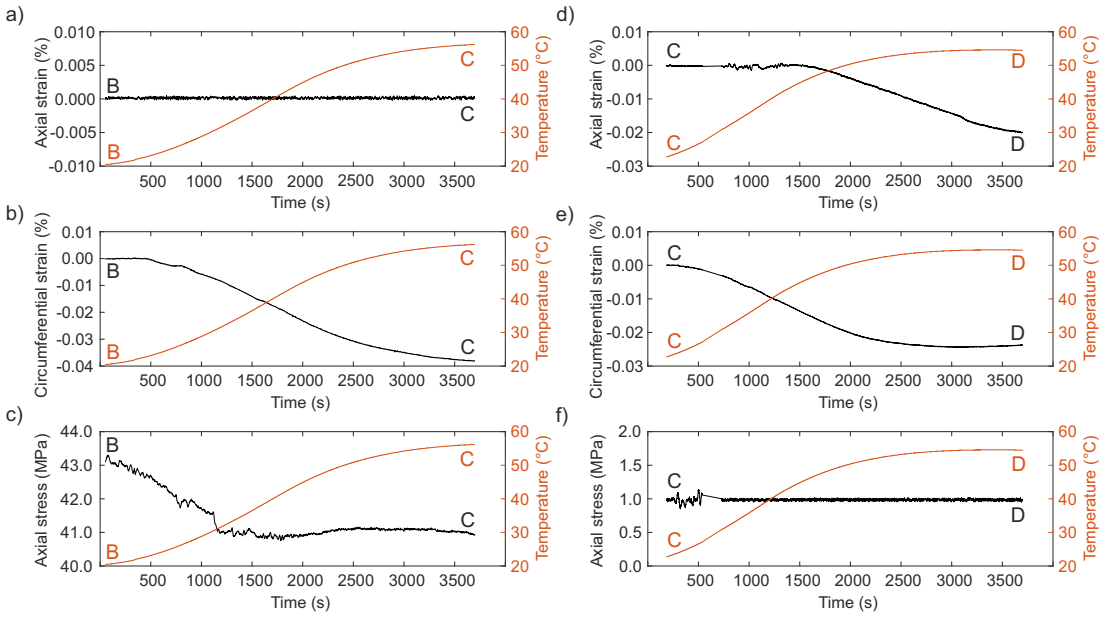

Figure 5.24: a) to c) Plots of axial strain, circumferential strain and axial stress during the heating phase of method one from 20 °C to 55 °C. Showing constant axial strain, with circumferential thermal expansion, and a drop in axial stress due to the servo-control counteracting the constant axial strain. d) to f). Plots of axial strain, circumferential strain and axial stress during the heating phase of method two from 20 °C to 55 °C. Showing axial and circumferential thermal expansion under constant preload conditions. Letters refer to different stages of testing as outlined on Fig. 5.23.

Consequently, when shearing was initiated again in method one at 55 °C, the specimen gradually strengthened with increasing shear displacement, returning back to the previous residual resolved shear stress value of 21 MPa (C to D on Fig. 5.23a). A small drop in shear stress at 3 mm of shear displacement is attributed to the roughness of the discontinuity, with an area of asperities being sheared. In comparison, when the

specimen in method two was reloaded at 55 °C, the discontinuity sheared consistently for 1 mm at a shear stress 2 MPa lower than the residual obtained at 20 °C (E on Fig. 5.23b) due to thermal micro-cracking causing a permanent reduction in shear strength.

After heating to 100 °C, the specimen in method one displays similar behaviour as at 55 °C, strengthening from the stress drop that occurred during heating back to 21 MPa with increasing shear displacement (E to F on Fig. 5.23a). In contrast, after unloading and heating the specimen to 100 °C in method two (F to G on Fig. 5.23b), additional thermal expansion and microstructural damage caused the discontinuity to continue shearing at a shear stress further reduced by 1.8 MPa (H on Fig. 5.23b).

In method one, a specimen with a pre-existing discontinuity was sheared in a multi-stage temperature test with constant axial strain held under load during heating between 20 °C and 100 °C. This heating displays little impact on the residual shear behaviour of the discontinuity. Conversely, in method two, a discontinuity is unloaded and allowed to deform during heating between 20 °C and 100 °C. This allows further thermal micro-cracking to occur, causing a reduction in residual shear strength of the discontinuity upon reloading. This is contrary to discussion in § 5.4.5 in which thermal loading did not affect the residual shear strength, but shows that the stress conditions at the time of thermal loading are key.

5.6 Chapter summary

In this chapter, mechanical characterisation testing of the Thornhill Rock and Midgley Grit was undertaken to provide baseline properties, allowing comparison with thermo-mechanical properties, and for use as input properties for numerical modelling (Chapter 6). In addition, thermo-mechanical triaxial testing was undertaken on intact specimens of Thornhill Rock and Midgley Grit. Both lithologies showed a reduction in peak strength with increased thermal loading, attributed to thermally induced micro-cracking. However, the Thornhill Rock showed a greater strength reduction with thermal loading than the Midgley Grit.

Thermo-mechanical triaxial testing was also undertaken on discontinuous specimens of Thornhill Rock and Midgley Grit, and a comparison made with the intact behaviour. Rather than a reduction in strength with increasing thermal loading, discontinuous specimens of both lithologies instead first showed an increase in shear strength under thermal loading to 50 °C, followed by a reduction in shear strength thereafter. This is interpreted as thermal discontinuity closure occurring initially, causing increased peak shear strength. At some point between 50 °C and 75 °C, maximum thermal closure is reached, beyond which further thermal expansion causes thermally induced micro-cracking of the intact material and asperities on the discontinuity surface, thus reducing the shear strength. Laser profilometry data from discontinuities before and after shear testing was assessed. A similar reduction in JRC is seen in both rock types, with the formation of slickensides and gouge material, but no correlation is found between thermal loading and evolution of the discontinuity roughness.

Finally, multi-stage temperature triaxial shear experiments were undertaken, which showed the potential for different thermal effects dependent on the mechanical conditions during thermal loading. In engineering scenarios, where the rock mass is excavated prior to the introduction of an anthropogenic heat source, stresses are removed by the excavation prior to thermal loading (akin to method two), potentially allowing thermal micro-cracking to occur and reduced residual shear strength.

Chapter 6

Thermo-mechanical numerical modelling

6.1 Introduction

Following laboratory thermo-mechanical triaxial testing on intact and discontinuous rock specimens in Chapter 5, Universal Distinct Element Code (UDEC) v6.0 (Itasca, 2014a) has been used to build Discrete Element Method (DEM) Grain Based Models (GBM) representing the micro-structure of the laboratory specimens. The aim of these models is to allow further investigation of the fundamental mechanisms of progressive damage under thermo-mechanical loads. The model setup and results are presented in this chapter and discussed with comparison to the thermo-mechanical behaviour observed in laboratory experiments.

6.2 UDEC GBM

The discrete element code UDEC allows 2D plane-strain and plane-stress analysis. Conventionally in UDEC, rock failure is captured either through plastic yielding of the rock matrix, or through sliding on explicitly modelled discontinuities (Lisjak et al., 2014). This means that the formation of fractures through intact rock cannot be simulated. However, Lorig and Cundall (1989) introduced Voronoi tessellation to UDEC. Voronoi tessellation is formed through the generation of a number of random points or "seeds" on a plane. The Voronoi polygons are then generated by forming boundaries bisecting each seed so that the distance to each seed is less than or equal to the distance to any other seed. The UDEC GBM utilises a Voronoi tessellation of deformable blocks to represent mineral grains, bonded at their contacts to represent the micro-structure of crystalline or granular rock. Fracture damage and development can therefore occur at the blocks boundaries when a stress level at the interface is exceeded either through thermal or mechanical loading (Lisjak et al., 2014). The strength and stiffness of a GBM is governed by the grain contact micro-properties, as well as the grain size and grain size distribution of the Voronoi blocks, with the explicit generation and propagation of both micro-cracks between Voronoi blocks and the accumulation of macro-cracks. When a thermal or mechanical load is applied to the model, a perturbation is induced and a series of mechanical interactions between Voronoi blocks leads to the development and transmission of contact forces, the generation of localised heterogeneous stresses and eventually motion, which causes disturbance to the equilibrium of the system.

The propagation speed of the movement depends on the physical micro-properties of the Voronoi elements within the discrete system. Further details on the equations of motion, conservation of momentum and energy equations, contact detection schemes, block deformability equations, and mechanical damping schemes for the 2D distinct element method utilised in UDEC is outlined in § C.1 of Appendix C (Itasca, 2014b).

In all models in this study, each Voronoi block is treated as an elastic continuum, subdivided into triangular finite difference zones (further details on the block deformability scheme utilised in UDEC is outlined in § C.1.5 of Appendix C). Voronoi contacts obey a linearly elastic-perfectly plastic model, with normal and shear deformability represented by normal (k_n) and shear (k_s) stiffnesses (Fig. 6.1). The shear strength of the Voronoi contacts follow the Mohr-Coulomb criterion. In all simulations, if the induced contact forces exceed the tensile or shear strength of Voronoi contacts, a plasticity flag is set to declare the irreversible plastic state of the contact. Instantaneous softening then occurs with the micro-cohesion (c_m) and micro-tensile strength (σ_{tm}) of the Voronoi contact reduced to zero and the micro-friction angle (ϕ_m) of the Voronoi contact reduced to a residual value. Forces are then redistributed allowing the relocalisation of stresses, which may in turn induce further micro-crack propagation and eventually macroscopic failure. This failure process allows the GBM to capture the progressive failure process of micro-cracking in brittle crystalline and granular lithologies.

6.3 Setup for intact mechanical & thermo-mechanical simulations

In this section, the geometry, boundary conditions, properties and monitoring of different models used in this study are outlined.

Specimens for numerical modelling were generated at the same scale as in the laboratory. The geometry of cylindrical laboratory specimens of 54 × 120 mm for uniaxial and triaxial compression testing were simulated as rectangular specimens in 2D plane strain. Similarly 54 mm diameter circular specimens were generated for indirect tension Brazilian disc testing (Fig. 6.2). Both specimen types were bounded by steel platens top and bottom.

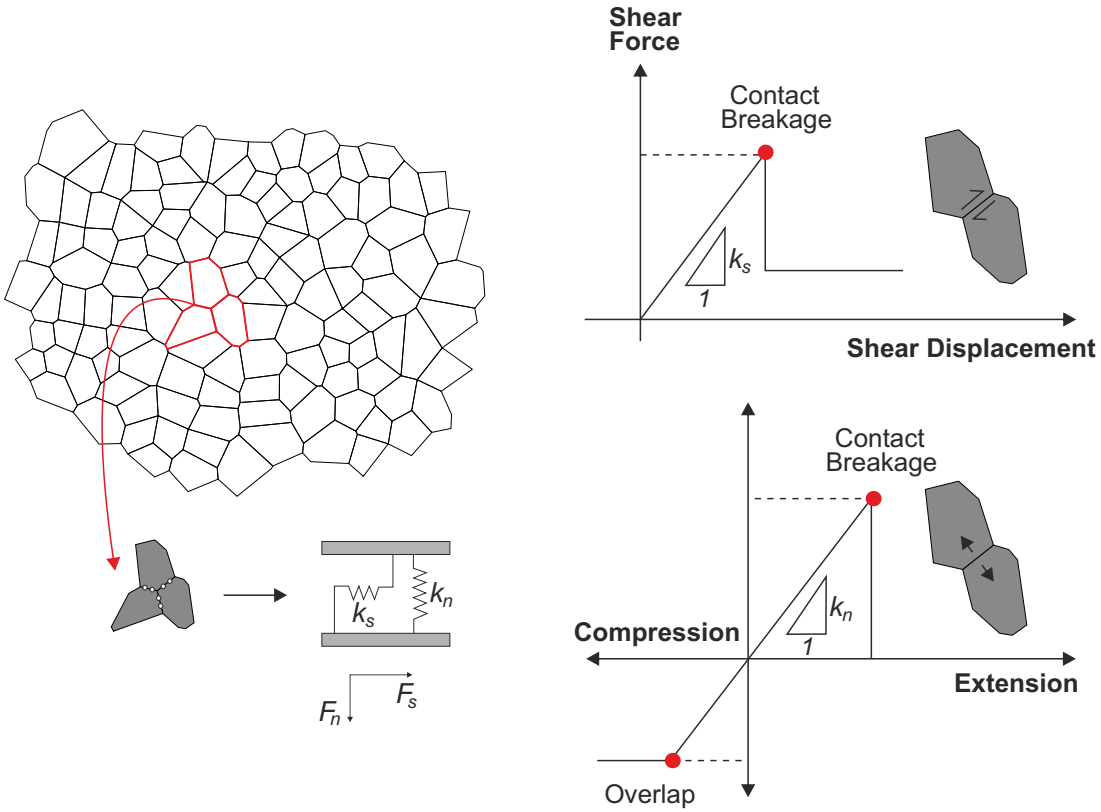

Figure 6.1: Voronoi structure and Mohr-Coulomb constitutive behaviour of the Voronoi contacts in the UDEC GBM. After (Stavrou and Murphy, 2018).

Numerically, 2D plane strain reduces the 3D strain matrix to 2D, this makes the assumption of a 2D geometry of infinite depth, with no strain in the z plane. Plane strain analyses are commonly used in GBM simulations as they allow computational efficiency compared to running 3D simulations. Because simulations in this study are biaxial ($\sigma_2 = \sigma_3$) it has been deemed that 2D plane strain boundary conditions are sufficient to model the problem. However, there are numerous assumptions and limitations that must be recognised. It is not possible to directly correlate volumes and crack densities between simulations and laboratory results, and out of plane strains are neglected, this means that potential displacements occurring due to anisotropic grain properties (mechanical and thermal) are not accounted for, and discontinuities are simplified to lines rather than planes.

Specimens were discretised into Voronoi tessellations with an average grain edge length of 3 mm. Different Voronoi block size and block size distributions are known to result in differing mechanical behaviour, as fractures can only form along contacts between adjacent Voronoi blocks, thus controlling the failure pattern. This phenomenon also results in models with a smaller block size having less effect on the failure pattern. Gao and Stead (2014) found that a 160 mm tall model with a Voronoi block size of 4 mm allowed for representative failure mechanisms of both axial splitting and shear failure. Therefore, despite the grain size in laboratory specimens of Thornhill Rock being in the range of 63 to 250 µm, and the grain size of the Midgley Grit being in the range of 500 to 1000 µm, in this study, a Voronoi block size of 3 mm is utilised for both lithologies. This allows for representative failure mechanisms, whilst maintaining computational efficiency, and also satisfies the recommendation that the specimen diameter in uniaxial compression testing should be at least ten times greater than the size of the largest grain (Ulusay, 2014). The Voronoi tessellation was developed with a relatively uniform grain size distribution to mimic the micro-structural homogeneity in the Thornhill Rock and Midgley Grit.

In uniaxial and triaxial compression testing simulations, the axial stress was measured using a *FISH* (Itasca's in-built scripting language) function at an imaginary crack within the upper platen (Appendix C.3). A grid of history points was created over the central 50 mm of the specimen (to simulate the area over which the axial and circumferential extensometers obtain measurements in the laboratory) and axial and

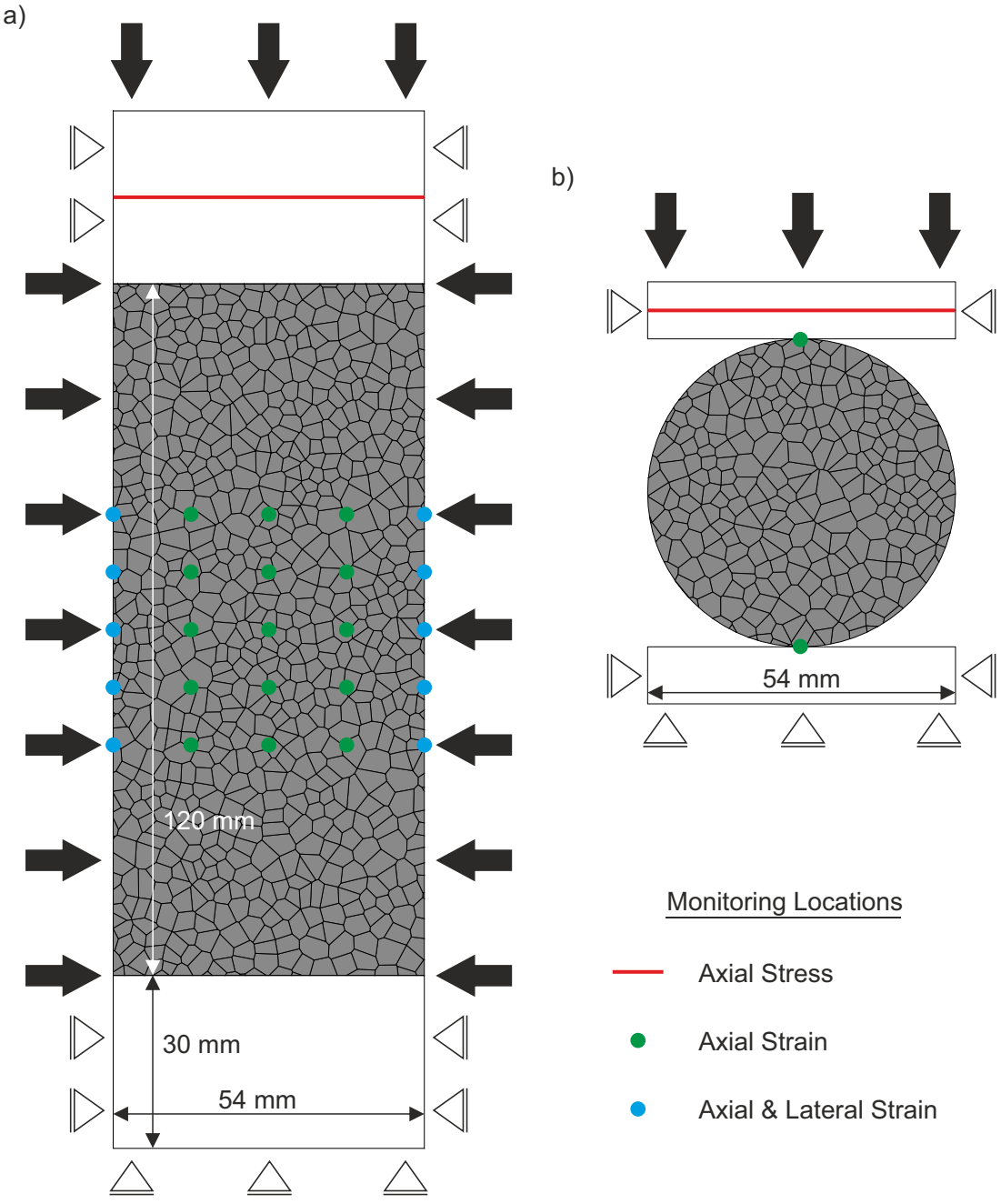

Figure 6.2: Model dimensions, boundary conditions and monitoring locations for numerical simulations. a) Uniaxial and triaxial compression testing simulations. b) Indirect tension Brazilian disc testing simulations.

radial strain measurements were monitored at these points (Fig. 6.2a). In indirect tension Brazilian disc simulations, the axial stress was monitored at an imaginary crack within the upper platen and axial strain was calculated from the differing displacement between two monitoring points located at the top and bottom of the specimen (Fig. 6.2b). In addition, a *FISH* function was written to monitor the accumulation of tensile and shear micro-cracks during loading (Appendix C.4).

In the uniaxial compression tests, no pre-load was applied as is customary in laboratory experiments. The axial loading was applied as a constant velocity of $0.01\,\mathrm{m\,s^{-1}}$ in the y-direction at the upper platen, whilst the lower platen was fixed in both the x and the y-directions. Although this is much faster than the rate that is applied in the laboratory (axial strain rate of $5 \times 10^{-6}\,\mathrm{s^{-1}}$), loading rate sensitivity analyses have shown that simulated strengths converge to consistent values when the loading rate is less than $0.25\,\mathrm{m\,s^{-1}}$ (Mahabadi et al., 2010; Tatone, 2014). In the case of triaxial compression testing, constant axial and confining pressures of equal magnitudes (i.e. hydrostatic stress) were applied at the specimens upper and lateral boundaries, and the models were taken to static equilibrium prior to the initiation of axial loading.

6.4 Mechanical model calibration

The following section presents the UDEC model properties and the approach adopted to calibrate the models to the mechanical behaviour of the Thornhill Rock and Midgley Grit by simulating standard laboratory scale responses.

The micro-parameters controlling the elasticity (micro-Young's modulus (E_m), micro-Poisson's ratio (ν_m), normal stiffness (k_n) and shear stiffness (k_s)) and strength (micro-cohesion (c_m), micro-friction angle (ϕ_m) and tensile strength (σ_{tm})) behaviour of the Voronoi micro-block assembly were estimated using a multi-stage parametric analysis in which the model response was calibrated against the deformability (E, ν) and strength (c, ϕ, σ_t) macro-mechanical properties of the Thornhill Rock and Midgley Grit. The iterative trial and error process approximately followed the procedures outlined by (Christianson et al., 2006; Farahmand and Diederichs, 2015; Gao and Stead, 2014; Kazerani, 2011; Stavrou and Murphy, 2018). A series of unconfined compression tests,

triaxial compression tests and indirect tensile Brazilian disc tests were carried out to calibrate the Voronoi contact and block micro-properties to produce macro-properties representative of the laboratory specimens. As discussed in § 2.7.1, for all models in this study a single set of micro-parameters are calibrated for all contacts and blocks within the model.

Unconfined compression test simulations were run to calibrate the macro-mechanical Young's Modulus (E), Poisson's ratio (ν) and uniaxial compressive strength (UCS). Both E and ν were calculated at 50% of the UCS using Eq.'s 3.7 and 3.8 respectively. The material bulk (K) and shear (G) moduli were also calculated using Eq.'s 5.1 and 5.2 respectively.

In a UDEC Voronoi model, the deformability of the model depends on the micro-deformability of both the Voronoi blocks and the contacts (i.e. normal stiffness (k_n), shear stiffness (k_s), micro-Young's modulus (E_m) and micro-Poisson's ratio (ν_m)). As a starting point for initial calibration, E_m and ν_m of the Voronoi blocks were set to be equal to the desired macro-properties of the rock specimens (i.e. $E_m = E$ and $\nu_m = \nu$) and, for computational speed, the normal stiffness of the contacts was set to a factor of the deformability of the blocks according to Itasca (2014a):

$$5 \leq \frac{K_m + \frac{4}{3}G_m}{bk_n} \leq 10 \tag{6.1}$$

Where K_m and G_m are the bulk and shear strength of the Voronoi blocks, respectively, and b is the average Voronoi block size.

The Poisson's ratio was calibrated by varying the Voronoi contact stiffness ratio (k_n/k_s). Fig. 6.3a shows the mechanical influence of the contact stiffness ratio on the intact rock E, ν and UCS values. With increasing contact stiffness ratio, there is a dramatic increase in the magnitude of the Poisson's ratio but only a small decrease in the magnitudes of the Young's modulus and UCS.

Once the contact stiffness ratio had been set, the Young's modulus was calibrated in three steps. Initially, a series of models were run where the micro-Young's modulus,

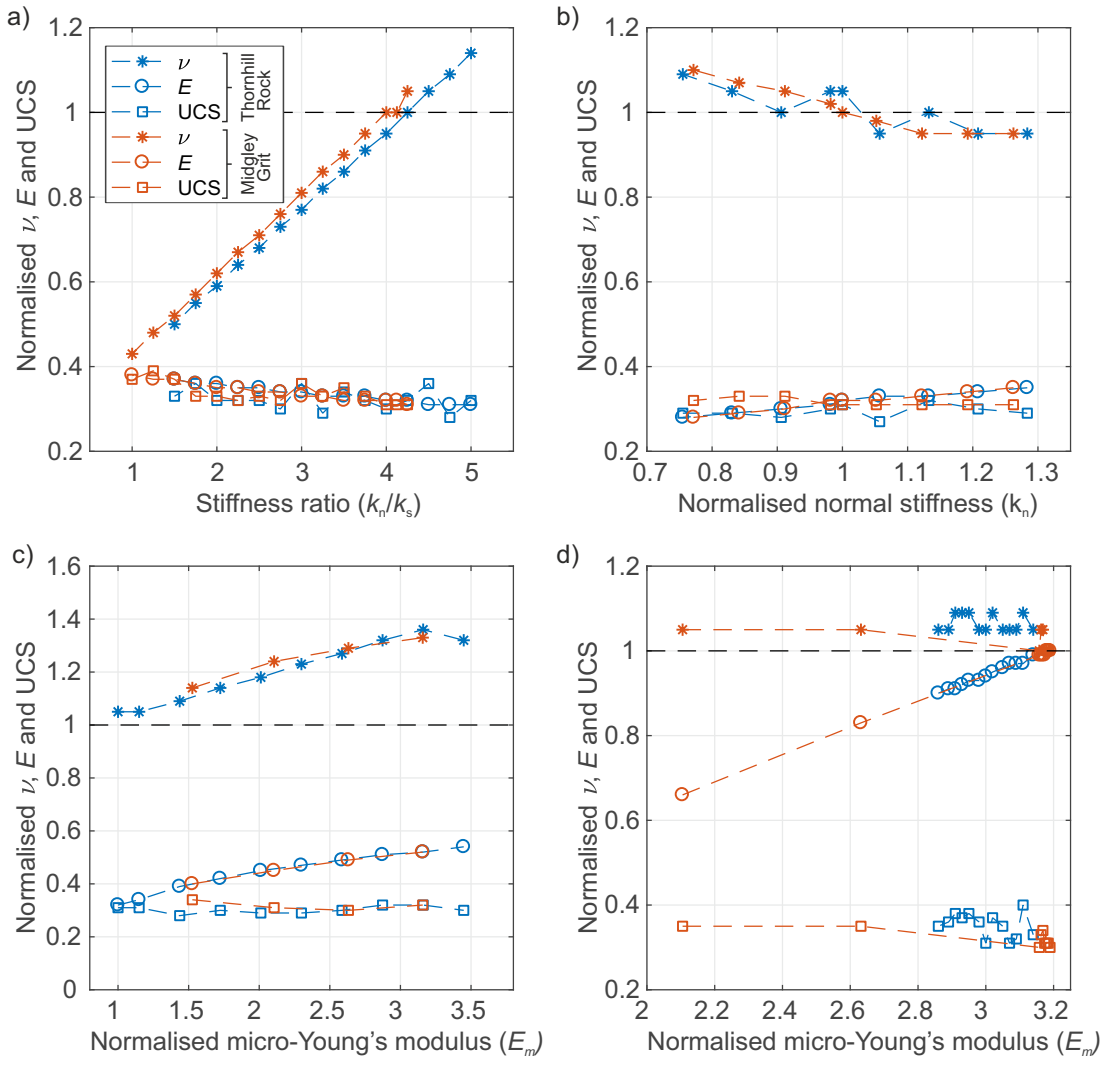

Figure 6.3: Calibration of the micro-parameters controlling elasticity for calibration of the Thornhill Rock (blue) and Midgley Grit (red). a) The output macro-Poisson's ratio (ν), Young's modulus (E) and uniaxial compressive strength (UCS) normalised to the desired macro properties of ν, E and UCS respectively, whilst altering the stiffness ratio of normal stiffness (k_n) to shear stiffness (k_s). b) Output macro ν, E and UCS normalised to the desired macro properties whilst altering k_n and maintaining the micro-Young's modulus (E_m), micro-Poisson's ratio (ν_m) and k_n/k_s constant. k_n is normalised to the initial k_n derived from Eq. 6.1. c) Output macro ν, E and UCS normalised to the desired macro properties whilst varying E_m whilst k_n and k_n/k_s were maintained constant. E_m is normalised to the desired E. d) Output macro ν, E and UCS normalised to the desired macro properties whilst varying k_n and E_m whilst k_n/k_s was maintained constant. E_m is normalised to the desired E.

micro-Poisson's ratio and stiffness ratio were kept constant whilst the normal stiffness was varied (Fig. 6.3b). Again, little change was seen in the Young's modulus or UCS, but a slight decrease was observed in the Poisson's ratio with increasing normal stiffness. Secondly, a series of models were run with varying micro-Young's modulus whilst the normal stiffness and stiffness ratio were maintained constant (Fig. 6.3c). As expected, increasing the micro-Young's modulus increases the Young's modulus, it also increases the Poisson's ratio above the desired values, but little effect is shown on UCS. Finally, due to the coupling and dependency, the normal stiffness and micro-Young's modulus were varied whilst the stiffness ratio was maintained to achieve the final macro elastic parameters of Young's modulus and Poisson's ratio of the specimens (Fig. 6.3d).

Once the micro-parameters controlling the elasticity had been calibrated, the micro-parameters controlling the strength were calibrated (i.e. micro-cohesion (c_m), micro-friction angle (ϕ_m) and micro-tensile strength (σ_{tm})). The tensile strength was calibrated by running a series of indirect tension Brazilian disc tests as is the standard test for measuring the tensile strength of rock (Bieniawski and Hawkes, 1978). The micro-tensile strength was varied whilst maintaining all other micro-elasticity and strength parameters. The normal load recorded in the centre of the upper platen during the indirect tension Brazilian disc test was converted to the peak tensile strength using Eq. 3.1 (where t = 1 in this 2D analysis).

Calibration of the Mohr-Coulomb strength properties (Eq. 2.2), cohesion (c) and friction angle (ϕ), were achieved through a series of triaxial compression tests with confining pressures of 5, 10 and 15 MPa. Firstly, the cohesion was calibrated by altering the Voronoi contact micro-cohesion (c_m). The friction angle was then calibrated by altering the Voronoi contact micro-friction angle (ϕ_m). The generalised Hoek-Brown failure criterion (Eq. 5.3 (Hoek et al., 2002)) was also fitted to the numerical simulation data for comparison with laboratory data. The final micro-properties from the calibration procedure are listed in Table 6.1. A comparison between the desired macro-properties derived from laboratory testing and the final macro-properties output from calibrated numerical simulations is given in Table 6.2. A good agreement is shown between all properties, with the majority of calibrated properties within 1% relative percentage difference of the laboratory derived properties, and all calibrated properties within 5% of the laboratory derived properties, which is less than the sample variability seen in

the laboratory. However, the Voronoi GBMs do not capture the initial poro-elastic behaviour of the laboratory specimens when loading is initiated and existing micro-cracks and pore spaces are closed (Fig. 6.4a). This is due to limitations of the Mohr-Coulomb constitutive contact model used in this study, and the fact that the model assumes 0% porosity. Despite this initial differing behaviour, the linear elastic behaviour of the GBM and laboratory specimens is extremely similar, and the Voronoi GBMs display the formation of conjugate shear planes and axial splitting (Fig. 6.4b) as observed in the laboratory.

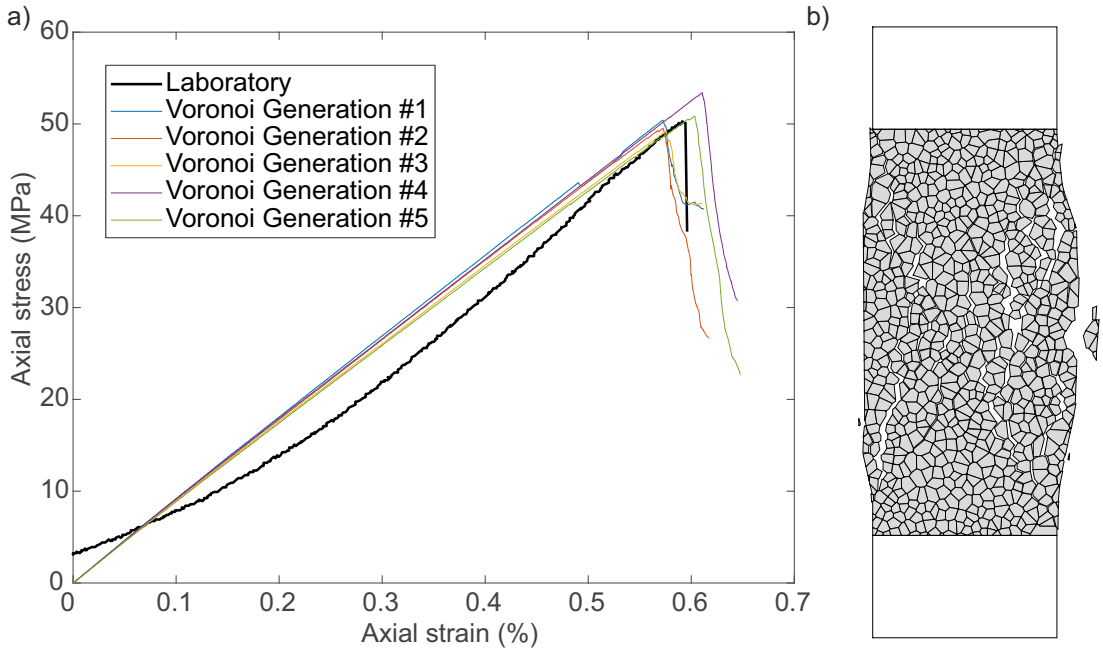

Figure 6.4: a) Axial stress strain data from unconfined compression tests on five different Voronoi generations of UDEC GBM models calibrated to the properties of the Thornhill Rock, compared to a laboratory unconfined compression test on a specimen of Thornhill Rock (Specimen #235). b) UDEC GBM model after an unconfined compression test showing the formation of conjugate shear planes and axial splitting.

Property	Units	Thornhill Rock	Midgley Grit
Elastic Properties of Voronoi Blocks			
Young's modulus (E_m)	GPa	27.90	30.30
Poisson's ratio (ν_m)	-	0.22	0.21
Bulk modulus (K_m)	GPa	16.61	17.41
Shear modulus (G_m)	GPa	11.43	12.52
Elastic Properties of Voronoi Contacts			
Normal stiffness (k_n)	$\mathrm{GPa\,m^{-1}}$	21235.36	22738.67
Shear stiffness (k_s)	$\mathrm{GPa\,m^{-1}}$	5308.84	5983.86
Stiffness ratio (k_n/k_s)	-	4.00	3.80
Strength Properties of Voronoi Contacts			
Cohesion (c_m)	MPa	48.0	36.0
Friction angle (ϕ_m)	∘	27.0	20.0
Tensile strength (σ_{tm})	MPa	8.0	3.5
Residual cohesion (c_{mr})	MPa	0.0	0.0
Residual friction angle (ϕ_{mr})	∘	15.0	15.0
Residual tensile strength (σ_{tmr})	MPa	0.0	0.0

Table 6.1: Calibrated micro-mechanical properties of the Voronoi block and contacts for the Thornhill Rock and Midgley Grit.

		Laboratory		UDEC GBM[1]	
Property	Units	Thornhill Rock	Midgley Grit	Thornhill Rock	Midgley Grit
Density (ρ)	$\mathrm{kg\,m^{-3}}$	2250.00	2220.00	2250.00 (0.00%)	2220.00 (0.00%)
Uniaxial compressive strength (UCS)	MPa	50.80	37.80	50.69 (0.22%)	37.49 (0.82%)
Young's modulus (E)	GPa	8.70	9.50	8.80 (1.15%)	9.58 (0.84%)
Poisson's ratio (ν)	-	0.22	0.21	0.22 (0.00%)	0.21 (0.00%)
Bulk modulus (K)	GPa	5.18	5.46	5.23 (0.97%)	5.50 (0.73%)
Shear modulus (G)	GPa	3.57	3.93	3.61 (1.12%)	3.96 (0.76%)
Tensile strength (σ_t)	MPa	4.20	1.92	4.22 (0.48%)	1.91 (0.52%)
Hoek-Brown material constant (m_i)	-	24.70	19.22	23.89 (3.28%)	18.94 (1.46%)
Hoek-Brown material constant (s)	-	1.00	1.00	1.00 (0.00%)	1.00 (0.00%)
Hoek-Brown material constant (a)	-	0.50	0.50	0.50 (0.00%)	0.50 (0.00%)
Cohesion (c)	MPa	9.63	7.32	9.99 (3.74%)	7.25 (0.96%)
Friction angle (ϕ)	$\circ$	49.73	47.20	48.00 (3.48%)	49.50 (4.87%)

Table 6.2: Comparison of properties derived from laboratory testing and from calibrated mechanical UDEC GBM simulations.

[1]Bracketed percentages are relative percentage differences between laboratory derived properties, and output macro-mechanical properties from UDEC GBM calibrated models.

To examine the repeatability of the desired properties using the calibrated micro-properties, and to prove that the mechanical behaviour of the model is independent of the generated Voronoi tessellation, five different random Voronoi tessellations were generated. For each of these generations, unconfined compression tests and triaxial tests at 5, 10 and 15 MPa were performed with identical procedures. The five different Voronoi generations show good repeatability, and demonstrate that the mechanical behaviour is also independent of the Voronoi generation (Fig. 6.4a).

6.5 Thermo-mechanical model setup

6.5.1 Application of thermal properties

Following on from the successful mechanical calibration of Voronoi GBM simulations to the mechanical laboratory behaviour of the Thornhill Rock and the Midgley Grit, thermal properties were also added to the Voronoi GBM simulations. Whilst only one set of mechanical properties are applied to all Voronoi blocks and contacts within the mechanical simulations, multiple different thermal properties (discussed further in § 2.6.1) corresponding to the mineralogy of the specimen lithologies were applied in the thermo-mechanical Voronoi GBM simulations, allowing for heterogeneous thermal loading to occur within the specimen. Whole rock mineral percentages for the Thornhill Rock and Midgley Grit were obtained from quantitative XRD analysis (§ 5.2, Fig. 5.2) and used to apply mineral percentages to the thermo-mechanical simulations. The minor mineral constituents of jarosite and siderite were not considered for thermal properties and the major mineral constituents were rounded to the nearest 5% for implementation of thermal properties (Table 6.3). A *FISH* function was written (Appendix C.5) to randomly assign the thermal properties for different minerals (Table 2.3) to Voronoi blocks with the relevant mineral percentages (Fig. 6.5).

Mineral	Thornhill Rock	Midgley Grit
Quartz	65%	75%
Muscovite	15%	5%
Albite	10%	5%
Chlorite	5%	0%
Kaolinite	5%	5%
Microcline	0%	10%

Table 6.3: Mineral percentages used in thermo-mechanical UDEC GBMs, obtained from quantitative XRD analysis (Fig. 5.2).

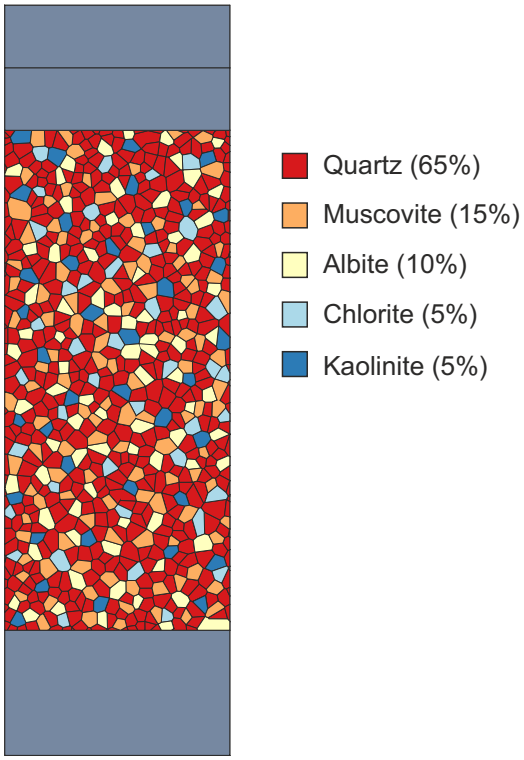

Figure 6.5: UDEC GBM with thermal material properties applied in mineralogical percentages for the Thornhill Rock.

6.5.2 Thermo-mechanical coupling

UDEC allows the simulation of transient heat conduction in materials, and the development of thermally induced displacements and stresses (Itasca, 2014a). The equation of conductive heat transfer is Fourier's law, written in a general dimension as:

$$Q_i = -k_{ij}\frac{\delta T}{\delta x_j} \tag{6.2}$$

where Q_i is the thermal flux in the i-direction, k_{ij} is the thermal conductivity tensor and T is the temperature. For any mass, the change in temperature can be written as:

$$\frac{\delta T}{\delta t} = \frac{Q_{net}}{c_p M} \tag{6.3}$$

where Q_{net} is the net heat flow into the mass, c_p is the specific heat capacity and M is the mass. For two-dimensional heat transfer, Eq. 6.3 can be written as:

$$\frac{\delta T}{\delta t} = \frac{1}{c_p \rho}\left[\frac{\delta Q_x}{\delta x} + \frac{\delta Q_y}{\delta y}\right] \tag{6.4}$$

where ρ is the density of the mass. Eq. 6.4 can then be combined with Eq. 6.2 to give:

$$\frac{\delta T}{\delta t} = \frac{1}{c_p \rho}\frac{\delta}{\delta x}\left[k_x \frac{\delta T}{\delta x}\right] + \frac{\delta}{\delta y}\left[k_y \frac{\delta T}{\delta y}\right] = \frac{1}{c_p \rho}\left[k_x \frac{\delta^2 T}{\delta x^2} + k_y \frac{\delta^2 T}{\delta y^2}\right] \tag{6.5}$$

assuming k_x and k_y are constant. The heat transfer within the model calculated from Eq. 6.5 can then induce changes in stress according to the following thermal-stress calculation:

$$\Delta\sigma_{ij} = -\delta_{ij} 3K\alpha_L \Delta T \tag{6.6}$$

where $\Delta\sigma_{ij}$ is the change in stress ij, δ_{ij} is the Kronecker delta ($\delta_{ij} = 1$ for $i = j$ and 0 for $i \neq j$), K is the bulk modulus, α_L is the linear thermal expansion coefficient and ΔT is the change in temperature. There is potential for mechanical changes to also cause temperature changes as energy is dissipated throughout the model, however, as

this effect is normally negligible it is not considered here (i.e. the thermo-mechanical coupling is uni-directional).

The thermal analysis uses an explicit solution method. At each thermal timestep, Eq. 6.2 and 6.3 are solved numerically. The thermal timestep (Δt) is limited by numerical stability, with the critical timestep for stability being:

$$\Delta t = \frac{(\Delta x)^2}{4\kappa\left[1 + \frac{h\Delta x}{2\kappa}\right]} \tag{6.7}$$

where Δx is the smallest zone dimension in the model, h is the convective heat transfer coefficient, and κ is the thermal diffusivity ($k/c_p\rho$). Heat transfers across block contacts without resistance, provided that the blocks are in contact. The same zoning is used for thermal calculations as the zoning for the mechanical finite difference zones (triangular in these models), although the triangles are further subdivided where a block is in contact with a corner on another block (Itasca, 2014a).

The above thermal calculation procedure is combined with the mechanical calculation procedures (§ 6.2, (Itasca, 2014a)) to perform the thermo-mechanical analyses. Firstly, initial mechanical equilibrium is reached. Thermal stepping is then initiated, within which the heat transfer within the model induces changes in stress (Eq. 6.6). After a small amount of thermal stepping, mechanical stepping is then resumed for the changes in stress to be solved and mechanical equilibrium to be regained. This procedure is repeated until the desired thermal load is applied to the model.

6.5.3 Thermal loading

The confining fluid surrounding the specimen used to apply a confining pressure and thermal load during laboratory testing is not included in numerical simulations, therefore thermal loading was applied directly to the boundaries of the specimen and platens. The temperature for the start of all thermo-mechanical simulations was initialised at 20 °C. Thermal loading was then applied to the outer 1 mm of the specimen and platens in 1.5 °C increments. A thermal timestep of 3.0×10^{-5} s was chosen and cycled for 3,000,000 thermal timesteps at every 1.5 °C increment. Thermo-mechanical coupling

was set to occur every 1,000 thermal timesteps and 100,000 mechanical timesteps (or when mechanical equilibrium was solved). This thermal loading rate of 1.0 °C min^{-1} is marginally lower than the observed thermal loading rate in the laboratory of ≈ 1.1 °C min^{-1} (§ 5.3). However UDEC automatically over-rides and reduces the thermal timestep to maintain numerical stability (as per Eq. 6.7) in some numerical simulations, depending on the Voronoi generation, resulting in a slightly increased thermal loading rate. The temperature throughout each model was monitored at a grid of history points over the central 50 mm of the specimen (equal to the strain monitoring locations on Fig. 6.2), and logged every 50,000 cycles. Fig. 6.6 shows the heating in numerical simulations at three different places within the specimen compared to the heating command and thermocouple readings within the triaxial cell during a laboratory experiment. It can be observed that the thermal gradient across the specimen in numerical simulations is extremely small (less than 2 °C) and that, apart from the initial heating lag and plateau upon reaching the desired temperature, which is observed in the laboratory (discussed further in § 5.3), the thermal loading rate in numerical simulations is extremely close to the thermal loading rate in the laboratory.

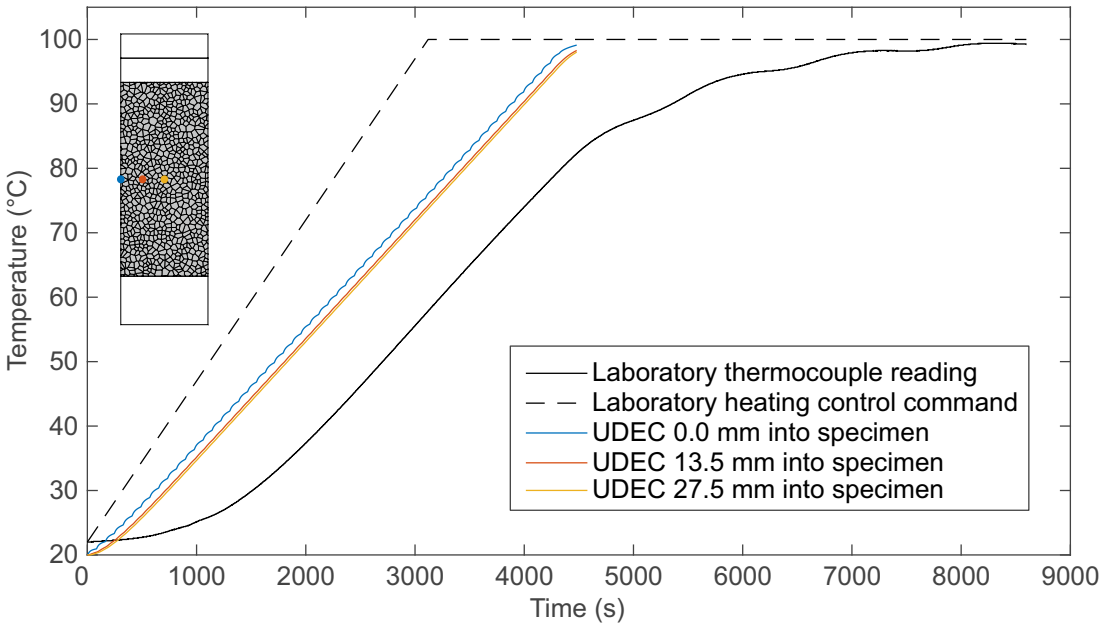

Figure 6.6: Monitoring of thermal loading throughout the model during numerical simulations compared with the thermal loading during laboratory experiments. Representative laboratory heating curve from test on Specimen #562.

Following the completion of the coupled thermal loading in numerical simulations, mechanical loading of the specimens was undertaken as in laboratory experiments. A confining pressure of 5 MPa was applied to the specimens and mechanical equilibrium was reached prior to initiating axial loading (as described in § 6.4).

6.6 Intact thermo-mechanical simulations

6.6.1 Thornhill Rock

Specimens were thermally loaded in numerical simulations to 50 °C, 75 °C and 100 °C. The development of localised thermally induced stresses, and the propagation and accumulation of thermally induced micro-cracks was monitored during thermal loading. Micro-cracking was monitored by tracking the development of plasticity flags being set within the model (i.e. contacts reaching the irreversible plastic state as described by the constitutive model), and also the normal load present on those contacts, to deduce whether they had failed in tension or in shear (Appendix C.4). Fig. 6.7a shows a subset of the model contoured with the x-component of the stress tensor (σ_{xx}) after thermal loading to 100 °C. As expected, no horizontal stresses occur at the model boundary (left hand edge) as no confinement has yet been applied, and displacement is free to occur as thermal expansion occurs. However, further within the model, it can be seen that localised stresses have started to develop, with regions both in tension and compression, and the formation of micro-cracks in areas of tension, where the tensile strength (σ_{tm} = 8.0 MPa for the Thornhill Rock) of the Voronoi contacts has been exceeded. Note that Fig. 6.7a is a snapshot of the model once the temperature in the model had equilibrated at 100 °C, therefore the stresses surrounding micro-cracks may no longer be representative of the stresses present when the micro-crack formed, as stresses will have re-distributed as model timestepping progressed.

Fig. 6.7b shows the development of thermally induced micro-cracking within models of the Thornhill Rock with increasing thermal loading. At 50 °C, only approximately 0.5% of Voronoi contacts within the model have cracked (approximately 25 Voronoi contacts, out of a total of 5,000 contacts in the model). This has increased to ≈ 2.5% of Voronoi contacts by 75 °C, and ≈ 6.0% of Voronoi contacts by 100 °C. The micro-cracks are seen

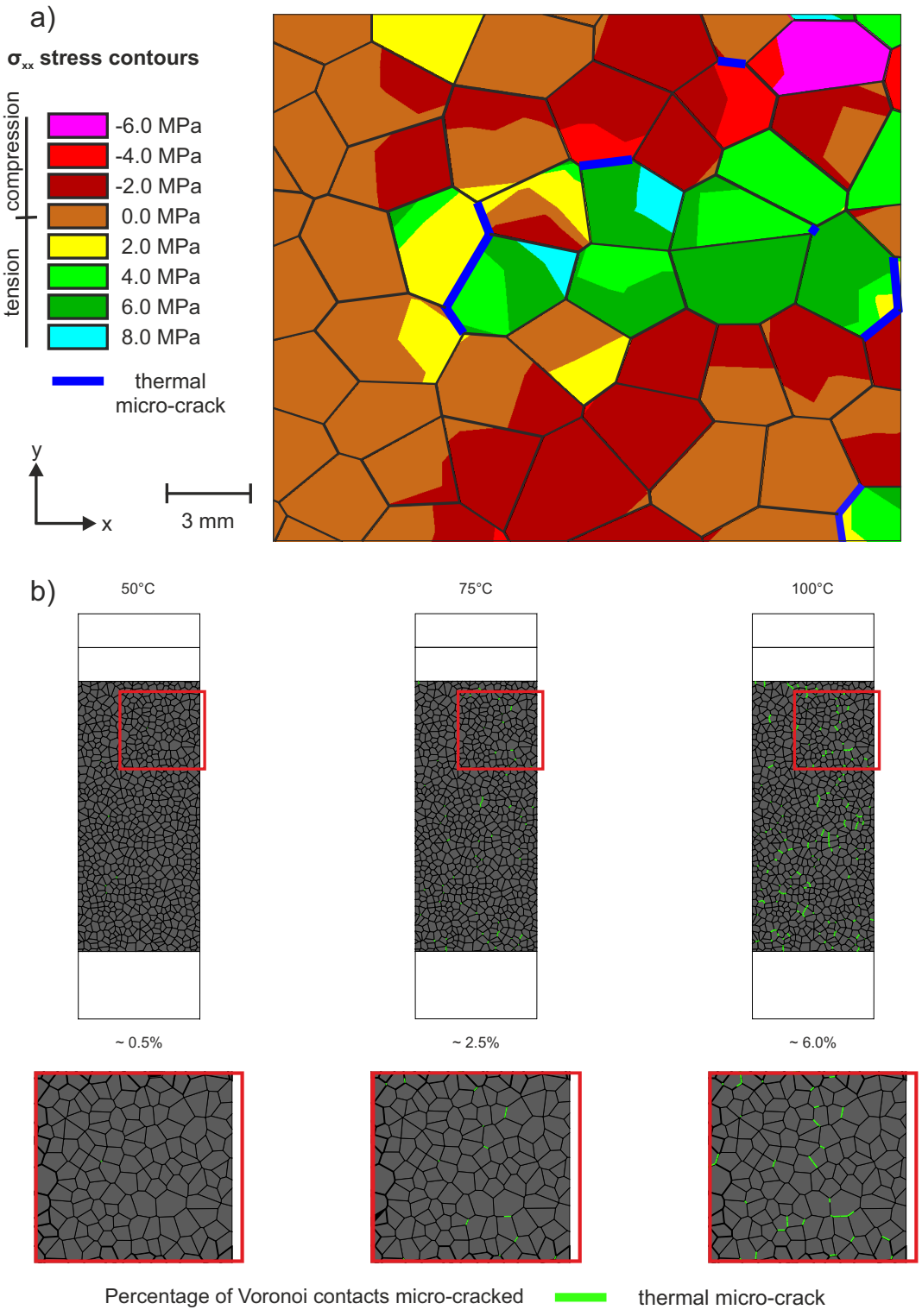

Figure 6.7: a) Subset of Thornhill Rock model thermally loaded to 100 °C showing x-component stresses (σ_{xx}). Left hand edge of subset is the edge of the model. Negative stresses are compressive. b) Amount of thermally induced micro-crack development in models of the Thornhill Rock at temperatures of 50 °C, 75 °C and 100 °C.

to develop randomly throughout the specimen, with the exception of the outer 5 mm of the specimen on the vertical edges, where displacement is free to occur and thermally induced stresses do not develop. All thermally induced micro-cracks form in tension and appear to have no preferred orientation, although further cracking nucleates and propagates from already existing micro-cracks.

Micro-cracking is seen to initiate at between 38 °C and 42 °C dependent on Voronoi generation (Fig. 6.8). Micro-cracks accumulate slowly initially up to 60 °C, accumulating approximately linearly thereafter up to 100 °C.

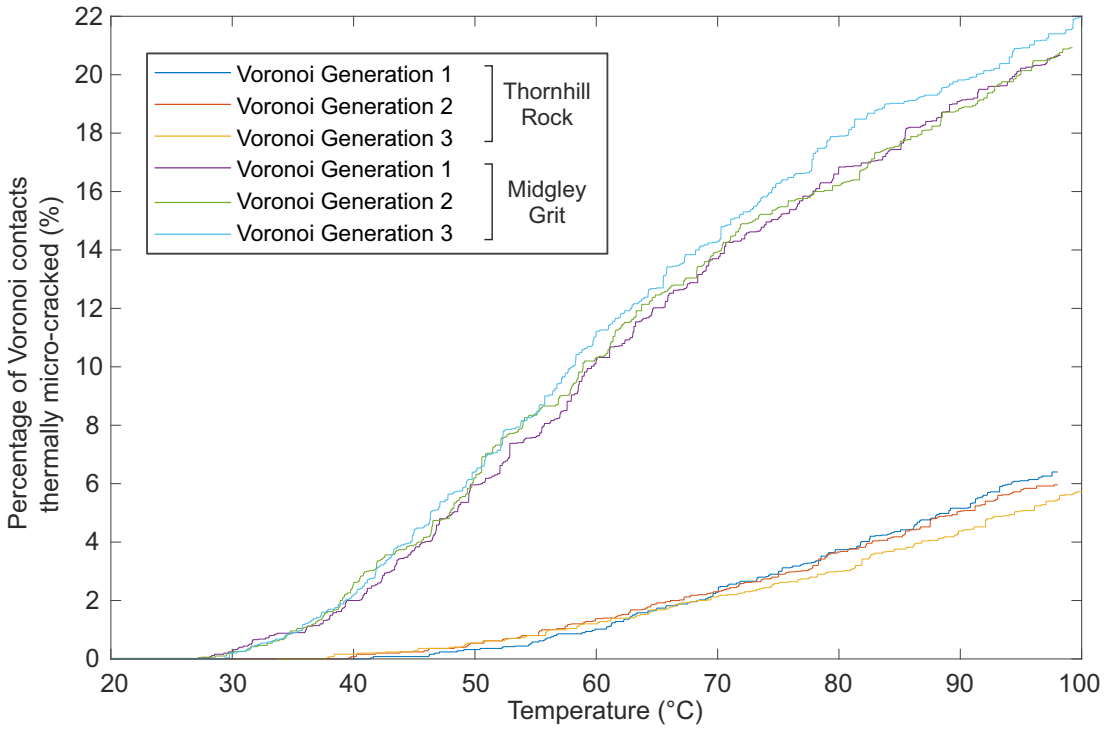

Figure 6.8: Percentage of thermally micro-cracked Voronoi contacts with increasing thermal loading for the Thornhill Rock and Midgley Grit. Models were run with three different random Voronoi generations for each lithology.

Upon mechanical loading after thermal loading to 50 °C, 75 °C and 100 °C, a reduction in peak strength is observed (Fig. 6.9b). No change is observed in Young's modulus with increasing thermal loading, and it is not possible to apply the same methods for calculating the crack initiation (CI) and crack damage (CD) thresholds as in the laboratory, due to the inability of the constitutive model to correctly capture the yielding

behaviour (as discussed in § 6.4), which also results in the very abrupt failure at peak strength in comparison to the laboratory results.

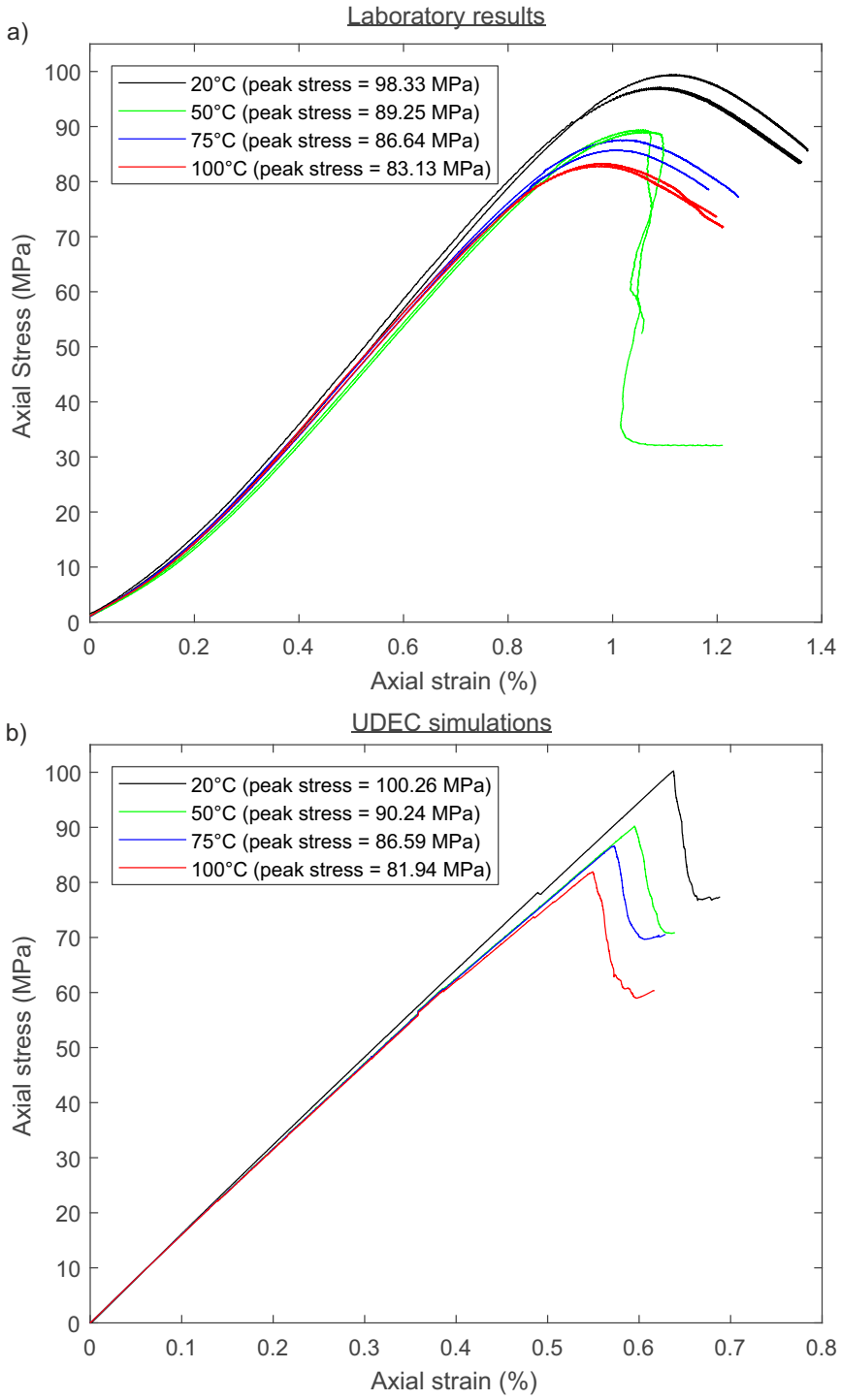

Figure 6.9: a) Axial stress vs. axial strain data for laboratory thermo-mechanical triaxial tests on intact specimens of Thornhill Rock (Batch 4), carried out at 5 MPa σ_3 and temperatures of 20 °C, 50 °C, 75 °C and 100 °C. b) Axial stress vs. axial strain data for UDEC GBM simulations of thermo-mechanical triaxial tests on Thornhill Rock, carried out at 5 MPa σ_3 and temperatures of 20 °C, 50 °C, 75 °C and 100 °C.

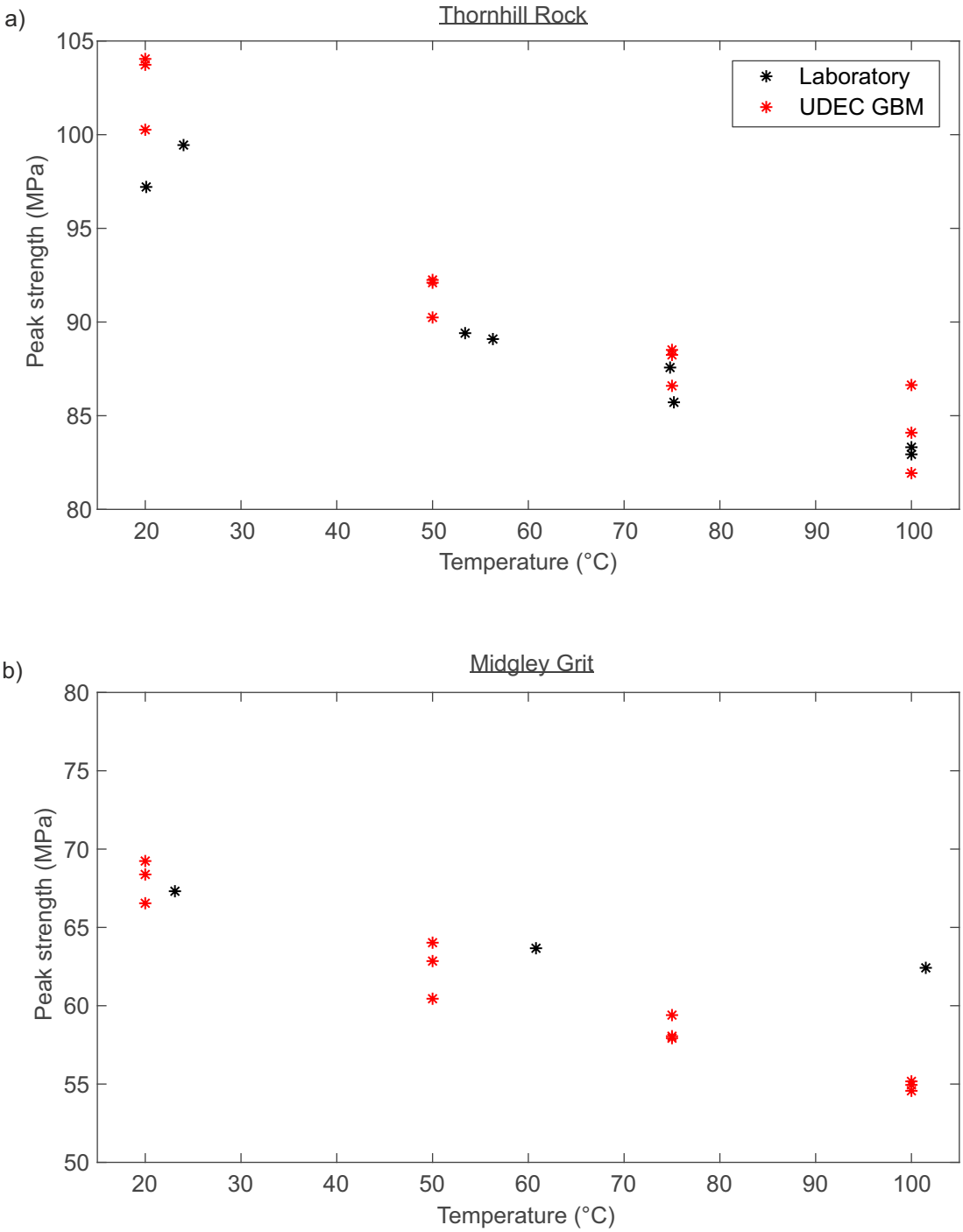

Figure 6.10: Comparison of peak strengths obtained for specimens subjected to different amounts of thermal loading in the laboratory and in UDEC GBM simulations: a) Thornhill Rock and b) Midgley Grit.

6.6.2 Midgley Grit

Thermo-mechanical simulations were also run on calibrated intact specimens of Midgley Grit (calibrated micro-mechanical properties tabulated in Table 6.1, thermal properties tabulated in Table 2.3, applied in mineral percentages tabulated in Table 6.3). Specimens were thermally loaded in the numerical simulations to 50 °C, 75 °C and 100 °C, whilst tracking the development of thermally induced stresses and formation of micro-cracking within the specimens. At 50 °C, approximately 4.0% of Voronoi contacts within the model were micro-cracked. This increased to 14% of Voronoi contacts by 75 °C, and approximately 21% of Voronoi contacts by 100 °C. Thermal micro-cracking initiated at 28 °C, and again developed randomly throughout the specimen with no preferred orientation.

Specimens were mechanically loaded with a confining pressure of 5 MPa and at an axial displacement rate of 0.01 m s^{-1} after the thermal loading to 50 °C, 75 °C and 100 °C. A reduction in peak strength with increasing thermal loading is again observed (Fig. 6.10b) with a reduction in strength of 9% by 50 °C, 14% by 75 °C, and 18% by 100 °C.

6.6.3 Discussion

The intact thermo-mechanical simulations of both the Thornhill Rock and Midgley Grit show comparable results to laboratory testing, with thermal loading alone causing progressive damage to specimens through the propagation and accumulation of tensile micro-cracks. Micro-cracking initiates at approximately 40 °C in specimens of Thornhill Rock, and 30 °C in specimens of Midgley Grit, and apart from the initial 15 °C the micro-cracks accumulate linearly with increasing temperature up to 100 °C. This linear behaviour is expected, as assigned thermal properties have been assumed and applied to be linear over the temperature range tested. Thermal micro-cracking accumulates much faster within specimens of Midgley Grit than Thornhill Rock, with approximately 30 micro-cracks per 1 °C increment in the Midgley Grit compared to approximately 7 micro-cracks per 1 °C increment in the Thornhill Rock (Fig. 6.8). The calibrated micro-tensile strength (σ_{tm}) of the Midgley Grit is only 3.5 MPa (compared to 8.0 MPa for the Thornhill Rock), which can explain the earlier onset of thermal micro-cracking and increased micro-cracking with thermal loading than in the Thornhill Rock, as

considerably lower localised stresses are therefore required to initiate micro-cracking. This coupled with slightly differing thermal properties between the Thornhill Rock and Midgley Grit, including a higher percentage of quartz in the Midgley Grit (that has a relatively high thermal expansion coefficient), will have potential to increase localised stresses due to heterogeneous thermal expansion.

Previous studies on the development of thermally induced micro-cracking found that micro-cracks are most likely to develop between minerals with the largest disparity in thermal properties, and least likely to form between grains of the same mineralogy (Fredrich and Wong, 1986) (discussed further in § 2.6.1). Tracking the formation of micro-cracks between different mineralogy Voronoi blocks throughout thermal loading does not show this behaviour. Fig. 6.11 shows the accumulation of micro-cracking between different grain contact mineralogies with increasing thermal loading. No particular grain contact type is seen to preferentially micro-crack. The two greatest percentages of contacts micro-cracked of any particular contact type in this numerical simulation of the Thornhill Rock are for chlorite/chlorite and albite/albite contacts (Fig. 6.11), the inverse of the trend observed by Fredrich and Wong (1986). Stresses and displacements are redistributed at every timestep within the model, and due to the complex interaction of all of the blocks in the model, it may not be possible to accurately assess whether there is a mineralogical control on the location of micro-cracks in this manner. It could also be because only one set of mechanical properties is applied to all Voronoi blocks and contacts, and different mineralogical grain contact strength and deformability could be key to the likelihood of micro-crack formation between certain mineralogies as well as the disparity in thermal properties.

When assessing the mechanical strength of specimens after thermal loading, simulations of the Thornhill Rock show good agreement with the loss in strength observed in the laboratory, with the progressive micro-cracking under thermal loading weakening the specimens (Fig. 6.9 & 6.10a). The reduction in strength is comparable between the laboratory results and the numerical simulations. The simulations of the Midgley Grit again capture the same strength reduction trend as observed in the laboratory, but the degree of strength reduction is much greater in the numerical simulations. The Midgley Grit had a lower linear thermal expansion coefficient ($1.30 \times 10^{-6}\,\mathrm{K}^{-1}$) in the laboratory than expected based on its mineralogy (discussed further in §5.3.3). The bulk

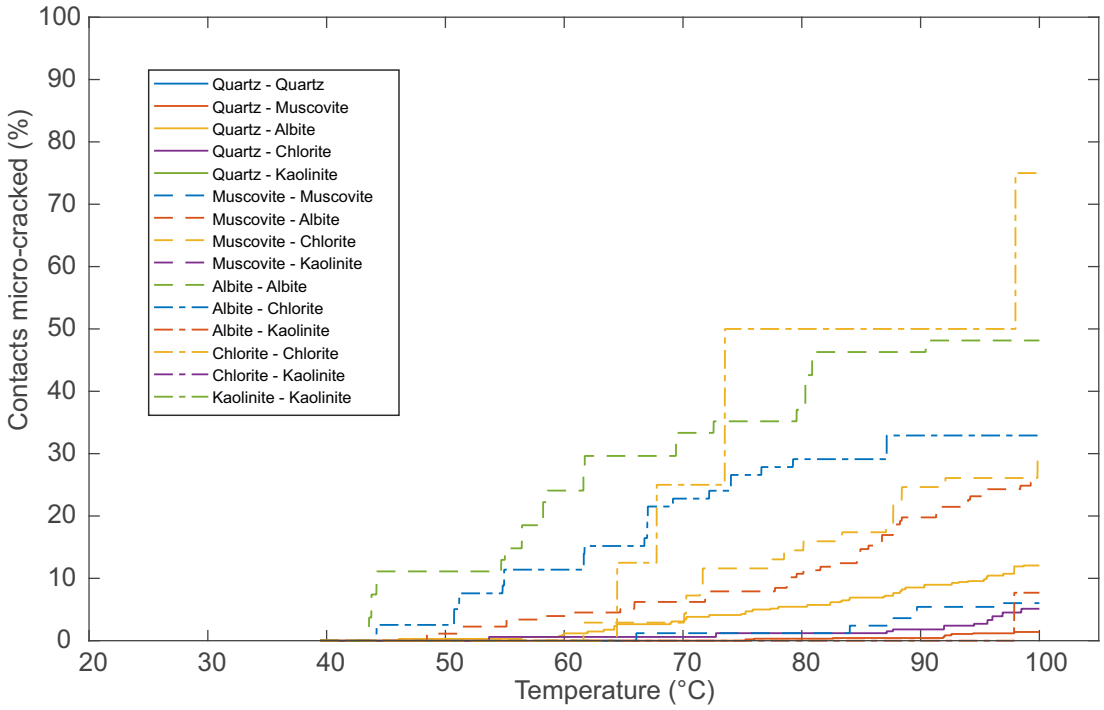

Figure 6.11: Cumulative micro-cracking with increasing thermal loading, divided in to the different types of contacts between Voronoi blocks assigned thermal properties of different minerals (Table 2.3). Cumulative values of micro-cracks presented as percentages of the total number of contacts of that type present in the model.

linear thermal expansion coefficient of Midgley Grit specimens in GBM simulations was $1.43 \times 10^{-5}\,\mathrm{K}^{-1}$. The difference in thermal expansion between the laboratory testing and numerical simulations is likely the cause for the discrepancy in strength reduction.

In laboratory tests the Thornhill Rock shows a greater strength reduction with increasing temperature than the Midgley Grit (Fig. 6.10), however in numerical simulations the Thornhill Rock exhibits fewer micro-cracks than the Midgley Grit (Fig. 6.8). As discussed, the difference in micro-cracking between the Thornhill Rock and Midgley Grit can be attributed to differences in the calibrated micro-tensile strengths of Voronoi contacts in the models. The greater strength reduction of Thornhill Rock specimens in the laboratory is likely due to other mechanisms of progressive damage as well as micro-cracking, such as grain comminution and pore collapse, which the numerical simulations are unable to capture.

Monitoring the accumulation of micro-cracks throughout the specimens shows that the thermally induced micro-cracks serve as nucleation points for the accumulation of further tensile micro-cracking when mechanical loading is initiated (Fig. 6.12b), until unstable accumulation and coalescence of micro-cracks starts to occur (Fig. 2.1) resulting in the formation of macroscopic shear fractures and the failure of the specimen (Fig. 6.12c).

Overall, the thermo-mechanically coupled, calibrated GBMs can capture micro-cracking as a mechanism of progressive damage, reproducing the stress-strain behaviour of laboratory specimens. However, the simulations are simplifications and therefore they neglect other mechanisms of progressive damage such as pore collapse, grain comminution, and heterogeneous mineralogical mechanical grain strength, that are all likely important factors in the progressive damage that occurs in laboratory specimens.

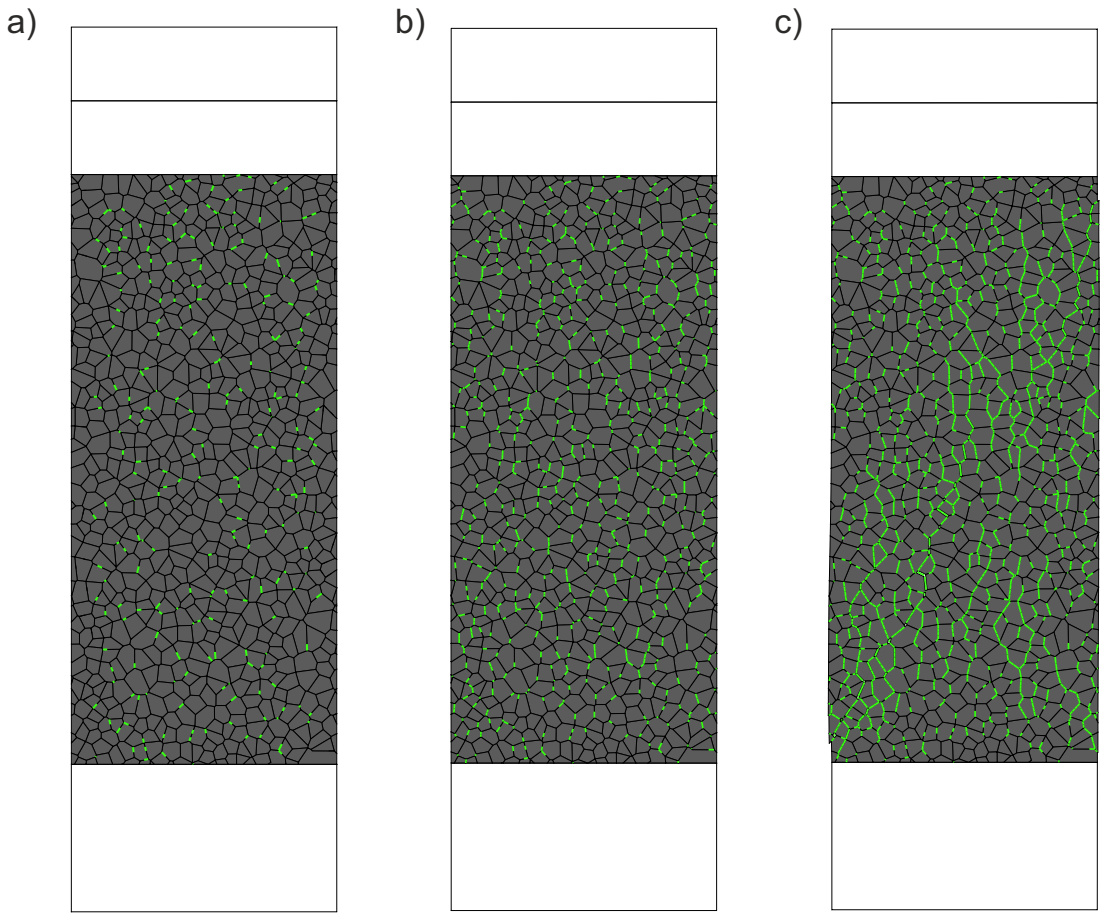

Figure 6.12: a) Tensile micro-cracks throughout the specimen after thermal loading to 100 °C. b) Further tensile cracking due to mechanical loading, with thermal micro-cracks acting as nucleation points. c) Accumulation and coalescence of micro-cracks into shear failure and a macroscopic fracture.

6.7 Discontinuous thermo-mechanical simulations

In addition to simulations of the laboratory thermo-mechanical triaxial experiments on intact specimens of Thornhill Rock and Midgley Grit, simulations were undertaken to further investigate thermo-mechanical discontinuity behaviour, as in the laboratory (§ 5.4). Simulations were undertaken to further examine the hypothesis of thermal closure occurring due to thermal expansion at temperatures up to 50 °C resulting in increased shear strength, followed by reduced shear strength with the initiation of thermal micro-cracking at thermal loading beyond 50 °C (§ 5.4.5). Due to the limited laboratory testing undertaken on discontinuous specimens of Midgley Grit, discontinuous thermo-mechanical simulations were only undertaken on specimens of Thornhill Rock.

Prior to running simulations of the discontinuous thermo-mechanical laboratory testing, it was first necessary to undertake further calibration of the mechanical properties of the discontinuity.

6.7.1 Normal stiffness calibration

The normal closure (u_n) of a discontinuity is the most important parameter when assessing discontinuity closure, particularly in thermo-mechanical modelling, where the thermal expansion of grains has the potential for thermal closure to occur on the discontinuity. The amount of normal closure that occurs on a discontinuity is controlled by the discontinuity normal stiffness, which in turn is dependent on the contact area, discontinuity roughness, strength and stiffness of discontinuity asperities and the presence of any infilling (Goodman, 1974; Goodman et al., 1968) (discussed further in § 2.4.3). The normal closure of discontinuities is normal stress dependent and hyperbolic with increasing stress.

All Voronoi contacts between blocks in UDEC GBM simulations in this study so far have been assigned a single normal stiffness regardless of the applied normal stress. To allow the assessment of normal closure with differing normal stresses, the Voronoi contacts along the discontinuity in the simulations must instead be given stress dependent normal stiffnesses, calibrated to representative macro stiffnesses.

Bandis et al. (1983) undertook laboratory normal stiffness testing on various lithologies, including a siltstone and sandstone from the Coal Measures of West Yorkshire, with similar mechanical characteristics to the Thornhill Rock. The laboratory setup for testing normal stiffness by Bandis et al. (1983) consisted of axially loading a cylindrical specimen with a single horizontal discontinuity running through the specimen. The axial displacement was recorded with increasing axial stress. The normal stress vs normal closure curve for just the discontinuity (Δu_d) was then derived by subtracting the axial displacement vs axial stress response for an intact specimen (Δu_i) under the same loading conditions from the total response of the specimen with the discontinuity (Δu_t):

$$\Delta u_d = \Delta u_t - \Delta u_i \tag{6.8}$$

Laboratory normal stiffness testing was simulated in UDEC to allow the calibration of the normal stiffness of the discontinuity, using the same set up as Bandis et al. (1983). A model was created with the same model dimensions as the UCS testing in Section 6.4, but with a horizontal discontinuity passing through the centre of the specimen (Fig. 6.13a), with a roughness profile obtained from the laser profilometry of a laboratory specimen of Thornhill Rock, providing a *JRC* of 10 to 12. Instead of a single normal stiffness value being assigned to contacts along the discontinuity, stress dependent normal stiffness values were assigned, thus providing increased stiffness with increased loading. The Voronoi contacts along the discontinuity were assigned the residual strength properties of the calibrated intact specimen (Table 6.1). The shear stiffness of contacts on the discontinuity were set to be equal to the normal stiffness throughout calibration. As a starting point for calibration, the initial stress dependent normal stiffness curve was defined by:

$$\sigma_n = \frac{-u_{nc} \cdot k_{ni}}{1 - \frac{u_{nc}}{u_{max}}} \tag{6.9}$$

where k_{ni} is the initial normal stiffness, u_{nc} is the current normal closure on the discontinuity, and u_{max} is the maximum allowable closure on the discontinuity. The maximum closure on the discontinuity was set to be equal to the overlap tolerance of the Voronoi blocks in the model (0.5 mm) to ensure mechanical stability. The initial normal stiffness

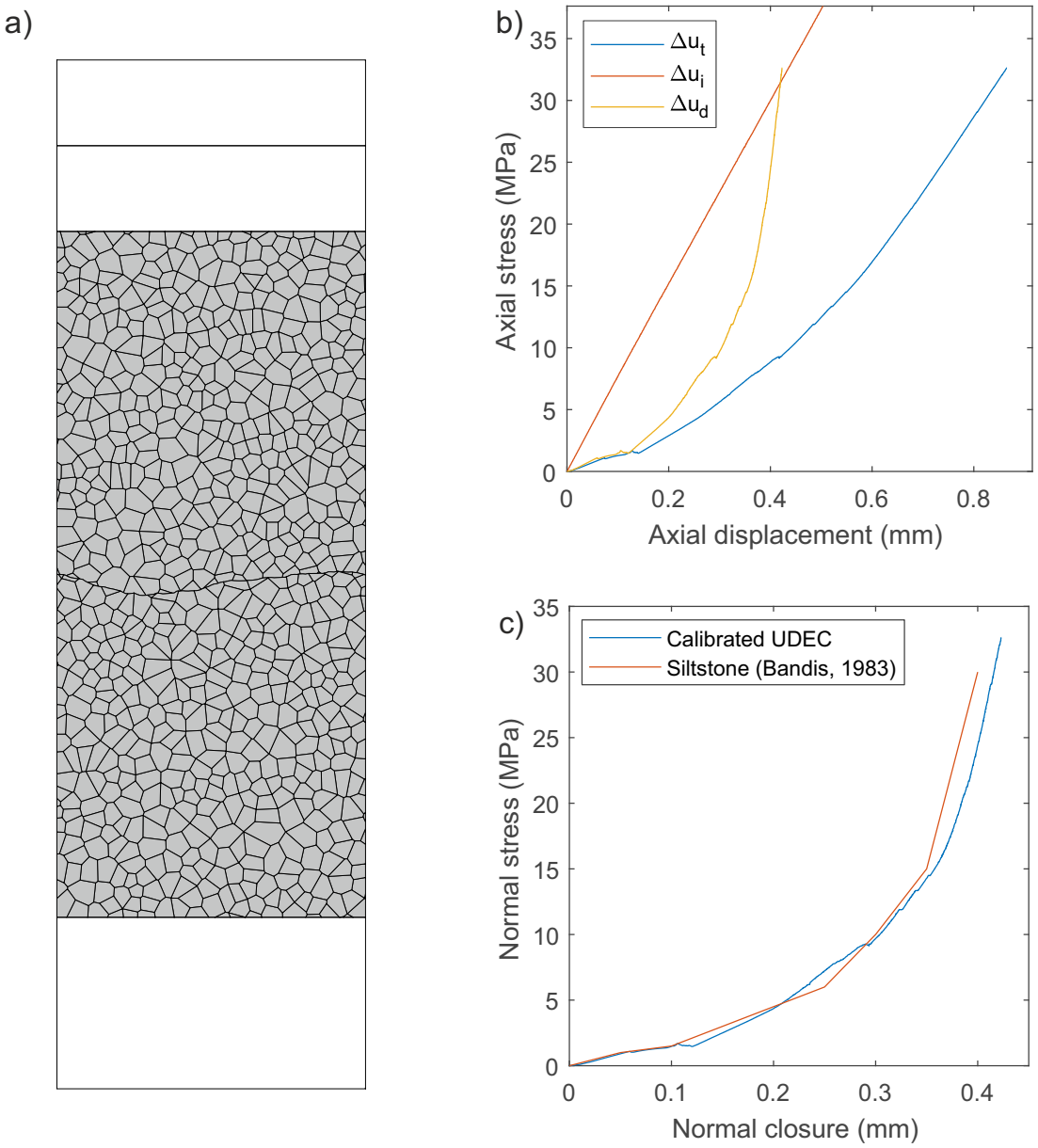

Figure 6.13: a) Model dimensions for normal stiffness simulations, with a horizontal discontinuity running through the specimen with roughness profile obtained from laser profilometry on a laboratory specimen of Thornhill Rock (*JRC* of 10 to 12). b) Normal closure of just the discontinuity (Δu_d) is calculated by subtracting the axial displacement of the intact specimen (Δu_i) from the total deformation of the discontinuous specimen (Δu_t) (Eq. 6.8). c) Comparison between the stress dependent normal stiffness calibrated in UDEC simulations and laboratory results on siltstone lithology by Bandis et al. (1983).

Normal closure (u_n) (mm)	Normal stress (σ_n) (MPa)	Normal stiffness (k_n) (GPa m^{-1})
0.000	0.00	—
0.010	0.20	20.0
0.050	1.00	20.0
0.100	2.00	20.0
0.133	2.66	20.0
0.166	3.32	20.0
0.200	10.00	50.0
0.250	16.00	64.0
0.300	24.00	80.0
0.350	40.00	114.3
0.400	130.00	325.0
0.450	300.00	666.7
0.475	500.00	1052.6
0.490	800.00	1632.7
0.500	10617.68	21235.4

Table 6.4: Calibrated stress dependent normal stiffness values assigned to Voronoi contacts along the discontinuity in normal stiffness simulations.

was set equal to the normal stiffness obtained in Bandis et al. (1983), and the normal stress at the maximum closure was set to produce a normal stiffness equal to the normal stiffness of the Voronoi contacts in the rest of the model (i.e. the normal stiffness of intact material). The normal closure of the discontinuity was calculated using Eq. 6.8 with the axial displacement vs. axial stress of the discontinuous specimen compared to the response of a simulated UCS test in UDEC (Fig. 6.13b). From the above starting point, an iterative procedure was undertaken, altering the stress dependent normal stiffness values of the discontinuity in the model until calibration was reached with the macro response of the siltstone specimen in Bandis et al. (1983) (Fig. 6.13b). The stress dependent normal stiffness values assigned to the discontinuity Voronoi contacts are tabulated in Table 6.4.

Following the calibration of the stress dependent normal stiffness for the discontinuity, models were built with the discontinuity plane at an angle ($\beta = 30°$) through the specimen as in laboratory discontinuous thermo-mechanical testing (§ 5.4). However, with the shear stiffness of the discontinuity set equal to the normal stiffness, mechanical equilibrium could not be reached. Instead, immediate shear failure occurred due to the disparity in the shear stiffness of the discontinuity and the surrounding Voronoi contacts. The implementation of a non-linear stress dependent shear stiffness is not possible in any of the pre-defined constitutive models currently implemented in UDEC, and a new constitutive model would need to be written within the software to allow this to be implemented. The testing required to produce a rigorous constitutive model is beyond the scope of this thesis. The effects of thermo-mechanical loading on discontinuity closure can, however, still be examined by thermally loading the calibrated specimen from the discontinuity normal stiffness calibration.

6.7.2 Thermo-mechanical discontinuity closure

Models with the same geometry as for the normal stiffness testing (§ 6.7.1, Fig. 6.13a) were thermally loaded to 100 °C (with the same boundary conditions applied as previously used for testing intact specimens (§ 6.5.3)), whilst monitoring the formation of micro-cracks, closure of the discontinuity and development of localised stresses.

With increasing thermal loading, the thermal expansion of the two halves of the specimen was accommodated by the closure of the discontinuity, with 0.1 mm of closure occurring on the discontinuity by thermal loading to 50 °C. Little further closure occurred above 50 °C, with the stress dependent stiffness of the discontinuity increasing with the increasing stresses. Fig. 6.14 shows the micro-cracking induced with increasing thermal loading. Thermal micro-cracking does not initiate until approximately 70 °C, 30 °C higher than when thermally loading intact specimens. Micro-cracking then continues linearly, with approximately 4% of contacts in the model micro-cracked by 100 °C.

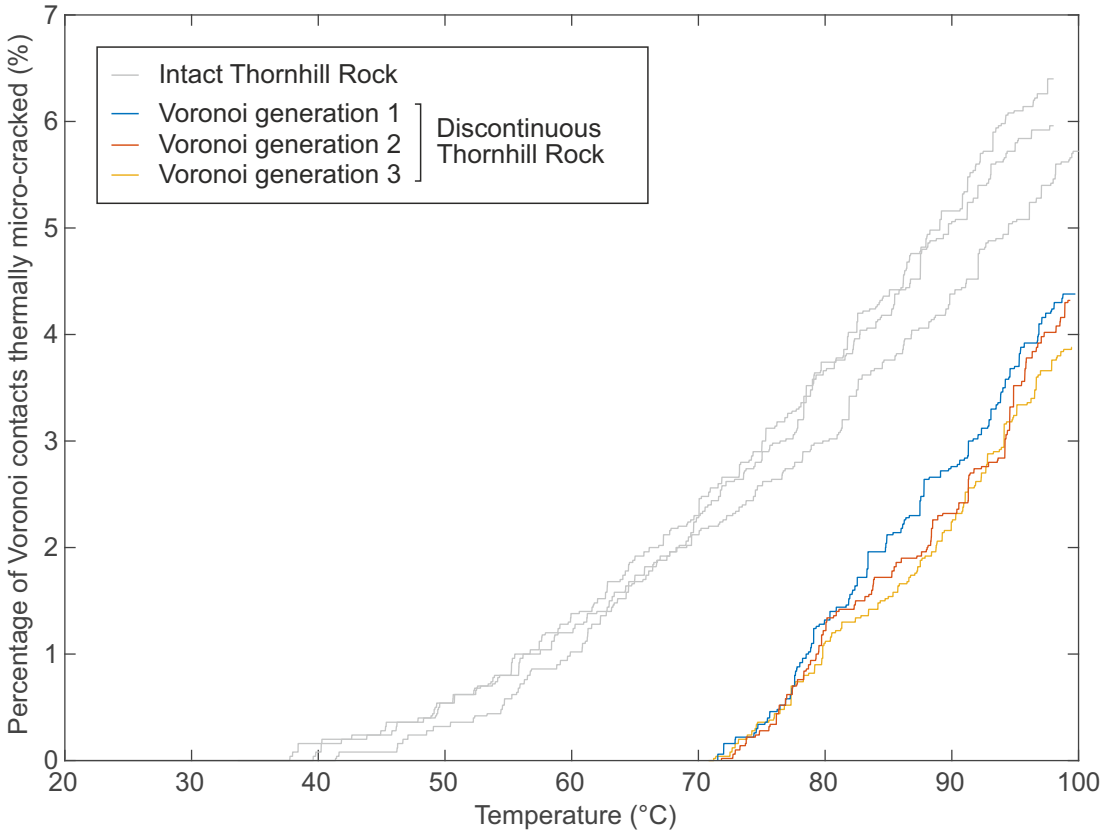

Figure 6.14: Percentage of thermally micro-cracked Voronoi contacts with increasing thermal loading in the discontinuous Thornhill Rock model. Thermally induced micro-cracking of intact Thornhill Rock specimens greyed out for reference (Fig. 6.8).

6.7.3 Discussion

In laboratory thermo-mechanical triaxial experiments on specimens of Thornhill Rock with a pre-existing discontinuity, an increase in peak shear strength was observed with thermal loading from room temperature to 50 °C, followed by a reduction in peak shear strength with continuing thermal loading to 100 °C. This behaviour was attributed to thermal closure occurring on the discontinuity up to 50 °C, resulting in increased shear strength. Once the maximum closure of the discontinuity was reached, micro-cracking then initiated on the discontinuity surface and throughout the intact material causing reduced strength with further thermal loading. The simulations of thermo-mechanical discontinuity closure show this to be the case, with thermal closure of

the discontinuity delaying the onset of micro-cracking until approximately 70 °C (Fig. 6.14). If it was possible to model the shear experiments, it would be expected that the simulations would capture the strength reduction observed in the laboratory at temperatures greater than 75 °C (due to the initiation of thermal micro-cracking) from approximately 70 °C. The strength increase would not be observed with closure on the discontinuity at temperatures up to 50 °C, as it is not possible to define an initial discontinuity aperture in a Mohr-Coulomb constitutive model. A new constitutive model capable of capturing thermal closure effects would therefore need to be written within the software.

The onset of thermal micro-cracking is evidently dependent on whether thermal expansion is constrained, causing the accumulation of localised stresses, or whether displacement can occur, allowing these stresses to dissipate. This has been shown both through the multi-stage temperature testing with thermal loading under different mechanical boundary conditions (§ 5.5), and through aforementioned thermal discontinuity closure experiments. In the laboratory environment, it would therefore be expected that the temperature at which the onset of thermal micro-cracking occurs (and therefore also the degree of mechanical weakening with thermal loading) will be dependent on specimen size. Scale effects related to mechanical behaviour in rock laboratory testing are well accepted (Cunha, 1990; Hoek and Brown, 1980; Stavrou and Murphy, 2018). Increasing specimen size results in greater heterogeneity and a greater probability of micro-defects being present within the specimen, resulting in a reduction in strength and stiffness. However, with micro-defects being potential areas for displacement to occur and thermal stresses to be dissipated, it is likely that increasing specimen size in thermo-mechanical laboratory testing would result in a smaller strength reduction due to a delayed onset of thermal micro-cracking.

6.8 Chapter summary

In this chapter, Voronoi DEM GBMs were built representing the micro-structure of laboratory specimens. The GBMs were calibrated to represent the mechanical properties of the Thornhill Rock and Midgley Grit obtained from laboratory testing. Thermal properties were then applied based on mineralogical percentages from XRD analysis and

thermo-mechanically coupled simulations were run of the laboratory thermo-mechanical triaxial experiments presented in Chapter 5. The thermo-mechanical simulations of intact specimens show the development of thermally induced micro-cracking within specimens, resulting in reduced strength with increasing thermal loading. The strength reduction with thermal loading correlates well with laboratory experiments, and suggests that in the specimens tested, thermal damage initiates at approximately 40 °C for the Thornhill Rock, and 28 °C for the Midgley Grit. After thermal loading to 100 °C, approximately 6% of contacts become thermally cracked in the Thornhill Rock, and approximately 24% of contacts in the Midgley Grit. It should be noted however, that whilst the models are able to simulate progressive damage through micro-cracking, model assumptions and simplifications mean that they are not able to capture all forms of progressive damage likely to occur in laboratory tests.

A horizontal discontinuity was then introduced to the specimen geometry for the Thornhill Rock. The stress dependent normal closure of the discontinuity was calibrated to laboratory experiments. Thermo-mechanical simulations were undertaken on specimens with a horizontal discontinuity. Thermal closure of the discontinuity occurred, accommodating for the thermal expansion of the minerals. This delayed the onset of thermal micro-cracking to approximately 70 °C, correlating well with laboratory shear experiments on discontinuities where strengthening is initially observed with thermal loading (due to thermal closure of the discontinuity), followed by weakening after the initiation of the delayed micro-cracking.

Chapter 7

Discussion, applications, future work & conclusions

7.1 Introduction

In this chapter, the results of Chapters 4, 5 and 6 are discussed in a wider context, as well as the potential applications of this study's findings to the rock engineering community. In addition, areas for future research that could develop upon this study are outlined, and conclusions are then drawn on this body of work.

7.2 Discussion & application of this study to the engineering community

There is a long history in experimental rock mechanics of using synthetic specimens as analogues for rock lithologies to control natural heterogeneity. This has typically been undertaken under low stress conditions e.g. shearbox testing for slope stability problems. In this study, it was attempted to use synthetic specimens for testing at higher stresses to examine fundamental behaviour, however, no synthetic composition tested behaved in a representative manner, with quasi-brittle behaviour occurring at lower stresses than expected. It is therefore suggested that if other workers wish to continue the trend of using synthetic specimens as we move to exploring mechanical (and thermo-mechanical) behaviour of rocks at higher stresses, then the baseline properties of the synthetic composition in use should be properly characterised and justified. Even at low stresses there is potential for localised high stresses to occur, particularly at an asperity level on discontinuities. The characterisation of synthetic compositions at high stresses should therefore not be neglected, even if only considering low stress applications.

It was observed in laboratory testing in Chapter 5 and numerical simulations of these laboratory experiments in Chapter 6 that under thermo-mechanical loading, heterogeneous thermal properties of the polymineralic specimens cause thermally induced micro-cracking, and related strength reductions. However, when a discontinuity is introduced to specimens, the thermal expansion is free to occur into the discontinuity, causing thermal closure and delaying the onset of micro-cracking in the intact material until after maximum closure has occurred on the discontinuity. In the laboratory

specimens tested in this study, the maximum peak shear strength of discontinuous specimens occurred at 50 °C. 120 mm length by 54 mm diameter specimens were used in this study. If the onset of micro-cracking and therefore the potential strengthening or weakening with thermal loading is directly related to whether a near free surface (i.e. a discontinuity) with room for closure to occur is available for localised thermal stresses to dissipate, then it can be expected that the thermo-mechanical behaviour will be scale dependent. The temperature at which the maximum shear strength of discontinuities and the temperature at which the onset of thermal micro-cracking initiates at will be dependent on this scaling. This scale dependency is likely to occur not only in a specimen size at the laboratory scale, but also when upscaling to discontinuous rock masses, with rock block size/joint spacing being key. The ability for thermal closure to occur on discontinuities will also be dependent on the existing normal forces already applied to the discontinuities during thermal loading (as discussed in § 5.5), and the ability for closure to occur on the discontinuities, related to the discontinuity roughness, aperture and infilling.

The thermal weakening of intact specimens in laboratory testing should also be of interest to the engineering community, particularly related to laboratory testing typically undertaken as part of ground investigation and characterisation. The temperature at which specimens are oven dried prior to rock mechanics strength testing by commercial testing laboratories for engineering contractors / consultants (e.g. uniaxial compression testing, triaxial testing, Brazilian disc testing), as recommended by the ISRM suggested methods (Ulusay, 2014), is commonly 105 °C. However, as shown by the intact thermo-mechanical triaxial testing undertaken in this study, a strength reduction of up to 15% (strength under triaxial conditions at 5 MPa σ_3) is observed in the Thornhill Rock, and similar strength reductions are likely to occur in other granular or crystalline rock types. Engineering contractors and consultants should therefore consider an applicable temperature at which their specimens should be oven dried if testing on oven dried specimens, and whether the strengths and stiffnesses obtained from their laboratory testing results are truly representative of the rock and appropriate for use as input parameters for engineering design.

To summarise, the most significant findings from this study, applicable to the engineering community are:

- this study has shown thermal loading can result in differing behaviour for intact rock and discontinuities at temperature up to 100 °C. Whilst further work is required to scale these effects to a rock mass scale, consideration of these effects should be taken into account when modelling and designing structures such as GDFs. Specifically, the limitations of numerical models not explicitly accounting for discontinuity behaviour at elevated temperatures should be highlighted;
- this study has shown that both of the granular lithologies tested in this study show the same relative mechanical behaviour at elevated temperatures, but at different magnitudes. When designing underground structures exposed to thermal loading, laboratory testing should be undertaken at the relevant elevated temperatures to quantify the effects on the particular lithology in question, rather than undertaking testing at ambient temperatures and factoring the results; and
- when undertaking laboratory rock mechanics strength testing, the moisture content and the temperature at which specimens are oven dried should be reasoned, and the appropriateness of using the strengths and stiffnesses obtained from laboratory testing results as input parameters for engineering design should be considered.

7.3 Conclusions

The main aim of this study was to provide a better understanding of the thermo-mechanical behaviour of intact rock and discontinuities that is not currently accounted for in engineering design. To try and achieve this aim, firstly intact and discontinuous specimens of synthetic rocks were created for laboratory testing. The use of synthetic specimens removes the inherent heterogeneity that is present in natural specimens, allowing the fundamental processes to be explored under varying conditions. A new method utilising 3D printed specimen moulds was created to allow the casting of replica discontinuities of representative topographies, and the method was shown to repeatedly produce discontinuities for testing. However, it was not possible to create a synthetic composition with mechanical properties representative of a lower strength sedimentary

lithology. When tested under high stresses, all compositions transitioned to quasi-brittle and ductile behaviour at much lower stresses than natural lithologies display.

Following testing on synthetic compositions, rock specimens of Thornhill Rock and Midgley Grit were prepared and thermo-mechanical triaxial testing was undertaken on both intact specimens and specimens with a pre-existing discontinuity at 30° from the vertical allowing shearing to occur under triaxial conditions. Intact specimens showed a reduction of up to 15% peak strength with increasing thermal loading between room temperature and 100 °C. Specimens with discontinuities displayed an initial increase in discontinuity peak shear strength with thermal loading to 50 °C, followed by a reduction in peak shear strength with further thermal loading to 100 °C. Both lithologies displayed the same relative behaviour (Fig. 5.16a and 5.18a), but the Thornhill Rock displayed a greater increase in peak shear strength up to 50 °C, followed by a larger decrease in peak shear strength thereafter. The discontinuity behaviour for each lithology at elevated temperature has been conceptualised with the behaviour of the Thornhill Rock represented by Eq.'s 7.1 and 7.2, and the Midgley Grit represented by Eq.'s 7.3 and 7.4.

$$\tau_p = 0.23T + 20.0 \qquad 20 \leq T \leq 50\,^{\circ}\mathrm{C} \tag{7.1}$$

$$\tau_p = -0.10T + 37.9 \qquad 50 < T \leq 100\,^{\circ}\mathrm{C} \tag{7.2}$$

$$\tau_p = 0.02T + 24.5 \qquad 20 \leq T \leq 50\,^{\circ}\mathrm{C} \tag{7.3}$$

$$\tau_p = -0.16T + 34.4 \qquad 50 < T \leq 100\,^{\circ}\mathrm{C} \tag{7.4}$$

Thermo-mechanically coupled DEM Voronoi GBM simulations were then undertaken to further explore the thermo-mechanical behaviour observed in the laboratory and the differences in behaviour between intact and discontinuous specimens. The numerical simulations displayed the onset and development of tensile thermal micro-cracking due to the accumulation of localised thermal stresses from the heterogeneous thermal grain properties. The thermal micro-cracking caused reduced strength with subsequent mechanical loading, with the strength reduction correlating well with laboratory results. The onset of micro-cracking was delayed in discontinuous specimens in comparison to intact specimens, with thermal expansion first causing thermal closure and hence strengthening of the discontinuity. Only once maximum closure of the discontinuity was reached did micro-cracking initiate. This gives an explanation for the differing behaviour between intact and discontinuous specimens observed in the laboratory.

To upscale these observations from laboratory scale specimens to a granular or crystalline rock mass, it is likely that the degree of thermal weakening or strengthening will be dependent on the joint set(s) present in the rock mass and the ability for thermal closure to occur on discontinuities, potentially causing strengthening. If thermal closure is not possible on discontinuities, and displacements are constrained, causing the accumulation of localised thermal stresses, weakening is likely to occur.

Overall, this study has achieved the aim, and shown that thermo-mechanical effects exist at temperatures and stresses relevant to rock engineering problems and are currently neglected in engineering design. There are clear additional areas for future research that could allow this body of work to be furthered and upscaled, and allow for significantly more intelligent engineering design, these are discussed below.

7.4 Limitations & future work

This study has demonstrated the problems with using synthetic compositions as rock analogues in rock mechanics testing, and explored the thermo-mechanical behaviour of intact rock and discontinuities in two sedimentary lithologies through laboratory testing and numerical simulations. Although attempting to use synthetic compositions as rock analogues to study fundamental discontinuity behaviour produced negative results,

there is potential to explore this area further. In particular, the thermo-mechanical laboratory testing and numerical simulations show promising areas for further research, with some ideas proposed below.

7.4.1 Use of rock analogues in laboratory testing

Whilst a synthetic composition with mechanical behaviour representative of a lower strength sedimentary rock type could not be created, the new method proposed for casting discontinuous synthetic specimens suitable for triaxial shear testing was proved to be consistent and repeatable (§ 4.5). This specimen creation methodology could be altered to produce discontinuities of different angles, allowing further investigation of the shear behaviour of discontinuities relative to the applied stress field. Dependent on orientation, pre-existing discontinuities are known to undergo closure and have shear strength sufficient enough for failure to occur along a new conjugate shear plane instead (Woodman et al., 2017). Further investigation of this concept would be worthwhile, particularly if traditional triaxial testing ($\sigma_2 = \sigma_3$) was altered instead to true triaxial testing ($\sigma_1 > \sigma_2 > \sigma_3$).

7.4.2 Laboratory testing

7.4.2.1 Triaxial thermo-mechanical testing

Throughout this study all the variables that could be controlled in the thermo-mechanical laboratory tests were controlled, whilst only the temperature was varied. However, there is huge potential to explore the thermo-mechanical behaviour whilst also changing other variables:

- confining pressure - all triaxial tests undertaken in this study (apart from characterisation testing to deduce a failure envelope) were undertaken at 5 MPa confining pressure. This equates to approximately 200 to 500 m depth. However, engineering design is already occurring at much greater depths. It may therefore be interesting to explore thermo-mechanical behaviour at much higher confining pressures (comparable to crustal process research discussed in § 2.6.1), likely outside of the purely brittle regime of deformation for many rock types, and where

micro-cracking may no longer be the dominant progressive deformation process;

- mineralogy - triaxial tests undertaken in this study were undertaken on two rock types with very similar mineralogy, the Thornhill Rock and Midgley Grit. There would be interest in exploring the effect of mineralogy and texture on thermo-mechanical behaviour. For example, it would be interesting to test a mono-mineralic rock type against a rock type with a large disparity in thermal properties. It would also be of interest to further examine the effects of grain size, and grain size distribution, as well as grain sorting, and grain cementation. It would of course also be prudent to test any specific rock type for which an engineering project with thermo-mechanical loading may be designed;

- fluids - testing in this study was undertaken on specimens oven dried at 40 °C for 48 h prior to testing, and no fluids were introduced to specimens during testing. Whilst there would be interest in altering the temperature at which specimens were dried at prior to testing (discussed further in § 7.4.2.3), it would also be worth introducing fluids to the triaxial tests in both drained and undrained states, to investigate the effects on thermo-mechanical behaviour, particularly on discontinuity strength and stiffness. Whilst it is proposed that GDFs will initially be built dry. Once constructed and closed, pumping of GDFs will be stopped, and saturation will occur. This allows the potential for substantial pore pressures to accumulate with thermal loading (Garitte et al., 2017). With fluid thermal expansion being substantially greater than mineralogical thermal expansion, localised stress distributions in undrained conditions would be very different in intact rock, and progressive damage could occur at lower temperatures. In discontinuities, fluid thermal expansion could cause increased normal stresses on discontinuity walls and even increase apertures, potentially causing decreased shear strength. Undertaking laboratory triaxial shear experiments at elevated temperatures with fluids are currently limited by the inability of pore pressure systems to handle multi-phase fluids, which is likely at temperatures approaching 100 °C; and

- specimen size - 54 mm diameter specimens were used for thermo-mechanical triaxial testing throughout this study. Results suggest that thermo-mechanical behaviour is directly related to the ability for localised stresses due to heterogeneous thermal expansion to be able to dissipate. Laboratory testing on different sized

specimens would therefore be useful to study potential scalable effects and look at relating behaviour to rock block size in fractured rock masses.

In addition, it would be beneficial to introduce the use of acoustic emission monitoring during thermo-mechanical triaxial testing, to monitor the initiation and accumulation of thermally induced micro-cracking, as has previously been utilised by Chen and Wang (1980), Johnson et al. (1978) and Widhalm et al. (1997).

When substantially more thermo-mechanical triaxial testing has been undertaken, it would be worthwhile compiling a database of all test results to aid in the creation of a constitutive model for the thermo-mechanical behaviour of intact rock and/or shear behaviour of discontinuities.

7.4.2.2 Thermal closure testing

Discontinuity closure tests were undertaken by Bandis et al. (1983); Goodman (1974) and Goodman et al. (1968) to deduce the stress dependence of discontinuity closure under different mechanical loads (discussed further in § 2.4.3 and 6.7.1). A similar laboratory set up could be used to examine discontinuity closure under thermal loading. However, laboratory thermal closure experiments are currently restricted by the ability to accurately measure axial displacement during thermal loading. It is not possible to use displacement readings from LVDTs on the current testing apparatus, due to the thermal expansion and deformation of the loading rig itself. As discussed in § 3.5.5 and 5.3, the axial extensometers used in this study did not accurately record deformation during thermal loading on specimens of aluminium or rock. This may have been due to deformation in the jacketing system during heating, which could be revised. Alternatively, it may be possible to utilise recent developments in the use of fibre optic strain measurement systems, similar to those currently being developed by McDermott et al. (2018).

If thermal closure experiments could be undertaken, then it would also be possible to undertake thermal over-closure experiments, by monitoring normal displacements on the discontinuity upon the removal of a thermal load. This would allow a smaller scale study of thermal over-closure effects to be undertaken and compared with large scale

experiments that have demonstrated the effects of thermal over-closure (e.g. Barton (1982, 2007); Hardin et al. (1982)). The potential for thermal over-closure effects has particular implications for the stability of GDFs, where the thermal loading will decrease over the thousands of years following disposal. A better understanding of thermal over-closure through laboratory scale testing would allow for the inclusion of thermal over-closure effects into complex THM models.

7.4.2.3 Thermal Kaiser effect

The Kaiser effect was discovered by Joseph Kaiser in the early 1950s (Kaiser, 1953) and was comprehensively reviewed by Lavrov (2003). It explains the 'stress memory' of materials, due to irreversible progressive damage accumulated when subjected to different mechanical loads. Goodman (1963) first investigated the Kaiser effect in sandstone, and found that under cyclic loading, acoustic emissions from micro-cracking only occurred when the peak stress from the previous loading cycle was surpassed.

Whilst the Kaiser effect is well understood for mechanical loading, the potential for a thermal Kaiser effect to also exist has been ignored until recent work by Browning et al. (2017). All specimens of Thornhill Rock and Midgley Grit used in this study were oven dried at 40 °C for 48 h prior to testing. 40 °C was selected as it was below the first thermal load applied in thermo-mechanical triaxial tests of 50 °C, however, numerical simulations discussed in § 6.6.3 suggest the onset of thermal micro-cracking in specimens of Midgley Grit from approximately 28 °C. Therefore, further investigating a thermal Kaiser effect would allow for increased knowledge of the thermal stress history of a lithology, the likely pre-existing state of micro-cracking within specimens, and the potential temperature for the onset of further thermally induced micro-cracking.

7.4.3 Numerical modelling

7.4.3.1 Simulation in other DEM codes

A review of different DEM software capable of simulating progressive damage in rock was provided in Chapter 2, with particle methods such as PFC providing the main other alternative to Voronoi generations in UDEC. Whilst PFC was not utilised in this study,

recent work utilising differing particle bond types have successfully navigated problems related to the use of round particles to simulate granular and crystalline materials (Peng et al., 2018; Wu and Xu, 2016). A comparative study between results in particle based and Voronoi based simulations could therefore be used to further validate and understand micro-mechanical processes occurring in the laboratory.

7.4.3.2 Changes in model geometry & properties

3 mm average Voronoi grain size was used in numerical simulations of both the Thornhill Rock and Midgley Grit in this study, despite being significantly larger than the grain size of laboratory specimens (discussed further and justified in § 6.3). A 3 mm grain size allowed for representative mechanical failure mechanisms to occur with maximum computational efficiency. It would, however, be of interest to undertake a sensitivity analysis of changing grain size on the thermo-mechanical simulations. Widhalm et al. (1997) examined the onset of thermal micro-cracking in laboratory specimens of fine-grained and coarse-grained crystalline marble and found that the onset of micro-cracking occurred at lower temperature in the coarse-grained marble.

Only one set of calibrated mechanical micro-parameters was applied to all blocks and contacts within the models in this study. It would be of interest to investigate the sensitivity of the models to this compared to calibrating the mechanical properties for relevant mineral percentages of the blocks and contacts and assessing the differences in progressive damage and failure mechanisms. It would also be of interest to apply a statistical variation to the micro-parameters and again assess the effect on progressive damage, and whether micro-cracking would then primarily propagate at weaker contacts. The thermo-mechanical simulations applied single thermal property values (specific heat capacity, thermal conductivity and linear thermal expansion coefficient) to Voronoi grains (Table 2.3) over the temperature range (20 to 100 °C). However, it is known that thermal properties of most rock types are non-linear with increasing temperature (Kant et al., 2017). The thermo-mechanical simulations could be refined by applying temperature dependent thermal properties. As with the mechanical properties discussed above, applying statistical variation (normal or log-normal distribution) to the thermal properties applied to blocks could also be explored, allowing further investigation of the build up of localised stresses due to differential thermal expansion.

7.4.3.3 Constitutive model development

The numerical simulations in this study utilise a Mohr-Coulomb constitutive model with residual strength for all Voronoi contacts. As discussed in § 6.4, the constitutive model limits the models ability to simulate yielding once unstable crack accumulation begins (Fig. 2.1E), instead resulting in an unrealistically brittle behaviour (Fig. 6.4). Whilst none of the other constitutive models currently commercially available in UDEC are more suitable than the Mohr-Coulomb constitutive model for simulating the materials used in this study, Farahmand (2017) and Vazaios (2018) have recently implemented a cohesive crack model in UDEC, which better simulates poro-elastic and yielding behaviour. It would be worthwhile replicating this work to further refine the numerical simulations in this study.

If further thermo-mechanical triaxial shear testing and thermal over-closure laboratory testing could successfully be undertaken to allow a constitutive model to be created that included thermal over-closure effects, it would be worthwhile implementing this model in to UDEC or a similar DEM software, as the first stage to including thermal closure and over-closure effects into complex THM models.

7.4.3.4 2D vs. 3D

The difficulty in generating 3D Voronoi geometries as well as computational efficiency has typically limited the application of Voronoi geometries to 2D simulations. However, expansion of numerical modelling from 2D plane strain to 3D would allow the accumulation of micro-cracks to occur in 3D, as well as representative discontinuity roughness to be modelled in 3D. Ghazvinian et al. (2014) and Ghazvinian (2015) utilised open-source software Neper (Quey, 2014; Quey et al., 2011) to generate and perform mechanical simulations of ambient temperature triaxial tests on 3D Voronoi geometries (Fig. 7.1a) in UDEC's 3D sister software 3DEC. Neper also allows the generation of anisotropic Voronoi geometries (Fig. 7.1b), allowing the simulation of mechanical testing on anisotropic rock types.

The thermo-mechanical GBM simulations undertaken in UDEC in this study are currently limited by computational efficiency, with thermo-mechanical simulations on 54

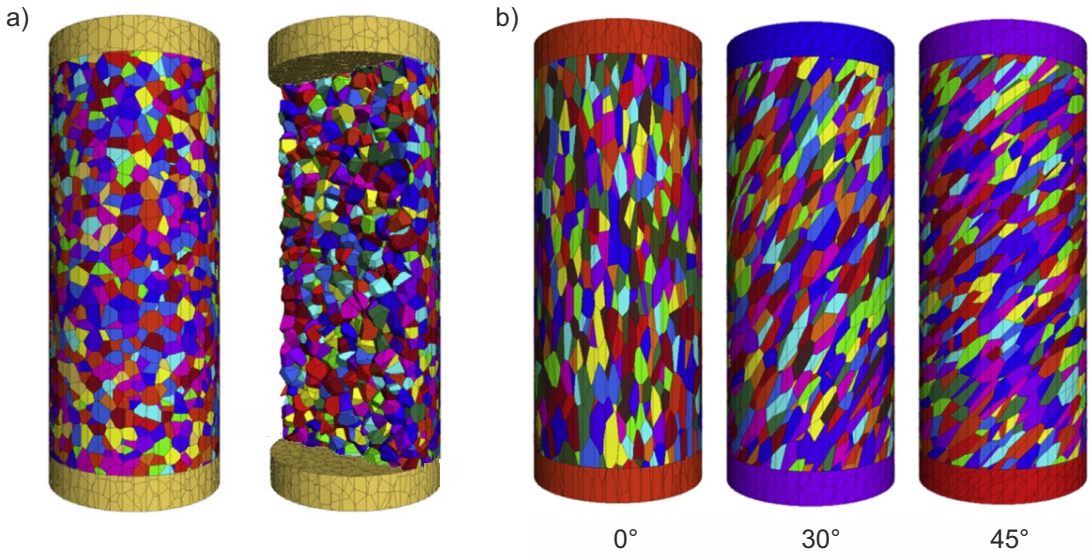

Figure 7.1: a) A 3D Voronoi GBM generated in Neper and imported to 3DEC. b) Anisotropic Voronoi GBMs generated in Neper and imported to 3DEC. After Ghazvinian et al. (2014).

by 120 mm rectangular specimens taking approximately 11 days to reach 100 °C (Table C.1) and requiring over 50 GB of random access memory. However, parallelisation of the code to use multiple cores could reduce run times considerably and make it feasible to run thermo-mechanical simulations in 3D. It would then be of interest to undertake a comparative study between 2D and 3D simulations.

7.4.4 Summary

To summarise, the aspects of future work that would be most interesting to research as direct follow-on work from the results of this study are:

- repeat the laboratory testing undertaken in this study on different sized specimens and on discontinuities with different roughness parameters, to understand the scaling effects on the thermo-mechanical behaviour;
- deduce a method for undertaking laboratory normal stiffness tests at elevated temperatures, to allow the effects of discontinuity over-closure upon cooling to be examined;
- introduce undrained fluids to the laboratory elevated temperature triaxial ex-

periments, to examine the effects of increased pore pressures on the thermo-mechanical behaviour of intact rock and discontinuities; and

- apply a different constitutive block model in numerical simulations to better capture the mechanical behaviour of the granular lithology, and apply or develop a different constitutive joint model to the discontinuity to allow shear simulations to be undertaken.

Bibliography

Alonso, E. E. and Pinyol, N. M. (2010). Criteria for rapid sliding I. A review of Vaiont case. *Engineering Geology*, 114(3-4):198–210.

AlpTransit (2016). Project data - raw construction Gotthard Base Tunnel. Technical report.

Amontons, G. (1699). De la resistance causee dans les machines. *Memoires de l'Academie Royale A*, pages 257–282.

Andersson, J. C. (2007). *Rock Mass Response to Coupled Mechanical Thermal Loading. Äspö Pillar Stability Experiment, Sweden.* PhD thesis, Royal Institute of Technology, Stockholm, Sweden.

Andersson, J. C., Martin, C. D., and Stille, H. (2009). The Äspö Pillar Stability Experiment: Part II— Rock mass response to coupled excavation-induced and thermal-induced stresses. *International Journal of Rock Mechanics and Mining Sciences*, 46(5):879–895.

ASTM (2008). Standard guides for using rock-mass classification systems for engineering purposes. In *American Society for Testing Materials. ASTM D 5878-08*, page 30.

Babanouri, N., Karimi Nasab, S., Baghbanan, A., and Mohamadi, H. R. (2011). Overconsolidation effect on shear behavior of rock joints. *International Journal of Rock Mechanics and Mining Sciences*, 48(8):1283–1291.

Bahrani, N., Kaiser, P. K., and Valley, B. (2014). Distinct element method simulation of an analogue for a highly interlocked, non-persistently jointed rockmass. *International Journal of Rock Mechanics and Mining Sciences*, 71:117–130.

BIBLIOGRAPHY

Bandis, S. (1980). *Experimental Studies of Scale Effects on Shear Strength and Deformation of Rock Joints*. PhD thesis, University of Leeds.

Bandis, S., Lumsden, A., and Barton, N. (1983). Fundamentals of rock joint deformation. *International Journal of Rock Mechanics and Mining Sciences & Geomechanics Abstracts*, 20(6):249–268.

Barton, N. (1972). A model study of rock-joint deformation. *International Journal of Rock Mechanics and Mining Sciences & Geomechanics Abstracts*, 9(5):579–582.

Barton, N. (1973). Review of a new shear-strength criterion for rock joints. *Engineering Geology*, 7(4):287–332.

Barton, N. (1976). The shear strength of rock and rock joints. *International Journal of Rock Mechanics and Mining Sciences & Geomechanics Abstracts*, 13(9):255–279.

Barton, N. (1982). Modelling rock joint behaviour from in situ block tests: implications for nuclear waste repository design ONWI-308. Technical report, Office of Nuclear Waste Isolation.

Barton, N. (2007). Thermal over-closure of joints and rock masses and implications for HLW repositories. *The Second Half Century of Rock Mechanics, 11th Congress of the International Society for Rock Mechanics*, pages 109 – 116.

Barton, N., Bandis, S., and Bakhtar, K. (1985). Strength, deformation and conductivity coupling of rock joints. *International Journal of Rock Mechanics and Mining Sciences & Geomechanics Abstracts*, 22(3):121–140.

Barton, N. and Choubey, V. (1977). The shear strength of rock joints in theory and practice. *Rock Mechanics*, 10(1-2):1–54.

Baud, P. and Meredith, P. G. (1997). Damage accumulation during triaxial creep of Darley Dale sandstone from pore volumometry and acoustic emission. *International Journal of Rock Mechanics & Mining Science & Geomechanics Abstracts*, 34(3-4):371.

Bauer, S. J. and Handin, J. (1983). Thermal expansion and cracking of three confined water-saturated igneous rocks to 800°C. *Rock Mechanics and Rock Engineering*, 16(3):181–198.

Bauer, S. J. and Johnson, B. (1979). Effects of slow uniform heating on the physical properties of the westerly and charcoal granites. In *Proceedings of the 20th U.S. Symposium on Rock Mechanics*, pages 7–18.

Beer, A. J., Stead, D., and Coggan, J. S. (2002). Technical Note Estimation of the Joint Roughness Coefficient (JRC) by Visual Comparison. *Rock Mechanics and Rock Engineering*, 35(1):65–74.

Belayachi, N., Mallet, C., and El Marzak, M. (2019). Thermally-induced cracks and their effects on natural and industrial geomaterials. *Journal of Building Engineering*, 25:1–12.

Bieniawski, Z. (1967). Mechanism of brittle fracture of rock: Part I - theory of the fracture process. *International Journal of Rock Mechanics and Mining Sciences & Geomechanics Abstracts*, 4(4):395–404.

Bieniawski, Z. and Bernede, M. (1979). Suggested methods for determining the uniaxial compressive strength and deformability of rock materials: Part 1. Suggested method for determining deformability of rock materials in uniaxial compression. *International Journal of Rock Mechanics and Mining Sciences & Geomechanics Abstracts*, 16(2):138–140.

Bieniawski, Z. and Hawkes, I. (1978). Suggested methods for determining tensile strength of rock materials. *International Journal of Rock Mechanics & Mining Science & Geomechanics Abstracts*, 15:99–103.

Blanpied, M., Lockner, D. A., and Byerlee, J. D. (1995). Frictional slip of granite at hydrothermal conditions. *Journal of Geophysical Research*, 100(B7):13045–13064.

Bobet, A. and Einstein, H. (1998). Fracture coalescence in rock-type materials under uniaxial and biaxial compression. *International Journal of Rock Mechanics and Mining Sciences*, 35(7):863–888.

Bombolakis, E. (1968). Photoelastic study of initial stages of brittle fracture in compression. *Tectonophysics*, 6(6):461–473.

Bowden, F. (1954). The friction of non-metallic solids. *J. Inst. Petrol.*, 40:89–103.

BIBLIOGRAPHY

Bowden, F. and Tabor, D. (1956). *The friction and lubrication of solids*. Oxford: Clarendon Press.

Brace, W. F., Paulding, B. W., and Scholz, C. (1966). Dilatancy in the fracture of crystalline rocks. *Journal of Geophysical Research*, 71(16):3939–3953.

Brown, S. R. and Scholz, C. H. (1985). Broad bandwidth study of the topography of natural rock surfaces. *Journal of Geophysical Research*, 90(B14):12575.

Browning, J., Daoud, A., Meredith, P. G., and Mitchell, T. M. (2017). Mineralogical control on thermal damage and the presence of a thermal Kaiser effect during temperature-cycling experiments. In *American Geophysical Union, Fall Meeting, San Francisco*.

Bruner, W. M. (1979). Crack growth and the thermoelastic behaviour of rocks. *Journal of Geophysical Research*, 84(B10):5578–5590.

Byerlee, J. D. (1967). Frictional Characteristics of Granite under High Confining Pressure. *Journal of Geophysical Research*, 72(14):3639–3648.

Čermák, V. and Rybach, L. (1982). Thermal Conductivity and Specific Heat of Minerals and Rocks. In Beblo, M., editor, *Geophyiscs - Physical Properties of Rocks*, chapter Landbolt-B, pages 305–343. Springer Berlin Heidelberg.

Chae, B. G., Ichikawa, Y., Jeong, G. C., Seo, Y. S., and Kim, B. C. (2004). Roughness measurement of rock discontinuities using a confocal laser scanning microscope and the Fourier spectral analysis. *Engineering Geology*, 72(3-4):181–199.

Chen, Y. and Wang, C.-Y. (1980). Thermally induced acoustic emission in Westerly Granite. *Geophysical Research Letters*, 7(12):1089–1092.

Chiu, C.-C., Wang, T.-T., Weng, M.-C., and Huang, T.-H. (2013). Modeling the anisotropic behavior of jointed rock mass using a modified smooth-joint model. *International Journal of Rock Mechanics and Mining Sciences*, 62:14–22.

Cho, N., Martin, C. D., and Sego, D. C. (2007). A clumped particle model for rock. *International Journal of Rock Mechanics and Mining Sciences*, 44(7):997–1010.

Christianson, M., Board, M., and Rigby, D. (2006). UDEC Simulation of Triaxial Testing of Lithophysal Tuff. In *The 41st U.S. Symposium on Rock Mechanics, 17-21 June, Golden, Colorado.*

Chryssanthakis, P. and Barton, N. (1990). Joint roughness (JRCn) characterisation of a rock joint and joint replica at 1m scale. *Proceedings of the International Symposium on Rock Joints, Loen, Norway*, pages 27–33.

Clark, V. A., Spencer, T. W., and Tittmann, B. R. (1981). The effect of thermal cycling on the seismic quality factor Q of some sedimentary rocks. *Journal of Geophysical Research*, 86(B8):7087–7094.

Collins, B. D. and Stock, G. M. (2016). Rockfall triggering by cyclic thermal stressing of exfoliation fractures. *Nature Geoscience*, 9(5):395–400.

Coulomb, C. (1776). Essai sur une application des règles de maximis et minimis à quelques problèmes de statique, relatifs à l'architecture. *Acad. R. Sci. Mém. Math. Phys. par Divers Savants*, 7:343–382.

Coulson, J. (1971). Shear strength of flat surfaces in rock. In *Proceedings of the 13th Symposium on Rock Mechanics, Illinois. ASCE.*, pages 77–105.

Cundall, P. A. (1979). A discrete numerical model for granular assemblies. *Geotechnique*, 29(1):47–65.

Cunha, A. (1990). Scale effects in rock mechanics. In *Proceedings of the 1st International Symposium on Scale Effects in Rock Masses*, pages 3–27.

Damjanac, B., Board, M., Lin, M., Kicker, D., and Leem, J. (2007). Mechanical degradation of emplacement drifts at Yucca Mountain—A modeling case study: Part II: Lithophysal rock. *International Journal of Rock Mechanics and Mining Sciences*, 44(3):368–399.

Deisman, N., Ivars, D. M., and Pierce, M. (2008). PFC2D Smooth joint contact model numerical experiments. In *Proceedings of the GeoEdmonton'08, Paper 83, Edmonton, Canada.*

Den Outer, A., Kaashoek, J., and Hack, H. (1995). Difficulties with using continuous fractal theory for discontinuity surfaces. *International Journal of Rock Mechanics and Mining Sciences & Geomechanics Abstracts*, 32(1):3–9.

Department for Business Energy & Industrial Strategy (2018). Implementing Geological Disposal-Working With Communities: An updated framework for the long-term management of higher activity radioactive waste. Technical report.

Diederichs, M. (2007). The 2003 Canadian geotechnical colloquium: Mechanistic interpretation and practical application of damage and spalling prediction criteria for deep tunnelling. *Canadian Geotechnical Journal*, 44(9):1082–1116.

Diederichs, M. S. (2003). Manuel Rocha Medal Recipient Rock Fracture and Collapse Under Low Confinement Conditions. *Rock Mechanics and Rock Engineering*, 36(5):339–381.

Donath, F. (1961). Experimental study of shear failure in anisotropic rocks. *GSA Bulletin*, 72(6):985–989.

Drennon, C. and Handy, R. (1972). Stick-slip friction of lightly loaded rock. *International Jounral of Rock Mechanics and Mining Science Geomechanics Abstracts*, 9(5):603–608.

Dunn, D. E., LaFountain, L. J., and Jackson, R. E. (1973). Porosity dependence and mechanism of brittle fracture in sandstones. *Journal of Geophysical Research*, 78(14):2403–2417.

Eberhardt, E., Stead, D., Stimpson, B., and Read, R. S. (1998). Identifying crack initiation and propagation thresholds in brittle rock. *Canadian Geotechnical Journal*.

EDF (2011). CloudCompare v2.9.

Eppes, M. C. and Keanini, R. (2017). Mechanical weathering and rock erosion by climate-dependent subcritical cracking. *Reviews of Geophysics*, 55(2):470–508.

Fairhurst, C. (2004). Nuclear waste disposal and rock mechanics: contributions of the Underground Research Laboratory (URL), Pinawa, Manitoba, Canada. *International Journal of Rock Mechanics and Mining Sciences*, 41(8):1221–1227.

Farahmand, K. (2017). *Characterisation of rock mass properties and excavation damage zone (EDZ) using a synthetic rock mass (SRM) approach.* PhD thesis, Queen's University.

Farahmand, K. and Diederichs, M. (2015). A calibrated Synthetic Rock Mass (SRM) model for simulating crack growth in granitic rock considering grain scale heterogeneity of polycrystalline rock. In *49th US Rock Mechanics/Geomechanics Symposium 28th June to 1st July, Sanfrancisco, California.*

Fardin, N., Stephansson, O., and Jing, L. (2001). The scale dependence of rock joint surface roughness. *International Journal of Rock Mechanics and Mining Sciences*, 38(5):659–669.

Ferrero, A. (1999). Interpretazione con modelli matamatici di misure di rugosita di discontinuita naturali in roccia. In *Contributo in Atti di Convegno*, pages 101–106.

Franklin, J. A., Vogler, U., Szlavin, J., Edmond, J., and Bieniawski, Z. (1981). Suggested Methods for Determining Water Content, Porosity, Density, Absorption and Related Properties and Swelling and Slake-Durability Index Properties. In Brown, E., editor, *Rock Characterisation Testing and Monitoring. The commission on Testing Methods International Society for Rock Mechanics*, pages 71–94.

Fredrich, J. T. and Wong, T.-f. (1986). Micromechanics of thermally induced cracking in three crustal rocks. *Journal of Geophysical Research: Solid Earth*, 91(B12):12743–12764.

Gao, F. and Stead, D. (2014). The application of a modified Voronoi logic to brittle fracture modelling at the laboratory and field scale. *International Journal of Rock Mechanics and Mining Sciences*, 68:1–14.

Garitte, B., Nguyen, T. S., Barnichon, J. D., Graupner, B. J., Lee, C., Maekawa, K., Manepally, C., Ofoegbu, G., Dasgupta, B., Fedors, R., Pan, P. Z., Feng, X. T., Rutqvist, J., Chen, F., Birkholzer, J., Wang, Q., Kolditz, O., and Shao, H. (2017). Modelling the Mont Terri HE-D experiment for the Thermal — Hydraulic — Mechanical response of a bedded argillaceous formation to heating. *Environmental Earth Sciences*, 76(345):1–20.

Ge, Y., Kulatilake, P. H., Tang, H., and Xiong, C. (2014). Investigation of natural rock joint roughness. *Computers and Geotechnics*, 55:290–305.

Gentier, S., Riss, J., Archambault, G., Flamand, R., and Hopkins, D. (2000). Influence of fracture geometry on shear behavior. *International Journal of Rock Mechanics and Mining Sciences*, 37(1-2):161–174.

George, J., Finley, R., and Riggins, M. (1999). Conduct of plate loading tests at Yucca Mountain, Nevada. In *The 37th U.S. Symposium on Rock Mechanics, 7-9 June, Vail, Colorado*, pages 721–727.

Ghazvinian, E. (2015). *Fracture Initiation and Propagation in Low Porosity Crystalline Rocks: Implications for Excavation Damage Zone (EDZ) Mechanics.* PhD thesis, Queen's University.

Ghazvinian, E., Diederichs, M. S., and Quey, R. (2014). 3D random Voronoi grain-based models for simulation of brittle rock damage and fabric-guided micro-fracturing. *Journal of Rock Mechanics and Geotechnical Engineering*, 6(6):506–521.

Glover, P., Baud, P., Darot, M., Meredith, P., Boon, S., LeRavalec, M., Zoussi, S., and Reusche, T. (1995). alpha/beta phase transition in quartz monitored using acoustic emissions. *Geophysical Journal International*, 120:775–782.

Goodman, R. E. (1963). Subaudible noise during compression of rocks. *Bulletin of the Geological Society of America*, 74:487–490.

Goodman, R. E. (1974). The mechanical properties of joints. In *Proceedings of the Third Congress of the International Society for Rock Mechanics, Denver, Colorado.*, pages 127–140.

Goodman, R. E., Taylor, R., and Brekke, T. (1968). A model for the mechanics of jointed rock. In *Proceedings of the American Society of Civil Engineers*, pages 637–659.

Grasselli, G. (2001). *Shear strength of rock joints based on quantified surface description.* PhD thesis, Ecole Polytechnique Federale de Lausanne.

Grasselli, G., Wirth, J., and Egger, P. (2002). Quantitative three-dimensional description of a rough surface and parameter evolution with shearing. *International Journal of Rock Mechanics and Mining Sciences*, 39(6):789–800.

Griffith (1924). Theory of Rupture. In *Proceedings of the First International Congress of Applied Mechanics*, pages 55–63.

Griffith, A. (1921). The phenomena of rupture and flow in solids. *Philosophical Transactions of the Royal Society of London. Series A, Containing Papers of a Mathematical or Physical Character*, 221:163–198.

Handanyan, J., Danek, E., D'Andrea, R., and Sade, J. (1990). The role of tension in failure of jointed rock. In *Proceedings of the International Symposium on Rock Joints, Loen, Norway*, pages 195–202.

Hardin, E., Barton, N., Lingle, R., Board, M., and Voegele, M. (1982). A heated flatjack test series to measure the thermomechanical and transport properties of in situ rock masses ONWI-260. Technical report, Office of Nuclear Waste Isolation, Columbus, OH.

Hawkes, I. and Mellor, M. (1970). Uniaxial testing in rock mechanics laboratories. *Engineering Geology*, 4(3):179–285.

Heard, H. C. and Page, L. (1982). Elastic moduli, thermal expansion, and inferred permeability of two granites to 350°C and 55 MPa. *Journal of Geophysical Research*, 87(B11):9340–9348.

Hencher, S. R. (1976). Simple sliding apparatus for measurement of rock joint friction. *Geotechnique*, 26(4):641–644.

Hencher, S. R. and Richards, L. R. (1982). The basic frictional resistance of sheeting joints in Hong Kong granite. *Hong Kong Eng*, 11(2):21–25.

Hencher, S. R. and Richards, L. R. (1989). Laboratory direct shear testing of rock discontinuities. *Ground Engineering*, 22(2):24–31.

Heuze, F. (1983). High-temperature mechanical, physical and Thermal properties of granitic rocks — A review. *International Journal of Rock Mechanics and Mining Sciences & Geomechanics Abstracts*, 20(1):3–10.

Hoek, E. (1964). Fracture of anisotropic rock. *Journal of the South African Institute of Mining and Metallurgy*, 64(10):501–518.

Hoek, E. and Bieniawski, Z. T. (1965). Brittle Rock Fracture Propagation In Rock Under Compression. *International Journal of Fracture Mechanics*, 1(3):137–155.

Hoek, E. and Brown, E. (1980). *Underground Excavations in Rock*.

Hoek, E., Carranza-Torres, C., and Corkum, B. (2002). Hoek-Brown Failure Criterion 2002 Edition. In *Proceedings of NARMS-TAC Conference, Toronto, 2002*, pages 267–273.

Horn, H. and Deere, D. (1962). Frictional characteristics of minerals. *Geotechnique*, 12:319–35.

Hoskins, E. R., Jaeger, J. C., and Rosengren, K. J. (1968). A medium scale direct friction experiment. *International Journal of Rock Mechanics and Mining Sciences*, 5:143–154.

Huang, T. and Doong, Y. (1990). Anisotropic shear strength of rock joints. In *Proceedings of the International Symposium on Rock Joints, Loen, Norway*, pages 211–218.

Huang, X., Haimson, B., Plesha, M., and Qiu, X. (1993). An investigation of the mechanics of rock joints - Part I. Laboratory investigation. *International Journal of Rock Mechanics and Mining Sciences & Geomechanics Abstracts*, 30(3):257–269.

Huotari, T. and Kukkonen, I. (2004). Thermal Expansion Properties of Rocks: Literature Survey and Estimation of Thermal Expansion Coefficient for Olkiluoto Mica Gneiss. Working Report 2004-04. Technical report.

ISRM (1978). International Society for Rock Mechanics commission on standardisation of laboratory and field tests: suggested methods for the quantitative description of discontinuities in rock masses. *International Jounral of Rock Mechanics and Mining Science Geomechanics Abstracts*, 15(6):319–368.

Itasca (2008). Particle Flow Code in 2 dimensions (PFC2D), Ver. 4.0.

Itasca (2014a). The Universal Distinct Element Code (UDEC), Ver. 6.0.

Itasca (2014b). UDEC Version 6.0. User's Guide — Theory and Background. Technical report.

Jaeger, J., Cook, N., and Zimmerman, R. (2007). *Fundamentals of Rock Mechanics*, volume 1. Blackwell Publishing Ltd, fourth edition.

Jaeger, J. C. (1959). The frictional properties of joints in rock. *Pure and Applied Geophysics*, 43(1):148–158.

Jang, H. S., Kang, S. S., and Jang, B. A. (2014). Determination of Joint Roughness Coefficients Using Roughness Parameters. *Rock Mechanics and Rock Engineering*, 47(6):2061–2073.

Jiang, Q., Feng, X., Gong, Y., Song, L., Ran, S., and Cui, J. (2016a). Reverse modelling of natural rock joints using 3D scanning and 3D printing. *Computers and Geotechnics*, 73:210–220.

Jiang, Q., Feng, X., Song, L., Gong, Y., Zheng, H., and Cui, J. (2016b). Modeling rock specimens through 3D printing: Tentative experiments and prospects. *Acta Mechanica Sinica/Lixue Xuebao*, 32(1):101–111.

Jing, L. and Stephansson, O. (2007). *Fundamentals of Discrete Element Methods for Rock Engineering Theory and Applications*. Elsevier.

Johnson, B., Gangi, A., and Handin, J. (1978). Thermal cracking of rock subjected to slow, uniform temperature changes. In *Proceedings of the 19th U.S. Symposium on Rock Mechanics, 1-3 May, Reno, Nevada*, pages 259–267.

Kaiser, J. (1953). Erkenntnisse und Folgerungen aus der Messung von Geräuschen bei Zugbeanspruchung von metallischen Werkstoffen. *Archiv Eisenhüttenwesen*, 24:43–45.

Kalman, K., Andreas, T., and Einstein, H. (1983). Suggested Methods for Determining the Strength of Rock Materials in Triaxial Compression: Revised Version. *International Jounral of Rock Mechanics and Mining Science Geomechanics Abstracts*, 20(6):285–290.

Kant, M. A., Ammann, J., Rossi, E., Höser, D., Rohr, P. R. V., and Madonna, C. (2017). Thermal properties of Central Aare granite for temperatures up to 500°C.

Irreversible changes due to thermal crack formation. *Geophysical Research Letters*, 44(2):771–776.

Kazerani, T. (2011). *Micromechanical Study of Rock Fracture and Fragmentation under Dynamic Loads using Discrete Element Method*. PhD thesis, Ecole Polytechnique Federale de Lausanne.

Kazerani, T., Yang, Z. Y., and Zhao, J. (2012). A discrete element model for predicting shear strength and degradation of rock joint by using compressive and tensile test data. *Rock Mechanics and Rock Engineering*, 45(5):695–709.

Kim, T. and Jeon, S. (2019). Experimental Study on Shear Behavior of a Rock Discontinuity Under Various Thermal, Hydraulic and Mechanical Conditions. *Rock Mechanics and Rock Engineering*, 52(7):2207 – 2226.

Kong, L., Ostadhassan, M., Li, C., and Tamimi, N. (2017). Rock Physics and Geomechanics of 3-D Printed Rocks. In *51st US Rock Mechanics / Geomechanics Symposium, San Francisco, California, USA, 25 Jun 2017 - 28 Jun 2017*, pages 1–8.

Kulatilake, P., Shou, G., Huang, T., and Morgan, R. (1995). New peak shear strength criteria for anisotropic rock joints. *International Journal of Rock Mechanics and Mining Sciences & Geomechanics Abstracts*, 32(7):673–697.

Kulatilake, P. and Um, J. (1999). Requirements for accurate quantification of self-affine roughness using the roughness-length method. *International Journal of Rock Mechanics and Mining Sciences*, 36(1):5–18.

Kulatilake, P., Um, J., and Pan, G. (1997). Requirements for accurate estimation of fractal parameters for self-affine roughness profiles using the line scaling method. *Rock Mechanics and Rock Engineering*, 30(4):181–206.

Kulatilake, P., Um, J., and Pan, G. (1998). Requirements for accurate quantification of self-affine roughness using the variogram method. *International Journal of Solids and Structures*, 35(31-32):4167–4189.

Kulatilake, P. H. S. W., Balasingam, P., Park, J., and Morgan, R. (2006). Natural rock joint roughness quantification through fractal techniques. *Geotechnical and Geological Engineering*, 24(5):1181–1202.

Kutter, H. and Otto, F. (1990). Influence of parallel and cross joints on shear behaviour of rock discontinuities. In *Proceedings of the International Symposium on Rock Joints, Loen, Norway.*, pages 243–250.

Lague, D., Brodu, N., and Leroux, J. (2013). Accurate 3D comparison of complex topography with terrestrial laser scanner: Application to the Rangitikei canyon (N-Z). *ISPRS Journal of Photogrammetry and Remote Sensing*, 82(February 2013):10–26.

Lajtai, E. and Lajtai, V. (1974). The evolution of brittle fracture in rocks. *Journal of the Geological Society*, 130(1):1–16.

Lamp, J. L., Marchant, D. R., Mackay, S. L., and Head, J. W. (2017). Thermal stress weathering and the spalling of Antarctic rocks. *Journal of Geophysical Research: Earth Surface*, 122(1):3–24.

Lan, H., Martin, C. D., and Andersson, J. C. (2013). Evolution of in situ rock mass damage induced by mechanical-thermal loading. *Rock Mechanics and Rock Engineering*, 46(1):153–168.

Lavrov, A. (2003). The Kaiser effect in rocks: Principles and stress estimation techniques. *International Journal of Rock Mechanics and Mining Sciences*, 40(2):151–171.

Lee, Y.-H., Carr, J., Barr, D., and Haas, C. (1990). The fractal dimension as a measure of the roughness of rock discontinuity profiles. *International Journal of Rock Mechanics and Mining Sciences & Geomechanics Abstracts*, 27(6):453–464.

Li, H., Li, K., Subhash, G., Kecskes, L. J., and Dowding, R. J. (2006). Micromechanical modeling of tungsten-based bulk metallic glass matrix composites. *Materials Science and Engineering: A*, 429(1-2):115–123.

Lisjak, A., Tatone, B. S. A., Grasselli, G., and Vietor, T. (2014). Numerical Modelling of the Anisotropic Mechanical Behaviour of Opalinus Clay at the Laboratory-Scale Using FEM/DEM. *Rock Mechanics and Rock Engineering*, 47(1):187–206.

Lockner, D. (1993). Room temperature creep in saturated granite. *Journal of Geophysical Research*, 98(B1):475–487.

Lockner, D., Summers, R., Moore, D., and Byerlee, J. (1982). Laboratory measurements of reservoir rock from the Geysers geothermal field, California. *International Journal of Rock Mechanics and Mining Sciences & Geomechanics Abstracts*, 19(2):65–80.

Lockner, D. A., Summers, R., and Byerlee, J. D. (1986). Effects of temperature and sliding rate on frictional strength of granite. *Pure and Applied Geophysics*, 124(3):445–469.

Lorig, L. J. and Cundall, P. A. (1989). Modeling of reinforced concrete using the distinct element method. In *Fracture of Concrete and Rock, SEM-RILEM International Conference*, pages 276–287. Springer Verlag.

Lü, C., Sun, Q., Zhang, W., Geng, J., Qi, Y., and Lu, L. (2017). The effect of high temperature on tensile strength of sandstone. *Applied Thermal Engineering*, 111:573–579.

Lu, Y., Martin, C. D., and Lan, H. (2013). Strength of intact rock containing flaws. *47th US Rock Mechanics/Geomechanics Symposium, 23 - 26 June, San Francisco, California*, pages 1–8.

Ma, Y. and Huang, H. (2018). A displacement-softening contact model for discrete element modeling of quasi-brittle materials. *International Journal of Rock Mechanics and Mining Sciences*, 104:9–19.

Maerz, N. H., Franklin, J. A., and Bennett, C. P. (1990). Joint roughness measurement using shadow profilometry. *International Journal of Rock Mechanics and Mining Sciences and Geomechanics Abstracts*, 27(5):329–343.

Mahabadi, O., Lisjak, A., Grasselli, G., Lukas, T., and Munjiza, A. (2010). Numerical modelling of a triaxial test of homogeneous rocks using the combined-finite discrete element method. In Zhao, J., Labouise, V., Dudt, J., Mathier, and J.F., editors, *Rock Mechanics in Civil and Environmental Engineering*, pages 173–176. Taylor and Francis Group, London.

Main, I. G. (2000). A damage mechanics model for power-law creep and earthquake aftershock and foreshock sequences. *Geophysical Journal International*, 142(1):151–161.

Mandelbrot, B. (1967). How long is the coast of britain? Statistical self-similarity and fractional dimension. *Science (New York, N.Y.)*, 156(3775):636–638.

Mandelbrot, B. (1983). *The fractal geometry of nature*. WH Freeman, San Francisco.

Martin, C. and Chandler, N. (1994). The progressive fracture of Lac du Bonnet granite. *International Journal of Rock Mechanics and Mining Sciences & Geomechanics*, 31(6):643–659.

McDermott, C. I., Fraser-Harris, A., Sauter, M., Couples, G. D., Edlmann, K., Kolditz, O., Lightbody, A., Somerville, J., and Wang, W. (2018). New Experimental Equipment Recreating Geo-Reservoir Conditions in Large, Fractured, Porous Samples to Investigate Coupled Thermal, Hydraulic and Polyaxial Stress Processes. *Scientific Reports*, (8):1–12.

McKinstry, H. (1965). Thermal expansion of clay minerals. *The American Mineralogist*, 50:212–222.

McLamore, R. and Gray, K. E. (1967). The Mechanical Behavior of Anisotropic Sedimentary Rocks. *ASME Journal of Engineering for Industry*, 89:62–76.

Meredith, P. G. and Atkinson, B. K. (1985). Fracture toughness and subcritical crack growth during high-temperature tensile deformation of Westerly granite and Black gabbro. *Physics of the Earth and Planetary Interiors*, 39(1):33–51.

Metcalfe, R., Watson, S., and McEwan, T. (2015). Geosphere Parameters for Generic Geological Environments, Quintessa report to RWM, QRS-1712C-1 Version 4. Technical Report September, Radioactive Waste Management Limited.

Michot, A., Smith, D. S., Degot, S., and Gault, C. (2008). Thermal conductivity and specific heat of kaolinite: Evolution with thermal treatment. *Journal of the European Ceramic Society*, 28(14):2639–2644.

Miller, S. M., McWilliams, P. C., and Kerkering, J. C. (1990). Ambiguities in Estimating Fractal Dimension of Rock Fracture Surfaces. In *The 31st U.S. Symposium on Rock Mechanics, Golden, Colorado*, pages 471–481.

Morelli, G. L. (2014). On Joint Roughness: Measurements and Use in Rock Mass Characterization. *Geotechnical and Geological Engineering*, 32(2):345–362.

Neingo, P. and Tholana, T. (2016). Trends in productivity in the South African gold mining industry. *Journal of the South African Institute of Mining and Metallurgy*, 116(3):283–290.

Neville, A. (1975). High Alumina Cement Concrete. *The Construction Press*.

Nicksiar, M. and Martin, C. D. (2012). Evaluation of methods for determining crack initiation in compression tests on low-porosity rocks. *Rock Mechanics and Rock Engineering*, 45(4):607–617.

Niemeijer, A. R., Spiers, C. J., and Peach, C. J. (2008). Frictional behaviour of simulated quartz fault gouges under hydrothermal conditions: Results from ultra-high strain rotary shear experiments. *Tectonophysics*, 460(1-4):288–303.

Odedra, A., Ohnaka, M., Mochizuki, H., and Sammonds, P. (2001). Temperature and pore pressure effects on the shear strength of granite in the brittle-plastic transition regime. *Geophysical Research Letters*, 28(15):3011–3014.

Ogilvie, S., Isakov, E., Taylor, C., and Glover, P. (2002). A New High Resolution Optical Method for Obtaining the Topography of Fracture Surfaces in Rocks. *Image Analysis Stereology*, 21(1):61–66.

Ohnaka, M., Akatsu, M., Mochizuki, H., Odedra, A., Tagashira, F., and Yamamoto, Y. (1997). A constitutive law for the shear failure of rock under lithospheric conditions. *Tectonophysics*, 277:1–27.

Olsson, W. A. (1974). Effects of temperature, pressure and displacement rate on the frictional characteristics of a limestone. *International Journal of Rock Mechanics and Mining Sciences and*, 11(7):267–278.

Osinga, S., Zambrano-Narvaez, G., and Chalaturnyk, R. (2015). Study of geomechanical properties of 3D printed sandstone analogue. In *Proceedings of the 49th U.S. Rock Mechanics/Geomechanics Symposium, San Francisco, California*, pages 15–547.

Papaliangas, T. (1996). *Shear behaviour of rock discontinuities and soil-rock interfaces*. PhD thesis, University of Leeds.

Park, J.-W., Park, C., Ryu, D., and Park, E.-S. (2015). Numerical simulation of thermo-mechanical behavior of rock using a grain-based distinct element model. In

ISRM Regional Symposium EUROCK 2015 - Future Development of Rock Mechanics. October 7 - 10, Salzburg, Austria, pages 707–712.

Patton, F. (1966). Multiple modes of shear failure in rock. In *Proceedings of the 1st International Congress of Rock Mechanics*, pages 509–513, Lisbon.

Patton, F. and Deere, D. (1970). Significant geological factors in rock slope stability. In *Proceedings symposium on planning open pit mines.*, pages 143–151.

Peng, J., Wong, L. N. Y., Teh, C. I., and Li, Z. (2018). Modeling Micro-cracking Behavior of Bukit Timah Granite Using Grain-Based Model. *Rock Mechanics and Rock Engineering*, 51(1):135–154.

Penman, A. (1953). Shear characteristics of a saturated silt measured in triaxial compression. *Geotechnique*, pages 312–28.

Plevová, E., Vaculíková, L., Kožušníková, A., Daněk, T., Pleva, M., Ritz, M., and Simha Martynková, G. (2011). Thermal study of sandstones from different Czech localities. *Journal of Thermal Analysis and Calorimetry*, 103(3):835–842.

Potyondy, D. and Cundall, P. (2004). A bonded-particle model for rock. *International Journal of Rock Mechanics and Mining Sciences*, 41(8):1329–1364.

Potyondy, D. O. (2012). A flat-jointed bonded-particle material for hard rock. *46th US Rock Mechanics/Geomechanics Symposium*, page 10.

Quey, R. (2014). Neper: numerical descriptors of polycrystals (version 2.0).

Quey, R., Dawson, P. R., and Barbe, F. (2011). Large-scale 3D random polycrystals for the finite element method: Generation, meshing and remeshing. *Computer Methods in Applied Mechanics and Engineering*, 200:1729–1745.

Quintessa (2012). Understanding the Post-Closure Thermal Impact of HLW / SF Waste Packages: An NDA RWMD Research Study QRS-1384Q-R2 V2.1. Technical report.

Richter, D. and Simmons, G. (1977). Microcracks in crustal igneous rocks: Microscopy. In Heacock, J., editor, *The Earth's Crust: Its Nature and Physical Properties. Geophysics Monograph Series vol. 20*, pages 149–180.

Rybach, L. and Pfister, M. (1994). Temperature predictions and predictive temperatures in deep tunnels. *Rock Mechanics and Rock Engineering*, 27(2):77–88.

Sabir, B., Wild, S., and Bai, J. (2001). Metakaolin and calcined clays as pozzolans for concrete: A review. *Cement and Concrete Composites*, 23(6):441–454.

Shen, B. (1995). The mechanism of fracture coalescence in compression-experimental study and numerical simulation. *Engineering Fracture Mechanics*, 51(1):73–85.

Shirono, T. and Kulatilake, P. (1997). Accuracy of the spectral method in estimating fractal/spectral parameters for self-affine roughness profiles. *International Journal of Rock Mechanics and Mining Sciences*, 34(5):789–804.

Siegesmund, S., Sousa, L., and Knell, C. (2018). Thermal expansion of granitoids. *Environmental Earth Sciences*, 77(2):1–29.

Simmons, G. and Cooper, H. W. (1978). Thermal cycling cracks in three igneous rocks. *International Journal of Rock Mechanics and Mining Sciences & Geomechanics Abstracts*, 15(4):145–148.

Sirdesai, N. N., Singh, T. N., Ranjith, P. G., and Singh, R. (2017). Effect of Varied Durations of Thermal Treatment on the Tensile Strength of Red Sandstone. *Rock Mechanics and Rock Engineering*, 50(1):205–213.

Stacey, T. (1981). A simple extension strain criterion for fracture of brittle rock. *International Journal of Rock Mechanics and Mining Sciences & Geomechanics Abstracts*, 18(6):469–474.

Stavrou, A. and Murphy, W. (2018). Quantifying the effects of scale and heterogeneity on the confined strength of micro-defected rocks. *International Journal of Rock Mechanics and Mining Sciences*, 102:131–143.

Stesky, R., Brace, W., Riley, D., and Robin, P.-Y. (1974). Friction in faulted rock at high temperature and pressure. *Tectonophysics*, 23(1-2):177–203.

Stesky, R. M. (1978). Rock Friction-Effect of Confining Pressure, Temperature, and Pore Pressure. *Pure and Applied Geophysics*, 116(4-5):609–704.

Stimpson, B. (1970). Modelling materials for engineering rock mechanics. *International Journal of Rock Mechanics and Mining Sciences and Geomechanics Abstracts*, 7(1):77–121.

Stone, P., Millward, D., Young, B., Merritt, J., Clarke, S., McCormac, M., and Lawrence, D. (2010). *British Regional Geology: Northern England*. Keyworth, Nottingham: British Geological Survey, fifth edition.

Tabor, D. (1975). A simplified account of surface topography and the contact between solids. *Wear*, 32(2):269–271.

Tatone, B. (2009). *Quantitative Characterization of Natural Rock Discontinuity Roughness In-situ and in the Laboratory*. Msc thesis, University of Toronto.

Tatone, B. (2014). *Investigating the evolution of rock discontinuity asperity degradation and void space morphology under direct shear*. PhD thesis, University of Toronto.

Tatone, B. S. and Grasselli, G. (2010). A new 2D discontinuity roughness parameter and its correlation with JRC. *International Journal of Rock Mechanics and Mining Sciences*, 47(8):1391–1400.

Thomas, T. and Sayles, R. (1977). Stiffness of Machine Tool Joints: a Random-Process Approach. In *Transactions of the ASME, Journal of Engineering for Industry*, pages 250–256.

Tse, R. and Cruden, D. (1979). Estimating joint roughness coefficients. *International Journal of Rock Mechanics and Mining Sciences & Geomechanics Abstracts*, 16(5):303–307.

Tullis, J. and Yund, R. (1977). Experimental deformation of dry Westerly granite. *Journal of Geophysical Research*, 82:5705–5718.

Tullis, T. and Weeks, J. (1986). Constitutive behaviour and stability of frictional sliding of granite. *Pure and Applied Geophysics*, 124(3):383.

Ulusay, R. (2014). *The ISRM Suggested Methods for Rock Characterization, Testing and Monitoring : 2007-2014*. Springer.

Vazaios, I. (2018). *Modelling of hard rock masses with non-persistent joints to assess the stress induced damage of deep excavations*. PhD thesis, Queen's University.

Vogler, D., Walsh, S. D., Bayer, P., and Amann, F. (2017). Comparison of Surface Properties in Natural and Artificially Generated Fractures in a Crystalline Rock. *Rock Mechanics and Rock Engineering*, pages 1–19.

Wang, X. Q., Schubnel, A., Fortin, J., Guéguen, Y., and Ge, H. K. (2013). Physical properties and brittle strength of thermally cracked granite under confinement. *Journal of Geophysical Research: Solid Earth*, 118(12):6099–6112.

Waples, D. W. and Waples, J. S. (2004). A review and evaluation of specific heat capacities of rocks, minerals, and subsurface fluids. Part 1: Minerals and nonporous rocks. *Natural Resources Research*, 13(2):97–122.

Widhalm, C., Tschegg, E., and Eppensteiner, W. (1997). Acoustic Emission and Anisotropic Expansion when Heating Marble. *Journal of Performance of Constructed Facilities*, 11(1):35–40.

Wong, L. N. Y. and Einstein, H. H. (2009). Crack coalescence in molded gypsum and carrara marble: Part 1. macroscopic observations and interpretation. *Rock Mechanics and Rock Engineering*, 42(3):475–511.

Wong, T.-f. (1982a). Effects of temperature and pressure on failure and post-failure behaviour of Westerly granite. *Mech Materials*, 1:13–17.

Wong, T.-f. (1982b). Shear fracture energy of Westerly Granite from post-failure behaviour. *Journal of Geophysical Research*, 87:990–1000.

Wong, T.-f. and Brace, W. (1979). Thermal expansion of rocks: some measurements at high pressure. *Tectonophysics*, 57(2-4):95–117.

Woodman, J., Murphy, W., Thomas, M., Ougier-Simonin, A., Reeves, H., and Berry, T. (2017). A novel approach to the laboratory testing of replica discontinuities : 3D printing representative morphologies. In *51st US Rock Mechanics / Geomechanics Symposium, San Francisco, California, USA, 25 - 28 June 2017*.

Wu, S. and Xu, X. (2016). A Study of Three Intrinsic Problems of the Classic Discrete Element Method Using Flat-Joint Model. *Rock Mechanics and Rock Engineering*, 49(5):1813–1830.

Yong, R., Ye, J., Li, B., and Du, S. G. (2018). Determining the maximum sampling interval in rock joint roughness measurements using Fourier series. *International Journal of Rock Mechanics and Mining Sciences*, 101:78–88.

Yow, J. and Wilder, D. (1994). Rock mass response to thermal loading and unloading of the spent fuel test. *International Journal of Rock Mechanics and Mining Sciences & Geomechanics Abstracts*, 31(4):186.

Yu, X. and Vayssade, B. (1991). Joint profiles and their roughness parameters. *International Journal of Rock Mechanics and Mining Sciences and Geomechanics Abstracts*, 28(4):333–336.

Zhang, K., Wu, M., and Feng, R. (2005). Simulation of microplasticity-induced deformation in uniaxially strained ceramics by 3-D Voronoi polycrystal modeling. *International Journal of Plasticity*, 21(4):801–834.

Zhang, Q., Li, X., Bai, B., and Hu, H. (2019). The shear behavior of sandstone joints under different fluid and temperature conditions. *Engineering Geology*, 257(May).

Zhang, T., Yue, X., Deng, Y., Zhang, D., and Liu, S. (2014). Mechanical behaviour and micro-structure of cement-stabilised marine clay with a metakaolin agent. *Construction and Building Materials*, 73:51–57.

Zhang, Y., Zhang, X., and Zhao, Y.-S. (2013). Process of Sandstone Thermal Cracking. *Chinese Journal of Geophysics*, 48(3):722–726.

Zhou, H., Liu, H., Hu, D., Yang, F., Lu, J., and Zhang, F. (2016). Anisotropies in Mechanical Behaviour, Thermal Expansion and P-Wave Velocity of Sandstone with Bedding Planes. *Rock Mechanics and Rock Engineering*, 49(11):4497–4504.

Zimmerman, R., Wilson, M., Board, M., Hall, E., and Schuch, R. (1985). Thermal-cycle testing of the G-Tunnel heated block. In *26th US Symposium on Rock Mechanics*, pages 749–758.

Appendix A

Properties of different synthetic compositions

A.1 Constituent ratios & mechanical behaviour of synthetic compositions

ID #	Mould	Constituent ratios[1]				Curing	Moisture Content	σ_3 (MPa)	Loading Rate	Peak Stress (MPa)	E[2] (GPa)	Comments
		Binder	Aggregate	H_2O	MK							
013	C1	1.00 (Port)	1.00 (BS)	0.40	0.00	28 days	Oven dried at 40°C	1.0	0.1 mm min^{-1}	35.93	-	Specimen continued absorbing strain post-peak. Macro-scopic failure did not occur.
014	C2	1.00 (Port)	1.00 (SS)	0.40	0.00	28 days	Oven dried at 40°C	1.0	0.1 mm min^{-1}	34.87	-	Macroscopic shear failure mechanism.
016	C1	1.00 (Port)	1.00 (BS)	0.40	0.00	28 days	Oven dried at 40°C	0.0	0.1 mm min^{-1}	32.92	7.45	Brittle failure. Single shear plane formed.
017	C2	1.00 (Port)	1.00 (SS)	0.40	0.00	28 days	Oven dried at 40°C	10.0	0.1 mm min^{-1}	66.37	-	Specimen continued strain hardening in completely ductile manner to 4.5% ε_a
020	C2	2.40 (Port)	4.00 (BS)	3.00	1.00	28 days	Oven dried at 40°C	5.0	0.1 mm min^{-1}	42.42	-	Specimen continued strain hardening in ductile manner to 3.0% ε_a
021	C1	2.40 (Port)	4.00 (SS)	3.00	1.00	28 days	Oven dried at 40°C	5.0	0.1 mm min^{-1}	52.38	-	Ductile strain hardening behaviour.

[1]All constituent ratios are provided as ratios by weight. Port = Ordinary Portland cement. CAC = Calcium aluminate cement. BS = Builders sand. SS = Sharp sand. Silica = Silica sand. Anda = Andalusite.

[2]For samples tested in triaxial conditions at the University of Leeds, no radial strain measurements were taken, meaning the volumetric deformation of the sample is unknown and therefore it is not possible to calculate E. Where E has been calculated, it has been calculated as the tangential Young's modulus at 50% of peak stress.

022	C2	2.40 (Port)	4.00 (SS)	3.00	1.00	28 days	Oven dried at 40°C	5.0	0.1 mm min^{-1}	50.49	-	Ductile strain hardening behaviour to 5.0% ε_a.
024	C1	2.40 (Port)	4.00 (SS)	3.00	1.00	28 days	Oven dried at 40°C	0.5	0.1 mm min^{-1}	25.91	-	Brittle failure with single shear plane.
050	C3	2.40 (Port)	4.00 (SS)	3.00	1.00	28 days	Oven dried at 40°C	0.0	0.1 mm min^{-1}	24.37	4.52	Brittle failure with shear failure.
063	C1	3.00 (Port)	4.00 (SS)	2.40	1.00	28 days	Oven dried at 40°C	5.0	0.1 mm min^{-1}	30.08	-	Strain hardening behaviour to 3.5% ε_a.
064	C2	3.00 (Port)	4.00 (SS)	2.40	1.00	28 days	Oven dried at 40°C	0.0	0.1 mm min^{-1}	16.81	2.39	Weak. Axial splitting/crumbling occurred.
065	C3	1.00 (Port)	2.50 (SS)	2.00	1.00	28 days	Oven dried at 40°C	0.0	0.1 mm min^{-1}	3.28	0.61	Specimen failed under pre-load.
067	C1	3.00 (Port)	4.00 (SS)	2.40	1.00	28 days	Oven dried at 40°C	10.0	0.1 mm min^{-1}	58.64	-	Ductile strain hardening behaviour to 4.0% ε_a.
069	C3	2.00 (Port)	4.00 (SS)	3.00	1.00	28 days	Oven dried at 40°C	0.0	0.1 mm min^{-1}	4.81	0.92	Specimen crumbled as soon as axial loading was initiated.
079	C3	1.00 (CAC)	0.13 (SS)	0.74	0.13	7 days	Oven dried at 40°C	0.0	0.1 mm min^{-1}	2.39	1.54	Specimen failed under pre-load.
083	C3	1.00 (CAC)	0.25 (SS)	0.43	0.00	7 days	Oven dried at 40°C	0.0	0.1 mm min^{-1}	29.62	3.69	Single shear plane formed.
084	C4	1.00 (CAC)	0.25 (SS)	1.13	0.13	7 days	Oven dried at 40°C	0.0	0.1 mm min^{-1}	0.34	9.58	Specimen failed under pre-load.

100	C3	1.00 (CAC)	1.50 (SS)	0.43	0.00	7 days	Oven dried at 40°C	0.0	0.1 mm min^{-1}	45.76	9.66	Quasi-brittle failure, with no macroscopic failure plane.
101	C4	1.00 (CAC)	1.50 (SS)	0.43	0.00	7 days	Oven dried at 40°C	0.0	0.1 mm min^{-1}	46.34	9.72	Quasi-brittle failure, stress drop after failure, but no macroscopic failure plane.
102	C4	1.00 (CAC)	3.00 (SS)	0.86	0.00	7 days	Oven dried at 40°C	0.0	0.1 mm min^{-1}	12.14	3.28	Single shear plane formed.
103	C2	1.00 (CAC)	1.50 (SS)	0.43	0.00	7 days	Oven dried at 40°C	0.0	0.1 mm min^{-1}	38.82	9.13	Quasi-brittle failure, with no macroscopic failure plane.
104	C1	1.00 (CAC)	2.00 (SS)	0.65	0.00	7 days	Oven dried at 40°C	0.0	0.1 mm min^{-1}	18.93	3.49	Single shear plane formed.
105	C2	1.00 (CAC)	2.00 (BS)	0.65	0.00	7 days	Oven dried at 40°C	3.0	0.1 mm min^{-1}	30.43	-	Specimen maintained peak strength with increasing strain for 3.0% ε_a.
106	C3	1.00 (CAC)	3.00 (SS)	0.86	0.00	7 days	Oven dried at 40°C	3.0	0.1 mm min^{-1}	23.94	-	Ductile strain hardening behaviour to 3.0% ε_a.
109	C3	1.00 (CAC)	1.50 (Silica)	0.55	0.00	7 days	Oven dried at 40°C	0.0	0.1 mm min^{-1}	29.12	5.14	Quasi-brittle failure.
111	C4	1.00 (CAC)	3.00 (Silica)	1.13	0.00	7 days	Oven dried at 40°C	0.0	0.1 mm min^{-1}	8.02	2.39	Specimen crumbled shortly after axial loading was initiated.

112	C3	1.00 (CAC)	1.50 (Anda)	0.43	0.00	7 days	Oven dried at 40°C	0.0	0.1 mm min^{-1}	41.79	6.05	Quasi-brittle failure, stress drop after failure, but no macroscopic failure plane.
113	C4	1.00 (CAC)	1.50 (Anda)	0.43	0.00	7 days	Oven dried at 40°C	3.0	0.1 mm min^{-1}	59.2	-	Quasi-brittle failure, stress drop after failure, but no macroscopic failure plane.
114	C1	1.00 (CAC)	1.50 (Anda)	0.43	0.00	7 days	Oven dried at 40°C	6.0	0.1 mm min^{-1}	69.31	-	Ductile failure, but not strain hardening.
115	C2	1.00 (CAC)	1.50 (Anda)	0.43	0.00	7 days	Oven dried at 40°C	0.0	0.1 mm min^{-1}	41.79	7.47	Quasi-brittle failure. No shear plane formed.
117	C4	1.00 (CAC)	1.80 (Anda)	0.6	0.00	7 days	Oven dried at 40°C	0.0	0.1 mm min^{-1}	21.3	6.23	Quasi-brittle failure.

Table A.1: Constituent ratios and the strength and stiffness behaviour of 20 synthetic compositions tested in an attempt to create a synthetic lithology representative of a lower strength sedimentary lithology.

A.2 Details of two synthetic compositions selected for further testing

ID #	Mould	Constituent ratios[1]				Curing	Moisture Content	σ_3 (MPa)	Loading Rate	Peak Stress (MPa)	E[2] (GPa)	ν[3]	Comments
		Binder	Aggregate	H_2O	MK								
032	C3	2.40	4.00	3.00	1.00	28 days	Oven dried at 40°C	5.00	5 x 10^{-6} $s^{-1}\varepsilon_a$	39.93	7.86	0.30	
033	C4	2.40	4.00	3.00	1.00	28 days	Oven dried at 40°C	5.00	5 x 10^{-6} $s^{-1}\varepsilon_a$	41.78	5.93	0.27	
038	C3	2.40	4.00	3.00	1.00	28 days	Oven dried at 40°C	10.00	5 x 10^{-6} $s^{-1}\varepsilon_a$	52.54	3.73	0.32	
039	C4	2.40	4.00	3.00	1.00	28 days	Oven dried at 40°C	15.00	5 x 10^{-6} $s^{-1}\varepsilon_a$	66.18	2.05	0.31	
051	C4	2.40	4.00	3.00	1.00	28 days	Oven dried at 40°C	5.00	5 x 10^{-6} $s^{-1}\varepsilon_a$	38.89	9.31	0.45	
085	C3	1.00	0.25	0.43	0.00	7 days	Oven dried at 40°C	5.00	5 x 10^{-6} $s^{-1}\varepsilon_a$	-	-	-	Specimen failed under pre-load. Possible equipment failure.
087	C3	1.00	0.25	0.43	0.00	7 days	Oven dried at 40°C	5.00	5 x 10^{-6} $s^{-1}\varepsilon_a$	0.00	0.00	0.00	
088	C4	1.00	0.25	0.43	0.00	7 days	Oven dried at 40°C	5.00	5 x 10^{-6} $s^{-1}\varepsilon_a$	51.25	11.99	0.46	

[1] All constituent ratios are provided as ratios by weight.
[2] Calculated as Tangential Young's modulus at 50% peak stress.
[3] Calculated as Tangential Poisson's ratio at 50% peak stress.

093	C3	1.00	0.25	0.43	0.00	7 days	Oven dried at 40°C	5.00[1]	5 x 10^{-6} s^{-1} ε_a	50.64	11.37	0.43

Table A.2: Constituent ratios and further strength and stiffness parameters of 2 synthetic compositions tested under higher stresses in triaxial conditions, in an attempt to create a synthetic lithology representative of a lower strength sedimentary lithology.

[1] A pre-consolidation phase was applied to the specimen prior to testing. The specimen was taken to 20 MPa σ_3 at 1 MPa min^{-1} and held for one hour, before being unloaded again. The test was then run as per the same procedure as all other tests.

Appendix B

Rock laboratory testing results

B.1 Characterisation testing of Thornhill Rock

Uniaxial and triaxial testing

Spec. #	**Length** mm	**Diam.** mm	ρ kg m^{-3}	φ	σ_3 MPa	**Peak** σ_1 MPa	E GPa	ν
270	117.8	53.96	2290.66	17.31%	0.0	49.12	6.68	0.24
271	118.70	54.01	2253.40	15.43%	0.0	32.06	7.66	0.28
272	119.87	53.87	2258.06	13.79%	0.0	47.91	8.3	0.28
273	85.46	39.68	2247.89	16.34%	0.0	58.12	9.71	0.24
274	86.79	39.14	2244.19	12.86%	0.0	47.81	8.34	0.21
275	84.39	39.69	2281.03	13.50%	0.0	65.70	11.33	0.25
276	80.11	36.78	2211.37	19.35%	0.0	55.81	10.16	0.26
277	86.29	39.96	2258.88	16.87%	0.0	50.73	8.21	0.21
207	122.76	54.45	2278.63	16.02%	0.0	51.29	8.70	
235	125.12	54.77	2215.62	16.67%	0.0	50.40	8.52	
250	89.1	36.54	2233.39	15.76%	4.0	97.00		
251	89.05	36.25	2225.69	13.84%	4.0	96.85		
252	85.70	36.94	2242.05	14.80%	4.0	90.34		
253	87.55	36.94	2241.88	15.79%	8.0	124.96		
254	88.40	36.03	2266.35	17.71%	8.0	125.20		
255	87.89	36.32	2228.77	14.95%	8.0	110.89		
256	89.87	36.51	2237.64	17.55%	12.0	142.93		
257	90.66	36.25	2275.36	16.13%	12.0	134.33		

Table B.1: Results of uniaxial and triaxial testing on specimens of Thornhill Rock.

Indirect tensile testing

Spec. #	**Length** mm	**Diam.** mm	ρ kg m^{-3}	φ	σ_t MPa
281	19.96	36.76	2246.18	15.91%	5.14
282	20.06	36.94	2253.45	14.46%	3.36
283	20.28	36.82	2253.81	14.16%	4.02
284	20.23	36.84	2263.07	15.29%	4.16
285	18.49	36.91	2279.79	15.17%	4.97
286	20.24	36.93	2278.33	13.03%	3.64
287	19.6	37.01	2273.52	16.03%	4.19

Table B.2: Results of indirect tensile testing on specimens of Thornhill Rock.

B.2 Characterisation testing of Midgley Grit

Uniaxial and triaxial testing

Spec. #	Length mm	Diam. mm	ρ kg m^{-3}	φ	σ_3 MPa	Peak σ_1 MPa	E GPa	ν
304	85.58	36.8	2202.69	13.35%	0.0	37.72	9.66	0.20
309	86.1	36.77	2219.87	13.41%	0.0	37.91	9.45	0.22
305	84.02	36.89	2268.69	13.51%	0.0	34.98	7.28	0.21
308	84.06	36.86	2207.67	13.30%	5.0	74.49		
318	89.44	40.32	2183.28	15.04%	5.0	70.08		
301	85.74	36.84	2234.81	13.09%	5.0	81.35		
306	84.69	36.88	2267.38	13.83%	10.0	96.47		
302	83.50	36.85	2221.69	13.71%	10.0	104.33		
319	88.69	40.32	2205.84	14.54%	10.0	105.66		
307	88.21	36.99	2200.41	13.31%	15.0	120.02		
320	89.36	40.33	2229.64	14.09%	15.0	120.21		
322	88.65	40.36	2219.27	13.78%	15.0	132.94		

Table B.3: Results of uniaxial and triaxial testing on specimens of Midgley Grit.

Indirect tensile testing

Spec. #	Length mm	Diam. mm	ρ kg m^{-3}	φ	σ_t MPa
311	20.05	36.87	2242.54	14.06%	2.13
312	16.08	36.94	2272.86	12.87%	2.15
313	20.55	36.83	2291.72	12.65%	1.84
314	22.23	36.76	2242.95	14.33%	1.51
315	17.30	36.81	2235.08	13.96%	1.66
316	19.82	36.81	2250.62	13.03%	2.11
317	20.33	36.81	2279.41	13.25%	2.09

Table B.4: Results of indirect tensile testing on specimens of Midgley Grit.

B.3 Intact thermo-mechanical testing of Thornhill Rock

Specimen #	**Batch**	**Temp.** °C	**Length** mm	**Diam.** mm	σ_3 MPa	**Peak diff. stress** MPa	E GPa	ν	**CI** MPa	**CD** MPa	α_L $10^{-6}\,K^{-1}$
210	3	21.8	125.14	54.38	5.00	83.24	16.44	0.216	34.78	59.61	—
223	3	17.7	129.26	54.02	5.00	81.15	15.59	0.218	35.25	60.41	—
231	3	54.0	124.96	54.45	5.00	77.04	16.32	0.220	33.64	59.08	3.17
213	3	55.2	126.05	54.41	5.00	80.88	16.51	0.218	33.52	58.93	5.07
236	3	51.9	124.57	54.52	5.00	79.92	12.85	0.211	33.08	60.37	3.78
216	3	79.2	126.70	54.43	5.00	78.15	15.87	0.214	31.82	28.84	1.53
209	3	101.0	126.91	54.45	5.00	67.67	15.72	0.234	29.27	52.10	3.20
565	4	24.0	128.80	54.02	5.00	99.45	13.81	0.202	38.93	74.45	—
566	4	20.1	124.71	54.04	5.00	97.21	15.90	0.185	40.03	74.76	—
504	4	56.3	119.79	53.98	5.00	89.09	15.55	0.202	37.05	66.82	3.15
503	4	53.4	117.65	53.98	5.00	89.41	15.64	0.203	35.68	67.00	4.29
501	4	75.2	121.46	53.99	5.00	85.72	15.78	0.212	35.40	63.67	3.78
505	4	74.8	119.22	53.99	5.00	87.57	15.77	0.206	36.23	64.64	2.99
562	4	100.0	124.46	53.98	5.00	83.32	15.47	0.210	35.22	62.38	3.43
563	4	100.0	129.97	54.00	5.00	82.94	15.00	0.215	33.84	61.31	3.19

Table B.5: Results of thermo-mechanical triaxial testing on intact specimens of Thornhill Rock.

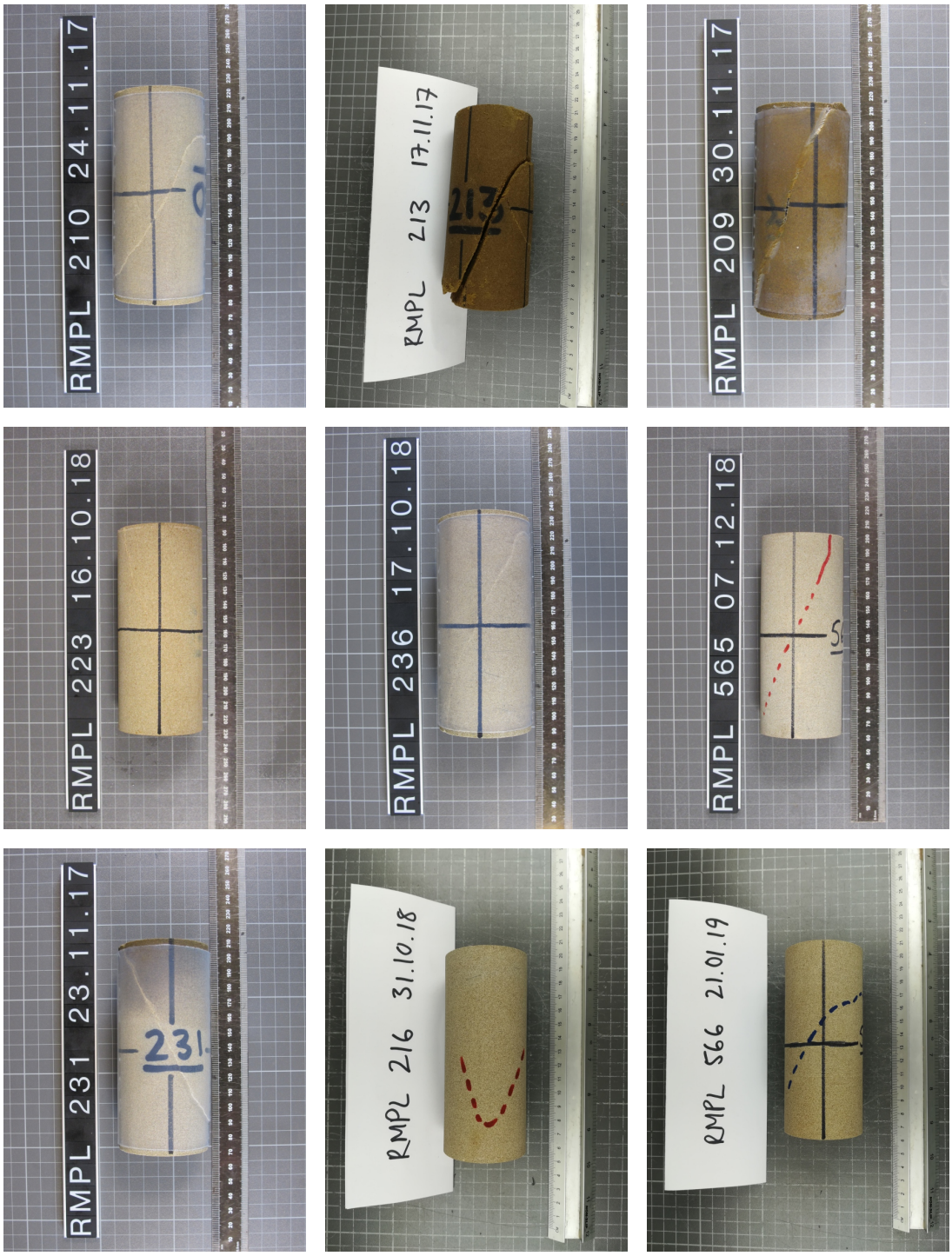

Figure B.1: Photographs of intact specimens of Thornhill Rock after thermo-mechanical triaxial testing.

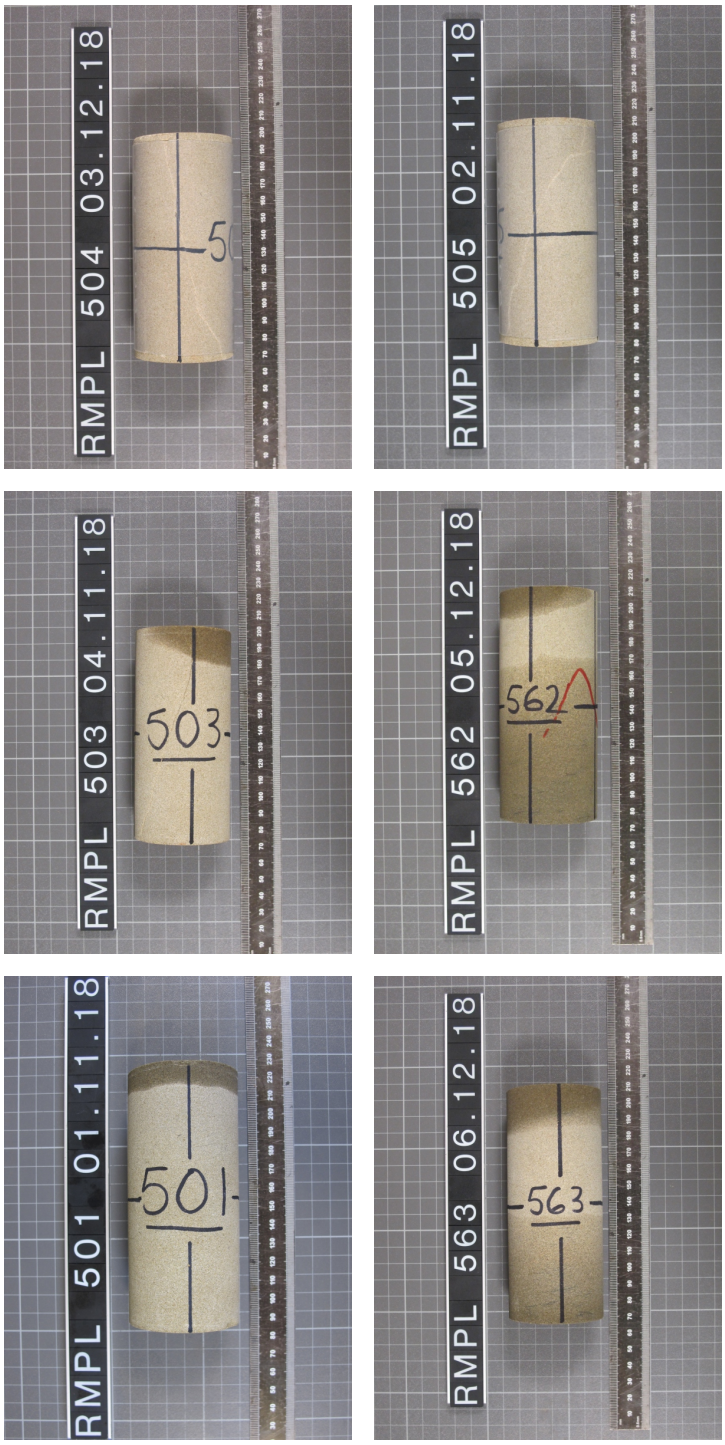

Figure B.2: Photographs of intact specimens of Thornhill Rock after thermo-mechanical triaxial testing.

B.4 Intact thermo-mechanical testing of Midgley Grit

Specimen #	**Batch**	**Temp.** °C	**Length** mm	**Diam.** mm	σ_3 MPa	**Peak diff. stress** MPa	E GPa	ν	**CI** MPa	**CD** MPa	α_L $10^{-6}\,K^{-1}$
450	2	101.5	134.79	54.04	5.00	62.42	20.03	0.262	25.11	46.68	1.38
451	2	60.8	136.10	54.90	5.00	64.67	19.57	0.260	28.28	46.40	1.22
452	2	23.1	134.91	54.92	5.00	67.31	22.23	0.225	30.05	49.74	—

Table B.6: Results of thermo-mechanical triaxial testing on intact specimens of Midgley Grit.

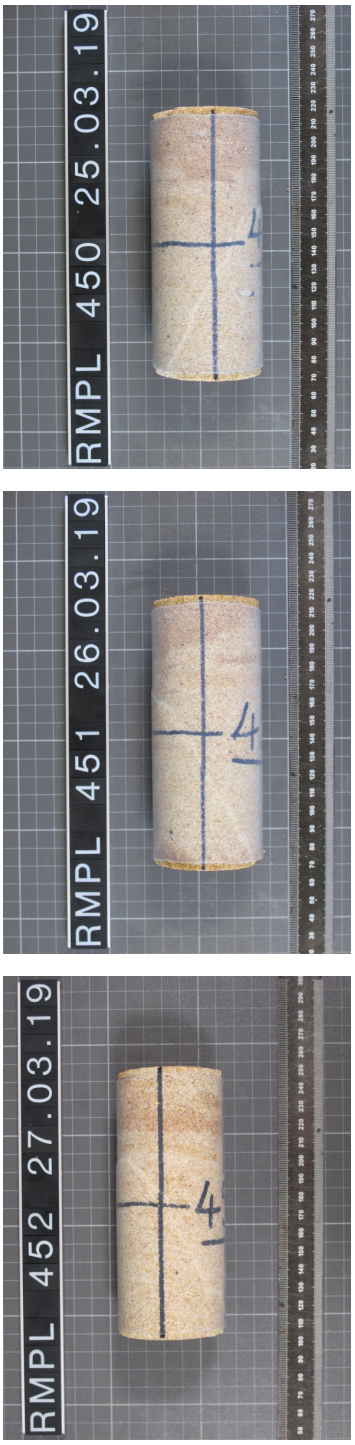

Figure B.3: Photographs of intact specimens of Midgley Grit after thermo-mechanical triaxial testing.

B.5 Discontinuous thermo-mechanical testing of Thornhill Rock

Specimen #	**Batch**	**Temp.** °C	**Roughness** JRC	**Length** mm	**Diameter** mm	β °	σ_3 MPa	τ_p MPa	τ_r MPa	G_c kJ m^{-2}	G_{c1} kJ m^{-2}	G_{c2} kJ m^{-2}	D_0 mm	D_a mm	D_c mm	D_{wc} mm
998	1	54.00	7.8	112.74	53.74	34	5.00	44.65	18.50	19.43	3.00	16.44	0.043	0.217	1.800	1.584
997	1	96.80	7.6	123.42	53.76	33	5.00	37.31	18.20	7.01	1.43	5.58	0.036	0.152	0.823	0.671
233	2	19.50	9.9	128.32	54.57	32	5.00	26.39	17.53	5.64	1.87	3.77	0.015	0.313	2.214	1.901
208	2	52.00	11.5	120.61	54.47	32	5.00	35.24	15.53	11.51	2.04	9.47	0.044	0.170	1.221	1.051
221	2	101.00	12.1	126.11	54.53	34	5.00	24.84	16.17	4.41	1.25	3.16	0.017	0.190	1.235	1.045
238	3	20.00	11.7	123.90	54.42	28	5.00	18.21	15.34	2.75	0.54	2.22	0.012	0.328	2.695	2.367
224	3	53.00	10.8	126.57	54.43	36	5.00	27.39	15.11	6.51	0.76	5.75	0.038	0.117	1.905	1.787
219	3	100.20	11.9	124.79	54.42	25	5.00	25.71	13.10	5.81	1.34	4.46	0.029	0.199	1.164	0.965
754	4	23.60	12.2	124.63	54.14	25	5.00	28.11	14.37	8.05	0.99	7.06	0.094	0.181	1.797	1.616
556	4	55.60	11.5	137.08	54.02	34	5.00	34.48	19.82	9.27	1.51	7.75	0.110	0.252	1.321	1.069
753	4	77.10	11.3	134.22	54.03	36	5.00	30.72	19.67	7.02	1.41	5.61	0.093	0.263	1.306	1.043
555	4	101.00	10.0	125.19	54.08	24	5.00	29.50	11.82	9.62	1.85	7.77	0.082	0.205	1.273	1.073
571	4	75.20	12.2	132.65	53.98	24	5.00	29.80	13.62	13.38	2.54	10.84	0.112	0.303	1.592	1.290
553	4	100.80	12.3	118.97	54.00	22	5.00	29.74	12.76	8.48	1.30	7.18	0.088	0.211	1.405	1.194
554	4	55.60	11.3	118.89	54.07	22	5.00	32.16	10.17	14.89	3.54	11.35	0.091	0.290	1.485	1.195
551	4	26.80	11.2	120.08	54.07	22	5.00	28.97	13.93	6.36	0.58	5.77	0.082	0.152	1.295	1.143

Table B.7: Results of thermo-mechanical triaxial testing on discontinuous specimens of Thornhill Rock.

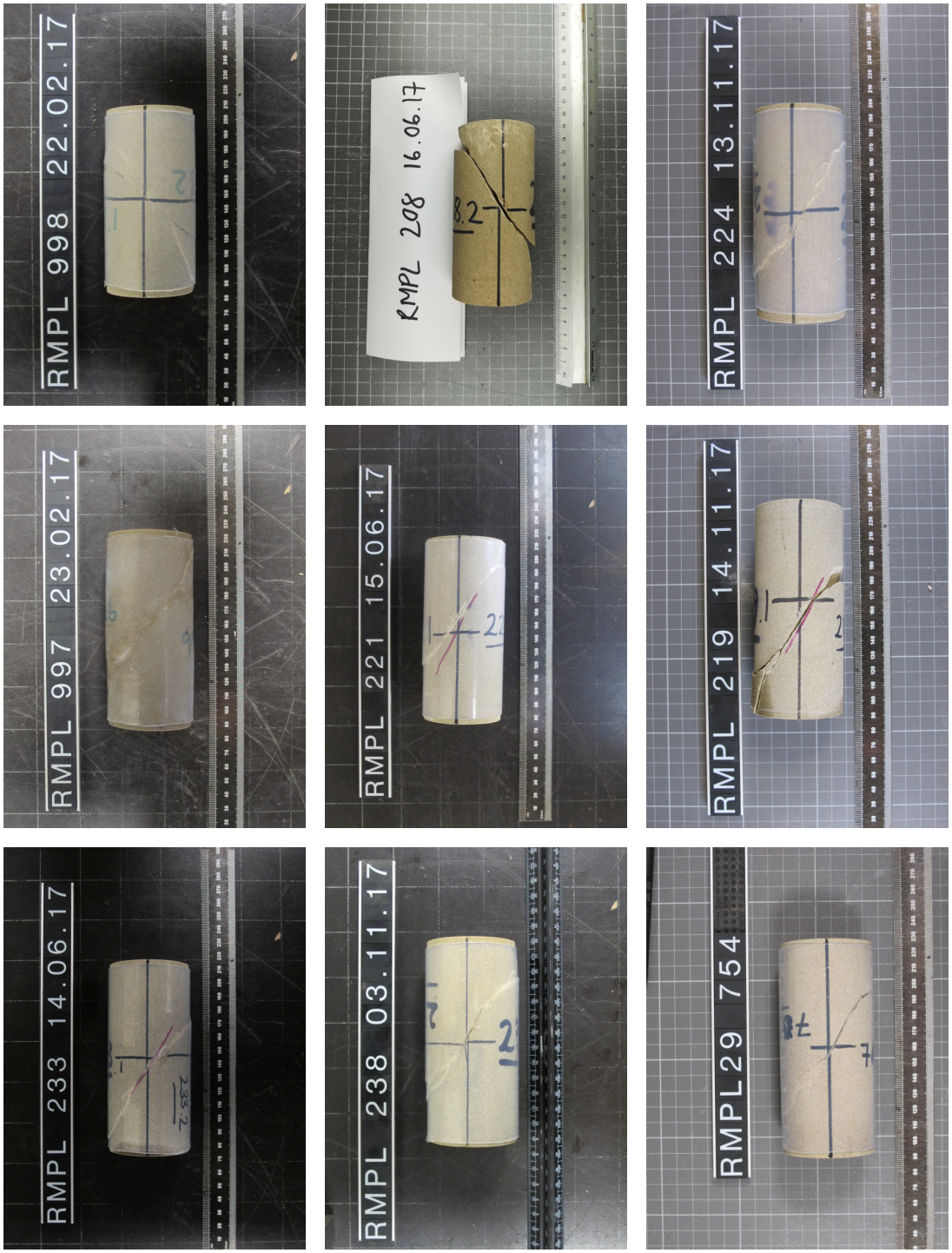

Figure B.4: Photographs of discontinuous specimens of Thornhill Rock after thermo-mechanical triaxial testing.

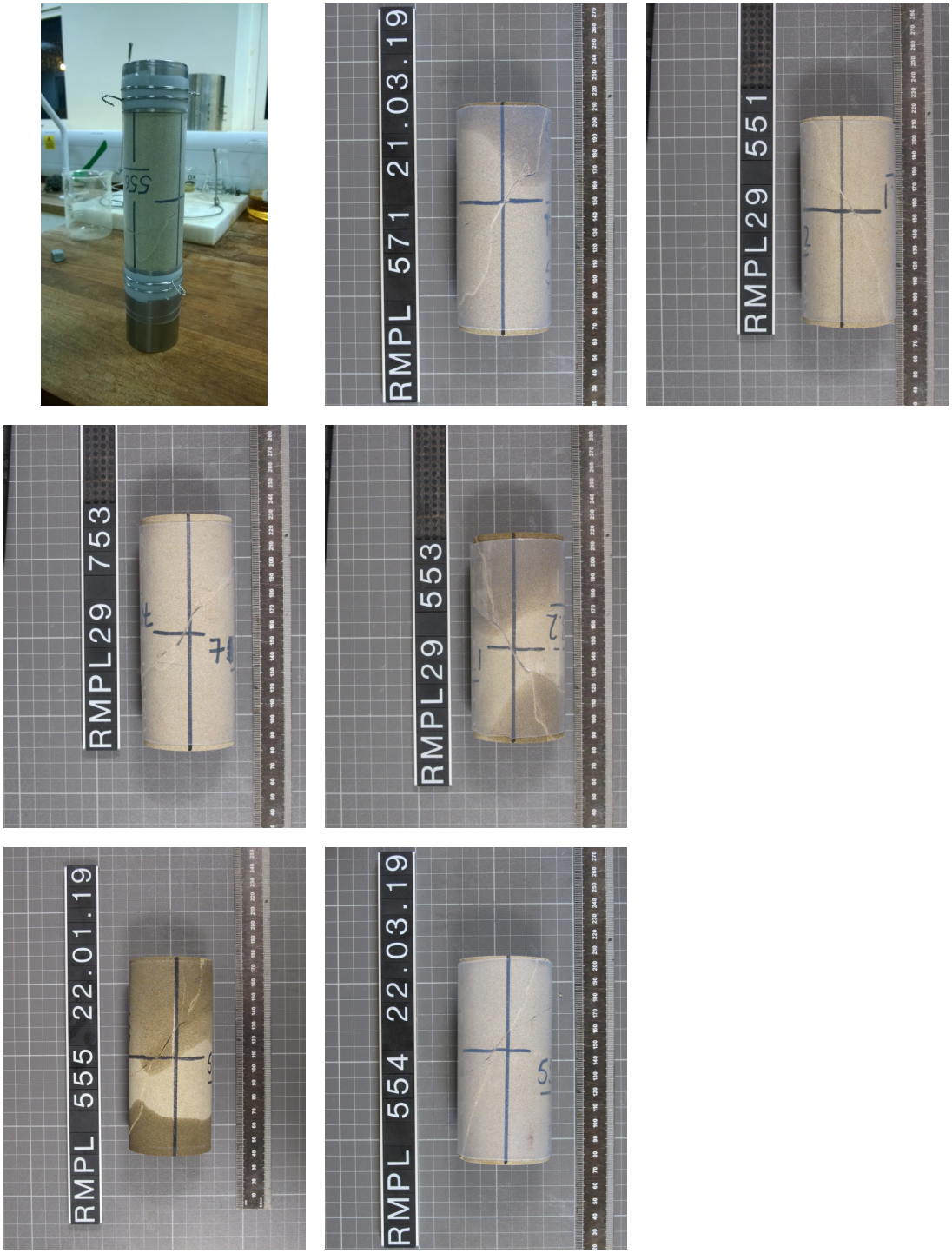

Figure B.5: Photographs of discontinuous specimens of Thornhill Rock after thermo-mechanical triaxial testing.

B.6 Discontinuous thermo-mechanical testing of Midgley Grit

Specimen #	**Batch**	**Temp.** °C	**Roughness** JRC	**Length** mm	**Diameter** mm	β °	σ_3 MPa	τ_p MPa	τ_r MPa	G_c kJ m^{-2}	G_{c1} kJ m^{-2}	G_{c2} kJ m^{-2}	D_0 mm	D_a mm	D_c mm	D_{wc} mm
993	1	18.50	16.9	122.65	53.84	30	5.00	27.27	14.10	16.30	1.85	14.44	0.007	0.242	3.244	3.002
975	1	20.80	16.4	119.39	53.93	28	5.00	20.89	13.11	5.96	1.05	4.91	0.029	0.209	4.271	4.062
979	2	23.70	17.3	126.91	54.45	26	5.00	26.43	12.25	13.86	2.49	11.37	0.033	0.262	3.079	2.817
990	1	56.00	16.5	121.28	53.82	37	5.00	24.54	18.04	10.04	1.83	8.21	0.032	0.370	3.521	3.151
974	1	53.00	16.7	125.33	54.02	30	5.00	26.75	11.76	9.86	1.84	8.02	0.042	0.186	2.733	2.546
992	1	100.50	16.2	117.77	53.82	23	5.00	20.09	12.06	10.27	2.47	7.80	0.005	0.411	2.699	2.288
976	1	100.00	13.9	122.63	53.99	35	5.00	16.54	11.99	2.89	0.87	2.02	0.008	0.273	1.681	1.408

Table B.8: Results of thermo-mechanical triaxial testing on discontinuous specimens of Midgley Grit.

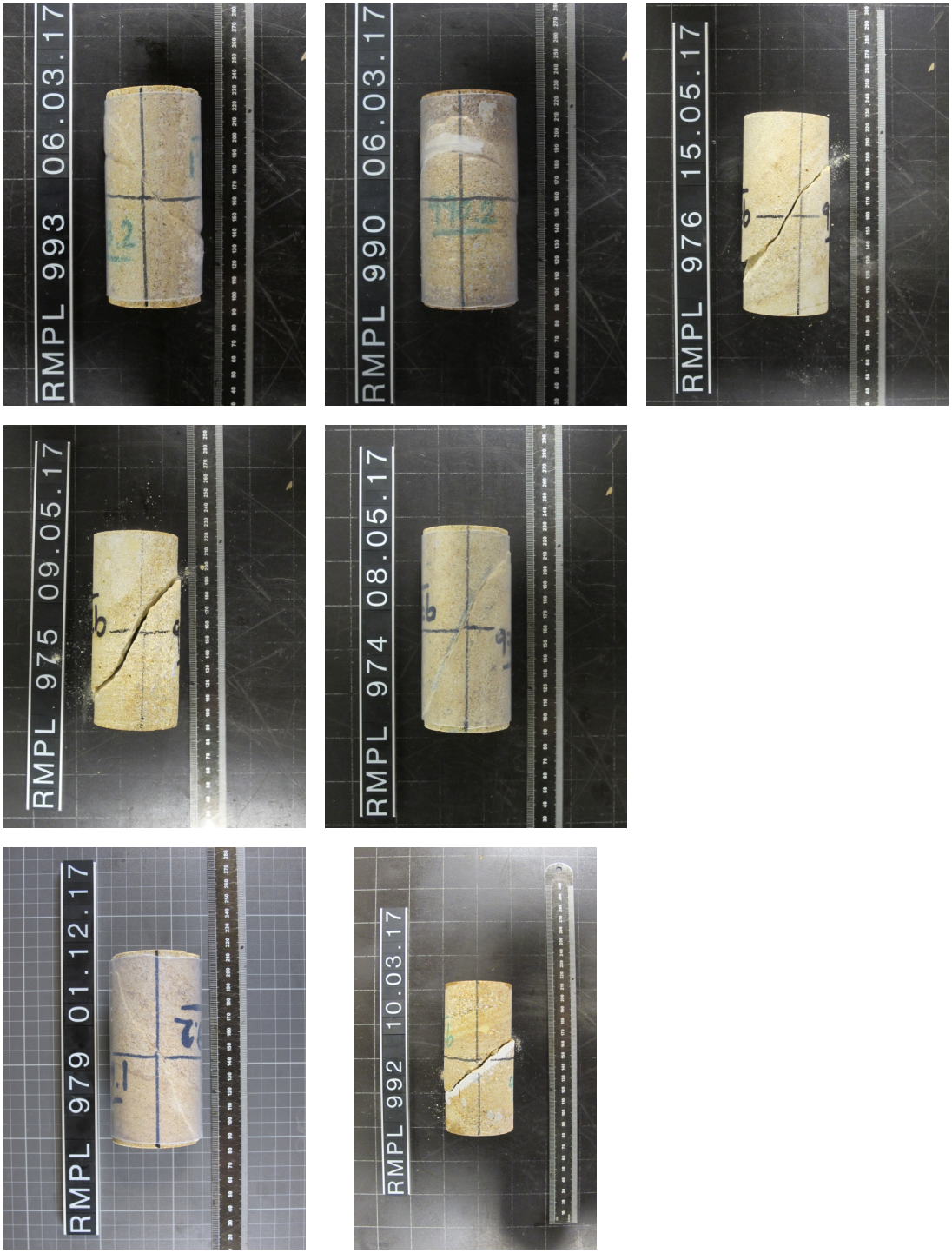

Figure B.6: Photographs of discontinuous specimens of Midgley Grit after thermo-mechanical triaxial testing.

Appendix C

UDEC modelling - *FISH* scripts & model run times

C.1 UDEC theory and calculation schemes

The following sections outline the equations of motion, conservation of momentum and energy equations, contact detection schemes, block deformability equations and mechanical damping schemes for the 2D distinct element method utilised in UDEC. Further details can also be found in Itasca (2014b).

C.1.1 DEM overview

When the distinct element method (DEM) is employed, the rockmass is represented as an assembly of discrete blocks. Discontinuities are simulated as interfaces between the distinct bodies with them being treated as boundary conditions. The movements of the blocks are traced and through a series of calculations the contact forces and displacements at the interfaces of the stressed block assembly are determined. The propagation of disturbances caused by applied loads or body forces results in movements, and the speed of propagation depends on the physical properties of the discrete system. The numerical representation of the dynamic response of the system is conducted by a time-stepping algorithm with the time step size constrained by the assumption that velocities and accelerations are constant within the time step. The DEM method is based on the concept of a sufficiently small time step so that during a single step disturbances do not propagate between a discrete body and the neighbours within its immediate vicinity, since the information transmission in any physical medium has a limited speed. The performed calculations can be divided into two groups including (i) the application of a force-displacement law at all interfaces, and (ii) Newton's second law at all blocks. Contact forces from known (and fixed) displacements are calculated based on the force-displacement law, and Newton's second law is utilised to calculate the motion of the blocks due to the known (and fixed) forces acting on them. In the case of deformable blocks motion, the grid points of triangular finite-strain elements within the blocks are used to calculate the motion. In Fig. C.1 the calculation cycle for the DEM method is demonstrated. The equations in Fig. C.1 are further discussed in the following sections.

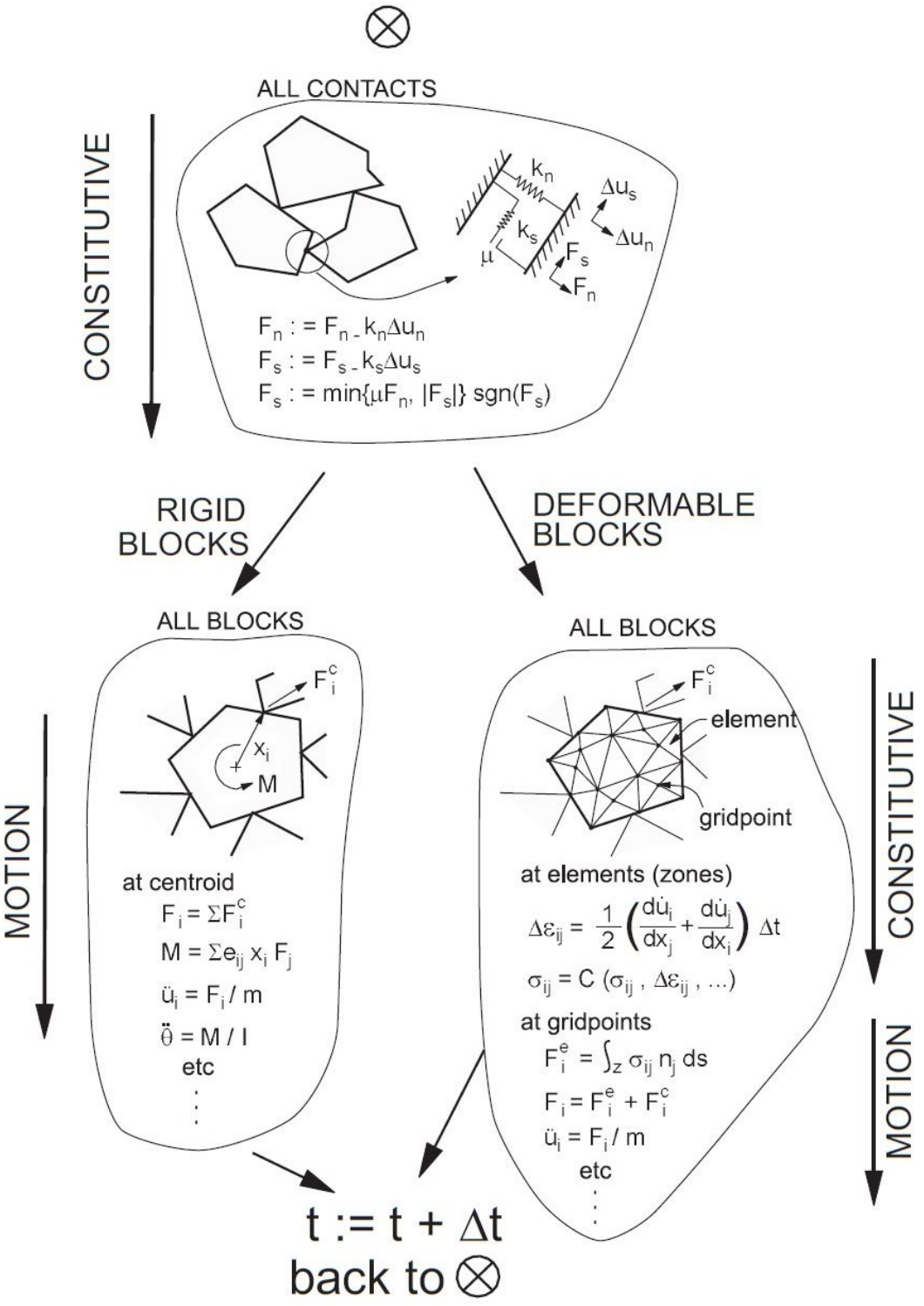

Figure C.1: Calculation cycle for the distinct element method

C.1.2 Equations of motion

The motion of an individual block is determined by the magnitude and direction of resultant out-of-balance moment and forces acting on it. The equations of motion that describe translation and rotation of the block about its centroid are outlined in this section. Consider the one-dimensional motion of a single mass acted on by a varying force, $F(t)$. Newton's second law of motion can be written as:

$$\frac{d\dot{u}}{dt} = \frac{F}{m} \tag{C.1}$$

where $\dot{u}$ is velocity, t is time and m is mass. The central difference scheme for the left-hand side of Eq. C.1 at time t can be written as:

$$\frac{d\dot{u}}{dt} = \frac{\dot{u}^{(t+\Delta t/2)} - \dot{u}^{(t-\Delta t/2)}}{\Delta t} \tag{C.2}$$

Substituting Eq. C.2 in Eq. C.1 and rearranging gives:

$$\dot{u}^{(t+\Delta t/2)} = \dot{u}^{(t-\Delta t/2)} + \frac{F^{(t)}}{m}\Delta t \tag{C.3}$$

With velocities stored at the half-timestep point, it is possible to express displacement as:

$$\dot{u}^{(t+\Delta t)} = \dot{u}^{(t)} + \dot{u}^{(t+\Delta t/2)}\Delta t \tag{C.4}$$

Because the force depends on displacement, the force/displacement calculation is performed at one time instant. For blocks in two dimensions that are acted upon by several forces as well as gravity, the velocity equations become:

$$\begin{aligned} \dot{u}_i^{(t+\Delta t/2)} &= \dot{u}_i^{(t-\Delta t/2)} + \left(\frac{\sum F_i^{(t)}}{m} + g_i\right)\Delta t \\ \dot{\Theta}^{(t+\Delta t/2)} &= \dot{\Theta}^{(t-\Delta t/2)} + \left(\frac{\sum M^{(t)}}{I}\right)\Delta t \end{aligned} \tag{C.5}$$

where $\dot{\Theta}$ is the angular velocity of a block about its centroid, I is the moment of inertia of the block, $\sum M$ is the total moment acting on the block, $\dot{u}_i$ is the velocity components of the block centroid, and g_i are the components of gravitational acceleration.

The new velocities in Eq. C.5 are used to determine the new block location as:

$$\begin{aligned} x_i^{(t+\Delta t)} &= x_i^{(t)} + \dot{u}_i^{(t+\Delta t/2)} \Delta t \\ \Theta^{(t+\Delta t)} &= \Theta^{(t)} + \dot{\Theta}^{(t+\Delta t/2)} \Delta t \end{aligned} \tag{C.6}$$

where Θ is the rotation of the block about its centroid, and x_i are the coordinates of the block centroid. In summary, each timestep produces new block positions that generate new contact forces. Resultant forces and moments are used to calculate linear and angular accelerations of each block. Block velocities and displacements are determined by integration over increments in time. The procedure is repeated until either a satisfactory state of equilibrium or one containing failure results. Mechanical damping is utilised in the equations of motion (Eq. C.5) to provide both static and dynamic solutions.

C.1.3 Conservation of momentum and energy

The distinct element method can be shown to satisfy conservation laws based on Newton's laws of motion. The equations used in UDEC are based on the interaction of bodies by means of springs, and the response of the bodies to applied forces. Although the following equations show that the conservation laws are satisfied exactly by using Newton's laws of motion, there will be some error introduced in the computer program by the numerical integration process; however, this error may be made arbitrarily small by the use of suitable timesteps.

Momentum balance can be shown by considering two bodies (denoted by subscripts $_{\mathrm{a}}$ and $_{\mathrm{b}}$) in contact for a period T. By Newton's laws, a common force F, acts in opposite directions on the two bodies, which accelerate in proportion to the forces:

$$m_a \ddot{u}_a = F \tag{C.7}$$

$$m_b \ddot{u}_b = -F \tag{C.8}$$

Combining Eq.'s C.7 and C.8 and integrating gives:

$$\int_0^{\mathrm{T}} m_a \ddot{u}_a dt = -\int_0^{\mathrm{T}} m_b \ddot{u}_b dt \tag{C.9}$$

$$m_a(\dot{u}_a^{(\mathrm{T})} - \dot{u}_a^{(0)}) = -m_b(\dot{u}_b^{(\mathrm{T})} - \dot{u}_b^{(0)}) \tag{C.10}$$

$$m_a \dot{u}_a^{(\mathrm{T})} + m_b \dot{u}_b^{(\mathrm{T})} = m_a \dot{u}_a^{(0)} + m_b \dot{u}_b^{(0)} \tag{C.11}$$

Eq. C.11 shows that the total momentum at the end of an arbitrary time period is identical to that at the beginning.

Energy balance can be demonstrated with a body with initial velocity v_0 brought to a final velocity of v in a distance, S, by a constant force, F:

$$m\dot{v} = F \tag{C.12}$$

Using the identity $\dot{v} = vdv/ds$:

$$m\int_{v_0}^{v} vdv = \int_0^S Fds \tag{C.13}$$

assuming m is constant gives:

$$\frac{1}{2}m(v^2 - v_0^2) = FS \tag{C.14}$$

Eq. C.14 shows that the work done by the force is equal to the change in kinetic energy of the body. If the force opposing motion is related to the displacement by the equation ($F = -ks$), where k denotes the spring stiffness, then Eq. C.13 can be re-written as:

$$m\int_{v_0}^{v} vdv = -\int_0^S ksds \tag{C.15}$$

Giving:

$$\frac{1}{2}m(v_0^2 - v^2) = \frac{1}{2}kS^2 \tag{C.16}$$

In this case, the decrease in kinetic energy equals the energy stored in the spring. The same argument may be used in reverse to show that the kinetic energy acquired by a body is equal to the decrease in energy stored in a spring. Hence, the kinetic energy of a body after an elastic collision is equal to the kinetic energy before the collision.

C.1.4 Discontinuity representation

A discontinuity is represented numerically as a contact surface (composed of individual point contacts) formed between two block edges. In general, for each pair of blocks that touch, data elements are created to represent point contacts. In UDEC, adjacent blocks can touch along a common edge segment or at discrete points where a corner meets an edge or another corner. When blocks are deformable (internally discretised), point contacts are created at all gridpoints located on the block edge in contact. Thus, the number of contact points can be increased as a function of the internal zoning of the adjacent blocks.

A specific problem with contact schemes is the unrealistic response that can result when block interaction occurs close to, or at, two opposing block corners. Numerically, blocks may become locked. This is a result of the modelling assumption that block corners are sharp or have infinite strength. In reality, crushing of the corners would occur as a result of a stress concentration. Explicit modelling of this effect is impractical. However, a realistic representation can be achieved by rounding the corners so that blocks can smoothly slide part one another when two opposing corners interact. Corner rounding is used in UDEC by specifying a circular arc for each block corner. The arc is defined by the distance from the true apex to the point of tangency with the adjoining edges. A rounding length of 0.03 mm is used in all simulations in this study and contact points are updated automatically as block motion occurs.

C.1.5 Block deformability

Blocks in UDEC may be rigid or deformable. The Voronoi blocks used in numerical simulations throughout this study are made deformable. Each Voronoi block is internally discretised into finite-difference triangular elements, with an average edge length of 3 mm. Fig. C.2 illustrates a generic example of blocks in UDEC further discretised into finite-difference triangular elements. The use of triangular elements eliminates the problem of hourglass deformations that may occur if using constrain-strain fiinite-difference quadrilaterals.

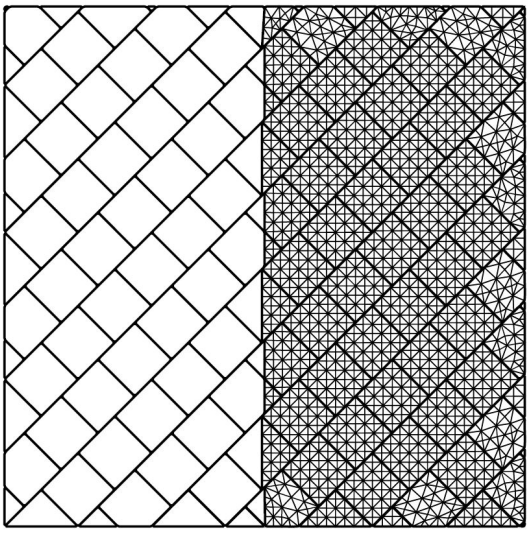

(a) distinct element blocks (b) zoning within blocks

Figure C.2: Zoning within a model containing a system of persistent and incipient discontinuities

The vertices of the triangular elements are gridpoints, and the equations of motion for each gridpoint are formulated as:

$$\ddot{u}_i = \frac{\int_s \sigma_{ij} n_j ds + F_i}{m} + g_i \tag{C.17}$$

where s is the surface enclosing the mass, m, lumped at the gridpoint. n_j is the unit normal to s. F_i is the resultant of all external forces applied to the gridpoint and g_i is the gravitational acceleration.

C.2 Model run times

The numerical simulations presented in this thesis were carried out using the Universal Distinct Element Code (UDEC) v.6 software by Itasca (Itasca, 2014a). The run times of selected simulations are tabulated in Table C.1. The software was run on a personal computer with an Intel Xeon E5-2650 CPU @ 2.60 GB with 64.0 GB of RAM. Descriptions of the different models can be found throughout Chapter 6.

Model	No. of Voronoi blocks	Mechanical timestep (s)	No. of mechanical timesteps	Thermal timestep (s)	No. of thermal timesteps	Total run time (hr)
Mechanical UCS test	≈ 780	1.26×10^{-7}	7.5×10^{5}	—	—	3.00
Mechanical triaxial test	≈ 780	1.26×10^{-7}	1.3×10^{6}	—	—	7.00
Brazilian disc test	≈ 280	1.21×10^{-7}	3×10^{5}	—	—	0.25
Intact thermo-mechanical triaxial test (50 °C)	≈ 780	1.92×10^{-8}	1.7×10^{7}	3×10^{-5}	6.60×10^{7}	≈ 168
Intact thermo-mechanical triaxial test (75 °C)	≈ 780	1.92×10^{-8}	2.3×10^{7}	3×10^{-5}	1.14×10^{8}	≈ 222
Intact thermo-mechanical triaxial test (100 °C)	≈ 780	1.92×10^{-8}	3×10^{7}	3×10^{-5}	1.65×10^{8}	≈ 273
Discontinuity normal stiffness test	≈ 800	1.23×10^{-7}	9×10^{5}	—	—	4
Discontinuity thermo-mechanical triaxial test	≈ 800	1.92×10^{-8}	3×10^{7}	3×10^{-5}	1.65×10^{8}	≈ 273

Table C.1: Run times of selected UDEC grain based models.

C.3 *FISH* script to monitor axial stress

```
; Contacts along the imaginary crack in the top platen
; are assigned material 4 properties

def sigma_v
whilestepping
sum_up=0.0
num_up=0.0
ic=contact_head
loop while ic # 0
if c_mat(ic) = 4 then
sum_up=sum_up+c_nforce(ic)
num_up=num_up+1
endif
ic=c_next(ic)
endloop
compress_up=sum_up
sigma_v=compress_up/bl_right
end
```

C.4 *FISH* script to monitor micro-cracking

```
def frac_count
whilestepping
ic=contact_head
unfractured = 0
no_of_contact = 0
shear_frac = 0
ten_frac = 0
loop while ic # 0
normal_force = 0
if (imem(ic+$MCCON)) = 5 then
no_of_contact = no_of_contact + 1
endif
if (imem(ic+$KGAM)) = 0 then
unfractured = unfractured + 1
endif
if (imem(ic+$KGAM)) # 0 then
normal_force = (fmem(ic+$KCFN))
if normal_force > 0.0 then
shear_frac = shear_frac + 1
endif
if normal_force <= 0.0 then
ten_frac = ten_frac + 1
endif
endif
ic=c_next(ic)
endloop
frac_count = no_of_contact - unfractured
end
```

C.5 *FISH* script to assign material properties

```
;----------
; Define Material Properties
;----------
;
def rockprop
;define the voronoi block properties
d = 2220.0 ;density
e = 30.30E9 ;youngs modulus
v = 0.21 ;poissons ratio
;calculate bulk and shear modulus from E & v
k = e/(3.0*(1.0-2.0*v)) ;bulk modulus
g = e/(2.0*(1.0+v)) ;shear modulus
;
;define the voronoi contact properties
j_kn = 22738.67E9 ;contact normal stiffness
j_ks = 5983.86E9 ;contact shear stiffness
j_c = 36.0E6 ;contact cohesion
j_f = 20.00 ;contact friction angle
j_t = 3.5E6 ;contact tensile strength
j_rc = 0.0 ;contact residual cohesion
j_rf  = 15.0 ;contact residual friction angle
j_rt = 0.0 ;contact residual tensile strength
;
end
rockprop
;
;----------
; Define Thermal Properties
;----------
;
def thermprop
;define the thermal properties of the voronoi blocks
```

```
;
;quartz
thermexp_1 = 1.60e-5
thermcond_1 = 7.69
specheatcap_1 = 698.0
;
;muscovite
thermexp_2 = 1.16e-5
thermcond_2      = 2.32
specheatcap_2 = 700.0
;
;albite
thermexp_3 = 0.54e-5
thermcond_3      = 2.31
specheatcap_3 = 709.0
;
;chlorite
thermexp_4 = 0.90e-5
thermcond_4 = 5.14
specheatcap_4 = 700.0
;
;kaolinite
thermexp_5 = 1.86e-5
thermcond_5 = 0.30
specheatcap_5 = 945.0
;
;microcline
thermexp_6 = 0.53e-5
thermcond_6 = 2.49
specheatcap_6 = 680.0
;
;define the thermal properties of the platens
p_thermexp = 12.5e-6 ;thermal expansion coefficient of steel
```

```
   platens
p_thermcond = 20.0 ;thermal conductivity of steel platens
p_specheatcap = 500.0 ;specific heat capacity of steel platens
;
end
thermprop
;
;----------
;Define Block Models and Apply Block Properties
;----------
;
;changes block material properties to isotropic, elastic for
   the sample region
change cons=1 range 0.0 0.054 0.030 0.150
;
;assign thermal properties in correct percentages
;assign qtz properties to 75% grains
property mat=1 density d bulk k shear g cond thermcond_1 thexp
    thermexp_1 specheat specheatcap_1 ID3
property mat=2 density d bulk k shear g cond thermcond_1 thexp
    thermexp_1 specheat specheatcap_1 ID3
property mat=3 density d bulk k shear g cond thermcond_1 thexp
    thermexp_1 specheat specheatcap_1 ID3
property mat=4 density d bulk k shear g cond thermcond_1 thexp
    thermexp_1 specheat specheatcap_1 ID3
property mat=5 density d bulk k shear g cond thermcond_1 thexp
    thermexp_1 specheat specheatcap_1 ID3
property mat=6 density d bulk k shear g cond thermcond_1 thexp
    thermexp_1 specheat specheatcap_1 ID3
property mat=7 density d bulk k shear g cond thermcond_1 thexp
    thermexp_1 specheat specheatcap_1 ID3
property mat=8 density d bulk k shear g cond thermcond_1 thexp
    thermexp_1 specheat specheatcap_1 ID3
```

```
property mat=9 density d bulk k shear g cond thermcond_1 thexp
    thermexp_1 specheat specheatcap_1 ID3
property mat=10 density d bulk k shear g cond thermcond_1
   thexp thermexp_1 specheat specheatcap_1 ID3
property mat=11 density d bulk k shear g cond thermcond_1
   thexp thermexp_1 specheat specheatcap_1 ID3
property mat=12 density d bulk k shear g cond thermcond_1
   thexp thermexp_1 specheat specheatcap_1 ID3
property mat=13 density d bulk k shear g cond thermcond_1
   thexp thermexp_1 specheat specheatcap_1 ID3
property mat=14 density d bulk k shear g cond thermcond_1
   thexp thermexp_1 specheat specheatcap_1 ID3
property mat=15 density d bulk k shear g cond thermcond_1
   thexp thermexp_1 specheat specheatcap_1 ID3
;
;assign muscovite to 5% of grains
property mat=16 density d bulk k shear g cond thermcond_2
   thexp thermexp_2 specheat specheatcap_2 ID4
;
;assign albite to 5% of grains
property mat=17 density d bulk k shear g cond thermcond_3
   thexp thermexp_3 specheat specheatcap_3 ID5
;
;assign kaolinite to 5% of grains
property mat=18 density d bulk k shear g cond thermcond_5
   thexp thermexp_5 specheat specheatcap_5 ID7
;
;assign microcline to 10% of grains
property mat=19 density d bulk k shear g cond thermcond_6
   thexp thermexp_6 specheat specheatcap_6 ID8
property mat=20 density d bulk k shear g cond thermcond_6
   thexp thermexp_6 specheat specheatcap_6 ID8
;
```

```
;----------
; Apply Block Properties
;----------
;
;loop through all blocks assigning thermal properties 1 to 6.
def ndisbl
bi = block_head
counter = 0
loop while bi # 0
_counter = _counter + 1
if _counter = 21
_counter = 1
endif
b_mat(bi) = _counter
bi = b_next(bi)
endloop
end
ndisbl
;
;----------
;Change Constitutive Models & Apply Contact Properties
;----------
;
group zone 'voronoi' range jreg 1       ; groups jreg 1 (the
   sample) in to group 'voronoi'
group zone 'platen' range jreg 2        ; groups jreg 2 (the
   bottom platen) in to group 'platen'
group zone 'platen' range jreg 3        ; groups jreg 3 (the
   top platen) in to group 'platen'
zone model elastic density 7750 shear 80.0E9 bulk 160.0E9 cond
    p_thermcond thexp p_thermexp specheat p_specheatcap range
   jreg 2 ; applies mechanical and thermal properties of steel
    to the platens
```

```
zone model elastic density 7750 shear 80.0E9 bulk 160.0E9 cond
    p_thermcond thexp p_thermexp specheat p_specheatcap range
   jreg 3 ; applies mechanical and thermal properties of steel
    to the platens
;
; apply friction to sample/platen contact
joint model area jkn=j_kn jks=j_ks jcoh=1E10 jfric=0.01 jten=1
   E10 range ID 11
;
; applies joint properties to the monitoring crack at the
   middle of the top platen
prop jmat=4 jkn=j_kn jks=j_ks jcoh=1E10 jfric=50 jten=1E10
change jmat=4 range ID 22
;
; Apply Coulomb slip model with residual strength to voronoi
joint model residual jkn=j_kn jks=j_ks jfric=j_f jrfric=j_rf
   jcoh=j_c jrcoh=j_rc  jten=j_t  jrten=j_rt range jreg 1
;
set jcondf joint model residual jkn=j_kn jks=j_ks jfric=j_f
   jrfric=j_rf jcoh=j_c jrcoh=j_rc  jten=j_t  jrten=j_rt
;
```